Light Separation in an ideal Water-Based Liquid Scintillator Detector

Dissertation
zur Erlangung des Doktorgrades
an der Fakultät für Mathematik, Informatik und
Naturwissenschaften
Fachbereich Physik
Universität Hamburg

vorgelegt von
Malte Niklas Stender

Hamburg
2023

Gutachter/innen der Dissertation: Prof. Dr. Caren Ines Hagner
Dr. Björn Sönke Wonsak

Zusammensetzung der Prüfungskommission: Prof. Dr. Caren Ines Hagner
Dr. Sarah Heim
Prof. Dr. Gudrid Moortgat-Pick
Prof. Dr. Peter Schleper
Dr. Björn Sönke Wonsak

Vorsitzender der Prüfungskommission: Prof. Dr. Peter Schleper

Datum der Disputation: 11.12.2023

Vorsitzender Fach-Promotionsausschuss PHYSIK: Prof. Dr. Günter H. W. Sigl

Leiter des Fachbereichs PHYSIK: Prof. Dr. Wolfgang J. Parak

Dekan der Fakultät MIN: Prof. Dr.-Ing. Norbert Ritter

Abstract

For many years unsegmented Liquid Scintillator (LS) and Water-Cherenkov (WC) detectors have made spectacular contributions to the field of neutrino physics. In recent years, the idea of mixing these detector types is pursued with using e.g. Water-based Liquid Scintillator (WbLS) as active medium, which gives access to Cherenkov radiation and scintillation light at once. This is desirable because of the advantages of both light types. The direction reconstruction of low energetic electrons ($< 10\,\mathrm{MeV}$) is an area, where Cherenkov radiation stands out. The lower energy threshold and the proportionality of the photon yield to the deposited energy makes scintillation light well suited for calorimetry. These advantages are only accessible though, when the photon hits on the photodetectors can be assigned to the light types and therefore a light separation can be conducted.
Here this thesis comes into play with a small and idealised WbLS detector with a radius of $2.185\,\mathrm{m}$ and a height of $4.285\,\mathrm{m}$, that was simulated with Geant4. This detector is completely covered with novel photosensors in form of the Large Area Picosecond Photodetector (LAPPD). These photodetectors are with a time and a spatial resolution of under $100\,\mathrm{ps}$ and $5\,\mathrm{mm}$ best suited to separate Cherenkov and scintillation photons based on their spatial and timing characteristics.
With help of simulated events in the low energy regime, a successful light separation algorithm is developed based on the Topological Track Reconstruction (TTR). The samples in question are $12,000$ events of electron, muon and gamma type below $120\,\mathrm{MeV}$ and $14,000$ events of proton type below $140\,\mathrm{MeV}$. Additionally, $10,000$ electron events with energies below $10\,\mathrm{MeV}$ are investigated.
In the best performing interval in terms of energy, purities from $(68 \pm 22)\,\%$ ($\pm 1\,\sigma$) for the muon sample to $(81 \pm 8)\,\%$ for the electron sample are reached with a simultaneous efficiency of $(75 \pm 31)\,\%$ and $(87 \pm 15)\,\%$ for the separation of Cherenkov and scintillation photons.
Based on that, the direction of the low energy electrons were determined with a maximum precision of $(13.45 \pm 11.22)°$. A result that hints that this detector technology could be used to suppress background from solar neutrinos based on the neutrinos direction. Furthermore, a successful Particle Identification (PID) was conducted, for which for example electrons and gammas were selected against a background of muons and protons. Here, for the electrons [gammas] a purity of $(98.5 \pm 0.8)\,\%$ $[(98.8 \pm 0.7)\,\%]$ with efficiencies of $(97.1 \pm 1.0)\,\%$ $[(93.9 \pm 1.6)\,\%]$ were reached. This can be used for example to suppress atmospheric neutrino backgrounds in the search for the Diffuse Supernova Neutrino Background (DSNB).

Zusammenfassung

Seit vielen Jahren haben unsegmentierte Flüssigszintillator- und Wasser-Cherenkov-Detektoren spektakuläre Beiträge zum Feld der Neutrinophysik geleistet. In jüngster Zeit wird die Idee einer Mischung dieser Detektortypen verfolgt, indem zum Beispiel wasserbasierter Flüssigszintillator als aktives Medium verwendet wird, was gleichzeitigen Zugang zu Cherenkovstrahlung und Szintillationslicht ermöglicht. Dies ist erstrebenswert, weil beide Lichttypen ihre Vorteile haben. Elektronenrichtungsrekonstruktion auch für niedrige Energien ($< 10\,\mathrm{MeV}$) ist ein Beispiel, bei dem sich Cherenkovstrahlung hervortut, während die niedrigere Energieschwelle und die zur deponierten Energie proportionale Photonausbeute beim Szintillationslicht exzellent für Kalorimetrie geeignet ist. Diese Vorteile sind allerdings nur zugänglich, wenn die Photonentreffer auf den Photodetektoren den Lichtsorten zugeordnet werden können und eine Lichttrennung erfolgen kann.
Hier setzt diese Arbeit an mit einem kleinen in Geant4 simulierten, idealisierten wasserbasierten Flüssigszintillatordetektor mit einem Radius von $2.185\,\mathrm{m}$ und einer Höhe von $4.285\,\mathrm{m}$. Dieser Detektor ist komplett ausgekleidet mit den neuartigen Photosensoren namens Large Area Picosecond Photodetector (LAPPD), die mit einer Zeitauflösung von unter $100\,\mathrm{ps}$ und einer örtlichen Auflösung von unter $5\,\mathrm{mm}$ hervorragend dafür geeignet sind, Cherenkov- und Szintillationsphotonen anhand ihrer örtlichen und zeitlichen Charakteristiken zu trennen.
Mithilfe von niederenergetischen, simulierten Ereignissen wird ein erfolgreicher Lichttrennungsalgorithmus entwickelt auf Basis der topologischen Spurrekonstruktion. Dabei handelt es sich um 12.000 Ereignisse für jeweils Elektronen, Myonen und Gammas unter $120\,\mathrm{MeV}$ und 14.000 Ereignisse für Protonen mit Energien unter $140\,\mathrm{MeV}$. Außerdem wurden 10.000 Elektronereignisse unter $10\,\mathrm{MeV}$ untersucht.
Dabei wurden im performantesten Energieintervall Reinheiten von $(68 \pm 22)\,\%$ ($\pm 1\,\sigma$) für die Myonenereignisse bis zu $(81 \pm 8)\,\%$ für die Elektronenereignisse erzielt bei gleichzeitiger Effizienz von $(75 \pm 31)\,\%$ und $(87 \pm 15)\,\%$ für die Separation von Cherenkov- und Szintillationsphotonen.
Davon ausgehend wurde die Richtung der niederenergetischen Elektronen mit einer maximalen Genauigkeit von $(13.45 \pm 11.22)^\circ$ bestimmt. Ein Ergebnis, das darauf hinweist, dass diese Detektortechnologie dafür geeignet sein könnte, solare Neutrinos anhand ihrer Richtung als Untergrund zu unterdrücken. Außerdem wurde eine erfolgreiche Teilchenidentifikation durchgeführt, bei der zum Beispiel Elektronen und Gamma aus einem Untergrund von Myonen und Protonen selektiert wurden. Dabei wurden im besten Fall für die Elektronen [Gammas] Reinheiten von $(98.5 \pm 0.8)\,\%$ $[(98.8 \pm 0.7)\,\%]$ bei Effizienzen von $(97.1 \pm 1.0)\,\%$ $[(93.9 \pm 1.6)\,\%]$ erreicht. Dies kann zum Beispiel genutzt werden um atmosphärische Neutrinos als Untergrund bei der Suche nach dem diffusen Supernovahintergrund zu unterdrücken.

Contents

1. Introduction

Neutrino physics is a dynamic field of research with many developments in the last decades and many expected to come within the near future. Two of the main questions in the context of neutrino oscillations are expected to be resolved in the next decades. The determination of the Mass Ordering (MO) as well as the magnitude of Charge Parity (CP) violation if any in the leptonic sector will have a huge impact on the fundamental understanding of particle physics and the Standard Model of particle physics (SM) and will help in resolving the remaining big open questions of neutrino physics like the search for sterile neutrinos, Neutrinoless Double Beta Decay ($0\nu\beta\beta$) and the scale of the absolute neutrino mass.

Two of the main detector techniques in neutrino physics are big Water-Cherenkov (WC) or Liquid Scintillator (LS) detectors. Whilst the first one yielded major results for measuring high energy neutrinos like accelerator and atmospheric neutrinos, the latter has excelled in the low energy sector by detecting solar, reactor and geoneutrinos. In recent years, the idea to combine these two techniques matured so that the first prototypes of big Water-based Liquid Scintillator (WbLS) detectors like Theia [1] are proposed, while smaller prototypes are under construction or currently tested. Detectors like Theia are expected to have access to the advantages of both Cherenkov radiation and scintillation light and help with the answering of the aforementioned questions and detecting low energy neutrinos like Diffuse Supernova Neutrino Background (DSNB) neutrinos.

Cherenkov radiation is emitted instantaneous and directional and is therefore a terrific instrument for direction reconstruction, Particle Identification (PID) via the structure and/or the number of Cherenkov rings and all reconstruction techniques that rely on a fast timing with the downside that particles have to exceed the Cherenkov threshold with sufficient kinetic energy. Scintillation light is emitted delayed and isotropic, but has a low detection threshold and a high number of emitted photons. With that, scintillation light is well suited to detect slow and heavy charged particles, identify hadronic showers and be used for calorimetry. A WbLS detector would have access to all of these advantages and more, like additional PID or event identification via the ratio of Cherenkov to scintillation photons, if fitting light separation algorithms are in place to separate between the photons of both emission mechanisms. It is therefore necessary to divide the hits of an event into a Cherenkov sample and a scintillation sample that are as pure as possible based on the timing, the direction with respect to the particle track or the wavelength of the photon hits.

This thesis is intended to do just that with the help of a simulated idealised WbLS detector and the Topological Track Reconstruction (TTR) [2], which was developed in the Neutrino group of Professor Hagner. Additionally, experiences gained and support received while working within the ANNIE collaboration contributed to this work. The Accelerator Neutrino Neutron Interaction Experiment (ANNIE) [3] is an accelerator neutrino experiment at Fermilab aiming to measure the neutron multiplicity and the cross section of neutrino-nucleus interactions with a WC detector. ANNIE is also a testbed experiment, in which R&D for WbLS as well as for the Large Area Picosecond Photodetector (LAPPD) is conducted, which is why it is the associated experiment of this work. LAPPDs [4] are the second centerpiece of the simulated detector in this thesis and is a novel photosensor technology similar to PhotoMultiplier Tube (PMT)s with an excellent time resolution of less than $100\,\mathrm{ps}$ and a spatial resolution of less than $5\mathrm{mm}$. With these characteristics, LAPPDs are expected to vastly outperform standard PMTs and are the best choice for light separation based on timing and position.

In this work not only a successful light separation algorithm is presented, but also two applications of such a separation in form of low energy electron direction reconstruction and PID via the ratio of Cherenkov and scintillation photons for particles of energies of up to $120\,\mathrm{MeV}$ are shown.

The following chapter 2 introduces the field of neutrino physics with some basic properties of neutrinos and their sources, the interaction of neutrinos with matter, the formalism of neutrino oscillations and the open questions of neutrino physics. In chapter 3, different types of photodetectors and their working principles are discussed to explain the advantages and disadvantages of LAPPDs. The theoretical foundations for light separation and particle detection in general in a WbLS detector together with a motivation for light separation is given in chapter 4. This is followed by chapter 5 that deals with the physics motivation, the design and the current status of ANNIE as associated experiment. Chapter 6 shows the Geant4 simulation of an idealised WbLS detector that is completely covered with LAPPDs with the relevant properties and workflows. The TTR is discussed in chapter 7, in which also the adaption of the TTR to a WbLS detector is covered as well as added features to the reconstruction algorithm. In chapter 8, the light separation algorithm and its results are shown followed by chapter 9 that describes the applications of light separation and the final results of this work. Finally, chapter 10 concludes this thesis with a summary and an outlook.

2. Neutrino Physics

The neutrino is one of the fundamental particles in particle physics and although some of its properties are known, there are also many open questions in neutrino physics waiting for answers.

As part of the SM, the neutrino is described as a massless Dirac particle with spin $S = \frac{1}{2}$ and no electromagnetic or color charge. As a result, the neutrino interacts only via the weak and the gravitational interaction, whereby gravitation can be neglected in all processes described in this work. Neutrinos act as the neutral counterpart to the electromagnetic charged leptons (antileptons) and exist in three flavours: ν_e, ν_μ and ν_τ ($\overline{\nu}_e$, $\overline{\nu}_\mu$ and $\overline{\nu}_\tau$).

The discovery of neutrino oscillations, which was rewarded with a Nobel Prize in 2015, showed that neutrino physics is indeed beyond the SM, since the neutrino oscillation formalism demands neutrinos to have masses. The oscillations as well as the mass gaining mechanism are covered later in this chapter.

There is a number of natural sources of neutrinos as well as a handful of man-made sources. The neutrino flux with respect to the neutrino energy is shown for the different sources in figure 2.1, as it would be seen on earth. The solid lines denote sources only emitting neutrinos, the dashed/dotted lines show sources of antineutrinos and the superimposition of both line types show sources that emit both neutrino and antineutrino. The neutrino sources are introduced shortly here in order of ascending energies based on [5]:

1. Cosmic Neutrino Background (CNB): These cosmological neutrinos originate from the decoupling of neutrinos and matter at around $1\,\mathrm{s}$ after the big bang and can be viewed as analogous to the Cosmic Microwave Background (CMB). The CNB consists of neutrinos and antineutrinos of all flavours and although it has the highest flux of all neutrino sources, the detection of CNB neutrinos has yet to happen due to their low energy in the area of meV. At these low energies, the scale of the absolute neutrino mass directly influences the neutrino energy and hence the CNB spectrum. The CNB flux is shown in the dashed black-grey line, where the mass eigenstates[1] were assumed to be $m_1 = 0$, $m_2 = 8.6\,\mathrm{meV}$ and $m_3 = 50\,\mathrm{meV}$ (minimal neutrino mass spectrum). With that, three individual spectra are shown for the different

---

[1] The mass eigenstates are introduced in section 2.2. Here, it suffices to know that the mass eigenstates influence the predicted spectrum and that there are constraints on the absolute neutrino mass from experiments and cosmology.

mass eigenstates: blackbody spectrum for m_1 from roughly 10^{-6} to $10^{-2}\,\mathrm{eV}$ and almost monochromatic peaks for m_2 and m_3 at their respective energies of $8.6\,\mathrm{meV}$ and $50\,\mathrm{meV}$. For more information see reference [5] and [6].

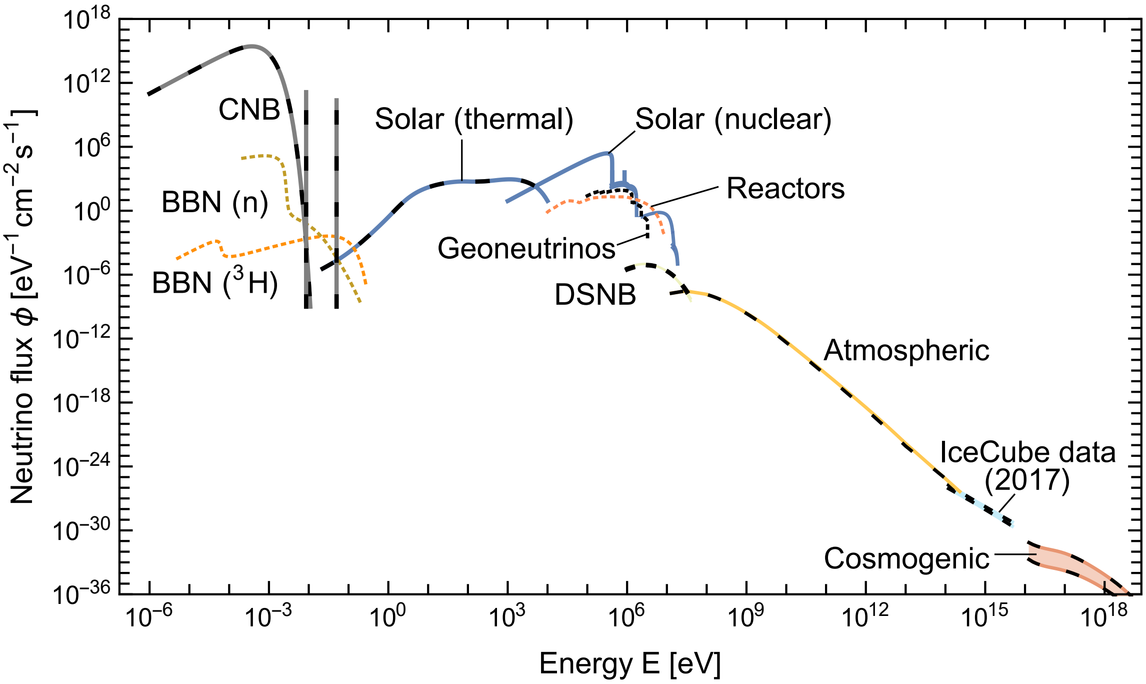

Figure 2.1.: Neutrino flux with respect to neutrino energy for different neutrino sources as seen on earth [5]. Solid (dashed) lines correspond to neutrino (antineutrino) emission. The superposition of a solid coloured line and a black dashed line denotes sources that emit both neutrinos and antineutrinos.

2. Big Bang Nucleosynthesis (BBN): These neutrinos originate from the nucleosynthesis in the first minutes of the universe, in which light elements were formed. Electron antineutrinos are then produced by the decay of neutrons (shown as brown dotted line titled BBN(n)) and tritons (shown as dotted orange line and titled BBN(^{3}H)) with energies below $200\,\mathrm{meV}$. As well as for the CNB neutrinos, the absolute neutrino mass plays a big role for the BBN energy spectrum, which will be discussed later, and a measurement is still to be conducted. For a more detailed picture also containing the decay of $^7\mathrm{Be}$ reference [7] can be considered.

3. Solar: There are two kinds of neutrino production mechanisms in the sun. The first one is the thermal production of neutrinos happening in the plasma via photoproduction, Bremsstrahlung, Plasmon decay, recombination of electrons with ions and deexcitation of ions [8], which is depicted in the blue solid-dashed line and which were not measured yet. These neutrinos range from eV to a few keV and are followed in energy by the other kind of solar neutrinos that are created via nuclear fusion processes, β^+-decays and

electron captures with energies in the MeV range. It is to note that the nuclear solar neutrinos are exclusively electron neutrinos. The nuclear fusion processes can be divided again into the proton-proton (pp) chain and the Carbon–Nitrogen–Oxygen (CNO) cycle. Nuclear solar neutrinos depicted by the solid blue line played historically a big role because of the solar neutrino problem and will be covered later in more detail (see section 2.3.1).

4. Reactor: These anti-electron neutrinos are man-made due to the β^--decays of elements resulting from fission processes inside of nuclear power plants. They are roughly in the same energy range as solar neutrinos and are depicted by the dotted orange line. Reactor neutrinos will be discussed in the context of neutrino oscillations parameters in more detail in section 2.3.1.

5. Geoneutrinos: The third source that is in the energy range of MeV and therefore overlapping the nuclear solar and reactor neutrinos is the earth. In the earth there are a number of radioactive isotopes like $^{238}\mathrm{U}$, $^{232}\mathrm{Th}$ and $^{40}\mathrm{K}$ that decay via chains of α- and β-decays producing anti-electron neutrinos. They are shown in the dotted black line.

6. Diffuse Supernova Neutrino Background (DSNB): Core-collapse supernovae produce neutrinos and antineutrinos of all flavours. The accumulated neutrinos from all past supernovae are called DSNB. They are depicted in a dashed lime line beginning at the order of MeV until about $30\,\mathrm{MeV}$ [9]. With that, the DSNB neutrinos overlap with the neutrinos from earth, reactors and the sun for lower energies and with atmospheric neutrinos towards higher energies. This presence of strong backgrounds hindered the detection of DSNB neutrinos to this day. It is expected that in the near future Super-Kamiokande (SK) [10] can present a measurement or that later the Jiangmen Underground Neutrino Observatory (JUNO) [11], Hyper-Kamiokande (HK) [12] or Theia [1] will do so [13, 14]. Such a measurement can estimate the supernova rate, help with improving star formation models and offers a new probe to explore the cosmos. DSNB neutrinos will be covered later from a detection perspective in section 4.5.

7. Accelerator: The second man-made source for neutrinos are produced by accelerators, which are not depicted in figure 2.1. Typically, accelerator neutrinos have an energy between hundreds of MeV and tens of GeV and a flux depending on the accelerator structure. Since accelerator neutrinos are the main neutrino source for ANNIE, accelerator neutrinos will be discussed in more detail in chapter 5 at the example of the Booster Neutrino Beam (BNB).

8. Atmospheric: Cosmic rays consisting of mainly protons and helium nuclei interact with the particles of the atmosphere to create secondary particles, of

which the kaons and pions are of interest, since they decay under the emission of electron and muon (anti)neutrinos as well as muons. These muons then decay also with the emission of said neutrino types. These neutrinos are depicted by a yellow dashed line and span an energy region from about $10\,\mathrm{MeV}$ to more than hundred TeV. The atmospheric neutrinos will also be discussed in more detail in the context of neutrino oscillation measurements (section 2.3.1).

9. Extragalactic neutrinos: $99\,\%$ of the neutrinos measured by IceCube at the highest energies above $100\,\mathrm{TeV}$ (shown by the teal dashed line) are expected to come not from the Milky Way. Instead, they are produced in proton-proton or proton-gamma-interactions in the context of for example active galactic nuclei, star-forming galaxies and gamma-ray bursts.

10. Cosmogenic: The neutrinos with the highest energies are shown in the red dashed lines and band and called cosmogenic neutrinos. The originate from interactions of the highest energy cosmic rays with the CMB or the extragalactic background light producing neutrinos and antineutrinos with energies exceeding tens of EeV of all flavours.

Neutrinos interact differently with matter depending on their flavour and energy. This will be covered in section 2.1 with focus on WC and LS detectors.

In section 2.2 the neutrino oscillation formalism is introduced for neutrinos traversing vacuum and matter. This is followed by a review of the open questions of neutrino physics in section 2.3. This incorporates also a description of the current status of the neutrino oscillation parameters together with the question of MO and the determination of the CP violating phase. Additionally, the absolute neutrino mass, the Dirac or Majorana nature of the neutrino and the search for sterile neutrinos is discussed.

2.1. Neutrino Interactions in Liquid Scintillator and Water

Due to its weak interacting nature, a direct detection of a neutrino is not possible. Neutrino detectors aim for the detection of the secondary particles created in the interaction of neutrinos with the components of the target matter. In order to understand the signal channels and the event signatures for measuring neutrino events, the interaction of neutrinos with matter is discussed in this chapter in the context of LS and WC detectors, based on references [15, 16].

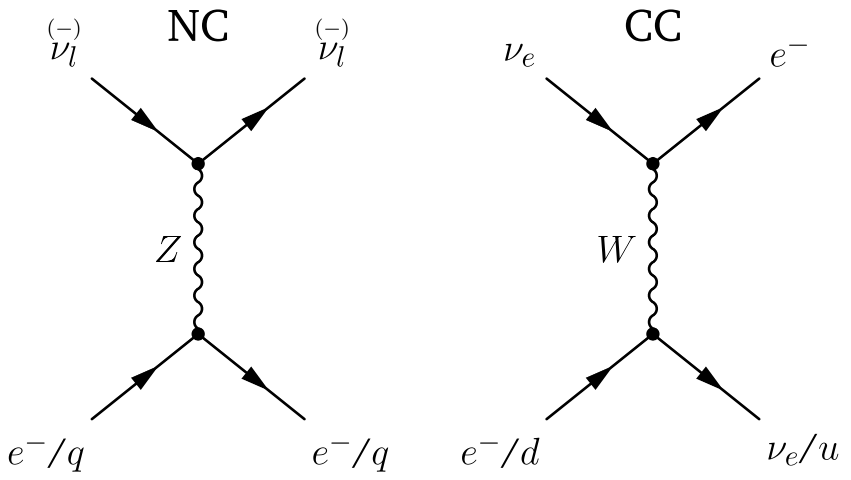

Figure 2.2.: Feynman diagrams for the fundamental interactions of neutrinos with leptons or quarks left for CC and right for NC.

The interaction of neutrinos with particles of the target can be divided into two categories based on the exchanged force carrier. If the exchanged boson is a W-boson the interaction is called a Charge Current (CC) interaction, whereas interactions via Z-bosons are called Neutral Current (NC) interactions. The fundamental difference between these categories is the flavour-changing nature of CC interactions, whilst NC interactions are flavour-conserving. This can be illustrated by the corresponding first-order Feynman diagrams for the electron neutrino on electron/quark scattering displayed in figure 2.2. On the left side the NC is shown, where a neutrino (or antineutrino) of any flavour scatters off an electron or an up- or down-quark via the exchange of a Z-boson, only altering the momentum of the particles. Here, l stands for the neutrino/charged lepton flavour e, μ and τ and q for the up- or down-quark, as these are the only quarks that occur in matter. An example for the CC can then be seen on the right side: The electron-neutrino scatters off an electron or down-quark mediated by a W-boson, which transforms the neutrino to an electron and the electron (down-quark) to an electron neutrino (up-quark). It is to note, that CC can also occur with anti-electron neutrinos on electrons in a s-channel diagram. Furthermore, CC scattering with quarks is also possible for other neutrino flavours, which will be discussed later. Additionally, muon-neutrinos can scatter off electrons as well in the so called inverse muon decay, which is neglected in this thesis due to its threshold of $11\,\mathrm{GeV}$ [17].

In the following sections, neutrino interactions are discussed in detail in two different energy regimes roughly ordered by their energy thresholds: The first part focuses on the low energy regime, which is in the context of this thesis defined in the area of $0\,\mathrm{MeV}$ (tresholdless processes) up to $100\,\mathrm{MeV}$. This regime is important for the search of $0\nu\beta\beta$ and the measurement of DSNB neutrinos. The second part focuses on the high energy regime, which is defined in this thesis in the energy range from $100\,\mathrm{MeV}$ up to $5\,\mathrm{GeV}$. This energy region covers accelerator neutrinos in general and specifically the BNB neutrinos, which are measured by ANNIE (up to roughly $2\,\mathrm{GeV}$) and the Long-Baseline Neutrino Facility (LBNF) neutrinos that are planned to be measured by Theia or the Deep Underground Neutrino Experiment (DUNE) [18] (up to roughly $5\,\mathrm{GeV}$).

2.1.1. Low Energy Regime (MeV-region)

In addition to the aforementioned references, this section is also based on reference [19]. Neutrinos with the lowest of energies (between 0 and $1\,\mathrm{MeV}$) have in principle three options for interacting with target material, that can be considered to be without threshold in the context of low energy neutrino detection: Coherent Elastic Neutrino-Nucleus Scattering (CEvNS), neutrino capture on radioactive nuclei and elastic electron scattering.

In CEvNS a neutrino interacts with a nucleus as a whole coherently via NC

$$\nu_l + A_N^Z \rightarrow \nu_l + A_N^{\star Z}, \tag{2.1}$$

leading to a recoil T_{max} of the nucleus

$$T_{\mathrm{max}} = \frac{E_\nu}{1 + \frac{M_A}{2E_\nu}}, \tag{2.2}$$

where M_A is the mass of the nucleus and E_ν is the incoming neutrino energy. A is the mass number equal to the sum of protons and neutrons, Z is the atomic number equal to the number of protons and N is the number of neutrons. Thus, neutrinos with energies in the MeV-range produce nucleus recoils of the order of tens of keV making such a reaction undetectable in LS and WC detectors, although this process has the highest cross section for neutrino energies of up to $100\,\mathrm{MeV}$ [20]. This is illustrated by figure 2.3, in which cross sections for different neutrino interactions in the low energy regime are depicted with respect to the neutrino energy in the context of the COHERENT target materials caesium ($^{133}\mathrm{Cs}$), iodine ($^{127}\mathrm{I}$), germanium ($^{\mathrm{nat}}\mathrm{Ge}$), argon ($^{40}\mathrm{Ar}$), natrium ($^{23}\mathrm{Na}$) and lead (Pb). The CEvNS cross sections for different target nuclei are shown, that are clearly exceeding the cross section for the Inverse Beta Decay (IBD) on free protons (in solid red) and the elastic scattering of electrons (in dashed red). Additionally, the elastic neutrino-electron scattering for iodine is shown in green and neutrino-induced neutron production on lead in black.

In fact despite its high cross section, detecting neutrinos with this channel did not happen until 2017, when the COHERENT collaboration used a CsL[NA] scintillator detector to measure neutrinos from a spallation neutron source [21] via CEvNS.

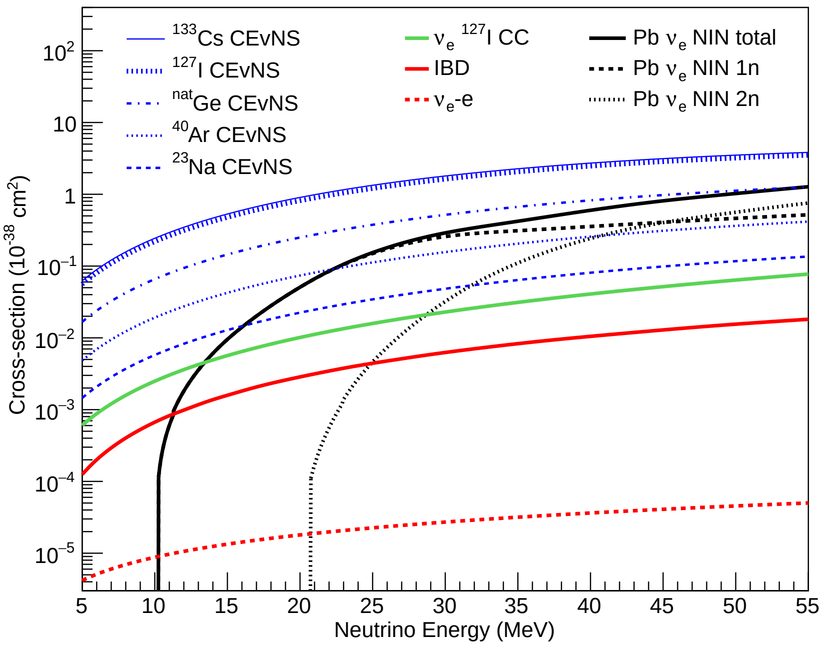

Figure 2.3.: Cross sections for low energy neutrino interactions in the context of the COHERENT target material [22].

Neutrino capture on radioactive nuclei

$$\nu_e + A_N^Z \rightarrow e^- + A_{N-1}^{Z+1} \tag{2.3}$$

is an exothermic process without threshold that is theoretically predicted but was not observed yet. The exothermic nature of this process makes the difference between this reaction and the IBD, that is discussed later and has a very similar form.

The elastic scattering of neutrinos of electrons

$$\overset{(-)}{\nu_l} + e^- \rightarrow \overset{(-)}{\nu_l} + e^- \tag{2.4}$$

is the interaction that is most relevant for WC and LS detectors, when speaking of processes without energy threshold. Thereby it is to note, that this interaction cannot be observed if the neutrino energy is below the detection threshold, which is fundamentally different than the process threshold. In WC detectors for example, the outgoing electron has to exceed the Cherenkov threshold to be detectable at all.

Being a NC process, the elastic electron scattering is open for any (anti-)neutrinos regardless of flavour which makes it a good channel for detecting supernova neutrinos.

Elastic NC scattering is also possible to happen on protons and nuclei resulting in

accelerated protons or nuclei, that are impossible to detect in WC detectors, but can be a relevant signal for LS detectors.
For higher energies, the NC production of giant resonances becomes relevant. The most relevant targets are oxygen and carbon:

$$\overset{(-)}{\nu_l} + {}^{12}\mathrm{C} \rightarrow \overset{(-)}{\nu_l} + {}^{12}\mathrm{C}^*, \tag{2.5}$$

$$\overset{(-)}{\nu_l} + {}^{16}\mathrm{O} \rightarrow \overset{(-)}{\nu_l} + {}^{16}\mathrm{O}^* \rightarrow \overset{(-)}{\nu_l} + \gamma + X. \tag{2.6}$$

${}^{12}\mathrm{C}^*$ decays with the emission of a $15.11\,\mathrm{MeV}$ gamma back to ${}^{12}\mathrm{C}$. This is a channel to consider (neglect) for LS (WC) detectors due to the high abundance (absence) of carbon atoms. The NC reaction on oxygen leads to an excited ${}^{16}\mathrm{O}^*$, which decays into ${}^{15}\mathrm{O}^*$ or ${}^{15}\mathrm{N}^*$ in the best case scenario. The deexcitation of these exited nuclei happens under the emission of a gamma in the energy range of 5 to $10\,\mathrm{MeV}$, which can be detected in WC detectors. It is to note that the decay of the exited oxygen can also happen to different atoms that do not yield a good signal.

The golden channel for neutrino interactions in the low energy range is the so called IBD

$$\overline{\nu}_e + p \rightarrow e^+ + n, \tag{2.7}$$

which is displayed in the Feynman diagram in figure 2.4 at quark level. The incoming electron antineutrino interacts with an up quark of the proton in the CC channel, resulting in an outgoing positron and the conversion of the up quark to a down quark and in turn the conversion of the proton to a neutron.

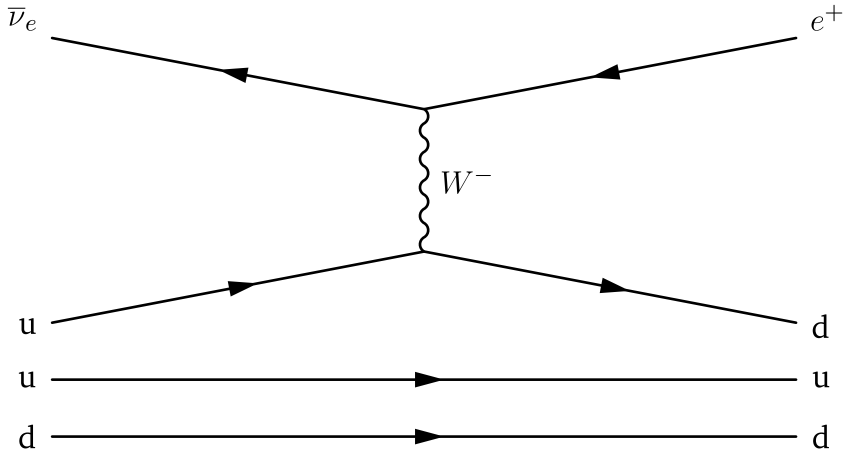

Figure 2.4.: Feynman diagram for the IBD.

This process has an interaction threshold of $1.806\,\mathrm{MeV}$ and can be considered as the best channel for detecting reactor neutrinos. This is because of its unique event signature consisting of the prompt positron signal due to the energy deposition of the positron and the two annihilation gammas with an energy of $511\,\mathrm{keV}$ each, which is then followed by the delayed neutron capture on hydrogen after thermalisation that results in the emission of a $2.2\,\mathrm{MeV}$ gamma roughly $200\,\mu\mathrm{s}$ after the neutrino reaction. The annihilation gammas are detectable in LS detectors. For WC detectors the excited electrons from the interaction of the gamma with the target material (see section 4.1.3) are below Cherenkov threshold and therefore invisible. For the deexcitation gammas from the neutron capture, the situation is similar. The higher energy of the gamma leads to electrons that can barely exceed the Cherenkov threshold and produce a low number of Cherenkov photons. It is therefore a common practice in WC detectors to load the water with gadolinium, so that the neutron is captured by a gadolinium atom instead, which leads to a deexcitation via a couple of gammas with a total energy of $8\,\mathrm{MeV}$, to enhance the visibility of the neutron and therefore the neutron-tagging efficiency. As it can be seen in figure 2.3, the cross section of the IBD is a factor of roughly 100 higher than the elastic neutrino-electron scattering, but it is only open for anti-electron neutrinos.

Another version of IBD is the so called stimulated beta decay

$$\nu_e + n \rightarrow e^- + p, \tag{2.8}$$

which is irrelevant in WC or LS detectors due to missing free neutrons. It is mentioned here, as it shows the reaction of equation (2.10) on nucleon level.

IBD or stimulated beta decay happening on atoms is referred to as neutrino capture, which is of importance for carbon in LS and oxygen in WC detectors:

$$\nu_e + {}^{12}\mathrm{C} \rightarrow e^- + {}^{12}\mathrm{N}, \tag{2.9}$$

$$\overline{\nu}_e + {}^{12}\mathrm{C} \rightarrow e^+ + {}^{12}\mathrm{B}, \tag{2.10}$$

$$\overset{(-)}{\nu}_e + {}^{16}\mathrm{O} \rightarrow e^{\pm} + X. \tag{2.11}$$

${}^{12}\mathrm{B}$ and ${}^{12}\mathrm{N}$ decay then via

$${}^{12}\mathrm{B} \rightarrow {}^{12}\mathrm{C} + e^- + \overline{\nu}_e, \tag{2.12}$$

$${}^{12}\mathrm{N} \rightarrow {}^{12}\mathrm{C} + e^+ + \nu_e. \tag{2.13}$$

The antineutrino channel on carbon leads therefore to a similar event signature to the IBD on a proton with a prompt photon emission due to the positron and the annihilation gammas followed by the decay of ${}^{12}\mathrm{B}$, which has a half-time of $20\,\mathrm{ms}$, that produce additional photons due to the emitted electron. The signature of the neutrino channel differs slightly, because of the missing annihilation gammas in the first photon emission, a half time of about $11\,\mathrm{ms}$ for ${}^{12}\mathrm{N}$ and the emission of the annihilation gammas in the second wave of photon emissions.

Before coming to the high energy region, the cross sections of the aforementioned processes and their event signatures will be discussed shortly. Figure 2.5 shows on the left the cross sections for a WC detector with the parameters of HK and on the right the same for a LS detector, that is modelled after Low Energy Neutrino Astronomy (LENA) [23], in the context of supernova neutrino interaction and detection[2].

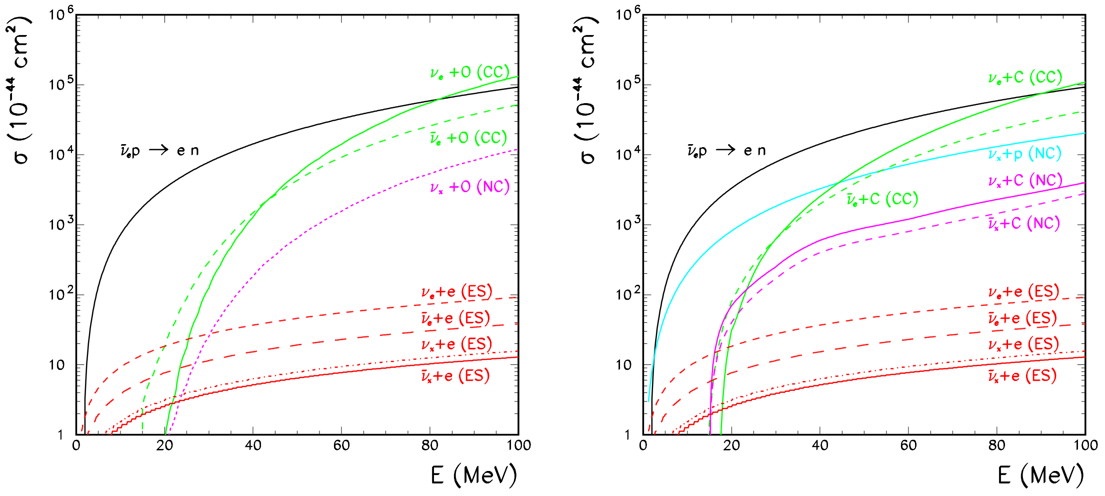

(a) (b)

Figure 2.5.: Cross sections for neutrino interactions in the low energy regime in an example for (a) WC and (b) LS detector [19]. Shown are the relevant processes for the supernova neutrino detection.

The red lines for both detector types correspond to the elastic scattering of electrons (see formula (2.4)), the purple lines show the giant resonance production channels (see equations (2.5) and (2.6)) on oxygen for WC and carbon for LS, the green lines display the neutrino capture on the same atoms (see formula (2.9), (2.10) and (2.11)) and the black line shows the IBD (see equation (2.7)). For the LS detector the cyan line shows the elastic scattering of protons, which does not play a role in the WC detector due to the mass of the proton and the resulting Cherenkov threshold of about $485\,\mathrm{MeV}$.

For both detectors, the elastic scattering of electrons has the lowest cross section. The difference between electron neutrinos and the other flavours originates from the additional CC interaction that is only open for the electron flavour. Next in cross section is the giant resonance process, then the neutrino capture and finally the IBD, which again shows the importance of this channel. The elastic proton scattering for the LS detectors has a higher cross section than all other processes except the IBD at the low end of the energy spectrum, but at around $40\,\mathrm{MeV}$ the cross section of the neutrino capture rises higher. It needs to be stressed that the

---

[2] It is safe to say that the detector model does not influence the cross sections directly with exception of the active medium that is used. The WC detector will of course use highly pure water, whereas the LS detector is filled with Phenylxylylethane (PXE) ($C_{16}H_{18}$).

detection threshold is not covered within this figure. This is especially important for the WC detector, as the outgoing lepton or gamma has to have an energy that exceeds the corresponding Cherenkov threshold.
From a reconstruction point of view, there are two fundamentally different event signatures, which are the single particle signature (the NC events open for all neutrinos) and the coincidence signature (the CC events only open for electron flavoured neutrinos). To distinguish between these two signature types and following that, also between the individual channels, can be a challenge that will not be covered here.

2.1.2. High Energy Regime (GeV-region)

In the high energy regime, neutrinos interact with the target matter in so called neutrino-nucleus interactions, in which a neutrino interacts with the nucleons bound inside of a nucleus in contrast to the low-energy interactions of free particles that were described before. The following section focuses on the neutrino-nucleus interaction assuming the nucleon to be a free particle. The complexity that arises from looking at the nucleon as a bound particle in a nucleus will then be discussed in the second section, whereas the third section deals with the event signatures.

Neutrino-Nucleus Interactions on Free Nucleons

There are three CC interaction scenarios, which will be discussed in order of prominence towards higher energies.
The first process is the Charge Current Quasi-Elastic (CCQE) interaction, which is considered to be the most important channel for neutrino oscillation measurements with LS and WC detectors in the high energy region due to its clean final state event topology of an outgoing lepton and hadron

$$\nu_l + n \rightarrow l^- + p, \qquad \overline{\nu}_l + p \rightarrow l^+ + n. \tag{2.14}$$

In figure 2.6 the Feynman diagrams for the CCQE interactions for neutrinos on the left side and antineutrinos on the right side are shown. The incoming neutrino (antineutrino) interacts with a neutron (proton) resulting in an outgoing lepton l^- (l^+) and the transformation of the nucleon into a proton (neutron). For the event signature an outgoing lepton and neutron/proton with recoil is expected. One can assume the reaction to be a 2-body scatter of a nucleon at rest, which gives the possibility to use the direction and the momentum of the lepton without any knowledge of the outgoing nucleon to calculate the neutrino energy via [24]

$$E_\nu^{\mathrm{QE}} = \frac{2M_{n(p)}E_l - M_{n(p)}^2 + M_{p(n)}^2 - m_l^2}{2\left(M_{n(p)} - E_l\sqrt{E_l^2 - m_l^2}\cos\theta_l\right)}. \tag{2.15}$$

Here, $M_{n(p)} = m_{n(p)} - E_b$ is set with the mass of the nucleon $m_{n(p)}$ and the binding energy E_b. E_l and m_l is the energy and mass of the lepton and θ_l denotes the scattering angle between incoming neutrino and outgoing lepton. This means, the direction of the incoming neutrino has to be known so that this formula can only be used if the source of the neutrino is well-known, as it is the case for accelerator neutrino experiments.

As it will be discussed later in the next section, the energy calculation assumption is only valid for a part of CCQE interactions because of the complex nature of nuclei. This is also a factor that can substantially alter the event signature.

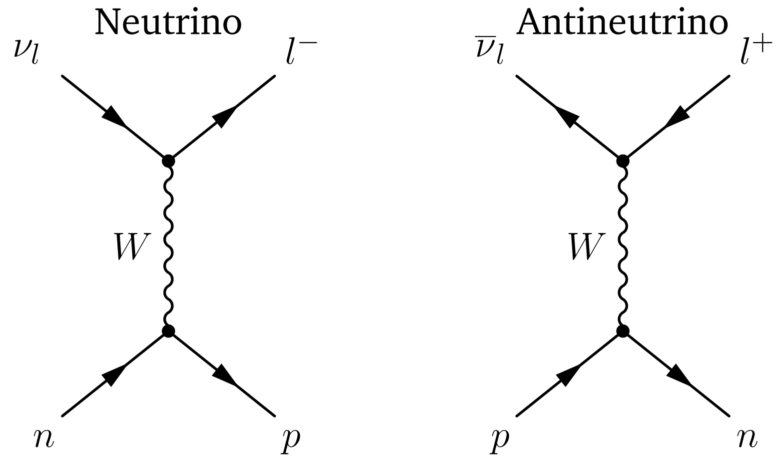

Figure 2.6.: Feynman diagrams for the CCQE interaction.

The second reaction is the Charge Current Resonant (CCRES) interaction, for which an example is shown in the Feynman diagram in figure 2.7. In this example, an incoming neutrino interacts with a neutron with sufficient energy to produce the Delta resonance Δ^+, which decays under the emission of a pion π^+ and a neutron.

CCRES can produce a number of resonances, which in turn can decay differently producing a number of event signatures. Most prominently, these processes produce a single pion in one of the following reactions [15]

$$\begin{aligned} \nu_l + p &\to l^- + p + \pi^+, & \overline{\nu}_l + p &\to l^+ + p + \pi^-, \\ \nu_l + n &\to l^- + p + \pi^0, & \overline{\nu}_l + p &\to l^+ + n + \pi^0, \\ \nu_l + n &\to l^- + n + \pi^+, & \overline{\nu}_l + n &\to l^+ + n + \pi^-, \end{aligned} \tag{2.16}$$

but there is also a possibility for heavier resonances decaying into multiple pions or into kaons together with sigma or lambda baryons.

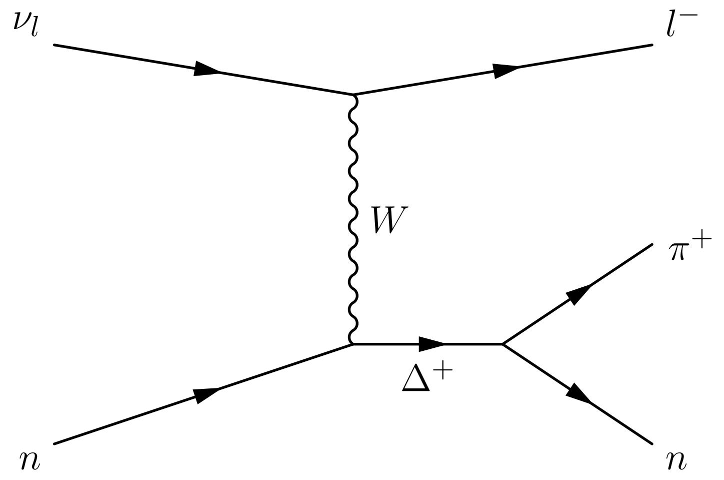

Figure 2.7.: Feynman diagrams for the CCRES interaction.

The last of the high energy CC interactions is the Charge Current Deep Inelastic Scattering (CCDIS) interaction, in which an incoming neutrino's energy is sufficient for scattering of individual quarks, which is followed by a hadronic shower

$$\nu_l + N \to l^- + X, \qquad \overline{\nu}_l + N \to l^+ + X. \tag{2.17}$$

Here, N stands for nucleon and X for the particles that constitute the hadronic shower. The neutrino variant of this process is shown in the Feynman diagram in figure 2.8.

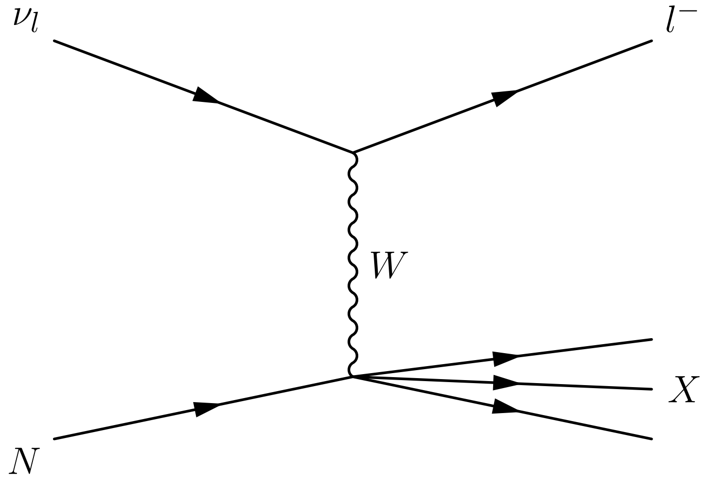

Figure 2.8.: Feynman diagrams for the CCDIS interaction.

In addition to these three dominant CC processes, there is also the possibility for coherent pion production

$$\text{NC}: \nu_l + A \to \nu_l + A + \pi^0, \quad \overline{\nu}_l + A \to \overline{\nu}_l + A + \pi^0, \tag{2.18}$$

$$\text{CC}: \nu_l + A \to l^- + A + \pi^+, \quad \overline{\nu}_l + A \to l^+ + A + \pi^-. \tag{2.19}$$

In this interaction the neutrino scatters of the nucleus coherently (similar to CEvNS) producing an outgoing pion and lepton for CC or neutrino in NC together with a nucleus with negligible recoil. Due to its signature in the CC reaction, this process is hard to distinguish from the CCRES interaction.

At last, it has to be mentioned that resonance production can also happen via NC interactions. Due to the absence of the charged lepton, these processes play a very minor role in the scope of WC and LS detectors in this energy range. The same can be assumed for NC elastic scattering of nucleons.

In figure 2.9, the comparison of measured cross section (data points) to the theory prediction (lines) is displayed for neutrinos on the left and antineutrinos on the right side considering the three processes CCQE (dotted line), CCRES (dotted/slashed line) including the coherent pion production and CCDIS (slashed line). The total cross section is displayed as a solid line.

As the order of the discussion above hinted, the CCQE is most relevant for neutrino energies of up to $1\,\mathrm{GeV}$, followed by CCRES for energies between $1\,\mathrm{GeV}$ and $4\,\mathrm{GeV}$ for neutrinos ($7\,\mathrm{GeV}$ for antineutrinos). Towards higher energies CCDIS is the dominant process. For all three processes, there is a significant overlap starting at around $300\,\mathrm{MeV}$ meaning that most neutrino accelerator experiments have to deal with all of the aforementioned interactions and their event signatures, so that event discrimination and selection becomes a vital tool, which will get more attention later. In fact, ANNIE has to deal mainly with CCQE and CCRES events, whereas for the long baseline neutrino experiments CCDIS is also a significant process.

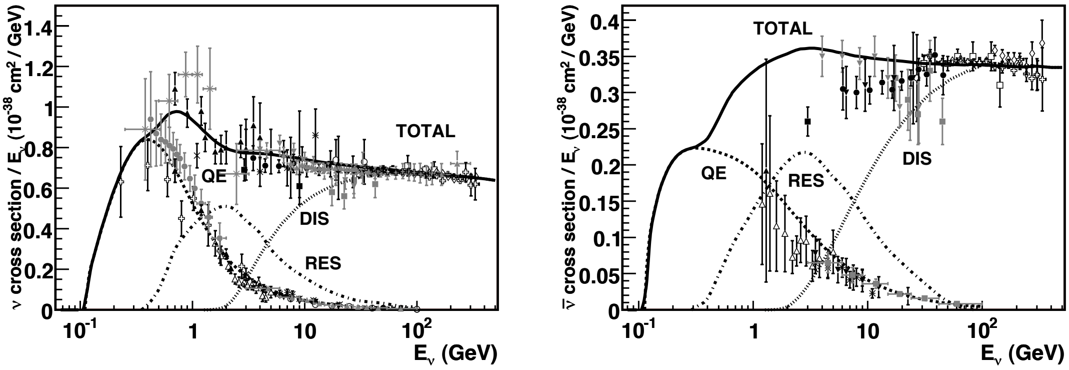

(a) (b)

Figure 2.9.: Cross sections for neutrino interactions in the high energy regime [15] for (a) neutrinos and (b) antineutrinos.

Neutrino-Nucleus Interactions on Bound Nucleons

Going from free nucleons to nucleons bound in nuclei introduce a handful of additional factors that needs careful consideration [25]:

1. Initial movement of nucleons (Fermi motion).

2. Nuclear correlations of nucleons.
3. Final State Interactions (FSI) of outgoing nucleons or mesons with other nucleons in the nuclear medium.

First of all, the initial movement of protons and neutrons inside of nucleon known as Fermi motion wrongs the assumption made for equation (2.15) of a nucleon at rest and alters the angle and momentum of the final state lepton decreasing the resolution of the neutrino energy reconstruction using said formula. The Fermi motion is depending on the binding energy of the nucleons as well as on the nucleon density in the areas of the nuclei. Additionally, the effect of Pauli blocking has to be taken into account for the outgoing nucleon. At last, nuclear correlations introduce further modifications to the nucleon movement.

There is a chance for the neutrino to interact not only with a single nucleon but with a pair of closely bound nucleons. Because such a reaction produces 2 outgoing nucleons and 2 holes in the nucleus, they are known as 2p-2h-interactions, whereas the CCQE process can be described as a 1p-1h-interaction. It is to note, that higher orders of np-nh-interactions are also possible but less likely. Such processes alter the event signatures substantially because of the higher number of outgoing nucleons.

Before leaving the nucleus, nucleons as well as pions have the opportunity to interact in various ways with other nucleons inside the nucleus. These interactions are known as FSI and can have severe impact on the event signature and topology. In figure 2.10, an illustration is shown for some examples of the FSI for outgoing pions. The shown examples are:

- Charge exchange of the pion with a proton (neutron) transforming a $\pi^-(\pi^+)$ to a π^0, that then leaves the nucleus.
- Elastic scattering of a pion off a nucleon altering pion's angle and momentum.
- Absorption of the pion on a nucleon pair (stuck pion).
- In the case of sufficient pion energy, the production of additional pions is possible.

The first two processes are from an experimental point of view less severe, since the initial single pion production reaction is still visible after the charge exchange[3] or the elastic scattering, whereas the other two interactions change the number of observable pions and therefore mimic other event signatures.

For nucleons, the situation is similar and the re-interaction of the outgoing nucleons within the nuclear medium can change the number, species, momentum and

---

[3] As it can be seen in equation (2.16), neutral as well as charged pions can be the result of the single pion production in CCRES interactions.

angle of the observable nucleons. For mesons as well as nucleons, the production of additional outgoing pions and/or nucleons is also of possibility.

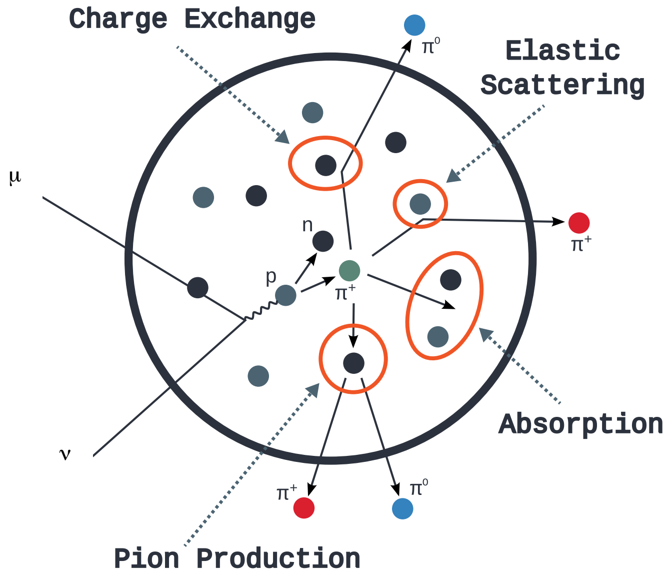

Figure 2.10.: Illustration for the event signature altering effects of FSI [25]. Shown is the charge exchange that converts a positive pion to a neutral pion, elastic scattering of a pion altering its momentum and direction, additional pion production, in which a positive pion creates an additional neutral pion that leaves the nucleus as well, which alters the overall number of pions in the event and the absorption of a pion leading to an pionless event signature as expected from a CCQE event.

Event signature

Energy reconstruction and event selection in the high energy regime poses a high challenge due to the overlapping interaction channels, the nuclear correlations (2p-2h-interactions especially) and the FSI. This is even the case if all resulting particles can be measured accurately because the event signatures of all three dominant CC processes as well as the coherent pion production can mimic each other. A CCRES process with a stopped pion can for example look like a CCQE event, whereas a CCQE event with additional pion production due to the nucleon interaction in the nuclear medium can mimic a CCRES event. A CCRES or even a CCQE event with additional nucleon production, be it due to FSI or due to a 2p-2h-interaction (or both) can be misidentified as a CCDIS event, when the pion is stopped inside the nucleus. In the case that particles are misidentified or escape the detection, the picture gets even more complicated. These examples illustrate the importance of measuring the number of pions and nucleons accurately for cross section measurements as well as for neutrino oscillation experiments and why the dominating systematic uncertainty for future high-energy long baseline neutrino experiments comes from the nuclear effects.

It is to note, that the situation differs for WC and LS detectors, because protons are invisible for WC detectors and the addition of Gadolinium is necessary for measuring neutrons accurately, whereas all outgoing particles produce photon emissions in LS detectors without the possibility of particle discrimination and the difficulty of saturation.

2.2. Neutrino Oscillations

It is crucial for the discussion of a few of the open questions of neutrino physics to derive and explain the mechanism of neutrino oscillations. This section deals first with neutrino oscillations in vacuum, before describing said oscillations in matter. This section is based on references [26, 27].

2.2.1. Neutrino Oscillations in Vacuum

In the theory of neutrino oscillations it is assumed that neutrinos have indeed mass and that the flavour eigenstates $|\nu_\alpha\rangle$ with $\alpha = e, \mu, \tau$ can be described as a superposition of mass eigenstates $|\nu_k\rangle$ with $k = 1, 2, 3$ assuming three neutrino flavours. The principle is the same for higher number of neutrino flavours n; this section focuses on the three flavour case though.

The flavour eigenstate is connected to the mass eigenstates by the unitary matrix $U_{\alpha k}$ via

$$|\nu_\alpha\rangle = \sum_{k=1}^{n} U_{\alpha k}|\nu_k\rangle\,,\ |\overline{\nu}_\alpha\rangle = \sum_{k=1}^{n} U^*_{\alpha k}|\overline{\nu}_k\rangle \tag{2.20}$$

with the retransformation

$$|\nu_k\rangle = \sum_{k=1}^{n} U^*_{\alpha k}|\nu_\alpha\rangle\,,\ |\overline{\nu}_k\rangle = \sum_{k=1}^{n} U_{\alpha k}|\overline{\nu}_\alpha\rangle. \tag{2.21}$$

For the sake of simplicity, the antineutrino case is neglected in the following and $\sum\limits_{k=1}^{n}$ is written as $\sum\limits_{k}$.

The propagation of the neutrino can be described as a time evolution according to

$$|\nu_k(x,t)\rangle = \mathrm{e}^{-iE_k t}|\nu_k(x,0)\rangle, \tag{2.22}$$

where E_k denotes the energy of the eigenstate k and $|\nu_k(x,0)\rangle$ is the mass eigenstate at the time $t = 0$. With a source at position $x = 0$, this can be expressed as

$$|\nu_k(x,0)\rangle = \mathrm{e}^{ipx}|\nu_k\rangle \tag{2.23}$$

with p as the neutrino momentum. Now the superposition equation (2.20) can be applied to the time evolution equation (2.22) to get

$$|\nu(x,t)\rangle = \sum_k U_{\alpha k} \mathrm{e}^{-iE_k t} |\nu_k(x,0)\rangle. \tag{2.24}$$

Hereby, it was assumed that the superposition of the mass eigenstates are equal to the flavour eigenstate $|\nu_\alpha\rangle$ and $|\nu(x,t)\rangle$ denotes the flavour eigenstate after propagation. Equation (2.23) applied gives then

$$|\nu(x,t)\rangle = \sum_k U_{\alpha k} \mathrm{e}^{-iE_k t} \mathrm{e}^{ipx} |\nu_k\rangle \tag{2.25}$$

for the time evolution of the flavour eigenstate $|\nu_\alpha\rangle$ in terms of the mass eigenstates. Assuming that the evolution of the mass eigenstates leads to another flavour eigenstate $|\nu_\beta\rangle$ and using the retransformation in equation (2.21) results into

$$|\nu(x,t)\rangle = \sum_{k,\beta} U_{\alpha k} U^*_{\beta k} \mathrm{e}^{-iE_k t} \mathrm{e}^{ipx} |\nu_\beta\rangle. \tag{2.26}$$

The transition amplitude A can then be calculated via

$$A(\alpha \to \beta)(t) = \langle \nu_\beta | \nu(x,t)\rangle = \sum_k U^*_{\beta k} U_{\alpha k} \mathrm{e}^{-iE_k t} \mathrm{e}^{ipx} \tag{2.27}$$

for turning flavour α to flavour β.
As it will be discussed later, the neutrino masses can be assumed to be very small so that the approximation $p \gg m$ and $E \approx p$ can be used

$$E_k = \sqrt{m_k^2 + p_k^2} \simeq p_k + \frac{m_k^2}{2p_k} \simeq E + \frac{m_k^2}{2E}. \tag{2.28}$$

This allows to calculate

$$\begin{aligned} \mathrm{e}^{-iE_k t} \mathrm{e}^{ipx} &= \exp\left[i\left(px - Et - \frac{m_k^2}{2E}t\right)\right] = \exp\left[i\left(EL - EL - \frac{m_k^2}{2E}L\right)\right] \\ &= \exp\left(-i\frac{m_k^2}{2}\frac{L}{E}\right), \end{aligned} \tag{2.29}$$

where $L = x = ct$ was assumed with c as the speed of light. With that, equation (2.27) can be rewritten in terms of the neutrino energy E and distance between source and detection L

$$A(\alpha \to \beta)(L) = \sum_k U^*_{\beta k} U_{\alpha k} \exp\left(-i\frac{m_k^2}{2}\frac{L}{E}\right). \tag{2.30}$$

Finally, the transition probability P is given by

$$P(\alpha \to \beta)(t) = |A(\alpha \to \beta)|^2 = \sum_k \sum_l U_{\alpha k} U^*_{\alpha l} U^*_{\beta k} U_{\beta l} e^{-i(E_k - E_l)t}. \tag{2.31}$$

Using equation (2.29) this also can be expressed in a real and an imaginary term [28]

$$\begin{aligned} P(\alpha \to \beta)(t) = \delta_{\alpha\beta} - 4 \sum_{k>l} \sin^2\left(\frac{\Delta m^2_{kl}}{4}\frac{L}{E}\right) \mathrm{Re}\left[U_{\alpha k} U^*_{\alpha l} U^*_{\beta k} U_{\beta l}\right] \\ - 2 \sum_{k>l} \sin\left(\frac{\Delta m^2_{kl}}{2}\frac{L}{E}\right) \mathrm{Im}\left[U_{\alpha k} U^*_{\alpha l} U^*_{\beta k} U_{\beta l}\right]. \end{aligned} \tag{2.32}$$

Here,

$$\Delta m^2_{kl} = m^2_l - m^2_k \tag{2.33}$$

was used as the quadratic mass difference between the neutrino mass eigenstates k and l. Assuming δ_{CP} to be $n\pi$ with n being a signed integer including 0, which means no CP violation in the neutrino sector[4], this can be written as

$$P(\alpha \to \beta)(t) = \delta_{\alpha\beta} - 4 \sum_{k>l} U_{\alpha k} U^*_{\alpha l} U^*_{\beta k} U_{\beta l} \sin^2\left(\frac{\Delta m^2_{kl}}{4}\frac{L}{E}\right). \tag{2.34}$$

Due to the symmetry of $\sin^2$ this formula is only sensitive to the absolute value of Δm^2_{kl} and not to the sign. The observation of neutrino oscillations that are described by the equation above shows that at least two of the mass eigenstates needs to be non-zero.

The calculation for the probability of flavour conversion is then straightforward and given by

$$P(\alpha \to \alpha) = 1 - \sum_{\alpha \neq \beta} P(\alpha \to \beta). \tag{2.35}$$

The conversion matrix as well as the different parameters in the theory of neutrino oscillations will be discussed later in section 2.3.1, where also the current status will be reviewed.

For the explanation of some phenomena it is sufficient to take only two neutrino flavours into consideration, which simplifies the transition probability to

$$P(\nu_\alpha \to \nu_\beta) = \sin^2(2\theta) \cdot \sin^2\left(\frac{\Delta m^2 L}{4E}\right) = \sin^2(2\theta) \cdot \sin^2\left(\pi \frac{L}{L_0}\right), \tag{2.36}$$

---

[4] As it will be discussed later, there is currently a hint that this assumption might not be true.

with the mixing angle θ defined by

$$\nu_e = \cos(\theta)\nu_1 + \sin(\theta)\nu_2, \quad \nu_\mu = -\sin(\theta)\nu_1 + \cos(\theta)\nu_2, \tag{2.37}$$

the squared mass difference Δm^2 and the oscillation length L_0

$$L_0 = 4\pi\hbar c \frac{E}{\Delta m^2}, \tag{2.38}$$

with the speed of light c and the reduced Planck constant $\hbar$. L_0 is the period of one cycle of the oscillation probability.

2.2.2. Neutrino Oscillations in Matter

For many experiments and measurements looking at neutrinos oscillating in vacuum does not suffice. The solution for the solar neutrino problem, as well as long baseline neutrino accelerator experiments rely on neutrino oscillations in the matter of the sun or earth respectively. These neutrino oscillations in matter will be discussed in the following based on reference [29].

Matter introduces a flavour asymmetric effect to the oscillation probabilities because only electron (anti)neutrinos can undergo CC interactions with the electrons in matter, whereas the NC reactions with electrons, neutrons and protons are flavour symmetric. This can be expressed via a potential V_α

$$V_\alpha = V_{\mathrm{CC}}\delta_{\alpha e} + V_{\mathrm{NC}} = \sqrt{2}G_F\left(N_e\delta_{\alpha e} - \frac{1}{2}N_n\right), \tag{2.39}$$

with

$$V_{\mathrm{CC}} = \sqrt{2}G_F N_e, \tag{2.40}$$

where G_F is the Fermi constant and N_e is the number density of electrons in the transversed medium and $\delta_{\alpha e}$ is the Kronecker delta that is zero for $\alpha \neq e$ and one for $\alpha = e$. The potential due to the NC interactions is

$$V_{\mathrm{NC}} = -\frac{1}{2}\sqrt{2}G_F N_n \tag{2.41}$$

with the number density of neutrons N_n. This potential is only dependent on the neutron number density because it is assumed that regular matter is electrically neutral and has therefore the same number of protons and electrons so that the NC potential of protons and electrons cancel out.

Assuming that the neutrino mass state is an eigenstate of the the Hamiltonian $\mathcal{H}_{\mathrm{vac}}$ in vacuum

$$\mathcal{H}_{\mathrm{vac}}|\nu_k\rangle = E_k|\nu_k\rangle. \tag{2.42}$$

The flavour eigenstate can then be described as an eigenstate of the Hamiltonian $\mathcal{H}_{\text{mat}}$ due to an additional potential V_α, that was introduced above

$$\mathcal{H}_{\text{mat}}|\nu_\alpha\rangle = V_\alpha|\nu_\alpha\rangle. \tag{2.43}$$

This gives the total Hamiltonian in matter $\mathcal{H}$

$$\mathcal{H} = \mathcal{H}_{\text{vac}} + \mathcal{H}_{\text{mat}}. \tag{2.44}$$

With that, also modified mass eigenstates and following that modified oscillation parameters can be introduced. This will be discussed in the two-flavour case, which is often used to describe the matter effect on neutrino oscillations.
For the three flavour case and analogous to the derivation of neutrino oscillations in vacuum, with this Hamiltonian the neutrino oscillations in matter can be derived to get

$$i\frac{\mathrm{d}}{\mathrm{d}x}\Psi_\alpha = H_{\text{F}}\Psi_\alpha \tag{2.45}$$

with the effective Hamiltonian matrix H_{F}

$$H_{\text{F}} = \frac{1}{2E}(U\mathbb{M}^2U^* + \mathbb{A}). \tag{2.46}$$

The matrices for the squared mass difference respective the vector of equation (2.45) are given by

$$\Psi_\alpha = \begin{pmatrix} \psi_{\alpha e} \\ \psi_{\alpha\mu} \\ \psi_{\alpha\tau} \end{pmatrix}, \quad \mathbb{M}^2 = \begin{pmatrix} 0 & 0 & 0 \\ 0 & \Delta m^2_{21} & 0 \\ 0 & 0 & \Delta m^2_{31} \end{pmatrix}, \quad \mathbb{A} = \begin{pmatrix} A_{\text{CC}} & 0 & 0 \\ 0 & 0 & 0 \\ 0 & 0 & 0 \end{pmatrix}. \tag{2.47}$$

$\psi_{\alpha\beta}$ is the transition amplitude for the flavour α to turn into flavour β and A_{CC} can be expressed as

$$A_{\text{CC}} = 2EV_{\text{CC}} = 2\sqrt{2}EG_FN_e. \tag{2.48}$$

This shows that the neutrino oscillation in matter is still dependent on the quadratic mass differences as well as an additional potential that is only relevant for electron neutrinos.
For the two flavour case assuming only electron and muon flavour to exist, the transition probability reads

$$P_m(\nu_e \to \nu_\mu) = \sin^2(2\theta_m)\sin^2\left(\frac{\Delta m^2_m}{4}\frac{L}{E}\right). \tag{2.49}$$

The effective mixing angle in matter θ_m is related to the mixing angle in vacuum θ via

$$\tan(2\theta_m) = \frac{\sin(2\theta)}{\cos(2\theta) - A_{\mathrm{CC}}/\Delta m^2}, \tag{2.50}$$

$$\sin(2\theta_m) = \frac{\sin(2\theta)}{\sqrt{(A_{\mathrm{CC}}/\Delta m^2 - \cos(2\theta))^2 + \sin^2(2\theta)}} \tag{2.51}$$

whereas the effective quadratic mass difference in matter is given by

$$\Delta m_m^2 = m_{2m}^2 - m_{1m}^2 = \Delta m^2 \sqrt{\left(\frac{A_{\mathrm{CC}}}{\Delta m^2} - \cos(2\theta)\right)^2 + \sin^2(2\theta)}. \tag{2.52}$$

Comparing equation (2.49) for the transition probability in matter to equation (2.36) for the transition probability in vacuum shows that the equation has the exact same form with the difference that the oscillation parameters θ and Δm^2 are replaced by θ_m and Δm_m^2. This raises the question why the matter oscillations are sensitive to the sign of the quadratic mass difference when the vacuum oscillation is not. This can be answered by looking at equation (2.52). Reverting the sign of Δm^2 in said formula not only changes the sign of Δm_m^2 but also the absolute value because the root term decreases (increases) for negative (positive) Δm^2.

The Michejew-Smirnow-Wolfenstein (MSW) effect denotes the total conversion possibility if the resonance condition

$$A_{\mathrm{CC}}^{\mathrm{R}} = \Delta m^2 \cos(2\theta), \tag{2.53}$$

or expressed in electron number density by inserting equation (2.53) into equation (2.48)

$$N_e^{\mathrm{R}} = \frac{\Delta m^2 \cos(2\theta)}{2\sqrt{2} E G_F} \tag{2.54}$$

is met. Note, that N_e^{R} is also dependent on the neutrino energy so that only neutrinos with sufficient energy are expected to convert. The behaviour of the effective mixing angle in matter with respect to the electron number density is worth a brief discussion for three cases:

1. For $N_e \gg N_e^{\mathrm{R}}$, the mixing angle is $90°$.
2. For $N_e = N_e^{\mathrm{R}}$, the mixing angle is $45°$.
3. For $N_e \ll N_e^{\mathrm{R}}$, the mixing angle is $0°$.

Considering equation (2.49) shows that the first case gives no oscillation at all, which is the same for the third case, whereas in the second case the mixing and the transition probability is maximal.

For the solar neutrinos, this can also be explained with a look at equation (2.37).

At creation (case 1), the electron neutrino flavour is almost equal to $\nu_{2,m}$. When case 2 is crossed adiabatically, the electron neutrino flavour is still equal to $\nu_{2,m}$, but due to the change of effective mixing angle in the vacuum, the neutrino of almost pure $\nu_{2,m}$ leaves as ν_μ. This effect also depends on the vacuum mixing angle. As it will be shown later, the Large Mixing Angle (LMA) scenario is favoured to explain the neutrino oscillations of the solar electron neutrinos.

2.3. Open Questions and Current Status

Although many properties of neutrinos and their oscillations are nowadays measured with good precision, a number of questions concerning neutrino physics is still not solved. In the following section, first the properties concerning the neutrino oscillations are covered with their associated open questions of MO and CP violation in the leptonic sector, followed by a discussion about the absolute neutrino mass, neutrinos as Majorana or Dirac particle and the possible existence of sterile neutrinos.

2.3.1. Neutrino Oscillation Parameters

As it was shown in section 2.2, the neutrino mass and flavour states are connected via a mixing matrix U

$$\begin{pmatrix}\nu_e\\ \nu_\mu\\ \nu_\tau\end{pmatrix} = U\cdot\begin{pmatrix}\nu_1\\ \nu_2\\ \nu_3\end{pmatrix} = \begin{pmatrix}U_{e1} & U_{e2} & U_{e3}\\ U_{\mu1} & U_{\mu2} & U_{\mu3}\\ U_{\tau1} & U_{\tau2} & U_{\tau3}\end{pmatrix}\cdot\begin{pmatrix}\nu_1\\ \nu_2\\ \nu_3\end{pmatrix}. \tag{2.55}$$

This matrix is commonly known as Pontecorvo-Maki-Nakagawa-Sakata (PMNS) matrix U_{PMNS} and can be parametrised for the three flavour neutrino case to [30]

$$U_{\text{PMNS}} = \begin{pmatrix} c_{12}c_{13} & s_{12}c_{13} & s_{13}e^{-i\delta_{\text{CP}}}\\ -s_{12}c_{23}-c_{12}s_{23}s_{13}e^{i\delta_{\text{CP}}} & c_{12}c_{23}-s_{12}s_{23}s_{13}e^{i\delta_{\text{CP}}} & s_{23}c_{13}\\ s_{12}s_{23}-c_{12}c_{23}s_{13}e^{i\delta_{\text{CP}}} & -c_{12}s_{23}-s_{12}c_{23}s_{13}e^{i\delta_{\text{CP}}} & c_{23}c_{13}\end{pmatrix}, \tag{2.56}$$

where $c_{kl} = \cos(\theta_{kl})$ and $s_{kl} = \sin(\theta_{kl})$ is used with the mixing angles θ_{12}, θ_{13} and θ_{23}. δ_{CP} stands for the CP-violating phase. The U_{PMNS} matrix needs to be multiplied by an additional matrix of phases P for the case that the neutrino is a Majorana particle (see section 2.3.3). P is given via

$$P = \begin{pmatrix} e^{i\alpha} & 0 & 0\\ 0 & e^{i\beta} & 0\\ 0 & 0 & 1\end{pmatrix} \tag{2.57}$$

with additional CP-violating Majorana phases α and β. For oscillation experiments, these phases can be neglected because they vanish due to the squaring of the mixing matrix for the calculation of the transition probabilities.
Neutrino oscillations depend hence on three mixing angles, two squared mass differences and the CP-violating phase, that have to measured precisely. The current global fit of these parameters is shown in table 2.1.

Table 2.1.: The latest global fit for the oscillation parameters from reference [31] (see also reference [32]) including the SK atmospheric neutrino data from 2018 [33].

	NO		IO	
Parameter	bfp $\pm 1\sigma$	3σ range	bfp $\pm 1\sigma$	3σ range
$\theta_{12}/^\circ$	$33.41^{+0.75}_{-0.72}$	$31.31 \rightarrow 35.74$	$33.41^{+0.75}_{-0.72}$	$31.31 \rightarrow 35.74$
$\theta_{23}/^\circ$	$42.2^{+1.1}_{-0.9}$	$39.7 \rightarrow 51.0$	$49.0^{+1.0}_{-1.2}$	$39.9 \rightarrow 51.5$
$\theta_{13}/^\circ$	$8.58^{+0.11}_{-0.11}$	$8.23 \rightarrow 8.91$	$8.57^{+0.11}_{-0.11}$	$8.23 \rightarrow 8.94$
$\delta_{\mathrm{CP}}/^\circ$	232^{+36}_{-26}	$144 \rightarrow 350$	276^{+22}_{-29}	$194 \rightarrow 344$
$\Delta m^2_{21}/(10^{-5}\,\mathrm{eV}^2)$	$7.41^{+0.21}_{-0.20}$	$6.82 \rightarrow 8.03$	$7.41^{+0.21}_{-0.20}$	$6.82 \rightarrow 8.03$
$\Delta m^2_{32}/(10^{-3}\,\mathrm{eV}^2)$	$2.507^{+0.026}_{-0.027}$	$2.472 \rightarrow 2.590$	$-2.486^{+0.025}_{-0.028}$	$-2.570 \rightarrow -2.406$

The PMNS matrix can also be parametrized into different regimes

$$U_{\mathrm{PMNS}} = \underbrace{\begin{pmatrix} 1 & 0 & 0 \\ 0 & c_{23} & s_{23} \\ 0 & -s_{23} & c_{23} \end{pmatrix}}_{\text{atmospheric}} \cdot \underbrace{\begin{pmatrix} c_{13} & 0 & s_{13}e^{-i\delta_{\mathrm{CP}}} \\ 0 & 1 & 0 \\ -s_{13}e^{i\delta_{\mathrm{CP}}} & 0 & c_{13} \end{pmatrix}}_{\text{reactor}} \cdot \underbrace{\begin{pmatrix} c_{12} & s_{12} & 0 \\ -s_{12} & c_{12} & 0 \\ 0 & 0 & 1 \end{pmatrix}}_{\text{solar}} . \tag{2.58}$$

The different regimes will be briefly discussed in the following with the focus on their contribution to the determination of the neutrino oscillations properties.

Solar

Solar neutrinos play a big role in neutrino physics due to the solar neutrino problem and the determination of θ_{12} and Δm^2_{21} and will be described in the following based on reference [34]. The solar neutrino problems describes the observed discrepancy of neutrino flux coming from the sun in comparison to the predicted flux by the Standard Solar Model (SSM) and will be covered in more detail later in this section.
In the SSM neutrinos are produced via the fusion of hydrogen nuclei to helium via

$$4p \rightarrow^4 \mathrm{He} + 2e^+ + 2\nu_e + Q \tag{2.59}$$

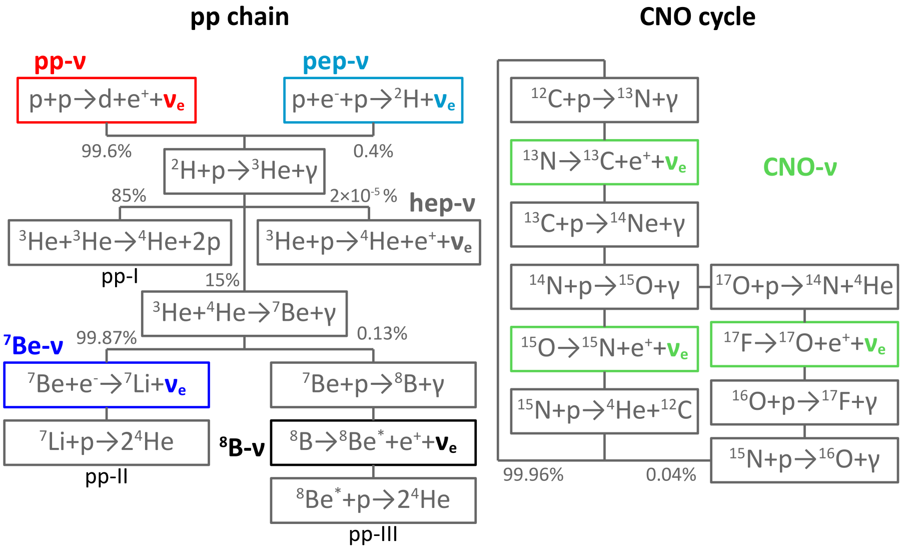

Figure 2.11.: The neutrino production mechanisms in the sun: pp chain (left) and CNO cycle (right) [35]. In blue, red, teal and black the neutrino producing reactions in the pp chain are indicated. The same is done in green for the CNO cycle.

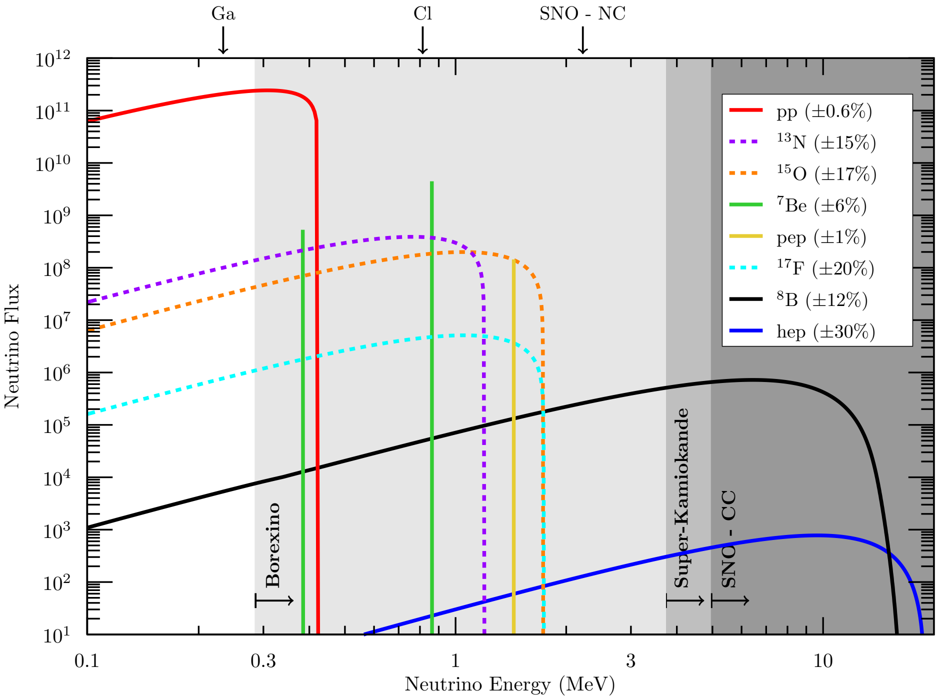

Figure 2.12.: Solar neutrino fluxes with indication of sensitivity ranges of the experiments [36]. The solid (dashed) lines show the neutrinos from the pp chain (CNO cycle).

with the released energy $Q = 26.73\,\mathrm{MeV}$, in which the positron annihilation is included. This is known as the beginning of the proton-proton (pp) chain. The complete pp chain is shown in figure 2.11 on the left side with the second neutrino production mechanism in form of the Carbon–Nitrogen–Oxygen (CNO) cycle on the right side. The CNO cycle only makes up roughly 1% of the hydrogen burning in the sun, but is expected to dominate the fusion processes in stars with higher masses and are a good probe for the metallicity of the sun. The neutrino production reactions in both mechanisms are highlighted with color resulting in a total of eight different neutrino producing reactions. Additionally, the branching ratios of the different processes are indicated.

In figure 2.12, the neutrino flux predicted by the SSM with respect to the neutrino energy is shown in solid (dashed) lines for pp chain (CNO cycle) reactions. For the fusion processes pp (red) and hep (blue), as well as for the β^+ decays of $^8\mathrm{B}$ (black), $^{13}\mathrm{N}$ (purple), $^{15}\mathrm{O}$ (orange), $^{17}\mathrm{F}$ (teal) the energy spectrum of the emitted neutrino follows a continuous spectrum with a cutoff at the maximum of transferred energy. The electron capture process for pep (yellow) shows a monoenergetic peak, since most of the energy is transferred to the neutrino. For the electron capture on $^7\mathrm{Be}$ (green), the energy spectrum shows two monoenergetic peaks, because $^7\mathrm{Li}$ can be produced in an excited state. Additionally, the energy threshold for different experiments and channels is indicated, whereby Cl and Ga represent the radiochemical experiments using Chlor and Gallium.

In essence, there are three detection techniques that are used for the measurement of solar neutrinos: radiochemical, WC and LS detectors. The radiochemical experiments Homestake [37] (The Soviet-American Gallium solar neutrino Experiment (SAGE) [38] and Gallium Experiment (GALLEX) [39]) use neutrino capture on Chlor (Gallium) for detection [5].

Homestake was with measurement start at 1970 the first experiment to observe solar neutrinos and hence first saw the deficit of solar electron neutrino, which then became to be known as solar neutrino problem. This was confirmed by the other radiochemical experiments.

On the WC side, Kamiokande [40] and SK [41] contributed to the measurement of solar neutrinos via elastic scattering of electrons (see equation (2.4)).

The Sudbury Neutrino Observatory (SNO) [42] aimed to measure $^8\mathrm{B}$ neutrinos using heavy water ($\mathrm{D_2O}$) as target material, which allowed to measure neutrinos in the following channels [43]

$$\nu_e + d \to p + p + e^-, \tag{2.60}$$

$$\nu_l + d \to p + n + \nu_l, \tag{2.61}$$

$$\nu_l + e^- \to \nu_l + e^-. \tag{2.62}$$

With the fact, that the elastic scattering process (equation (2.62) has a low scattering angle with respect to the neutrino's direction, the CC channel (equation 2.60) emits light in backward direction and the NC channel (equation (2.61)) is isotropically, the measured events can be sorted into the different samples. Combining

---

[5] See equation (2.9) for neutrino capture on carbon.

the fluxes gave values in good agreement with the SSM meaning that a part of the electron neutrinos had to be converted into other neutrino species [43].

Lastly, Borexino [44] as a liquid scintillator detector had the most significant impact on the detection of solar neutrinos. Borexino was as first experiment able to measure CNO neutrinos [45] and as it will be shown later in section 4.5 to use Cherenkov light to measure the direction of sub-MeV neutrinos from the sun. The measured electron survival probability by Borexino is shown in figure 2.13, where the corresponding neutrino producing mechanism in the sun is indicated. Furthermore, the expected survival probability for the MSW-LMA scenario is shown in a pink band and the vacuum-LMA in grey. As it can be seen, the measured values are in good agreement with the theoretic MSW-LMA prediction. Additionally, the energy dependence for the MSW effect is clearly visible, since neutrinos with energies less than $1\,\mathrm{MeV}$ follow the vacuum prediction. The two extra data points around the $^8\mathrm{B}$ data point stand for different energy regimes that were used for better background rejection.

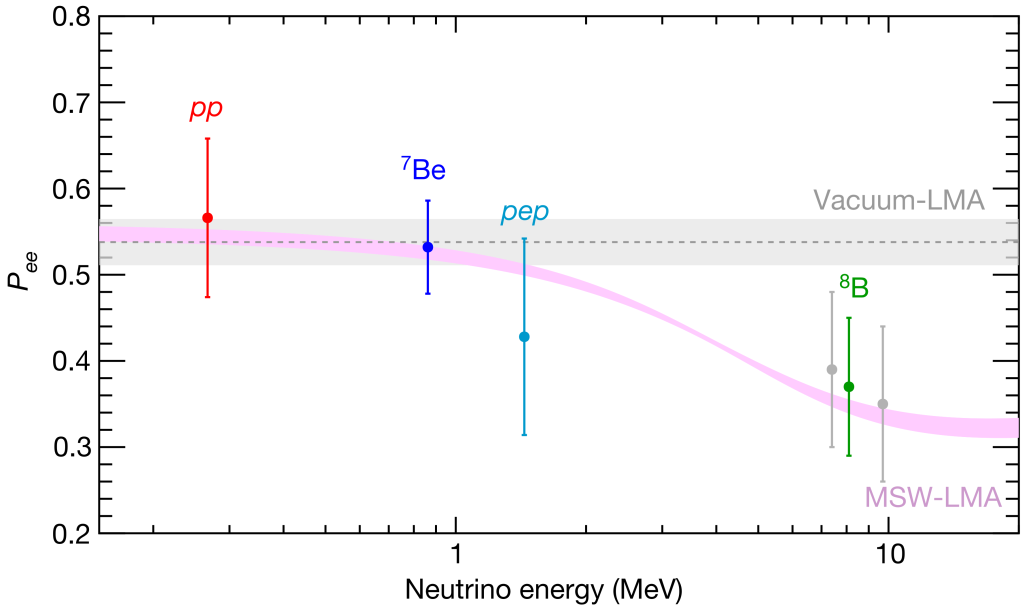

Figure 2.13.: Measurements of solar neutrinos in relation to the MSW effect by Borexino [46]. The data points for the different reactions in the pp chain are indicated via the coloured markers; the grey and pink band shows the expected electron survival probability for the vacuum-LMA and MSW-LMA solution. The agreement of the vacuum (MSW) band with the first two (last four) data points show the energy dependence of the MSW effect.

Figure 2.14 shows the parameter space of θ_{12} and Δm^2_{21} (left) and the current fits for Δm^2_{21} (right). The contour lines show the 1σ to 3σ allowed regions for the solar neutrino measurements with different models. The GS98 model is shown as full regions and the black star denotes the best fit value. The black dotted contours are for the AGSS09 model with the white dot as best fit value and orange is the GS98 model with the SK4 data. The green contours are from Kamioka Liquid Scintillator Antineutrino Detector (KamLAND) [47], a liquid scintillator reactor neutrino experiment. Both sides of the figure hint at a tension between the KamLAND data and the measurement of the solar neutrino experiments regardless of solar model.

JUNO is expected to improve the sensitivity of the solar mixing parameters even further [11].

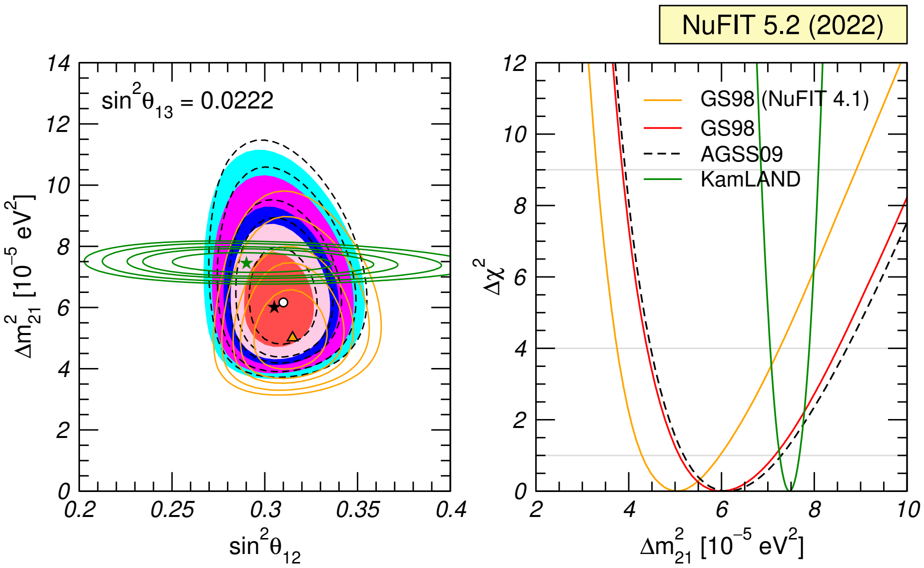

Figure 2.14.: Allowed parameter regions for the solar neutrino parameters (left) and the best fit value for Δm_{21} (right) [31, 32].

Reactor

Next in energy, the reactor anti-electron neutrinos played an important role in determining the mixing angle θ_{13}, that was the last measured mixing parameter aside from the CP violating phase. Reactor neutrinos produced in fission processes of $^{235}\mathrm{U}$, $^{238}\mathrm{U}$, $^{239}\mathrm{Pu}$ or $^{241}\mathrm{Pu}$ are detectable via the IBD (see equation 2.7) with its valuable coincidence event signature [48]. Currently, the best measurement of θ_{13} comes from Double-Chooz [49], the Reactor Experiment for Neutrino Oscillation (RENO) [50] and Daya Bay [51]. All of these experiments use LS loaded with Gadolinium for the superior capture of neutrons.

The current 2σ regions for the parameter θ_{13} with respect to Δm^2_{31} for Normal Ordering (NO) (top) and Δm^2_{32} for Inverse Ordering (IO) (bottom) is shown in figure 2.15 on the right side. The NO refers to the case $m_1 < m_2 < m_3$, whereas the IO refers to $m_3 < m_1 < m_2$, which is the two remaining options to order the neutrino mass eigenstates. This will be explained in more detail in section 2.3.1. The regions of Double-Chooz (pink), Reno (purple) and DayaBay (orange) are displayed together with their combination in black.

Furthermore, reactor neutrino experiment are actively searching for sterile neutrinos, which will be discussed in section 2.3.4.

Atmospheric

The atmospheric sector is historically connected to the determination of Δm^2_{32} and θ_{23}. Experiments like IceCube [52], a neutrino telescope using with PMTs instrumented ice as detector medium, and SK [41], a WC detector that also functions as accelerator neutrino detector in the context of the Tokai-to-Kamioka (T2K) experiment [53], give constraints on the atmospheric mixing parameters. In addition to T2K, Main Injector Neutrino Oscillation Search (MINOS) [54] and NuMI Off-Axis ν_e Appearance (NOνA) [55] as accelerator experiments conducted measurements regarding Δm^2_{32} and θ_{23}.

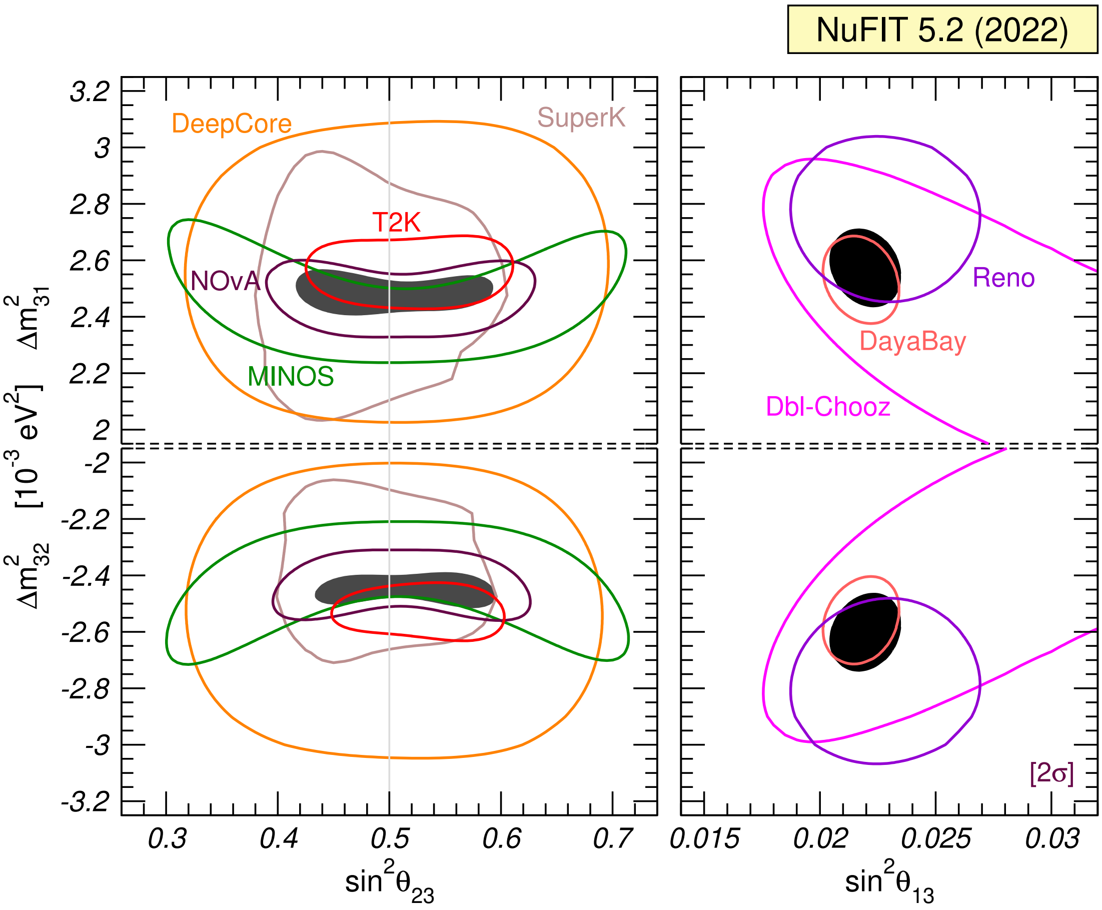

Figure 2.15.: 2σ allowed regions for the atmospheric oscillation parameters (left) and θ_{13} with respect to Δm^2_{32}, Δm^2_{31} respectively (right) [31, 32]. The top (bottom) panels show the NO (IO).

It is to note, that in the energy regime of accelerator and atmospheric neutrinos, the neutrino interactions introduced in section 2.1.2 are of importance.

The 2σ allowed regions for the parameter θ_{23} with regard to Δm^2_{31} for NO (top) and Δm^2_{32} for IO is shown on the left side of figure 2.15. Hereby, DeepCore in orange denotes a subarray of the IceCube detector with better and more PMTs in the area of clearest ice leading to a better energy sensitivity [56]. The second atmospheric contribution is showed in light purple for SK and the accelerator experiments are shown in red (T2K), green (MINOS) and purple (NOνA). The combination is given by the grey area.

Mass Ordering

As it was discussed, most of the neutrino oscillation parameters are known with decent precision, but there are two exceptions to this rule. On one hand, only the absolute value but not the sign of Δm^2_{32} is known, on the other hand the value of δ_{CP} is yet to be determined. The efforts to unravel these two mysteries of the oscillation parameters will be discussed in the following.

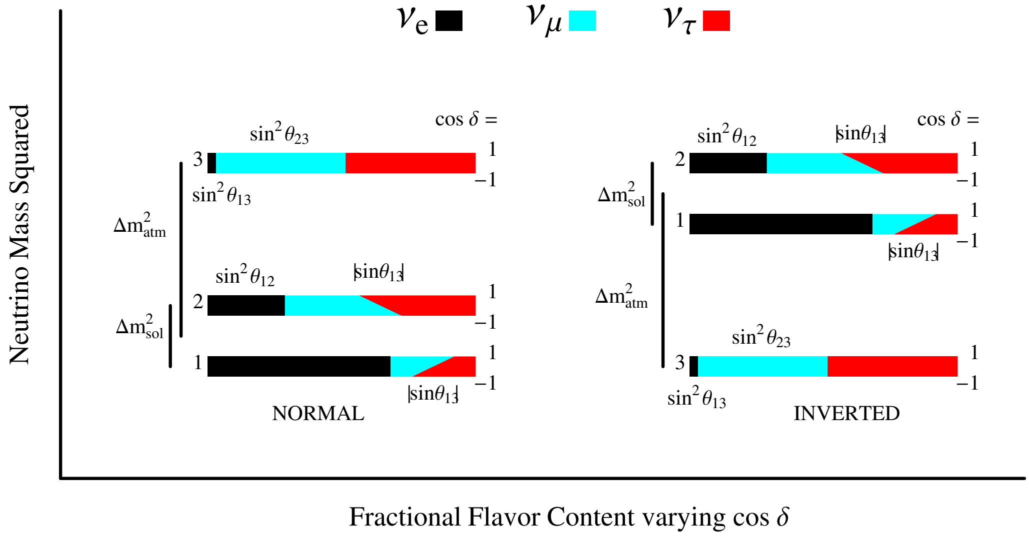

Figure 2.16.: Illustration of the two options of the neutrino mass ordering [57], left the NO and right the IO is shown. The color represents the composition of the mass eigenstates out of the flavour eigenstates. The numbers on the right side of the bars show the assumed values for $\cos(\delta_{\mathrm{CP}})$ that influences the flavour composition.

The Mass Ordering (MO) problem follows directly from the ambiguity of the sign of the atmospheric squared mass difference $\Delta m^2_{\mathrm{atm}} = \Delta m^2_{32}$[6]. m_3 is either the heaviest of the neutrino mass eigenstates (positive Δm^2_{32}) or the lightest (negative Δm^2_{32}). The former is referred to as Normal Ordering (NO) with $m_1 < m_2 < m_3$, while the latter is called Inverse Ordering (IO) with $m_3 < m_1 < m_2$. This is illustrated in figure 2.16, where the ordering for NO (IO) is shown on the left (right) side. The color code represents the flavour contents of the different mass eigenstates. These contents vary depending on the assumed value for the CP-violating

---

[6] Due to the difference in magnitude of Δm^2_{32} and Δm^2_{21}, the atmospheric squared mass difference is sometimes displayed as being equal to Δm^2_{31}, since the precision on $\Delta m^2_{\mathrm{atm}}$ was not high enough to resolve a difference in the order of Δm^2_{21}.

phase, in the figure only denoted as δ. The top of the bars represent to $\delta_{\mathrm{CP}} = 0$, whereas the bottom shows the composition for $\delta_{\mathrm{CP}} = \pi$.

The determination of the MO is expected to help with other open questions of neutrino physics and to improve the precision on the oscillation parameters by constraining the available parameter space. As it will be shown later, the MO directly influences the determination of δ_{CP}, the available area of the effective Majorana mass and can limit the absolute neutrino mass [58]. Hence, many current and future experiments aim to contribute to determining the MO. This is done in mainly three different approaches: Neutrino oscillation experiments, $0\nu\beta\beta$ experiments or cosmological studies.

For the neutrino oscillation experiments, a variety of neutrino sources can be studied mostly making use of the matter effect. Firstly, long baseline accelerator neutrino experiments like the T2K experiment [53] and the NOνA experiment [55] hinted in 2020 a better agreement for the IO with 1.2σ [32, 59] using neutrino oscillations in matter. This is illustrated in figure 2.17, where the combination of T2K (red) and NOνA (blue) data is shown in terms of the parameter space of δ_{CP} and $\sin^2(\theta_{23})$. The black line shows the combination of both with 1σ allowed region dashed, whereas the 2σ allowed areas are solid. The brighter (darker) areas are the 1σ (2σ) allowed regions. The left side shows the IO, where both data sets show good agreement. The right side shows the NO case, in which the 1σ areas barely touch.

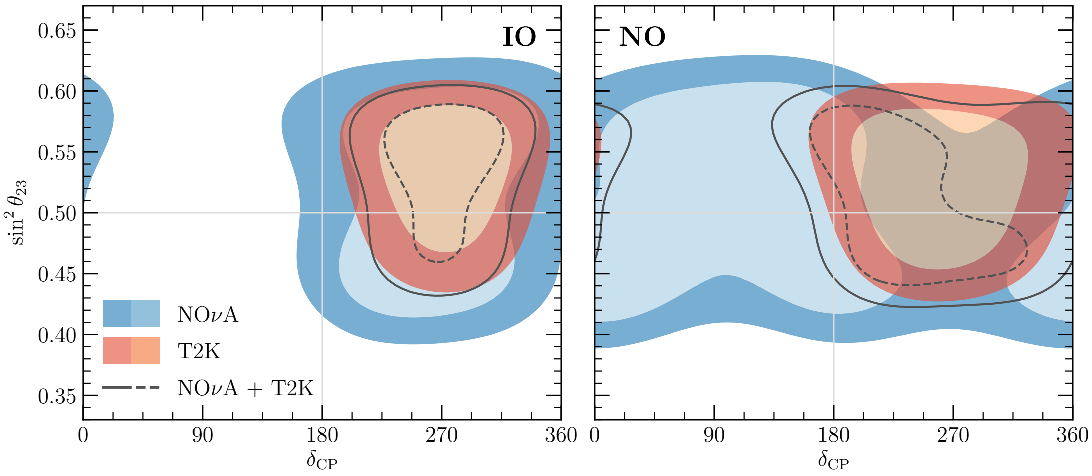

Figure 2.17.: Measured parameter space of T2K and NOνA as of 2020 [32]. The brighter (darker) areas show the 1σ (2σ) allowed range for the individual experiments. The dashed (solid) lines shows the 1σ (2σ) allowed area for the combination of the experiments. While the 1σ areas show small overlap for the NO near $\delta_{\mathrm{CP}} = 180°$, the IO case shows a good agreement.

The upcoming upgrade of T2K to Tokai-to-Hyper-Kamiokande (T2HK) as well as the proposed DUNE [18] are promising additions to the accelerator long baseline neutrino landscape. The former is expected to resolve the MO with 3σ significance for $46\,\%$ of δ_{CP}-values for $\sin^2(\theta_{13}) = 0.1$ in five years of runtime [12]. The latter is expected to be able to determine the MO with 5σ significance after three years for all values of δ_{CP} assuming that all modules are built [18]. Additionally, Theia is also expected to contribute here.

Another possibility to resolve the MO is the precise measurement of the substructure of reactor antineutrinos oscillations in medium baselines, where the matter effect can be neglected. The prime example for this methodology is the JUNO experiment, that is currently under construction in China and that is assumed to take first data this or next year. JUNO, a $20\,\mathrm{kton}$ liquid scintillator detector, aims to measure anti-electron-neutrinos from nuclear power plants with a baseline of $53\,\mathrm{km}$ and is expected to determine the MO with about 3σ after six years of measurement [11].

One option to determine the MO in the next few years (before 2028) is the combination of the upcoming JUNO data with the existing and upcoming data samples of T2K and NOνA [60]. The MO sensitivity for this combination is shown in figure 2.18 for $1\,\%$ (top), $0.75\,\%$ (middle) and $0.5\,\%$ (bottom) uncertainty on Δm^2_{32} from the long baseline experiments. The coloured bands are for JUNO alone (blue), the combination of T2K and NOνA (green), the combination of all three experiments (orange) without maximal CP violation and unrestricted values for δ_{CP} (grey). In both cases the $\pm 1\sigma$ fluctuation of Δm^2_{32} is considered. The blue dotted line shows the mean of the combination. Additionally, the former best fit value for the CP violating phase is shown with the black dot and the 1σ range displayed via the yellow band. The NO (IO) scenario is shown on the left (right) side. First of all, this figure illustrates that the disappearance channel of JUNO is not sensitive to δ_{CP} and the aforementioned sensitivity of 3σ is shown across all values of δ_{CP}. Furthermore, it is shown that the long baseline experiments combined have decent sensitivity for some values of the CP violating phase, but outside of the best fit value for that phase. The influence of the uncertainty on Δm^2_{32} is clearly visible by the decrease of significance with higher uncertainty. It is also visible that even for the worst case, the significance is still across all values of δ_{CP} higher than 4σ. The NO can be determined with 5σ with a probability higher than $50\,\%$ ($84\,\%$) for $1.0\,\%$ ($0.75\,\%$) uncertainty on Δm^2_{32} for the favoured value of δ_{CP}. The IO might be only determinable with a resolution better than $0.75\,\%$ on Δm^2_{32} [60].

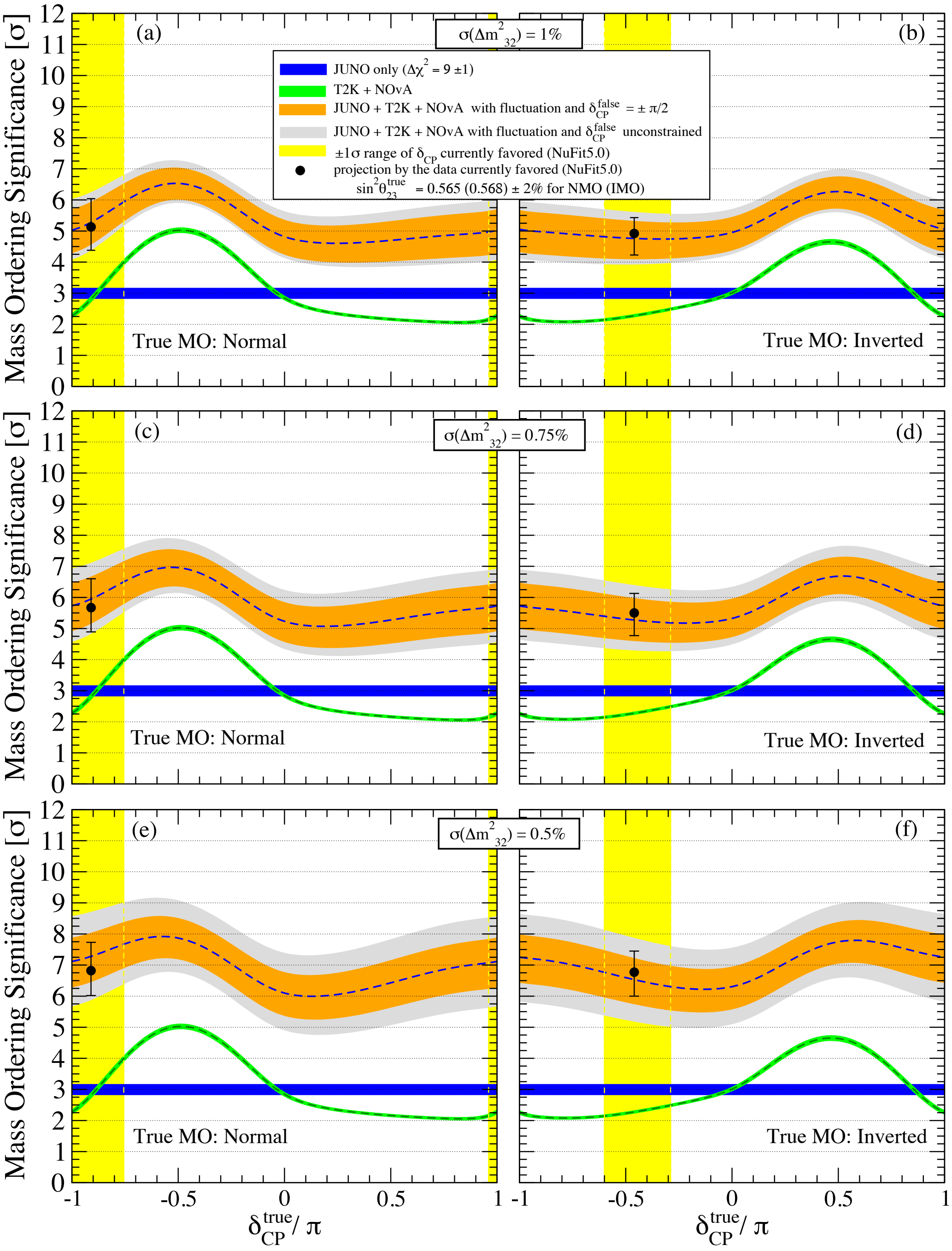

Figure 2.18.: Combined MO sensitivity for JUNO, T2K and NOνA [60].

It is to note that current reactor experiments like Daya Bay [51], KamLAND [47] and Double Chooz [49] already can contribute to the determination of the MO. In contrast to aforementioned results of long baseline accelerator neutrino experiments, the current reactor experiments hint to the NO so that a combination of accelerator and reactor experiments produce an insignificant hint to the NO with

1.6σ [32, 59].

The situation improves, taking atmospheric neutrino measurements into account. These measurements are part of the secondary physics program of SK [61] and from IceCube [62], where the matter effect of neutrinos traversing the earth enables to access the MO. With these data added, MO (IO) is (dis)favoured by 2.7σ under the assumption that these orderings are the only option. In the future, the atmospheric sector will be measured more precisely by for example HK [12], Precision IceCube Next Generation Upgrade (PINGU) [63], JUNO and Theia. Except for PINGU, the atmospheric sector is secondary for their ability to determine the MO. PINGU alone is expected to measure the MO with about 3σ with five years of operation [63].

Constraints on the MO from cosmology making use of the fact that the total neutrino mass

$$m_{\text{total}} = \sum_{i=1}^{3} m_i \tag{2.63}$$

is slightly higher for IO with $m_{\text{total}}^{\text{IO}} \gtrsim 0.10\,\text{eV}$ than for NO with $m_{\text{total}}^{\text{NO}} \gtrsim 0.06\,\text{eV}$ [64]. Since the neutrino masses influences the anisotropy of the CMB and the formation of Large Scale Structures (LSS), these cosmological observables can be investigated to find upper bounds on the total neutrino mass and hence to determine the MO [65]. Reference [64] claims in a Bayesian analysis a hint of 2.7σ preference for NO including not only the oscillation data but also cosmological bounds and the minimum neutrino mass from Karlsruhe Tritium Neutrino Experiment (KATRIN). KATRIN will be discussed in section 2.3.2.

For the case of Majorana neutrinos the search for $0\nu\beta\beta$ is also a possibility to determine the MO, as it will be shown later.

CP-Violation in the Leptonic Sector

The determination of the CP violating phase δ_{CP} is an important goal in the field of neutrino physics. A possible CP violation in the leptonic sector can contribute to resolve the problem of the matter-antimatter asymmetry and hence answer the question why matter even exists, since CP violation is necessary for explaining said asymmetry [66]. CP violation in the quark sector is already measured in the decay of for example K and B mesons [67, 68], but the measured phases are too small to solely explain the observed matter-antimatter asymmetry [69].

In order to measure δ_{CP}, neutrino oscillation channels like the $\nu_\mu \to \nu_e$ appearance are compared to antineutrino oscillation channels like $\overline{\nu}_\mu \to \overline{\nu}_e$. For this task, long baseline accelerator neutrino experiments are well-suited because of the option to reverse the orientation of the magnetic field of the horns and thus have Forward Horn Current (FHC) for ν_μ beam and Reverse Horn Current (RHC) for $\overline{\nu}_\mu$ beam. With that, the flux and position of the neutrinos and antineutrinos are essentially the same, so that differences in the observed fluxes hint towards differences in the oscillation behaviours and thus to a CP violation in the leptonic sector.

Currently, there are essentially two experiments contributing to the measurement of δ_{CP} in form of NOνA and T2K, whose measured parameter space in δ_{CP} and $\sin^2(\theta_{23})$ of 2020 is shown in figure 2.17. The combination of the results of these experiments hinted toward a CP violation, because the conserving values of $\delta_{CP} = 0, \pm\pi$ are barely touched by the 1σ area of the combination shown as the black dotted line in the NO case. For the IO case, the situation is stronger, where even the 2σ areas do not reach CP conserving values. In addition, the MINOS experiment [54], an sandwich steel-scintillator calorimetry experiment running until 2016, also gives an input to the determination of δ_{CP}.

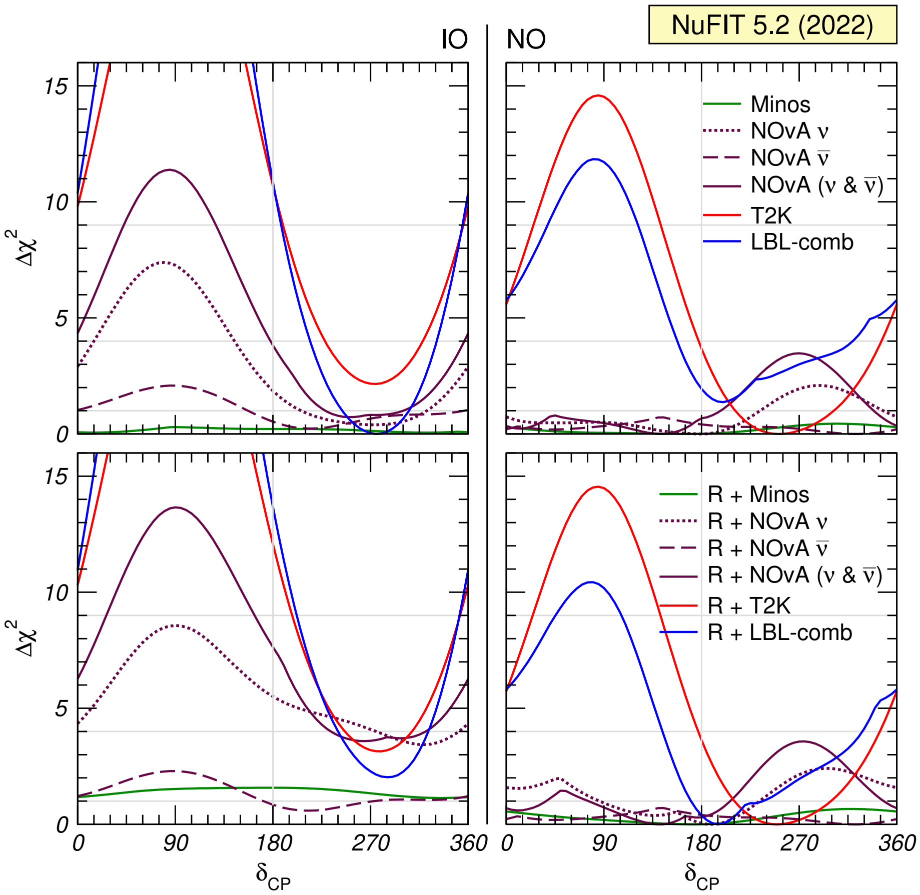

Figure 2.19.: Current best fit on CP violating phase [31, 32].

The current best fit for the CP violating phase is shown as a $\Delta\chi^2$ plot over the angles of δ_{CP} in figure 2.19, where the left (right) side corresponds to true IO (NO). The top panel shows the results of the aforementioned experiments alone (green for MINOS, dark red for NOνA with the solid line for both modes, the dotted line for neutrino mode and the dashed line for antineutrino mode and red for T2K) and the combination of the long baseline neutrino experiments in blue. The bottom panel also uses the results of the reactor neutrino experiments as an input so that the color coding persists but with the addition of the reactor data.

The aforementioned hint towards the IO of T2K and NOνA is also observable here, since the agreement of the fits is visibly better for the IO than the NO. This tension in the data leads also to the better limit on CP conservation for the NO for T2K alone, instead of the combination of the long baseline experiments for both panels. Without the reactor data, CP conservation can be excluded by roughly 1.4σ for the long baseline combination or by 2σ by the T2K data alone in the NO. With the reactor data, $\delta = 180^\circ$ can be basically viewed as allowed in the combination, whereas T2K alone has roughly the same significance as without the reactor data. For the IO, the limits are clearer so that CP conservation can be excluded by roughly 3σ.

In the future, DUNE, T2HK, Theia and European Spallation Source neutrino Super Beam (ESSνSB) will tackle the determination of δ_{CP}. DUNE is expected to reach 5σ for $50\,\%$ of δ_{CP} values after roughly ten years of measurement time [70], T2HK will be able to measure CP violation even with unknown MO with 3σ for $55\,\%$ of δ_{CP} values assuming $\sin^2(2\theta_{13}) = 0.1$ [12] with 5 years of measurement. Theia is expected to have similar performance as a DUNE module of roughly same size within an exposure of 7 years [71]. Lastly, ESSνSB should be able to confirm CP violation with 5σ for $71\,\%$ of δ_{CP} values with 10 years of beam time [72].

2.3.2. Absolute Neutrino Masses

The discovery of neutrino oscillations showed that neutrinos have indeed a non-zero mass in contrast to the assumption in the SM. The scale of the absolute neutrino mass is still not entirely resolved yet, but various limits exist coming from different perspectives.

Currently, only one option exists to get experimentally access to the absolute neutrino mass without considering squared mass differences. This option is in the form of weak decays. The most used decays are the β-decay of tritium (^{3}H)

$$^3\mathrm{H} \rightarrow {}^3\mathrm{He} + e^- + \overline{\nu}_e, \tag{2.64}$$

whose molecular form (T_2) is often worked with

$$\mathrm{T}_2 \rightarrow {}^3\mathrm{HeT}^+ + e^- + \overline{\nu}_e \tag{2.65}$$

and the electron capture on Holmium (^{163}Ho)

$$^{163}\mathrm{Ho} + e^- \rightarrow {}^{163}\mathrm{Dy}^* + \nu_e. \tag{2.66}$$

The tritium decay is used by KATRIN [73] in order to precisely measure the energy of the outgoing electron and hence to limit the maximum mass of the anti-electron-neutrino. Herefore, a system of filter spectrometers is used to detect only electrons at the end of the β decay energy spectrum with silicon detectors. KATRIN is able to limit the absolute neutrino mass to $m_\nu^{\mathrm{KATRIN}} < 0.8\,\mathrm{eV}$ at $90\,\%\,\mathrm{C.L.}$ [74]. It is

expected that this limit will be lowered towards $0.45\,\mathrm{eV}$ this year [75] and that within a few years the targeted sensitivity of $0.2\,\mathrm{eV}$ will be reached [76].
Another experiment planning to investigate tritium is the Project 8 experiment. Project 8 uses atomic tritium and a spectroscopy method based on cyclotron radiation of the outgoing electron with the goal to reach a sensitivity of $40\,\mathrm{meV}$ [77].
The Electron Capture in $^{163}\mathrm{Ho}$ experiment (ECHo) [78] uses a bolometric approach (a principle shortly explained in next section) to measure the deexcitation energy of $^{163}\mathrm{Dy}^*$ in form of emitted gammas. These efforts lead to an upper limit of $m_\nu^{\mathrm{ECHo}} < 150\,\mathrm{eV}$ at $95\,\%\,\mathrm{C.L.}$ [79]. In the future, ECHo aims to upscale their experiment to reach sub eV sensitivity.
Aside from the direct measurements, also the search for the $0\nu\beta\beta$ as well as cosmological observations can limit the absolute neutrino mass. The first one will be discussed in the following section, whereas the second one was shown in the discussion of mass ordering (section 2.3.1).

2.3.3. Majorana or Dirac Particle

This section is based on references [26, 29]. The existence of neutrino masses that are very small compared to the masses of all other fermions in the SM is puzzling, since the difference in masses also means that the Yukawa coupling to the Higgs field has a large gap in scale. One approach to explain that gap in coupling strengths is to describe the neutrino as a Majorana particle. This means that the neutrino is its own antiparticle, because a Majorana neutrino has another mechanism to gain mass, which will be explained in the following. Furthermore, proving that neutrinos are realised as Majorana particles in nature would be a big step to explain the matter-antimatter-asymmetry. The second option is that the neutrino can be described as a Dirac particle so that every neutrino flavour has its own distinct antiparticle with the same mass. This is done in the SM, where neutrinos are assumed to be massless Dirac particles, which can be motivated by looking at the Lagrangian leading to the Dirac equation

$$\mathcal{L} = \overline{\psi}\left(i\gamma_\mu \frac{\partial}{\partial x_\mu} - m_D\right)\psi. \tag{2.67}$$

γ_μ are the gamma matrices, ψ is a fermion field, x_μ are the components of the four-vector and m_D is the Dirac mass, whose term can be simply written as

$$\mathcal{L} = m_D\overline{\psi}\psi. \tag{2.68}$$

ψ can be splitted into its chiral components (left-handed ψ_L and right-handed ψ_R) resulting in

$$\mathcal{L}_{\mathrm{Dirac}} = m_D(\overline{\psi}_L\psi_R + \overline{\psi}_R\psi_L). \tag{2.69}$$

When considering neutrinos the above equations mean that in order to give mass to the neutrino in the SM also a right-handed neutrino is needed. This is not the case in the SM due to the non existing coupling of the W-boson to right-handed fermions.
When including CP conjugated spinors ψ^C two combinations of spinors are added that behave like Lorentz scalars leading to a formula similar to equation (2.68)

$$\mathcal{L} = \frac{1}{2}\left(m_M \overline{\psi}\psi^C + m_M^* \overline{\psi}^C \psi\right) = \frac{1}{2} m_M \overline{\psi}\psi^C + \mathrm{h.c.} \tag{2.70}$$

m_M stands for the Majorana mass and $\mathrm{h.c.}$ denotes the Hermitian conjugate. It can be used that

$$\psi^C_{L,R} = (\psi^C)_{R,L} = (\psi_{R,L})^C \tag{2.71}$$

to write equation (2.70) in terms of left- and right-handed spinors

$$\mathcal{L}^L = \frac{1}{2} m_L \left(\overline{\psi}_L \psi_R^C + \overline{\psi}_R^C \psi_L\right) = \frac{1}{2} m_L \overline{\psi}_L \psi_R^C + \mathrm{h.c.} \tag{2.72}$$

$$\mathcal{L}^R = \frac{1}{2} m_L \left(\overline{\psi}_L^C \psi_R + \overline{\psi}_R \psi_L^C\right) = \frac{1}{2} m_R \overline{\psi}_L^C \psi_R + \mathrm{h.c.} \tag{2.73}$$

$m_{L,R}$ are the real Majorana masses. This equations can be combined with the similar Dirac mass term from equation (2.69) to get

$$2\mathcal{L} = \begin{pmatrix} \overline{\psi}_L & \overline{\psi}_L^C \end{pmatrix} \begin{pmatrix} m_L & m_D \\ m_D & m_R \end{pmatrix} \begin{pmatrix} \overline{\psi}_R^C \\ \psi_R \end{pmatrix} + \mathrm{h.c.} \tag{2.74}$$

$$= \overline{\Psi}_L M \Psi_R^C + \overline{\Psi}_R^C M \Psi_L \tag{2.75}$$

with

$$M = \begin{pmatrix} m_L & m_D \\ m_D & m_R \end{pmatrix}, \quad \Psi_L = \begin{pmatrix} \psi_L \\ \psi_L^C \end{pmatrix} = \begin{pmatrix} \nu_L \\ N_L^C \end{pmatrix} \text{ and } \Psi_R^C = \begin{pmatrix} \psi_R^C \\ \psi_R \end{pmatrix} = \begin{pmatrix} \nu_R^C \\ N_R \end{pmatrix}, \tag{2.76}$$

where a notation was used to represent that only left-handed neutrinos or right-handed antineutrinos interact weakly (ν_L and ν_R^C). The remaining spinors correspond to sterile neutrinos and antineutrinos (N_R and N_L^C). With that, there are three special cases that deserve a short discussion here:

1. Vanishing Majorana masses ($m_L = m_R = 0$) lead to the regular Dirac expression.

2. Vanishing Dirac mass ($m_D = 0$) corresponds to pure Majorana fields, which is an option to give neutrinos mass without introducing sterile neutrinos.

3. The combination of one huge Majorana mass ($m_R \gg m_D$) and a vanishing second Majorana mass ($m_L = 0$) leads to one version of the seesaw mecha-

> nism. In the seesaw mechanism, the mass eigenstates of the SM neutrino m_ν and the mass eigenstate of the sterile neutrino m_N are then given by
>
> $$m_\nu = \frac{m_D^2}{m_R} \text{ and } m_N = m_R\left(1+\frac{m_D^2}{m_R^2}\right) \approx m_R. \tag{2.77}$$
>
> This means, the small masses of neutrinos in the SM can be explained by the existence of very heavy sterile right-handed neutrinos, which directly motivates the search for heavy sterile neutrinos.

It is to note that in all cases except the pure Dirac one, the neutrino is its own antiparticle ($\psi^C = \psi$) and therefore the lepton number is not conserved.
A way to prove the Majorana nature of the neutrino is the observation of the Neutrinoless Double Beta Decay ($0\nu\beta\beta$), a process that violates the lepton number conservation and is only expected if the neutrino is its own antiparticle [80]. The in the SM allowed double beta decay happens under the emission of two neutrinos so that the lepton number is conserved [81]

$$(A,Z) \to (A,Z+2) + 2e^- + 2\overline{\nu}_e + Q_{\beta\beta}. \tag{2.78}$$

Here A is the atomic mass number, Z the nuclear charge number and $Q_{\beta\beta}$ the released energy. The $0\nu\beta\beta$ on the other hand happens without the emission of neutrinos

$$(A,Z) \to (A,Z+2) + 2e^- + Q_{\beta\beta} \tag{2.79}$$

and therefore violates the lepton number by two units.
The principle of experiments searching for $0\nu\beta\beta$ is based on the calorimetry of the two resulting electrons. For the regular double beta decay, a continuous energy spectrum is expected due to the missing energy of the neutrinos, whereas the energy spectrum of the electrons from a $0\nu\beta\beta$ are expected to show a sharp peak at $Q_{\beta\beta}$. Currently, there is no evidence for the existence of the $0\nu\beta\beta$, but there are limits on the effective Majorana mass $\langle m_{\beta\beta}\rangle$ and the half-life of the decay process $T^{0\nu}_{1/2}$. These quantities are related via [81]

$$T^{0\nu}_{1/2} \simeq 10^{27-28}\left(\frac{0.01\,\mathrm{eV}}{\langle m_{\beta\beta}\rangle}\right)^2 \text{ years} \tag{2.80}$$

for light mass neutrinos. The limits on the effective Majorana mass are visualised in figure 2.20 via the boxes denoted with the isotope used in the corresponding experiments. These boxes are shortened for visualisation purposes; the experiments cover the full range of the lightest neutrino mass from 10^{-4} to $1\,\mathrm{eV}$.
The limit for molybdenum $^{100}\mathrm{Mo}$ comes from the CUORE Upgrade with Particle Identification in Molybdenum (CUPID-Mo) experiment, that operated 20 scintil-

lating crystals as bolometers measuring the change of temperature of the active medium. The shown limit is $\langle m_{\beta\beta}^{^{100}\mathrm{Mo}} \rangle < (0.31 - 0.54)\,\mathrm{eV}$ [82], although this was improved to $\langle m_{\beta\beta}^{^{100}\mathrm{Mo}} \rangle < (0.28 - 0.49)\,\mathrm{eV}$ in 2022 [83], both at $90\,\%$ CL, which is also the case for all other results presented in the following. The bolometric detector technique is also used in the previous iterations of CUPID measuring $^{82}\mathrm{Se}$ in CUPID-0 and $^{130}\mathrm{Te}$ in Cryogenic Underground Observatory for Rare Events (CUORE), hence the blue color of the corresponding boxes. The shown limits are $\langle m_{\beta\beta}^{^{82}\mathrm{Se}} \rangle < (0.311 - 0.638)\,\mathrm{eV}$ [84] and $\langle m_{\beta\beta}^{^{130}\mathrm{Te}} \rangle < (0.075 - 0.350)\,\mathrm{eV}$ [85]. Both experiments improved on this limits 2022 to $\langle m_{\beta\beta}^{^{82}\mathrm{Se}} \rangle < (0.263 - 0.545)\,\mathrm{eV}$ [86] and $\langle m_{\beta\beta}^{^{130}\mathrm{Te}} \rangle < (0.090 - 0.305)\,\mathrm{eV}$ [87].

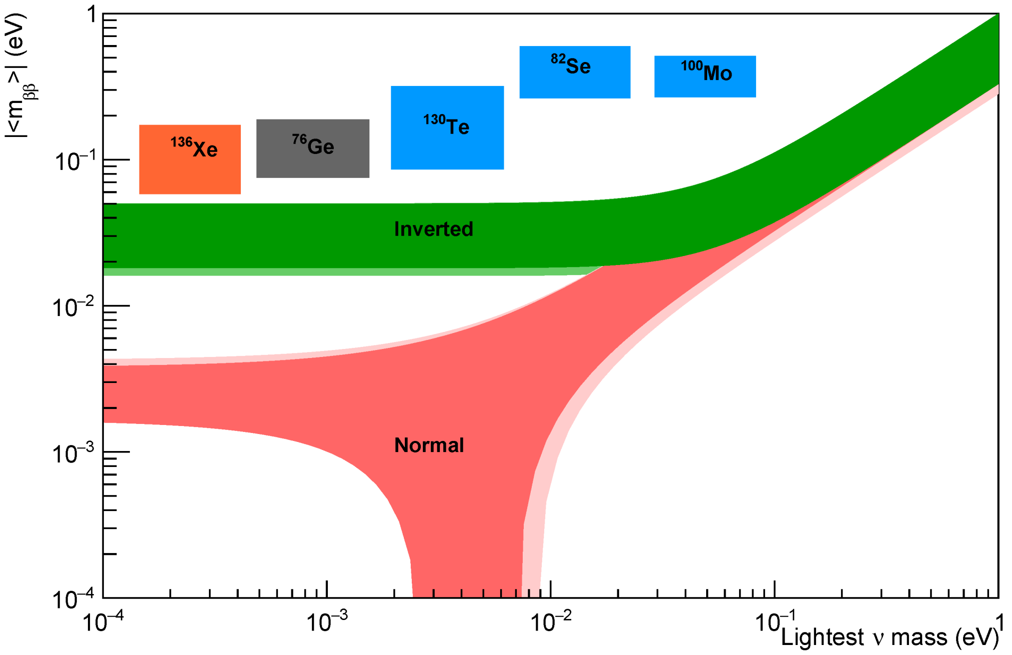

Figure 2.20.: Effective Majorana mass with respect to the lightest neutrino mass with the exclusions of current experiments and the bands for inverted and normal ordering [88].

The limit for germanium $^{76}\mathrm{Ge}$ comes from The GERmanium Detector Array (GERDA), an experiment that operates semiconductor germanium detectors enriched with said isotope. The limit is $\langle m_{\beta\beta}^{^{76}\mathrm{Ge}} \rangle < (0.079 - 0.180)\,\mathrm{eV}$ [89].

Lastly, KamLAND was loaded with $^{136}\mathrm{Xe}$ in the KamLAND Zero-Neutrino Double-Beta Decay (KamLAND-Zen) experiment measuring as of 2022 $\langle m_{\beta\beta}^{^{136}\mathrm{Xe}} \rangle < (0.036 - 0.156)\,\mathrm{eV}$, which excludes the first values in the inverted ordering band [90]. The shown limit in the figure is $\langle m_{\beta\beta}^{^{136}\mathrm{Xe}} \rangle < (0.061 - 0.165)\,\mathrm{eV}$ from 2016 [91].

In the future, it is planned to scale up GERDA and CUORE to a target mass of one ton. For GERDA this experiment is called The Large Enriched Germanium Experiment for Neutrinoless $\beta\beta$ Decay (LEGEND) [92], of which the first phase with $200\,\mathrm{kg}$ of target mass is currently running, whereas CUORE's upgrade is named CUPID-1T [93]. With these next versions it is planned to exclude the inverse ordering band and reach into the normal ordering band [94]. This is another gateway to the determination of the mass ordering but only if the neutrino proves to be a Majorana particle.

2.3.4. Sterile Neutrinos

The search for sterile neutrinos, neutrinos that do not interact weakly, is well motivated on low as well as on high mass scales. The idea being that additional to the three active neutrinos the existence of up to three right-handed sterile neutrinos is possible. The discovery of said neutrinos would shed light on different observed phenomena or theoretical problems depending on the mass regime. Here, the focus is on the search for light sterile neutrinos, whereas the search for heavy neutral leptons is not covered.

The number of light active neutrinos with a mass less than half of the mass of the Z^0 boson is well-known due to the measurement of the Z^0 decay width at the different experiments at the Large Electron-Positron Collider (LEP) to be $N_\nu = 2.9963 \pm 0.0074$ [95]. Furthermore, cosmological calculations of the influence of the effective neutrino number on the CMB provides $N_{\text{eff}} = 3.0440 \pm 0.0002$ [96] and confirms the LEP measurement. With that, any additional light active neutrino is ruled out.

There is a number of hints in the light neutrino regime that point toward the existence of a light sterile neutrino. The first one is the Reactor Antineutrino Anomaly (RAA), an about $6\,\%$ lower detection rate compared to theory for reactor neutrinos observed by reactor neutrino experiments [97]. Examples for these experiments are the liquid scintillator experiments Daya Bay [98] and Double Chooz [99]. This deficit could hint to an oscillation of the reactor neutrinos into sterile neutrinos. There are other approaches to explaining this anomaly by for example adjusting the theoretical models predicting the neutrino flux [100]. This resolves also a second reactor neutrino anomaly, often referred to as $5\,\text{MeV}$ bump, that comes from an excess of events between 4 and $6\,\text{MeV}$ of about $10\,\%$ [100]. This bump was also measured by the aforementioned experiments among others.

The second observation that can be explained by light sterile neutrinos is the gallium anomaly. This anomaly describes the observed deficit in electron neutrino flux of calibration sources for the radio-chemical solar neutrino experiments SAGE [38] and GALLEX [101]. These experiments observed about $80\,\%$ of the expected flux when combining their results [102]. This is confirmed by the Baksan Experiment on Sterile Transitions (BEST) experiment that also measured a deficit of $21\,\%$ or $23\,\%$ depending on the detector region [103].

The third hint is an anomaly in the accelerator experiments Liquid Scintillator Neutrino Detector (LSND) [104] and Mini Booster Neutrino Experiment (MiniBooNE) [105]. Both measured an excess of electron (anti)neutrinos in muon (anti)neutrino beams, MiniBooNE with 4.8σ and LSND with 3.8σ. This anomaly is further investigated with the MicroBooNE experiment that does not observe the excess and hence finds no evidence for sterile neutrinos [106].

Other efforts are made to investigate these anomalies in form of reactor neutrino experiments with very short baselines. Neutrino Experiment for Oscillation at Short baseline (NEOS) [107] shows in combination with RENO data an allowed region of $0.1 < |\Delta m^2_{41}| < 7\,\mathrm{eV}^2$ at $95\,\%\,\mathrm{C.L.}$ and best fit values of $|\Delta m^2_{41}| = 2.41\,\mathrm{eV}^2$ and $\sin(2\theta_{41}) = 0.08$ [108]. The Neutrino-4 experiment [109] reports $|\Delta m^2_{41}| = 7.30 \pm 1.17\,\mathrm{eV}^2$ and $\sin(2\theta_{41}) = 0.36 \pm 0.12$ [110]. This result is contradicted by other very short baseline experiments like the DANSS experiment [111], that finds no evidence for sterile neutrinos and excludes the best-fit parameter of the BEST experiment [112]. This is confirmed by the Precision Reactor Oscillation and SPECTrum Experiment (PROSPECT) [113], that also does disfavour sterile neutrinos for the best-fit parameters of the aforementioned experiments [113]. In conclusion, there is a strong tension concerning the RAA and the gallium anomaly that has to be resolved with detector upgrades and more statistics in the future.

3. Photodetectors

Photodetectors are an essential component for many neutrino detectors like ANNIE (see chapter 5). They are used for detecting the optical photons that are emitted when a charged particle traverses the active medium of a detector. This will be covered in more detail in the next chapter 4. With the positions and the times of the photon hits on the photodetector, reconstructions of the event topology are possible, which will be discussed in the chapter 7.

In addition to the long existing PhotoMultiplier Tube (PMT), newer technologies in form of the Silicon PhotoMultiplier (SiPM) and the Large Area Picosecond Photodetector (LAPPD) are covered in this chapter. The topic is concluded by a section discussing parameters characterising the quality of photodetectors, that are important for detecting and reconstructing particles in neutrino detectors.

3.1. PhotoMultiplier Tube (PMT)

This section is based on reference [114] if not otherwise stated and referenced. Due to their size, prize and sensitivity, PMTs are essential for neutrino physics as they were, are and will be used in many neutrino experiments like ANNIE [3], Icecube [115], SK [10], Borexino [44] and JUNO [11] to name a few.

A PMT consists of a photocathode, an amplification mechanism and an anode in order to convert a photon into a measurable current. It is necessary to house these components inside of an evacuated tube, typically with a glass window, to prevent interactions of electrons with gas molecules and to use the external photoelectric effect. Photons can pass through the window and interact with the photocathode, which is usually evaporated unto the inside of the window. Via the external photoelectric effect the photon can be absorbed under the emission of a so called Photoelectron (PE) in the photocathode. The resulting PE travels due to the electric field between photocathode and anode to the amplification mechanism leading to an electron avalanche unto the anode. This avalanche results in a current peak measurable with an oscilloscope or an analog-to-digital converter.

PMTs exist in two different types dependent on the amplification structure (dynode or MicroChannel Plate (MCP)), which will be described in the next sections.

3.1.1. Dynode PMT

In figure 3.1 the functioning scheme of a dynode PMT is shown. The incoming photons travel from a source on the left, e.g. scintillation light in a scintillation neutrino detector, to the PMT. They pass through the input window and hit the photocathode. The resulting PE is released into the vacuum and accelerated by the electric field between photocathode and anode. The direction of the PE is modified by focusing electrodes in order to maximise the probability of the PE hitting the first dynode. A dynode is a metal electrode (e.g. stainless steel) coated by a major secondary emissive material like beryllium oxide. Due to secondary emission the PE releases multiple electrons off the first dynode, which in turn are accelerated unto the second dynode repeating the process. The acceleration is given via an increasing voltage between the dynode pairs. The number of secondary electrons in each stage is dependent on the material and the accelerating voltage. In this way, a single PE results in for example 10^7 electrons[1] hitting the anode, leading to a measurable current peak at the PMT's output.

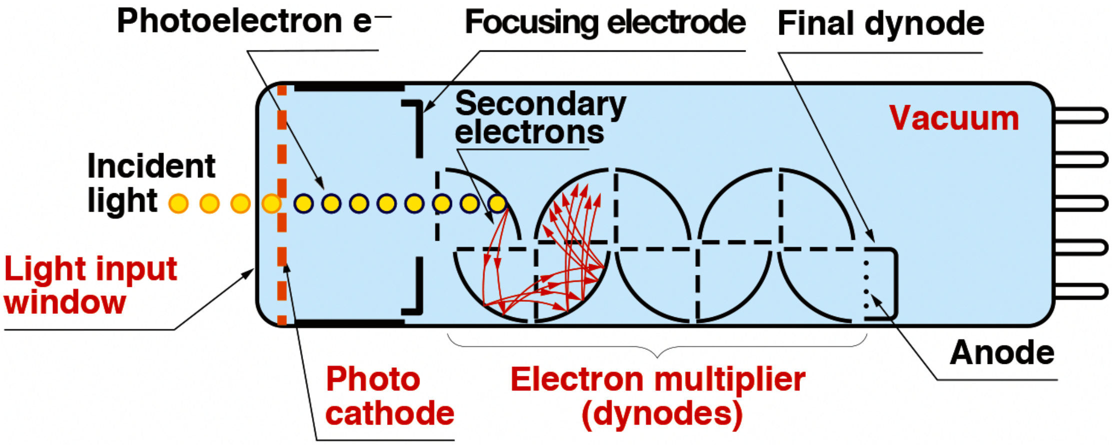

Figure 3.1.: Scheme of a dynode PMT taken from reference [116].

3.1.2. MicroChannel Plate (MCP) PMT

In principle, the structure of a MCP PMT is the same as the structure of a dynode PMT with the difference that the multiplication mechanism is realised by a microchannel plate, which is depicted in figure 3.2. On the left side the scheme of a MCP is shown as a round disk. The disk with a thickness in the order of millimetres is traversed by parallel capillaries with a typical diameter between 6 and $25\,\mu\text{m}$. Usually, MCPs are made of electrically highly resistant glass and the inner wall of the capillaries are coated with metal for a high secondary electron emission probability. The channels are inclined with respect to the disk's surface in order to ensure that the incoming PE hits the wall. Similar to the dynode type, a electric field is used between the photocathode and the anode for the acceleration

---

[1] This factor is commonly known as gain.

of the PE and the secondary electrons.

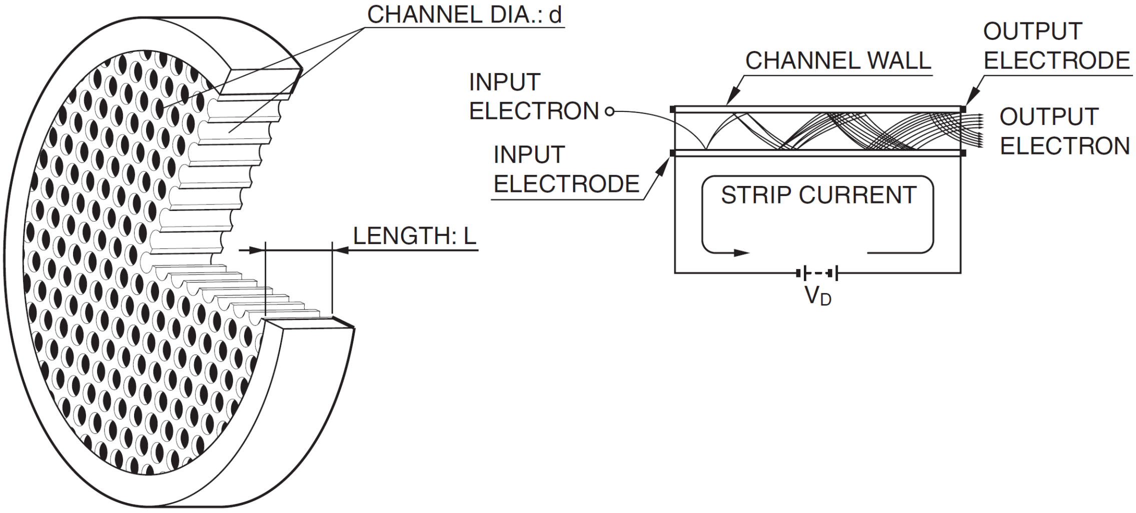

Figure 3.2.: Scheme of a MCP PMT taken from reference [114]. The left side shows a MCP; the right side depicts the functioning principle of a single channel.

A detailed view of a single channel is displayed on the right side of figure 3.2. An incoming PE hits the wall and releases multiple secondary electrons. The aforementioned electric field accelerates these electrons towards the anode. The inclination of the MCP walls ensures that the secondary electrons, that are accelerated orthogonal to the disk's surface, hit the wall again to repeat the process. The resulting electron avalanche is then detected by the anode yielding a measurable current. It is useful to combine multiple MCPs in one photodetector to increase the gain and decrease the noise. In opposite to dynode PMTs, MCP PMTs give the opportunity to extract a spatial information from photon hits with the use of segmented anode pixels or anode strips. The combination of multiple MCPs and anode strips for readout is one of the key features of the later discussed LAPPDs.

3.2. Silicon PhotoMultiplier (SiPM)

The following introduction to SiPMs is based on reference [117] and [118].
The principle of a Single Photon Avalanche Diode (SPAD), which is a special form of an Avalanche PhotoDiode (APD), is the starting point for building a SiPM. The functioning principle of an APD as a semiconductor detector can be seen in figure 3.3 and is the following: Silicon is highly doped with e.g. phosphor for a n-type and with e.g. aluminium for a p-type semiconductor in order to create a p-n junction. In between the highly doped p^+ (shown in dark red) and n^+ (shown in blue) zones, a lightly doped zone p is brought in. The resulting p^+-p-n^+ diode is operated in reverse bias, which leads to the travel of electrons into the p-type

semiconductor and vice versa [2].

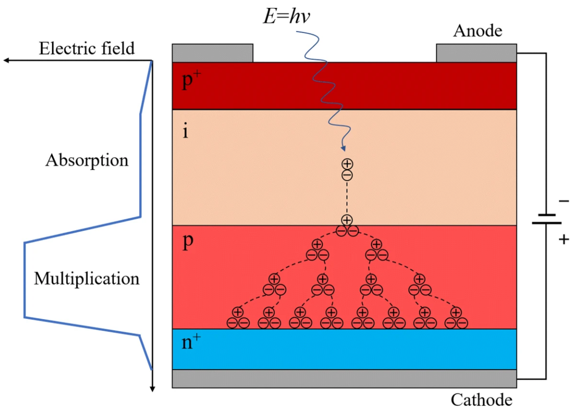

Figure 3.3.: Scheme of a APD taken from reference [119].

Due to the recombination of electron and holes, a part of the p-zone adjacent to the p^+-zone is depleted of charge carriers. With that, a depletion or absorption zone i or p^- is created, which is depicted in beige, whereas the part of the p-zone without recombinations is shown in light red. The p-zone is also called multiplication zone, since the charge distribution between the p and the n^+ zone results into a high electric field, which is shown in the left side of figure 3.3. Thereby, an APD has the structure p^+-i-p-n^+. Photons hitting such a diode are capable of transferring enough energy to electrons in the valance band to move them to the conduction band, effectively creating electron-hole pairs in the absorption zone. The electrons are accelerated to the cathode, entering the multiplication zone. Here, the aforementioned high electric field accelerates the electrons further, so that it is able to create secondary charge carrier pairs via impact ionisation on the way to the cathode. In turn, the resulting secondary electrons are also accelerated to repeat this effect leading to an electron avalanche. The reverse bias voltage has to be chosen carefully so that the primary electron is able to start the avalanche process.

If the bias voltage of an APD exceeds the nominal breakdown voltage of the diode, the diode is operated in the so called Geiger mode and - provided with a quenching mechanism - can be referred to as SPAD. In this case, the incoming photon leads to a carrier density high enough to create a self-sustaining avalanche and for the diode to become conductive resulting in a macroscopic current. This process is also known as Geiger discharge. It is necessary to have a quenching mechanism in place in order to limit the current, stop the avalanche and recharge the bias of the diode. The quenching is achieved via a resistor (passive) or via a circuit reducing the bias voltage (active).

The signal of an APD is proportional to the number of photons on the diode,

---

[2] It is to note that the travel of charge carriers and the recombination also happens without an external electric field. This results in a depletion zone and an internal voltage because of the two differently charged and separated zones. The reverse bias only enhances this effect.

but due to the randomness of the multiplication process the determination of the number of incoming photons is subject to a high uncertainty. Furthermore, single photon detection is not possible. The signal of a SPAD on the other hand is a binary one depending on whether current is flowing. Because of the high bias voltage even single photons are sufficient to result in a Geiger discharge, but in turn it is impossible to calculate the number of photons that hit the diode. Although the quenching and reloading of the bias leads to a dead time, the SPAD is the better alternative for detecting photons in a WC or LS detector for low energy events, since the resolution of energy and track reconstructions in these scenarios rely on the ability to detect even single photons.

In order to fight the missing counting capabilities of a single SPAD, a SiPM (often referred to as Multi-Pixel Photon Counter (MPPC)) consists of an array of SPADs with densities between 100 to several 1000 SPADs per mm^2. With the number of firing SPADs the incoming photon flux can be estimated, so that a SiPM has not only the ability to detect single photons but also to do photon counting.

In neutrino physics, SiPMs are in use in the near detectors of the T2K experiment Interactive Neutrino GRID (INGRID) [120] and ND280 [121]. For the future, it is planned to use SiPMs for example at the DUNE experiment [18] or at the near detector Taishan Antineutrino Observatory (TAO) for the JUNO experiment [122]. Further examples for the application of SiPMs can be found in reference [123].

3.3. Large Area Picosecond Photodetector (LAPPD)

The structure of a LAPPD consists like a PMT of three main components: Window with photocathode, multiplication mechanism and anode. These components are housed in an evacuated glass cuboid. A scheme of a LAPPD is shown in figure 3.4. Again, a photon can release a PE from the photocathode, which is then accelerated via an electric field unto the first MCP, which produces a high number of secondary electrons. These electrons are directed unto a second MCP repeating the process. The resulting electrons are then collected on silver anode strips allowing for a reconstruction of the PE emission point in the following way.

The coordinate along the strips can then be reconstructed via the time difference of the signals arriving at the individual ends of the strips. With these positions, the coordinate across the strips can be determined analysing the amplitudes of the strips, since the strips directly under the photon hit are expected to collect the highest number of electrons and therefore measure the highest amplitude.

Between the individual components x-shaped spacers are placed, which in combination with the frame bring the active front area from $20\,\mathrm{cm} \cdot 20\,\mathrm{cm}$ to $350\,\mathrm{cm}^2$. More details can be found in reference [4].

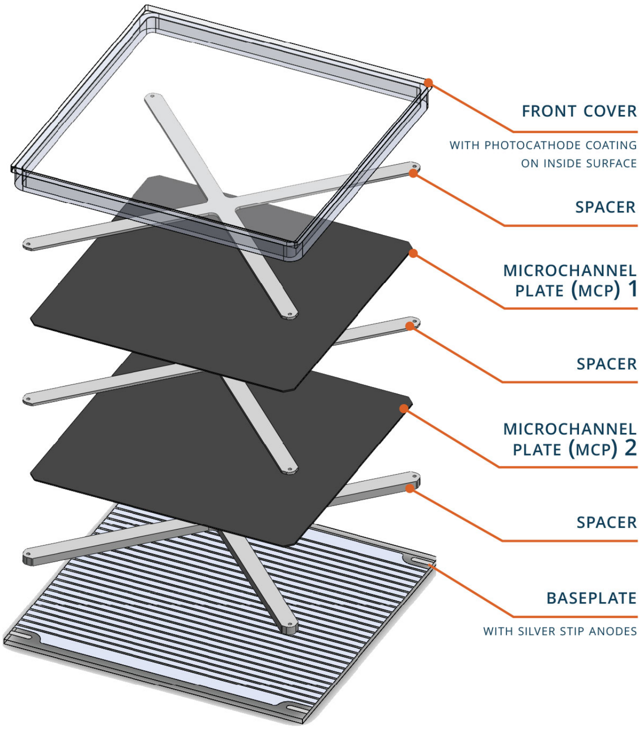

Figure 3.4.: Scheme of a LAPPD taken from reference [124].

The LAPPDs, which were discussed in this section, are manufactured by Incom Inc. (see reference [125] for their web appearance). These LAPPD type is also used in ANNIE and in the simulated idealised detector (see chapter 6).

3.4. Characterising Parameters

In this section, the most important parameters for track reconstruction and light separation of the aforementioned photodetectors are discussed. This includes an explanation of the terms and a comparison of the detector types in order to motivate the usage of LAPPDs in this work.

3.4.1. Dark Count Rate (DCR)

DCR is the number of output pulses per time interval for a photodetector sitting in complete darkness. There are a number of effects that cause dark counts of a photodetector listed in the following based on references [114, 118]. The effects differ not only in rate but also in height of output pulses.

1. Thermionic emission: The thermionic emission describes the thermal release of an electron in the photocathode, the dynodes, the walls of a MCP detector or the thermal creation of an electron-hole pair in a SiPM resulting in an avalanche.

2. Leakage current: Due to imperfect insulation, leakage current occurring between the last dynode and the anode or the socket's pins can result in an output pulse. This effect does not affect the DCR of SiPMs.
3. External radiation: External natural radioactivity as well as radioactivity in the detector material itself can create electrons at any stage in a photodetector. Furthermore, cosmic radiation, mostly muons, can create photons due to Cherenkov radiation.

Since the DCR can mimic real photon hits, a low rate is necessary to reduce this source of detection error.

3.4.2. Transit Time Spread (TTS) and Single Photon Time Resolution (SPTR)

The TTS is a crucial parameter for reconstructions, since it is directly linked to the time resolution of a photodetector and thereby has a great influence on determining a photon's emission point in time and space. The transit time is the time it takes for a photodetector to generate an output pulse after a photon hit. In the case of PMTs and LAPPDs, the PE trajectory depends on the position of the emission point at the photocathode and the direction of its momentum. Therefore, the difference in PE trajectories is the reason for the transit time to have a variance and the position of a photon hit on the photocathode has major influence on the transit time [114].

For SiPM a similar parameter in the form of the SPTR is defined. The position of the photon hit on a SiPM is in two ways relevant for the time resolution. On the one hand, the position on a pixel is linked to the electron-hole pair's drift time from the depletion into the multiplication zone. On the other hand, the pixels have different distances to the readout introducing a time dependency on the position of the pixel. Additionally, the avalanche creation is a statistical process, inherently causing a time jitter [126].

The measurement of the timing resolution of all the mentioned photodetectors follows the same principle: A light source with a pulse width that is sufficiently smaller then the time resolution of the considered photodetector is used with an intensity resembling the generation of one PE on average at the photodetector. For example, a laser with a pulse width of about $50\,\mathrm{ps}$ can be used. Displaying the time difference between the triggered photon emission at the laser and the output pulse of the detector results in a Gaussian distribution. Taking the Full Width at Half Maximum (FWHM) of this distribution gives then the TTS or SPTR, respectively [114, 118].

As explained above, typical values for the TTS of PMTs strongly depend on the size and shape of the photocathode.

3.4.3. Photon Detection Efficiency (PDE)

The PDE describes the ratio of incoming photons N_p and detected photons N_d of frequency ν. The PDE $\mu(\nu)$ is the product of the Quantum Efficiency (QE) $\eta(\nu)$ and the Collection Efficiency (CE) α [114]

$$\mu(\nu) = \frac{N_\mathrm{d}}{N_\mathrm{p}} = \alpha \cdot \eta(\nu). \tag{3.1}$$

For PMTs and LAPPDs, the QE is the probability for the creation of a PE for an incoming photon and depends on the wavelength ν of the photon, since the photon's energy is relevant for the photoelectric effect inside the photocathode. For SiPM, the QE also depends on the wavelength and describes the probability that an electron-hole pair is created in the semiconductor for an incoming photon. The CE is then the probability for a released PE to hit the multiplication mechanism in form of the first dynode or the wall of a microchannel for PMTs and LAPPDs. In the case of the SiPM, the collection efficiency is the probability, that an avalanche is created due to the electron-hole pair and that the incoming photon hits the active part of a pixel in the first place [118].

The PDE is an important parameter for the reconstruction of low energy events with in average less than one photon hit per photodetector, since missing photons decreases the precision of the reconstruction algorithms. Typically, the QE is the crucial parameter for the PDE, since the CE is often above $90\,\%$, whereas the QE is in the region of $30\,\%$. For this thesis, a distinction is not necessary so that the term QE as equivalent to PDE will be used, as it is often done in the literature.

3.4.4. Spatial Resolution (SR)

PMTs and SiPM do not give any spatial information about the photon hit on their respective surfaces. Therefore, the spatial resolution of these devices can be considered to be related to their size. For simplicity, the diameter of spherical detectors or the pixel length for quadratic detectors is referred to as spatial resolution in this work.

LAPPDs on the other hand are capable of measuring the position of the photon hit on their photocathode due to their anode strip structure. The number of anode strips, the timing capabilities of the readout electronics and the performance of the cluster to hit matching algorithm is crucial for the spatial resolution of an LAPPD. For reconstructions, the spatial resolution is a relevant parameter, since it is directly influencing the matching of hits to the emission point in time and space.

3.4.5. Comparison

Table 3.1.: Typical values for the introduced parameters for PMTs, SiPMs and LAPPDs. The column for TTS corresponds to the SPTR for SiPM.

Type	DCR	PDE [%]	TTS [ps]	SR [mm]
PMT [127, 128]	$15.3\,\mathrm{kHz}$	$28.1\,@\,420\,\mathrm{nm}$	2500	508
SiPM [117, 126]	$1\,\mathrm{MHz}$	$40\,@\,420\,\mathrm{nm}$	$100-300$	$30-60$
LAPPD [129]	$1000\,\mathrm{Hz/cm^2}$	$17-25\,@\,365\,\mathrm{nm}$	50	along strips: 3.2 across strips: 0.76

In table 3.1, typical values for the aforementioned parameters are shown. It is to note that many special subtypes of photodetectors exists, which are not taken into consideration. Furthermore, photodetectors come in many different sizes. This is especially true for the long available PMTs. For this comparison, the $20\,\mathrm{inch}$ dynode PMTs, that will be used in JUNO in the future and which are comparable in size to a LAPPD is chosen.

The numbers for the DCR show that the PMT is in this point preferable, since the number for the LAPPD translates to a DCR of $400\,\mathrm{kHz}$ taken the whole active area into account. The PDE clearly favours the SiPM, whereas the better LAPPD exemplars[3] can compete with PMTs. The difference in peak sensitivity wavelength has to be taken into account for pure LS detectors, when the optical photon emission spectrum also peaks a $420\,\mathrm{nm}$. In this thesis, the Cherenkov radiation is of more importance, where the highest emission probabilities are towards lower wavelengths, which will be discussed in the next chapter.

Although DCR and PDE are of vital importance for reconstructions, they are less important for events with a sufficient number of emitted photons, which will be studied in this thesis. In the crucial time resolution, the LAPPD has a huge advantage over SiPMs and especially over PMTs. Furthermore, the LAPPDs spatial resolution allows to determine the timing even more precisely, because the spatial resolution introduces an uncertainty on the timing of $\frac{5\,\mathrm{mm}}{c} = 17\,\mathrm{ps}$, which is compared to even the smaller SiPMs with $\frac{3\,\mathrm{cm}}{c} = 100\,\mathrm{ps}$ a significant improvement[4].

Besides the fact that LAPPDs are best suited for reconstructions and light separation and the natural choice for a simulated detector aiming to be ideal without considerations of funding and budget, the associated experiment (ANNIE) has access to multiple LAPPDs. Therefore, the existing simulation for and knowledge of LAPPDs from the ANNIE collaboration can be used. It was also planned to work with real ANNIE detector data including LAPPDs, but due to the pandemic the deployment of the LAPPDs into the ANNIE detector was delayed.

---

[3] Due to the early stage of commercialisation, the performance of LAPPDs can vary in the range displayed in the PDE field.

[4] A slightly higher number for the spatial resolution of the LAPPDs is used in this thesis. This will be further explained in the chapter 6

4. Light Separation in Water-based Liquid Scintillator (WbLS) Detectors

This chapter discusses the theoretical aspects of WbLS detectors and light separation. In short, the WbLS as well as WC or LS detectors covered here work with an unsegmented volume filled with the respective liquid. Neutrinos interact in the volume via one of the reactions described in section 2.1 and produce secondary particles. The secondary particles deposit energy within the active volume of the detector (section 4.1). The energy deposition leads to the emission of optical photons (section 4.2). These photons propagate through the liquid and are detected by the photosensors (section 4.3). In that way, a neutrino interaction leads to hits of optical photons on photosensors, which can be used to reconstruct the vertex of the interaction, the neutrino's energy and direction. Backgrounds have to be taken into careful consideration, which is a reason for many neutrino detectors to be build deep underground to shield the detectors from mostly muons produced by cosmic rays. Depending on the reaction that is searched for, a high number of other sources of background e.g. neutrinos in the same energy range or natural radioactivity has to be discriminated from the signal process. Light separation can help with this task. This chapter continues with section 4.4 where ideas for light separation are introduced and section 4.5, in which the motivation for light separation and with that the motivation for this thesis is explained. A brief section of the production of WbLS and the current status in form of the CHErenkov/Scintillation Separation (CHESS) experiment concludes this chapter.

4.1. Energy Deposition

As explained in chapter 2, neutrinos interact only weakly and cannot be detected directly in WbLS detectors. Instead, secondary particles from neutrino interactions with the target medium are detected. These secondary particles travel the target volume while depositing energy, which results in the emission of optical photons. The mechanism of energy deposition differs depending on the particle type and will be in the following explained based on references [130, 131]. In this section, the particles are grouped into charged particles, photons and neutrons. It is to note

that photons are in the following referred to as **gammas**, if they result from particle interactions and have an energy in the keV-range or higher, whereas photons resulting from Cherenkov or scintillation radiation, that have visible wavelengths and energies in the eV-range are called **optical photons** or simply **photon**. The term **photon** is also used for the force carrier in the Standard Model which is clarified via the context.
In the following the energy deposition is discussed first for heavy charged particles like protons and muons, secondly for electrons and positrons, thirdly for gammas and lastly for neutrons.

4.1.1. Heavy Charged Particles

The effects of energy loss heavily depends on the considered velocity and the mass of the particle and so does the mathematical description. The velocity is referred to in terms of $\beta\gamma$. For intermediate particle velocities $0.1 \lesssim \beta\gamma \lesssim 1000$ with masses higher than the electron mass, the dominating effects of energy loss are ionization and excitation. Both effects can be described with quantum electrodynamics as the energy transfer via photons to electrons of the target material leading to excitation or, for higher transfer energy, to ionization. The differential energy loss per track length or the linear stopping power in the units $\mathrm{MeV/cm}$ can be described with the Bethe-Bloch equation

$$-\left\langle \frac{\mathrm{d}E}{\mathrm{d}x} \right\rangle = K\frac{Z}{A}\rho\frac{z^2}{\beta^2}\underbrace{\left[\frac{1}{2}\ln\left(\frac{2m_ec^2\beta^2\gamma^2W_{\mathrm{max}}}{I^2}\right) - \beta^2 - \frac{\delta(\beta\gamma)}{2}\right]}_{L_a(\beta)} \tag{4.1}$$

with the maximum energy transfer W_{max} to an electron given by

$$W_{\mathrm{max}} = \frac{2m_ec^2\beta^2\gamma^2}{1+2\gamma m_e/M+(m_e/M)^2}. \tag{4.2}$$

The variables occurring in above equations can be found in table 4.1 with a short description.
It is to note that in the literature often $-\langle \mathrm{d}E/\mathrm{d}x\rangle$ is implicitly used for $-\langle \mathrm{d}E/(\rho\mathrm{d}x)\rangle$ (dividing equation (4.1) by ρ), which is the mass stopping power in terms of $\mathrm{MeVg^{-1}cm^2}$. In this thesis, $\mathrm{d}E/\mathrm{d}x$ is used implicitly for $-\langle \mathrm{d}E/(\rho\mathrm{d}x)\rangle$.
For interpreting equation (4.1) and discussing its boundaries it is useful to take a look at figure 4.1. In this figure, the mass stopping power is plotted in terms of the velocity $\beta\gamma$ and the momentum respectively for a positively charged muon traversing a copper target. The colors and labels denote the different models used to describe the mass stopping power across the shown momentum range.
Starting at low energies $\beta\gamma < 0.01$, the energy loss is dominated by elastic collisions of the particle with the atom cores (nuclear stopping power) and inelastic

Table 4.1.: Meaning of the variables in the Bethe-Bloch-formula

Symbol	Definition
$K = 4\pi N_A r_e^2 m_e c^2$	coefficient constant
N_A	Avogadro constant
r_e	classical electron radius
m_e	electron mass
c	speed of light in vacuum
Z	atomic or charge number of atoms of target medium
A	mass number of atoms of target medium
M	incident particle mass
ρ	density of target medium
z	charge number of particle in terms of the electron's charge
β	ratio of the velocity of the particle to c
γ	Lorentz factor
I	mean excitation energy
δ	density correction for high particle energies
$C(\beta)/Z$	sum of shell corrections for low particle energies
$zL_1(\beta)$	Barkas correction for low particle energies
$z^2L_2(\beta)$	Bloch correction for low particle energies

collisions with the electrons (electronic stopping power) in the target. This energy loss, which is depicted by the purple dotted line, can be described as being proportional to β as it has been done by Lindhard, Scharff and Schiøtt [132, 133]. Substantially lower particle energies less than $1\,\mathrm{keV}$ are not depicted in figure 4.1, but hinted at with a grey arrow in the bottom left corner. Here, the energy loss is solely dominated by the nuclear stopping power.

Going to higher energies in the interval $0.01 < \beta\gamma < 0.05$, the energy loss can be described with a phenomenological fit by Andersen and Ziegler, which is represented by the pink line in figure 4.1 to describe the mixture of electronic and nuclear stopping power.

Above this energy $\beta\gamma > 0.05$, the Bethe-Bloch equation can be used to describe the mass stopping power with the introduction of correction terms. The corrected Bethe-Bloch formula for low energies then reads

$$-\left\langle \frac{\mathrm{d}E}{\mathrm{d}x} \right\rangle = K\frac{Z}{A}\rho\frac{z^2}{\beta^2}\cdot\left[L_a(\beta) - \frac{C(\beta)}{Z} + zL_1(\beta) + z^2L_2(\beta)\right]. \tag{4.3}$$

The variables are again listed in table 4.1. The sum of the shell corrections is necessary towards lower energies, since the assumption that the particle is faster than the shell electrons does not hold anymore and the motion of the shell electrons have to be taken into account, which lowers the mass stopping power. The Barkas correction accounts for the attracting force between the electron clouds and a positively charged particle and a repulsing force for negatively charged particles meaning that the energy loss is higher for positively charged particles in comparison to their antiparticles. This effect is indicated by the green dotted line at the end of Andersen-Ziegler peak. The Bloch correction describes the effect of perturbations in the wave function of the electrons, which only have a significant effect on low energy particles.

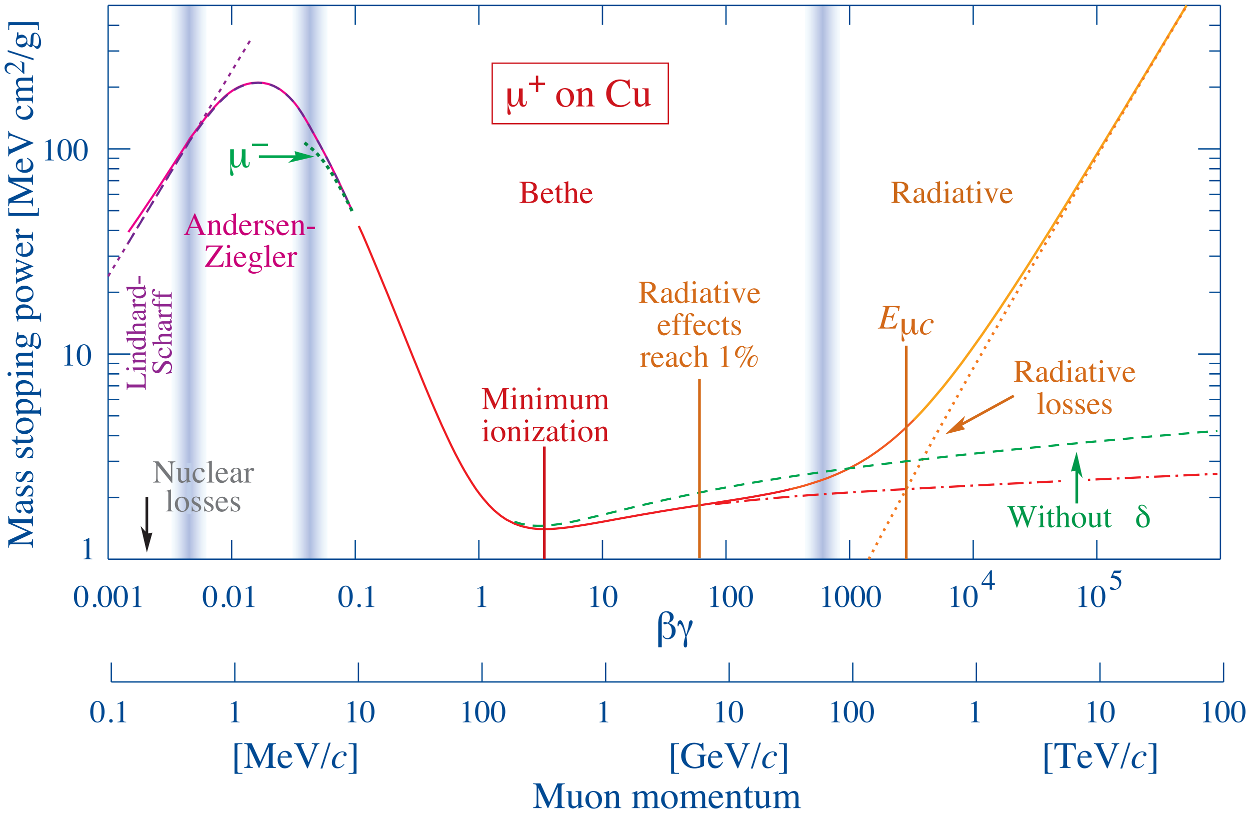

Figure 4.1.: Depiction of the differential energy loss of a positively charged muon in copper [130].

The next region of energy is covered by equation 4.1, as it was mentioned earlier and is shown in figure 4.1 as a red solid line denoted Bethe. Here, the $1/\beta^2$ term is first dominating, representing that the interaction probability is higher the longer the particle travels through the medium. At $\beta\gamma = 3.0$ a minimum, where the aforementioned time effect equals to the logarithmic term describing the fact that the electric field of the particle is relativistically extended in transverse direction, which increases the cross section and the rise of the maximum energy transfer with higher energies. Particles with velocities in this area are called minimum-ionizing particles. The extension of the particle's electric field does not ionize the medium in a higher range but rather has a polarising effect meaning that the rise of the logarithmic term has to be corrected. This is done by the density corrections for high energy particles δ. The effect of this corrections is indicated by the dashed green line.

For sufficiently high energies (in the muon case starting at a momentum of a few hundreds of GeV), the energy loss for charged particles is dominated by radiation

effects. This means, bremsstrahlung, electron-positron pair production and photonuclear interactions come into play. The first one is the emission of gammas due to an (negative) acceleration of a charged particle in the Coulomb fields of electrons or nuclei, which will be again covered later in more detail. Electron-positron pair production denotes the emission of gammas with a sufficient high energy to create an electron-positron pair and photonuclear interactions are the interaction of a radiated gamma with a nucleus. While the first two effects are likely to create electromagnetic showers, the latter can additionally result in hadronic showers. An electromagnetic shower denotes the cascade of secondary particles that is created by the interaction of an e.g. electron with matter. Due to bremsstrahlung, the incident electron creates gammas that when having sufficiently high energies, create electron-positron pairs, that can in turn emit gammas and so on. The starting point can also be a gamma or a positron entering matter. A hadronic shower on the other hand is mostly created by hadrons interacting with matter. Via various processes e.g. pions and other hadrons are produced that in turn interact again with the target material. Often, a hadronic shower is accompanied by an electromagnetic shower produced for example by a decaying π^0.
The energy loss due to the Cherenkov effect, which will be discussed in section 4.2.2, can be calculated via the Frank-Tamm formula [134]

$$\frac{\mathrm{d}^2E}{\mathrm{d}\omega\mathrm{d}x} = \frac{z^2e^2}{4\pi\epsilon_0c^2}\omega\left(1-\frac{1}{\beta^2n^2(\omega)}\right) \tag{4.4}$$

with the absolute dielectric permittivity ϵ_0 and the frequency ω. The remaining variables are defined in table 4.1. Since this energy loss is very small (a few percent at most) compared to the energy loss due to ionisation, it can be neglected [130].

4.1.2. Electrons/Positrons

The mass stopping power of electrons has two parts, which are the energy loss by ionisation and scattering and the energy loss by bremsstrahlung. The former can be described by a modified Bethe-Bloch-formula [135, 130]

$$-\left\langle\frac{\mathrm{d}E}{\mathrm{d}x}\right\rangle = \frac{1}{2}K\frac{Z}{A}\frac{1}{\beta^2}\left[\ln\frac{m_ec^2\beta^2\gamma^2\left\{m_ec^2(\gamma-1)\right\}}{2I^2}-\delta+F(\gamma)\right]. \tag{4.5}$$

$F(\gamma)$ is a correction term taking scattering effects into account. This term differs depending on whether a positron or an electron is the primary particle traversing the detector. For electrons it reads

$$F(\gamma)_{e^-} = (1-\beta^2)-\frac{2\gamma-1}{\gamma^2}\ln 2+\frac{1}{8}\left(\frac{\gamma-1}{\gamma}\right)^2, \tag{4.6}$$

and considers the Møller cross section for electron-electron scattering [136], in which the electron of the target medium is assumed as free.

Positron-electron scattering on the other hand is described by

$$F(\gamma)_{e^+} = 2\ln 2 - \frac{\beta^2}{12}\left(23 + \frac{14}{\gamma+1} + \frac{10}{(\gamma+1)^2} + \frac{4}{(\gamma+1)^3}\right), \tag{4.7}$$

for which Bhabha scattering [137] has to be taken into account.

It is to note, that the difference in mass stopping power between electrons and positrons does not end here, since the effect of positron-electron annihilation with the target's electrons also plays a role for positrons traversing the target.

The energy loss of electrons and positrons due to bremsstrahlung, which is again the emission of photons caused by the acceleration in the coulomb field of atoms and atomic electrons can be approximated for particles of energies above a few MeV via [138, 135]

$$-\left\langle \frac{\mathrm{d}E}{\mathrm{d}x} \right\rangle = 4\alpha\rho N_A \frac{Z(Z+1)}{A} z^2 r_e^2 E \ln\left(\frac{183}{Z^3}\right). \tag{4.8}$$

Most of the variables can be found in table 4.1 with the exception of α, which is the fine structure constant. The classical electron radius is given by

$$r_e = \frac{e^2}{4\pi\epsilon_0 m_e c^2}, \tag{4.9}$$

in which ϵ_0 is the electric field constant.

If equation (4.8) is used to approximate the energy loss for other particles like muons, $m_e = m_\mu$ is set in r_e. This gives then the famous proportionality of the energy loss of bremsstrahlung

$$\left\langle \frac{\mathrm{d}E}{\mathrm{d}x} \right\rangle \propto \frac{E}{m^2}, \tag{4.10}$$

which is often used to motivate muon-colliders.

Equation (4.8) can also be written with Z^2 instead of $Z(Z+1)$. In the first form the influence of the atomic electrons on the mass stopping power is neglected. It is also to note, that complete screening of the nucleus' electric field by the atomic electrons is assumed for equation (4.8).

Up to $10\,\mathrm{MeV}$ in lead, the ionisation and the scattering processes are dominant for the energy loss of electrons and positrons. For higher energies, the ionisation energy loss is decreasing due to the reduced time in the medium and the bremsstrahlung energy loss dominates because of the energy dependence in equation (4.8) meaning that higher energy gammas are emitted.

4.1.3. Gammas

The energy loss processes for gammas differ depending on the energy range. The cross sections for the different processes are depicted in figure 4.2 for carbon in the top and lead in the bottom. The measured cross sections are depicted in dots denoted with σ_{tot}, which is the total cross section. For low energies of up to $50\,\mathrm{keV}$ in carbon and $1\,\mathrm{MeV}$ in lead, the dominant effect is the photoelectric effect with the cross section $\sigma_{\mathrm{p.e.}}$. The photoelectric effect is the absorption of a gamma by an atom and the subsequent emission of an PE, which was discussed in chapter 3. This means the energy of the gamma is completely deposited and the further energy loss of the PE has to be considered. If the emitted PE comes from an inner shell, an electron from an outer shell fills the hole under the emission of an optical photon. It is also possible that the energy of the electron transition is transferred to another electron of the outer shell leading to the emission of said electron, which is a so called Auger-electron.

As it is depicted in the mentioned figure, Rayleigh scattering ($\sigma_{\mathrm{Rayleigh}}$) also contributes to the cross section in the low energy range. Rayleigh scattering is the coherent elastic scattering of gammas (or optical photons) off of atoms (or molecules) in the target material, when the wavelength of the gamma is much smaller than the size of the atom. The electric field of the gamma induces a dipole moment in the atom leading to the emission of a gamma with the same wavelength, but a different direction, which will be covered in more detail in section 4.3.1. Rayleigh scattering is therefore no process of energy loss.

Compton scattering ($\sigma_{\mathrm{Compton}}$) contributes not only to the cross section but also to the energy loss. It designates the inelastic scattering of gammas and electrons from the target medium leading to a change of direction and an energy loss of the gamma (Compton shift) and the excitation or ionisation of the electron. The energy of a gamma after a Compton scattering E'_γ can be calculated via [134]

$$E'_\gamma = \frac{E_\gamma}{1 + \frac{E_\gamma}{m_e c^2}(1 - \cos\theta_\gamma)}. \tag{4.11}$$

θ_γ represents the scattering angle of the gamma with respect to the prior travel direction. The missing energy $T = E_\gamma - E'_\gamma$ is transferred to the electron. Compton scattering plays a role starting at around $100\,\mathrm{eV}$ and becomes dominant at approximately $50\,\mathrm{keV}$ until $20\,\mathrm{MeV}$ in carbon ($1\,\mathrm{MeV}$ until around $10\,\mathrm{MeV}$ in lead).

When the gamma's energy is greater than twice the mass of the electron $m_e = 511\,\mathrm{keV}$, pair production can occur. In the presence of the coulomb fields of electrons (κ_e) or nucleons (κ_{nuc}), a gamma of sufficient energy can be transformed into an electron-positron pair. Pair production becomes dominant at the end of the Compton scattering's dominance.

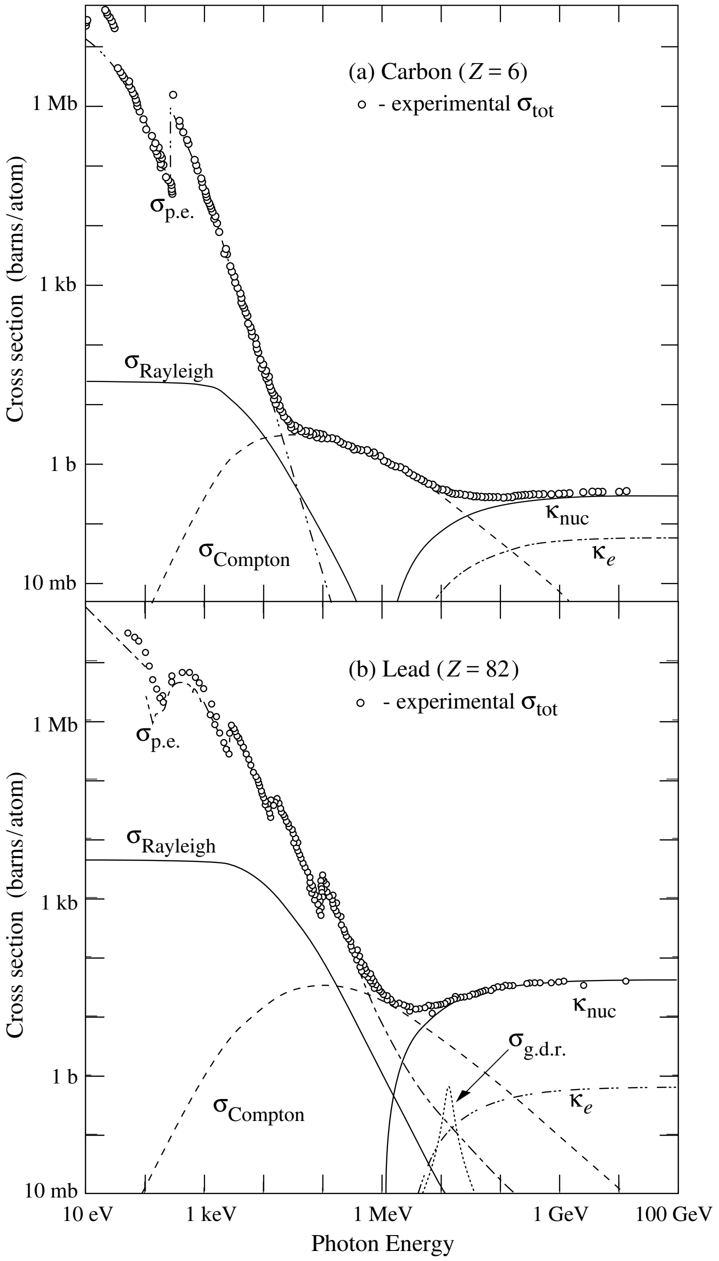

Figure 4.2.: Cross sections of photon/gamma interaction processes in matter in carbon (top) and lead (bottom) [130].

It is to note, that for lead photonuclear interactions contribute at around 10 MeV to the cross section and to the energy loss. Photonuclear interactions is the disintegration or fission of a nucleus after absorbing a high energy gamma meaning that the gamma energy is completely deposited and distributed along the parts of the nucleus.

4.1.4. Neutrons

The energy loss for neutrons from FSI or IBD is dominated by elastic scattering with nuclei of the target material leading to unmeasurable recoils of the nuclei. After a sufficient number of interactions, the neutron is thermalised with an energy of less than 1 eV and is captured by a proton. The neutron capture process happens under the emission of a gamma with an energy of $E_\gamma = 2.223\,\mathrm{MeV}$ [79]. Due to the capture time of about $200\,\mu\mathrm{s}$ after the neutron emission, the signal of the gamma is a great tool for background reduction, especially for the IBD [11]. The advantages of the neutron capture signature can be enhanced with the addition of Gadolinium to the active medium of a neutrino detector. This is done for WC detectors like Super-Kamiokande [139] and ANNIE, which will be covered in more detail in chapter 5, as well as for LS detectors like Daya Bay [140]. In comparison to the neutron capture on protons, the capture on Gadolinium has three advantages [141]:

1. The capture time on Gadolinium is tens of microseconds, which is a factor of 10 to the capture time on protons.

2. The cross section for the capture process is $49\,\mathrm{kb}$, whereas the one of protons is $0.3\,\mathrm{b}$.

3. The emitted gammas have a total energy of about $8\,\mathrm{MeV}$ distributed on typical two or three gammas, which is more than three times the energy of the single gamma emitted by the capture on protons.

Gadolinium-loading is especially useful for the IBD-signal, since the reduced capture time decreases the chance of accidental backgrounds in the time window between positron and gamma detection. In general, the increase in cross section and deposited energy enhances the detection and tagging efficiencies of neutrons, which is advantageous not only for IBD-signals but also for neutron-multiplicity measurements.

4.2. Light Emission

In the following, the mechanisms of light emission in WbLS are discussed based on [134, 142] if not stated otherwise. The focus thereby lies on the explanation of the effects and the mathematical description of their properties. A (graphical) comparison of Cherenkov and scintillation light follows in section 4.4.

4.2.1. Scintillation Light

In general, scintillation light describes luminescence, which is the light emission resulting from the deexcitation of molecules, that were excited by a primary particle traversing the scintillator. The explanation of the actual emission process differs depending whether an organic or an inorganic scintillator is considered. Since the detector simulation in chapter 6 uses LS belonging to the group of organic scintillators mixed with water as active medium, the scintillation process in inorganic scintillators is not covered in this thesis.

To explain the scintillation process in organic scintillators it is necessary to start with the concept of covalent bonds for the formation of molecules out of atoms. In more detail, the formation of benzene ring structures $\mathrm{C_6H_6}$ out of carbon and hydrogen has to be considered. In such a structure, covalent double bonds between half of the carbon atoms exist in an alternating way. These bonds can be classified into σ and π bonds. The σ bonds are the result of overlapping hybrid orbitals that, graphically speaking meet end-to-end. In the case of benzene rings, these hybrid orbitals are a mixture of $2s$ and $2p$ orbitals creating sp^2 orbitals, whereas one p orbital is not hybridised. The carbon atoms in $\mathrm{C_6H_6}$ are connected by the σ bonds in the shape of a hexagon, which has a hydrogen atom at each corner (also connected by σ bonds). The not hybridised p orbitals are orthogonal to the plane of the hexagon and overlap, again graphically speaking side-by-side, forming the so called π bond, which is the second ingredient to the double bonds. Although only half of the bonds between the carbon atoms are double bonds, all of the carbon atoms have the same distance to their neighbours, which can be explained by a delocalisation of the π electrons and the creation of molecular orbitals. The six π electrons are thus shared by all of the carbon atoms to enhance the strength of the bonding, which is an effect also known as aromaticity. Therefore, the π electrons can be considered as molecular valence electrons.

The π electrons can occupy different energy levels and the transition between some of the levels happens via energy absorption or photon emission, analogous to valence electrons in atoms. The energy levels are depicted in figure 4.3, whereby the main levels ($S_0, S_1, ..., T_3$) are splitted into sublevels (e.g. S_{12}) representing different vibration states. On the left side the singlet and on the right side the triplet states are shown. The allowed absorption transition as well as the deexcitation transitions in the form of fluorescence and phosphorescence are indicated via arrows. Furthermore, the inter-system crossing between the singlet state S_{10} and the triplet state T_1 is on display, which is a process explained by spin-orbit coupling for states that have a considerable overlap due to different vibration states. More details to inter-system crossings can be found in reference [143].

The deposited energy of a particle traversing a volume of liquid scintillator excites the π electrons to higher energy levels. The deexcitation of the electrons back to the S_{10} level happens via vibration and without the emission of photons. The prompt fluorescence, which is the deexcitation from the S_{10} level to any of the ground sublevels, whereby a photon is emitted isotropically on a time-scale of nanoseconds, is the main part of the scintillation light.

Two other effects are also part of the scintillation process: Firstly, the electrons can go from a singlet state to a triplet state via inter-system crossing nonradiatively, which is an effect of spin-orbit interaction. The deexcitation happens then similar to the prompt fluorescence, but on a time-scale of milliseconds and is due to the change of multiplicity called phosphorescence. Secondly, electrons in a triplet state can be lifted back to a singlet state, when the molecule gains energy due to interaction with other molecules or due to additional deposited energy. The emission of a scintillation photon happens then with respect to the first energy deposition on a scale of micro- to milliseconds and is called delayed fluorescence.

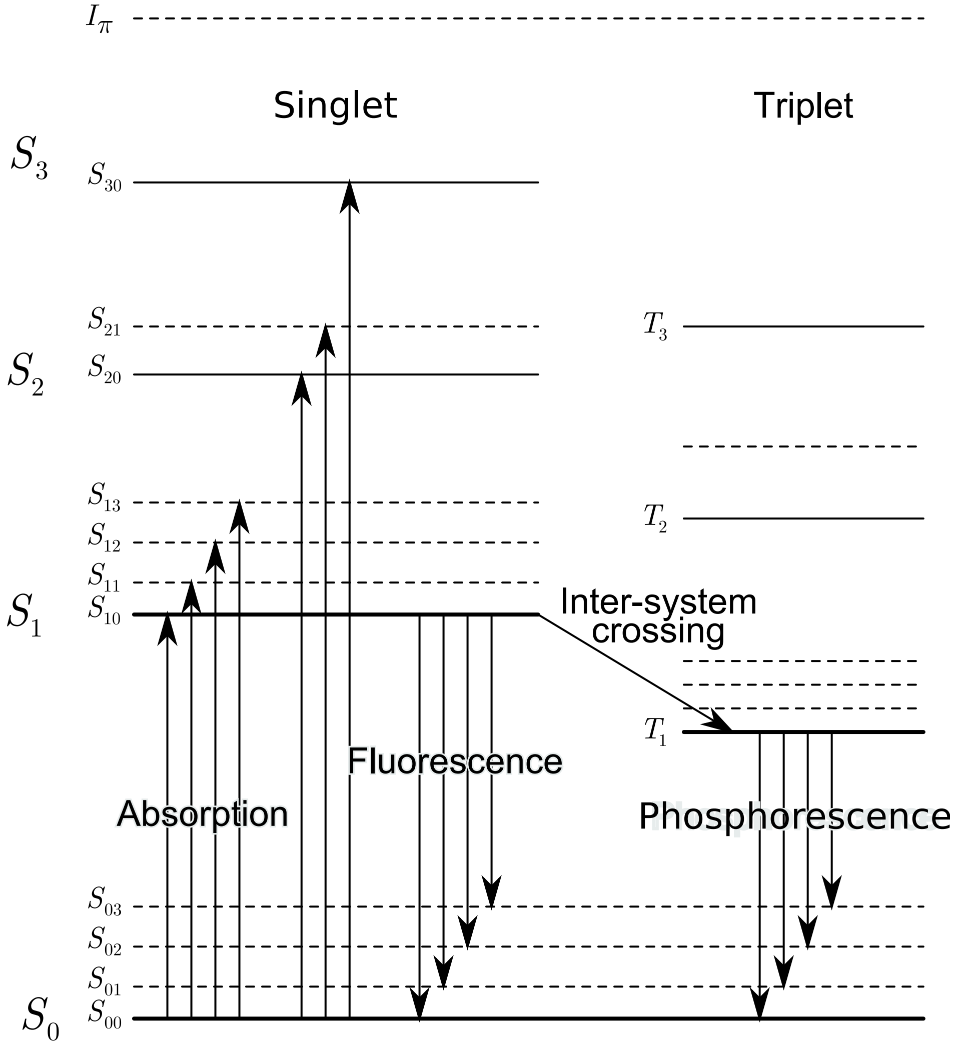

Figure 4.3.: Scheme of energy levels in organic scintillators [144].

Although the scintillation emission spectrum is different from the absorption spectrum due to the Stokes shift[1], the existing overlap of both spectra lead to reabsorption (and in the following reemission), which reduces the possibility for the photons to reach a photosensor in a decent time if at all, since each reemission process is again isotropically. Furthermore, the topological information of the original scintillation photons is reduced by reabsorption and reemission. Because of this, particle detectors typically use a mixture of different scintillators.

The primary scintillator, which is in liquid scintillator called solvent, makes up the majority of the mixture. Small proportions of a secondary and a tertiary scintillator

---

[1] The Stokes shift is caused by vibrational energy loss of the excited electrons, so that the emitted photon has less energy than than the gap of excited state to ground state.

are added, that are called fluors in the liquid scintillator context, whereby the tertiary scintillator is also denoted as wavelength shifter. For example, the JUNO scintillator consists of Linear AlkylBenzene (LAB) as solvent, in which about $2.0\,\mathrm{g/L}$ of 2,5-diphenyloxazole (PPO) and about $1.0\,\mathrm{mg/L}$ of 1,4-Bis-(2-methylstyryl)-benzol (bis-MSB) as fluors are added. A investigation of different liquid scintillator mixtures for JUNO can be found in reference [145]. With the Förster resonance energy transfer, which is the dipol-dipol interaction between two molecules that are closer than the wavelength of the emitted scintillation light, the primary scintillator deexcites nonradiatively and the energy is transferred to molecules of the secondary scintillator. The secondary scintillator emits then scintillation photons with an emission spectrum that is less overlapping with the absorption spectrum of the primary scintillator reducing reabsorptions. To further enhance the transparency, the tertiary scintillator has an absorption spectrum in the range of the secondary's emission spectrum, but emits photons with even longer wavelengths. For that reason, the tertiary component is also referred to as wavelength shifter and due to its low concentration, reabsorption is unlikely. Furthermore, the tertiary component is typically chosen to have an emission spectrum compatible with the maximum of the sensitivity spectrum of the photodetectors.

The number of emitted photons due to the scintillation effect is in first order linearly linked to the deposited energy per track length with a proportionality constant dependent on the scintillator material. This makes scintillation detectors excellent for calorimetry and hence for shower reconstructions. In more detail, a quenching factor has to be introduced to describe the fact that the scintillator material can experience a saturation effect, when the number of non-excited molecules shrinks near the particle path. This means, the number of emitted photons is reduced for high ionisation densities and that heavy particles like protons or ions produce a significant lower number of scintillation photons than e.g. gammas or electrons. This non-linearity can be described by Birks' law

$$\frac{\mathrm{d}L}{\mathrm{d}x} = S\frac{\frac{\mathrm{d}E}{\mathrm{d}x}}{1+k_\mathrm{B}\frac{\mathrm{d}E}{\mathrm{d}x}}, \tag{4.12}$$

where L is the light yield, S denotes the scintillation efficiency and k_B describes Birks' constant or the quenching factor. S as well as k_B are material dependent properties and have to be experimentally determined.

The emission time spectrum of scintillation light can be described as a statistical process by the sum of exponential decay functions [146]

$$d_\mathrm{scintillation}(t) = \sum_{i=1}^{n} \frac{\omega_i}{\tau_i} \exp\left(-\frac{t}{\tau_i}\right). \tag{4.13}$$

n is the number of components of the scintillator, ω_i are the weights of the components, which have to sum up to one and τ_i stands for the time constants of the components.

To conclude, scintillation light is emitted isotropically on a time-scale of nanoseconds, has a wavelength spectrum depending on the chosen scintillators and has an energy threshold in the range of the energy levels of the scintillator, which is typically a few eV. The scintillation photon emission is thereby proportional to the deposited energy making scintillator detectors ideal for energy measurements.

4.2.2. Cherenkov Radiation

Cherenkov radiation is the effect of photon emission resulting from charged particles traversing a medium with a velocity v higher than the phase velocity of light in said medium v_p, which is dependent on the refractive index of the medium n. In turn, n is dependent on the wavelength λ or the frequency ω of the traversing light. Charged particles polarise the molecules in a dielectric medium, which emit electromagnetic waves. If the velocity of the particle is less than the phase velocity of light in the medium, the waves from neighbouring molecules do not interfere. If

$$v > v_p = \frac{c}{n} \Leftrightarrow \beta = \frac{v}{c} > \frac{1}{n} \tag{4.14}$$

holds with c denoting the speed of light in vacuum, the waves interfere constructively and form a wavefront resulting in detectable (and visible) light. This criteria can be rewritten in terms of the particle's kinetic energy E_{kin} and its mass m using natural units, which results in

$$E_{\text{kin}} > E_{\text{thr.}} = m \cdot (\gamma - 1) = m \cdot \left(\frac{1}{\sqrt{1 - \left(\frac{1}{n}\right)^2}} - 1 \right). \tag{4.15}$$

This lower energy limit $E_{\text{thr.}}$ is of great use for particle discrimination in WC or especially in WbLS detectors, since it is dependent on the mass of the particle. This can be seen in table 4.2, where the Cherenkov threshold in terms of kinetic energy is depicted for different particles. The refractive index is assumed to be $n = 1.35$, which is the mean of the WbLS mixture used in the idealised simulation (see figure 6.4) and roughly corresponds to the maximum sensitivity wavelength of the used LAPPDs. The table also illustrates why heavy particles can lead to missing energy in WC detectors.

Table 4.2.: Cherenkov threshold for different particles in terms of kinetic energy for a refractive index of 1.35.

Particle	$e^\pm$	$\mu^\pm$	$\pi^\pm$	$K^\pm$	$p^\pm$	$\tau^\pm$
$E_{\text{thr.}}/\text{MeV}$	0.25	51.62	68.19	241.19	458.40	868.09

Furthermore, the directionality of Cherenkov light is crucial for WC detectors in neutrino physics, as it allows for a handle on background events, and can be used for separation of Cherenkov and scintillation photons as well. The directionality results from the Cherenkov wavefront, which has an opening angle θ_C given by

$$\theta_\mathrm{C} = \mathrm{acos}\left(\frac{1}{\beta n}\right). \tag{4.16}$$

This directionality leads to the characteristic Cherenkov rings that can be seen in the photon hit structure on the detector wall of e.g. SK. It has been found that the structure of the Cherenkov rings is a useful tool for discriminating electron and muon events, since electron events create due to the electromagnetic shower rings with a higher expansion, also known as fuzziness, while the rings for muons are sharper [147].

Of similar significance as the directionality is the emission time of Cherenkov photons, which happens to be on a time-scale of a few picoseconds [148], a feature extremely useful for precise reconstructions.

Another feature of Cherenkov light usable for light separation is its wavelength emission spectrum, as it will be discussed later. It can be calculated via

$$\frac{\mathrm{d}^2N}{\mathrm{d}x\,\mathrm{d}\lambda} = \frac{2\pi\alpha z^2}{\lambda^2}\left(1 - \frac{1}{\beta^2 n^2(\lambda)}\right) = \frac{2\pi\alpha z^2}{\lambda^2}\sin^2[\theta_\mathrm{C}(\lambda)], \tag{4.17}$$

which is directly derived from the Frank Tamm formula in equation (4.4). N is the emitted number of Cherenkov photons, λ denotes the wavelength of said photons, whereas x corresponds to the path length of the particle. z stands for the charge of the particle and α for the fine-structure constant. The wavelength distribution has the form λ^{-2} and experiences a cutoff at short wavelengths $(100 - 200\,\mathrm{nm})$, when $n^2 < \beta^{-2}$ occurs due to anomalous dispersion of $n(\lambda) < 1$.

4.3. Light Propagation and Detection

After the emission of optical photons because of Cherenkov radiation or the scintillation effect, these photons traverse the detector with the group velocity v_g. The group velocity has to be considered instead of the phase velocity v_p in equation (4.14) due to the dependency of the dispersion on the wavelength or the frequency of the photons $n = n(\omega) = n(\lambda)$. v_g can be calculated via [130]

$$v_g = \frac{\mathrm{d}\omega}{\mathrm{d}k} = \frac{c}{n(\omega) + \omega\dfrac{\mathrm{d}n}{\mathrm{d}\omega}}. \tag{4.18}$$

$k = 2\pi/\lambda$ stands for the wavenumber, ω for the photon's frequency and λ for its wavelength.

Optical photons travel along a straight line through the detector until they hit the detector edge, if not one of the following effects occur, that can alter the energy or direction of the photon and therefore substantially reduce the quality of the photon's information.

4.3.1. Optical Photon Interactions with Matter

Optical photon interactions with the detector material can be grouped into two categories. The first category are scattering processes, which will be discussed in the next three sections, whereas the second group is absorption.

Raman Scattering

Raman scattering [149] describes the inelastic scattering of optical photons off of molecules. It can be explained via the excitation of a molecule to a virtual energy level. One of three things can happen following this excitation. If the molecule deexcites a part of the energy via vibration, the molecule falls down to a vibration state emitting a scattered photon with less energy than the incoming photon. This process is also called Stokes scattering. If the molecule is already in a vibration state before excitation and it falls back to a lower state, a photon with a higher energy is emitted, which is called anti-Stokes scattering. Lastly, if the molecule deexcites all energy via the emission of the scattered photon, the process is elastic and called Rayleigh scattering. Since Raman scattering has a cross section several magnitudes lower than that of Rayleigh scattering, it can be neglected in this thesis [150] and Rayleigh scattering is discussed further in the following section.

Rayleigh Scattering

Rayleigh scattering was introduced in section 4.1.3 and explained with a different approach in the section above. It is an elastic scattering process of photons on molecules or atoms, which changes the direction of the scattered photon but not its energy. Rayleigh scattering does not happen isotropically but has favoured and suppressed scattering angles, which can be derived from the proportionality of the differential cross section [150]

$$\left(\frac{\mathrm{d}\sigma}{\mathrm{d}\Omega}\right)_{\mathrm{ray}} \propto \left(\frac{1+\cos^2\theta}{2}\right). \tag{4.19}$$

σ is the cross section, Ω denotes the solid angle and θ is the scattering angle with respect to the incident direction. The scattering angle of $\theta = 90^\circ$ is fully suppressed, whereas backward scattering ($\theta = 180^\circ$) or no change in direction ($\theta = 0^\circ$) is favoured by a factor of two over the suppressed angles.

Mie Scattering

While Rayleigh scattering describes the elastic scattering off of objects much smaller than the optical photon's wavelength, Mie scattering corresponds to elastic scattering off of objects with similar wavelengths. This means that Mie scattering is more likely to happen on dirt and dust particles inside the active medium of a WbLS detector. Mie scattering features more complicated cross sections with forward scattering favoured [150, 151]. In general, the influence on the direction of the scattered photon is smaller than in Rayleigh scattering and the energy is conserved.

Absorption

As it was stressed in section 4.2.1, the emission and absorption spectrums of scintillator components usually overlap. This leads to the absorption of emitted photons by the target molecules. In turn, the excited molecule can deexcite via vibration, which completely eliminates a photon's information for the reconstruction process, or with the emission of an optical photon. Since this reemission happens isotropically and due to the Stokes shift with a different energy, the direction information of the original photon is lost, while the energy information is distorted. Additionally, the reemission happens on a similar time scale than the scintillation process, decreasing the quality of the time information [152].

4.3.2. Attenuation Length

In order to combine all of the effects above into one value, the attenuation length L can be introduced. The attenuation length is defined as the distance from a starting point, after which $1/e$ of the initial number of photons is remaining unscattered and not absorbed. This can be formulated as

$$N(x) = N_0 \cdot \exp\left(-\frac{x}{L}\right) \tag{4.20}$$

with the initial number of photons N_0 and the number of photons $N(x)$ after travelling the distance x. The relation between the combined attenuation length and the individual ones is [150]

$$\frac{1}{L} = \frac{1}{L_{\mathrm{ray}}} + \frac{1}{L_{\mathrm{mie}}} + \frac{1}{L_{\mathrm{abs}}} + \frac{1}{L_{\mathrm{are}}} \tag{4.21}$$

with the Rayleigh L_{ray}, the Mie L_{mie}, the absorption without reemission L_{abs} and the absorption with reemission L_{are} attenuation length. The combined attenuation length is a useful value to estimate the number of photons that carry unaltered information from the emission point to the photodetector and can be measured directly. L is dependent on the material and the optical photon energy and can be tuned to a certain degree by choosing the optimal liquid mixture as active volume.

4.3.3. Light Detection

Eventually, the optical photon hits a photodetector (or an uninstrumented part of the detector wall leading to absorption or reflection) and is detected with a probability depending on the type of photodetector. The photodetectors in question were discussed in detail in chapter 3. For the photon detection, the optical coverage by photosensitive surfaces of the detector wall, the angular detection efficiency and the PDE of the photodetectors are of vital importance to detect a maximum number of photons.

4.4. Light Separation

Light separation designates the ability to assign the photon hits of an event to the two classes Cherenkov radiation or scintillation light to get a Cherenkov and a scintillation sample that are as pure and efficient as possible. A successful light separation enables the experiment to access the advantages of Cherenkov and scintillation light and to improve the reconstruction results. The motivation is discussed in more detail in the next section, whereas this section focuses on the characteristics that can be used to discriminate Cherenkov and scintillation photons.

There are essentially three ways to separate Cherenkov and scintillation photons in theory by using their different properties, which were presented in the respective sections. The separation ideas for the individual properties will be presented in the following three sections. Often, more than one of the differences is used to build a successful separation. Furthermore, light separation is not limited to WbLS detectors, as also in pure LS detectors a low percentage of Cherenkov photons (for example roughly 4% of all photons are Cherenkov photons for a $1\,\mathrm{MeV}$ electron without quenching effects in JUNO [153]) is emitted. For a pure LS it is expected though that a light separation is of lower quality and therefore the applications of said separation is more limited. This is because an unfavourable ratio of Cherenkov to scintillation photons leads to a high number of early scintillation photons that can be misidentified and hence decrease the purity of the selected Cherenkov sample.

4.4.1. Wavelength

While the wavelength spectrum of scintillation photons is dependent on the used scintillator, the Cherenkov wavelength spectrum follows λ^{-2} with a cutoff at short wavelengths. Figure 4.4 illustrates these wavelength distributions for Cherenkov (scintillation) photons in blue (red) and is created by running the simulation in chapter 6 with a $700\,\mathrm{MeV}$ muon starting from $(-150, 0, 0)\,\mathrm{cm}$ in $(1, 0, 1)$ direction as primary particle. The plots in the following section stem from the same event, whereby only the PDE of the LAPPDs is considered, while distorted photons (scattered or reflected) are deleted and the emission of secondary particles is turned off to get ideal example pictures. In both plots, the wavelength in nm is shown against the number of photons. On the left side the spectra are shown on emission, whereas the right side shows the distributions on detection. It is clearly visible that the number of scintillation photons in red is significantly higher than the number of Cherenkov photons in blue, which is expected for the chosen WbLS mixture of $5\,\%$ LS solved in water, that is discussed in chapter 6. Furthermore, the scintillation distribution peaks twice on roughly $360\,\mathrm{nm}$ and $380\,\mathrm{nm}$ coming from the different components in the scintillator, both at emission and at detection. Comparing (a) and (b) shows the effect of the PDE that lowers the overall number of hits and that leads to a higher number of hits at around $380\,\mathrm{nm}$ for Cherenkov photons.

The Cherenkov distribution at emission starts at $200\,\mathrm{nm}$ with a sharp rise and then decreases until it is cut off at around $800\,\mathrm{nm}$. The rising as well as the falling edge are not motivated by physics, but rather by the end of the refractive index tables used in the simulation, although a cutoff to shorter wavelengths would also be expected as mentioned above. Since the QE of the LAPPDs is defined to be non-zero in an area within this wavelength-range (see section 6.1.3), it is fair to not extend the refractive index tables and to not simulate outside of this range. The QE is also the reason for the difference in emitted and detected spectrums, so that in the detected spectrum the distribution rises at around $300\,\mathrm{nm}$ until about $350\,\mathrm{nm}$ to be vanishing around $600\,\mathrm{nm}$. Furthermore, it is obvious that the QE reduces the amount of entries substantially in the detected spectrum. Since the highest detection probabilities of the LAPPDs overlap with the wavelength spectrum of the scintillation photons, the influence of the QE is rather small on the scintillation spectrum.

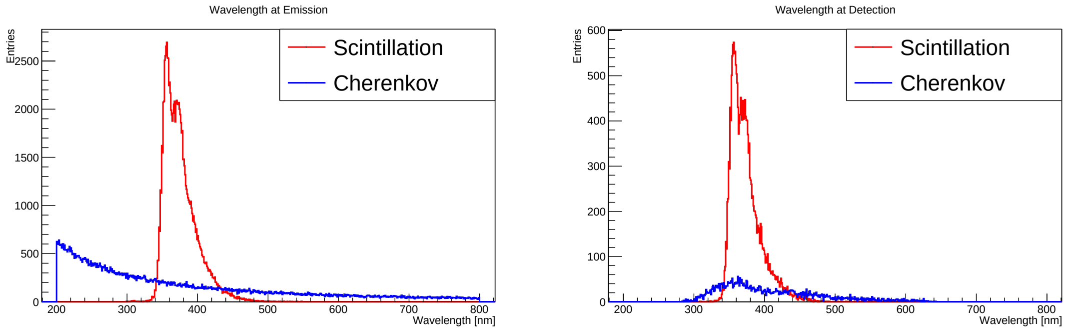

(a) (b)

Figure 4.4.: Simulated wavelength spectra on (a) emission and (b) detection for Cherenkov (blue) and scintillation (red) photons.

In order to make use of the difference in wavelength spectra, filters must be used before the photon detection. This can be done using a so called dichroicon, which is a system of photodetectors and dichroic filters [154]. The filters and the photodetectors are arranged in a way that blue light is sent to a photodetector with peak sensitivity for blue wavelengths, whereas the same is true for red wavelengths. Since the scintillation emission spectrum peaks at blue wavelengths and has minor contribution in red wavelengths, the blue photodetector mostly detects scintillation photons with a contribution of Cherenkov photons, while the red photodetector measures Cherenkov photons with a contribution of scintillation photons. With that, one has a separation into a scintillation sample contaminated with Cherenkov photons and vice versa. These samples can then be purified using the timing characteristics, which will be discussed in section 4.4.3, if the used photodetector have a timing resolution small enough. Comparing the red Cherenkov/scintillation sample and the blue scintillation/Cherenkov sample to simulations gives a valid guess to the ratio of Cherenkov to scintillation photons in that area, which can be of use for particle identification for example.

4.4.2. Directionality

Another property that can be used for the separation is the directionality. The emission of scintillation photons happens isotropically, whereas Cherenkov photons are emitted under an angle resulting in the famous Cherenkov rings. This behaviour is depicted in figure 4.5. On the left side the emission angle is depicted with respect to the primary track. The Cherenkov spectrum shows a sharp peak at around 40° and no contribution below 20° and above 45°, while the scintillation spectrum shows a broad distribution across all angles. The shape of the scintillation distribution is a purely geometrical effect with the maximum at 90°. The detected spectrum on the right side shows little difference to the emitted spectrum except the lower number of entries due to the PDE. It needs to be stressed that this distribution makes use of the true emission position of the photons for the angle calculation and is therefore not directly obtainable in a reconstruction context. Nevertheless, it is of use to show that the characteristics are conserved at detection for this ideal example.

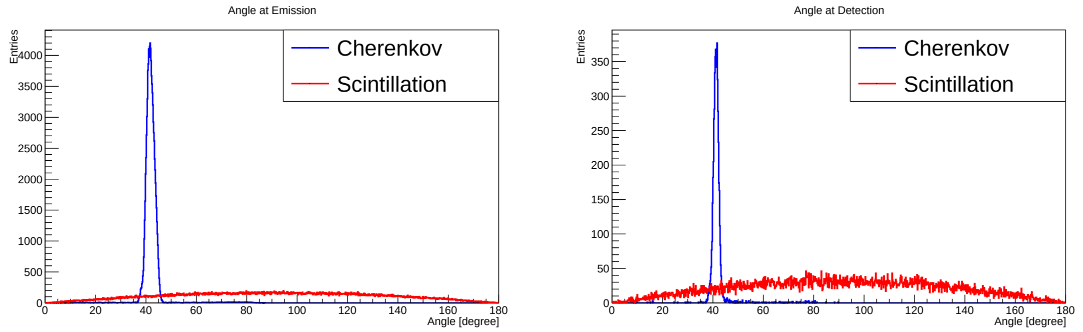

(a) (b)

Figure 4.5.: Simulated angles with respect to the primary track for Cherenkov (blue) and scintillation (red) photons at (a) emission and (b) detection.

A high granularity in the direction of the primary particle is essential for using the directionality difference of Cherenkov and scintillation photons, since the ability to resolve the Cherenkov ring(s) is needed. LAPPDs are a great tool, since they provide a hit position on the LAPPD itself. With a vertex and track reconstruction, basically all hits outside of the Cherenkov angle can be excluded from the Cherenkov photon sample. Within this sample, a further separation can be done with the aforementioned timing and/or wavelength characteristics. The granularity is also of high importance after a successful separation to access the number of Cherenkov rings, that is great for background reduction and their structure or fuzziness, which is an excellent tool for particle identification [155].

4.4.3. Time

The most important characteristics of Cherenkov and scintillation light for this thesis is the timing characteristics. The emission of Cherenkov photons can be considered instantaneous, whereas scintillation light is mostly emitted after a few nanoseconds. In figure 4.6 the emission time corrected to the time of flight of the primary particle is depicted on the left side. The correction makes use of the true emission position of the individual photons, which is not obtainable outside of a simulation context. The Cherenkov photons are indeed emitted on a time-scale that they can be assumed to be instantaneous, whereas the scintillation photons show an exponential decrease. Due to statistical nature of the scintillation process, some of the scintillation photons are emitted on a similar time-scale than the Cherenkov photons. On the right side the detected hit times are shown. Due to the flight time of the primary particle, these distributions are broader in comparison to the shown emission spectrum. The Cherenkov spectrum peaks at around 7 ns in comparison to the scintillation peak at around $12\,\mathrm{ns}$, but there is a big overlap of both distributions. Since the refractive index is depending on the wavelength, Cherenkov photons are generally speaking faster in the active medium than scintillation photons. This effect has little effect on the measured hit times in this detector because of its small size.

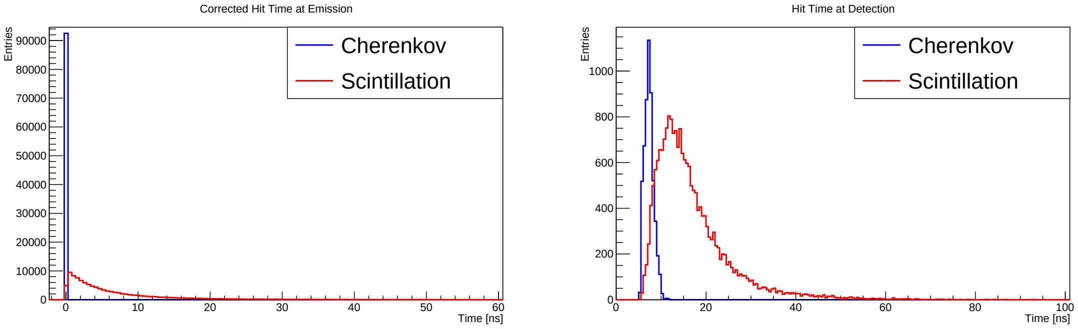

(a) (b)

Figure 4.6.: Simulated emission (a) and hit times (b) for Cherenkov (blue) and scintillation (red) photons.

With the type of scintillator used in the simulation in chapter 6, very fast photosensors are necessary to resolve the difference in timing of Cherenkov and scintillation photons. The LAPPD with a timing resolution of $50\,\mathrm{ps}$ is capable of doing that, which will be shown in this thesis.

4.5. Motivation

This section aims to motivate light separation in WbLS and LS detectors. In general, a successful light separation allows the simultaneous usage of the Cherenkov's and scintillation's light advantages. For Cherenkov light these advantages are the excellent emission timing enhancing track and vertex reconstructions, the directionality for great direction reconstructions and the ring structure for particle identification due to the fuzziness of the ring and background rejection via number of rings. Scintillation light on the other hand is great for shower identification because of the high number of emitted photons, the low energy threshold and the accumulation of emitted photons on shower locations. Furthermore, scintillation light can be used for calorimetry and therefore for energy reconstruction. The quality of the light separation influences how well these advantages can be used if at all.

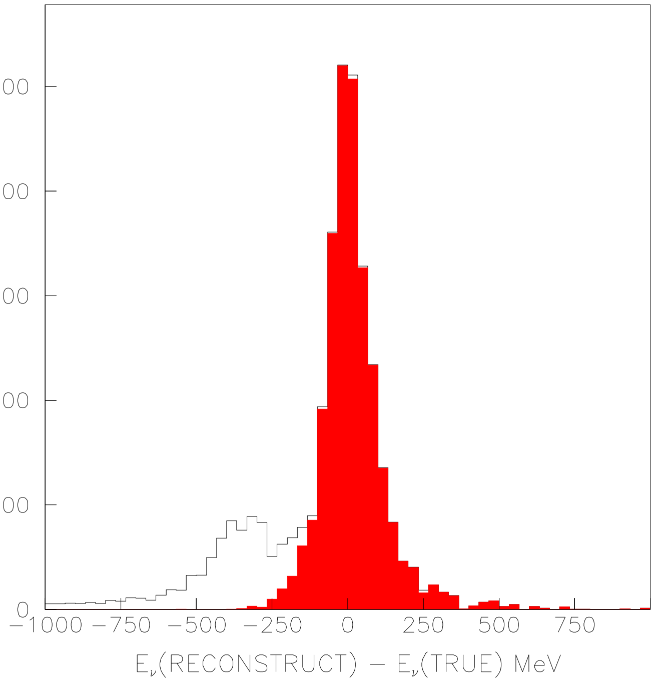

Figure 4.7.: Difference between true and reconstructed energy of a simulated energy reconstruction of SK [156]. The tail towards negative residuals shows that the energy is underestimated for CCRES and CCDIS events because of the invisibility of protons in WC detectors.

High energy neutrino measurements in the GeV-regime is an area that is governed by WC detectors like SK, because in that regime the number of Cherenkov photons is sufficiently high enough for an energy reconstruction with the downside that heavy and slow particles are invisible. A WbLS detector can help in that situation and improve upon the energy resolution of WC detectors, as it is described in the following.

The simulated energy reconstruction of SK, that is shown in figure 4.7, is able to motivate the building of WbLS detectors and subsequent light separation algorithms. The picture shows the difference of true and reconstructed energy on the x-axis versus the number of entries on the y-axis. In the red area CCQE are shown, whereas the white area shows all CC events. Whilst the energy reconstruction of CCQE events gives a Gaussian distribution centered slightly towards higher differences, the energy of events coming from CCRES and CCDIS is heavily underestimated. Aside from effects of FSI, the dominating effect for this underestimation is the invisibility of slow and heavy particles in WC detectors. This includes slow pions and kaons as well as protons. Due to the low threshold of the liquid scintillator technique, a WbLS detector should be able to resolve this discrepancy. With a sufficient light separation algorithm, particles that are below Cherenkov threshold could be identified giving a handle on particle identification. Furthermore, liquid scintillator detectors are expected to have difficulties discriminating

between electron and π^0 events in the high energy regime, where the neutrino energy is in the order of GeV. This is, because electrons as well as the decay gammas of the π^0 create electromagnetic showers. If one of the gammas escapes detection or the decay angle of the gammas is small due to a high boost, a π^0 can be misidentified as electron. This can be fought in a WbLS detector with a successful light separation, since the separation gives access to the number of Cherenkov rings in the event, so that a two ring event can be identified as π^0 and a one ring event as electron. It is to note, that this technique comes also to its limits if the boost of the pion and therefore the overlap of the gamma rings is too high.
In the following, two specific examples for the application of light separation in the low energy regime will be given.

4.5.1. Background Reduction in $0\nu\beta\beta$ Searches

As it was discussed in section 2.3.3, liquid scintillator detectors can be used to search for Neutrinoless Double Beta Decay ($0\nu\beta\beta$). For KamLAND-Zen 800 and SNO+ for example a main background for the search for $0\nu\beta\beta$ is the presence of $^8\mathrm{B}$ solar neutrinos producing elastically scattered electrons in the same energy range (around $2.6\,\mathrm{MeV}$ as the electrons from $0\nu\beta\beta$ [157, 158]). In this energy range, conventional direction reconstructions show little success e.g. in reference [159] it was shown, that the TTR produces a cloud-like structure with no opportunity to resolve the direction of the particle. A selection of Cherenkov photons would allow to reconstruct the direction of the electron and therefore to reject events with accordance to the sun's position. This was investigated in reference [160], in which a WbLS and a LS detector is simulated and the direction is reconstructed via a likelihood approach after performing a separation in the form of timing cut on the photon hit times to have a Cherenkov enriched sample. It was found that the reconstruction performs better in pure liquid scintillator because of the higher refractive index and therefore a dispersion caused increase in the hit time difference between scintillation and Cherenkov photons from the same point of origin. In figure 4.8 the $0\nu\beta\beta$ half-life sensitivity of $5\,\%$ natural $^{130}\mathrm{Te}$ in linear alkylbenzene and 2,5-Diphenyloxazole is plotted against a cut on $\cos(\theta_{\mathrm{sun}})$, in which θ_{sun} denotes the angle between reconstructed direction and the sun. The detector mass is $50\,\mathrm{kt}$ and an energy resolution of $3\,\%/\sqrt{E}$ is assumed.
Figure 4.8 shows that the expected sensitivity on the half-life increases with a higher cut value due to the increasing statistics until a maximum at around 0.7 for all but the standard PMT represented by the blue line, for which no cut at all is ideal. After that maximum the increasing impurity of the selected sample based on the cut value reduces the sensitivity for the other three photodetectors. As it is expected, the LAPPDs (red line) performs best due to the superior time resolution.
Regarding solar neutrinos, the Borexino collaboration was able to show in data, that the direction of solar neutrinos with sub-MeV energy can be reconstructed

with help of the low number of Cherenkov photons emitted in liquid scintillator by using only the first two hits per PMT [161]. It needs to be stressed that this was not possible on a event-to-event basis, but as a statistical approach. In a WbLS detector with low backgrounds a similar performance should be possible.

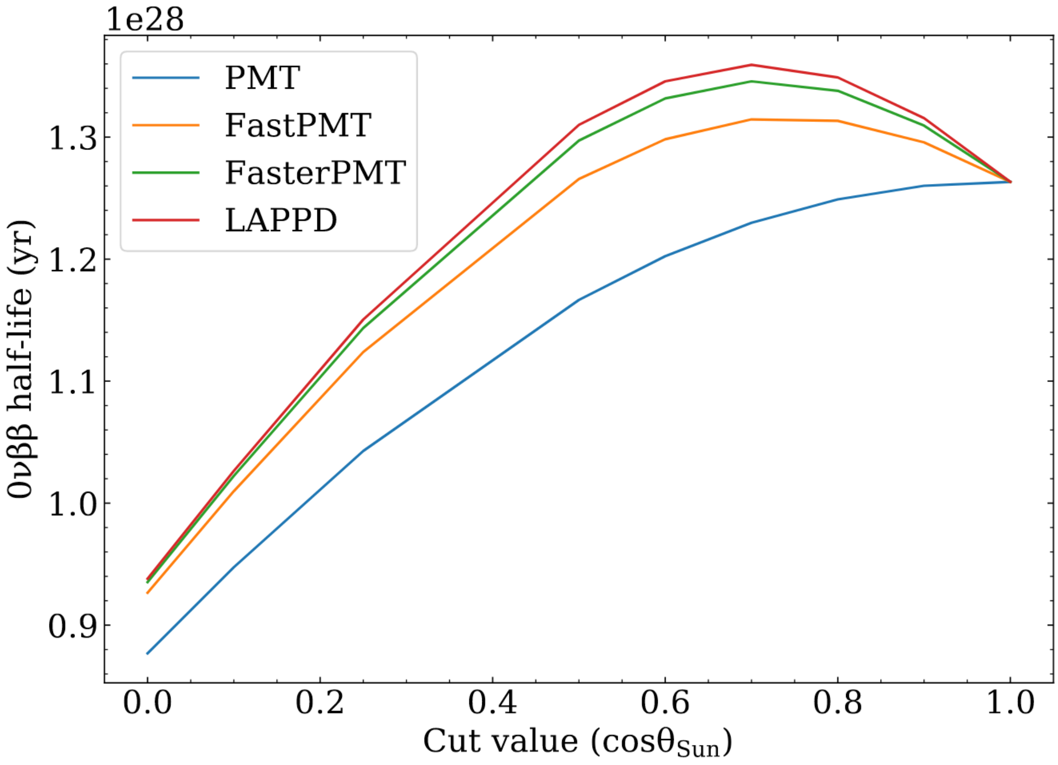

Figure 4.8.: $0\nu\beta\beta$ half-life sensitivity with respect to solar angle cut [160].

4.5.2. Background Reduction in DSNB Measurements

The search for the DSNB in LS or WC detectors is limited by the presence of strong backgrounds. Neutrinos from the DSNB have energies of up to $40\,\mathrm{MeV}$ overlapping with the reactor neutrino spectrum, which ends at around $8\,\mathrm{MeV}$ [162] and is the dominant background for the low end of the spectrum. Since DSNB searches focus on the IBD from electron antineutrinos, the electron neutrinos from the sun, which are in a similar energy range like reactor neutrinos, can be excluded. For higher energies around $30\,\mathrm{MeV}$ atmospheric $\overline{\nu}_e$ come into play and overshadow the expected event number from the DSNB. Furthermore, atmospheric $\overline{\nu}_\mu$ can cause the creation of muons with energies below Cherenkov threshold in the detector, which are referred to as invisible muons. The decay of these muons via

$$\mu^- \to e^- + \overline{\nu}_e + \nu_\mu \tag{4.22}$$

can mimic the IBD signature because of the emission of a so called Michel electron, when an accidental neutron capture, or an event that is misidentified as neutron capture, happens in the coincidence time window. The number of expected $\overline{\nu}_\mu$ events rises above the DSNB event rate at around $20\,\mathrm{MeV}$. The best energy range for DSNB searches is therefore between $8\,\mathrm{MeV}$ and $30\,\mathrm{MeV}$ to reduce the $\overline{\nu}_e$ background [163]. In this energy range, atmospheric muon events are a relevant background due to the possibility of misidentification or the creation of spallation products, whose decays have a similar signature to an IBD event. This is especially true for the aforementioned case of the emission of a Michel electron. Neutron tagging can be used to identify the neutron from the IBD with the possibility of adding gadolinium to the active medium. This would allow for a more precise neutron identification to discriminate between the neutron from the IBD events and signatures, that mimic a neutron capture. Additionally, the creation of spallation products can be identified by the number of neutrons. Another option is PID, that can be used to reduce the background from muons and less prominent from recoiling protons from neutral current interactions. PID is possible via the ratio of Cherenkov to scintillation photons in an event [164]. The reason is that the number of emitted Cherenkov photons depends on the velocity of the particle and therefore on its mass for a fixed kinetic energy, whilst the number of scintillation photons is related to the particle type due to quenching effects.

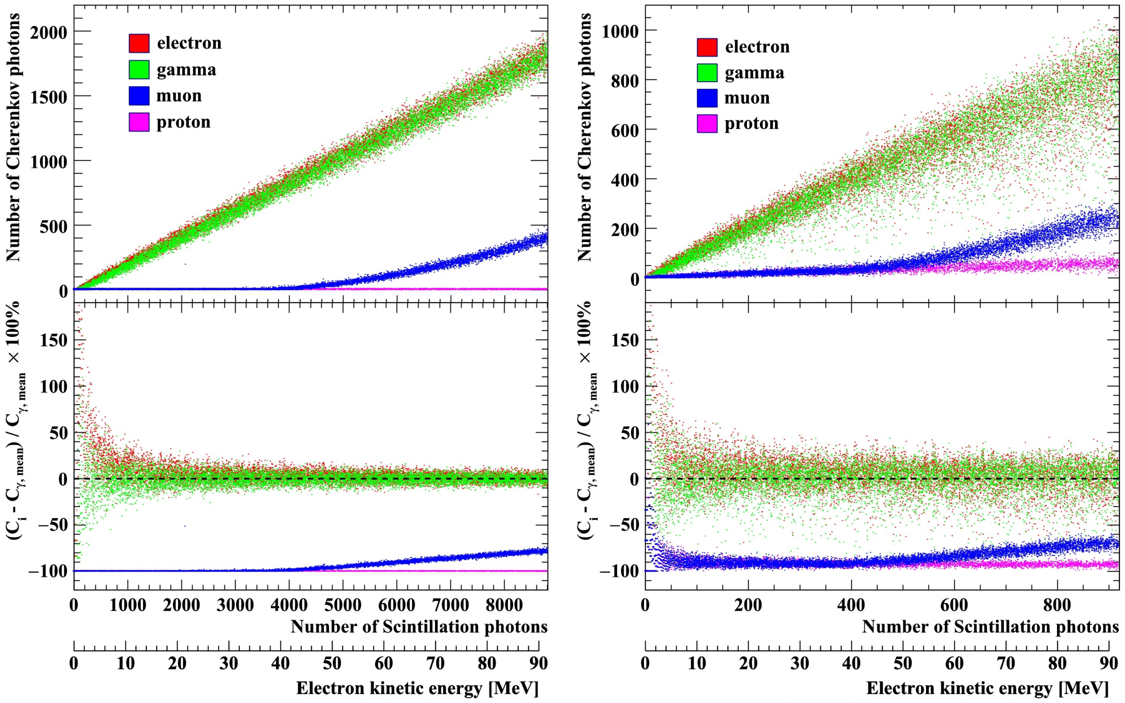

(a) Ideal case (b) Realistic case

Figure 4.9.: The number of Cherenkov photons (top) and the fractional difference of the number of Cherenkov photons to the mean number of Cherenkov photons for gammas (bottom) with respect to the number of scintillation photons. An ideal case is shown on the left side and a more realistic one on the right side [164].

This is illustrated in figure 4.9, where at the top the number of Cherenkov photons with respect to the number of scintillation photons is plotted, whereas in the bottom the fractional difference of the number of Cherenkov photons to the mean number of Cherenkov photons for a gamma is shown with respect to the number of scintillation photons. A second x-axis is displayed showing the kinetic energy of an electron producing the corresponding number of scintillation photons. The plots are produced with a Geant4 simulation assuming a spherical detector with a radius of about $10\,\mathrm{m}$ and filled with LAB with a decay time constant of $37\,\mathrm{ns}$ [164]. The left side shows an ideal case with a perfect separation only taking the PDE into account; the right side shows a more realistic study, where a simple timing separation is done assuming all photons to be Cherenkov photons with a hit time smaller than $10\,\mathrm{ns}$. Furthermore, attenuation is taken into account for the right side. Figure 4.9 shows that PID is possible for the ideal as well as for the realistic case for distinguishing electrons and muons, while a discrimination of electrons and gammas is not possible. For higher energies, when protons start producing Cherenkov photons, even a discrimination between muon, protons and electrons is possible.

One of the main goals of this thesis is to reproduce figure 4.9 with the combination of the detector simulation of chapter 6 and a method based on the TTR in chapter 7. The result can be seen in figure 9.3.

A study in the same region of interest is conducted in reference [14] showing the ability to discriminate between DSNB events and atmospheric neutrino NC events based on the Cherenkov to scintillation ratio. For this study, the two proposed Theia designs are simulated in Geant4 using a WbLS mixture with $10\,\%$ liquid scintillator, with which all relevant events in the corresponding fluxes are simulated. After event selection and a cosmogenics as well as a fiducial volume cut, figure 4.10 is obtained. The x-axis shows the number of scintillation PE; the y-axis shows the ratio of Cherenkov to scintillation photons. The black dots are the atmospheric background events, whereas the blue dots are events from the DSNB. Although there is some overlap at low energies (below roughly $15\,\mathrm{MeV}$), there is an area towards higher energies (between 15 and $50\,\mathrm{MeV}$), where almost exclusively the DSNB events have a high ratio of Cherenkov to scintillation photons. This means, that the atmospheric NC events have lower Cherenkov photon emission due to the hadronic component.

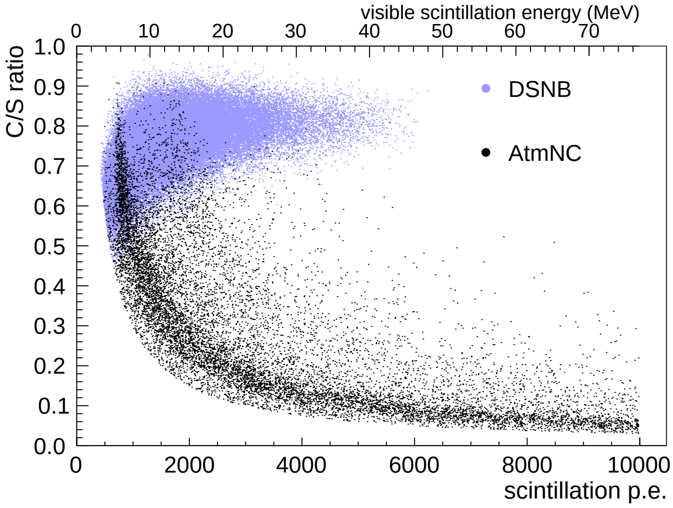

Figure 4.10.: Ratio of Cherenkov to scintillation photons for DSNB and atmospheric NC events [14].

Since figure 4.10 is the result of an extensive sensitivity study, this application is outside of the scope of this thesis, which is focused on the development of the light separation algorithm in an ideal detector.

4.6. Production of WbLS and Current Status

The mixing of LS and water poses a challenge due to the chemical characteristics of the WbLS components. A simple mixture of water and e.g. LAB would quickly separate itself into two layers due to the difference in polarity. Whilst LS is hydrophobic and lipophilic, the opposite is true for the water phase being hydrophilic and lipophobic. It is therefore necessary to introduce another component to emulsify the LS and water component. Such a component is known as surface-active agent or in short surfactant and consists of molecules that possess a hydrophilic and lipophilic group on opposite ends. The surfactant molecules form around the molecules of the organic LS molecules in a spherical manner, creating micelles that are surrounded by water molecules [165, 166].

As previously discussed, there are a number of properties that have to be known before deploying the chosen mixture of WbLS. These properties are the light yield, the attenuation length best divided into the different scattering and absorption processes, the time constants for the emission of scintillation photons and quenching effects in form of Birk's constant.

The measurement of these properties for different WbLS mixtures is an ongoing endeavour, but first results have been published. In reference [167], different surfactants (Triton X-100, CS-124 and HCO-60 in particular) were tested in regard of their light yield and the emission, absorption and transmittance spectra. Reference [168] measured the attenuation length, the emission and excitation spectra, the

light yield and Birk's constant for 0.4% and 1% LS by mass solved in water based on the components PseudoCumene (PC), PPO and bis-MSB. The time response as well as the light yield of 1%, 5% and 10% of LAB and PPO solved in water was measured in reference [169]. Lastly, in reference [170] the proton light yield of 5% WbLS was measured and with that the quenching constants.
Additionally, the CHESS experiment [171] was conducted to show the possibility of light separation with fast PMTs. A similar setup was later used to characterize 1%, 5% and 10% WbLS in terms of light yield, time response and light separation capabilities in reference [172]. This was followed by a similar study using an LAPPD for light separation in WbLS samples in reference [173] to demonstrate the possibility of light separation with the combination of WbLS and LAPPDs, which are the techniques also used in this thesis.

5. Accelerator Neutrino Neutron Interaction Experiment (ANNIE)

Located at Fermi National Accelerator Laboratory (Fermilab) in the United States of America, the Accelerator Neutrino Neutron Interaction Experiment (ANNIE) is a short baseline neutrino beam experiment. It is one of the first experiments to use LAPPDs as photodetectors and WbLS as active medium. This chapter discusses in section 5.1 the physics motivation for ANNIE. It is followed by an overview of the experiment and more closely the detector in section 5.2 and the measurement principle in section 5.3. This chapter is concluded with a description of the first results and the current status of the experiment (section 5.4).

5.1. Motivation

The physics motivation for ANNIE can be divided into three categories. The first one are the cross section measurements of neutrino-nucleus interactions on water, the second one is the final state neutron multiplicity measurement and the third one is the gaining of experience and testing of new detector techniques for future experiments. These categories are covered in the next sections in the named order.

5.1.1. Cross Section Measurements

One of the relevant systematic uncertainties in current and future WC detectors measuring atmospheric and accelerator neutrinos is the cross section of neutrino-nucleus interactions in water, that was briefly discussed in section 2.1.2. These interactions are the dominant processes in the typical energy range of said neutrino types of hundreds of MeV to several GeV. Since ANNIE is able to determine the angle and energy of the outgoing muon from neutrino interactions, the cross section can be measured in relation to the kinematics of the muon as well as integrated over energy and angle. This means, the differential cross section in terms of muon momentum and angle can be determined as well as the double differential cross section with respect to both muon momentum and direction. Depending on the event signature, different samples can be selected like CCQE with exactly one pion or zero pions to pin down the cross sections of these processes.

Furthermore, ANNIE aims to measure the Neutral Current Quasi-Elastic (NCQE) cross section [174], which has a fundamentally different event signature due to the missing lepton and therefore lower light emission. This is motivated by the atmospheric NC background in DSNB searches, which was briefly introduced in section 4.5.2.

In addition, ANNIE sits together with other experiments in the BNB that makes a combined cross section measurement attractive [174]. This is especially of high interest in combination with the Short-Baseline Near Detector (SBND) [175], an Liquid Argon Time Projection Chamber (LArTPC) experiment in Fermilab's short baseline neutrino program measuring in direct neighbourhood to ANNIE. A combined cross section measurement on hydrogen and liquid argon will greatly help in constraining the systematic uncertainties for future liquid argon experiments like DUNE.

The combination with data from SBND also offers the unique opportunity to combine a measurement of the final state neutron multiplicity, that will be covered in the next sections, with the measurement of the final state protons, which is achievable with a LArTPC. Such a measurement would essentially measure the number of nucleons in high energy neutrino nucleus interaction, which will help understanding the nuclear models and further tune the neutrino generators, that are in use for the simulation of neutrino interactions.

5.1.2. Neutron Multiplicity for Proton Decay Searches, Long Baseline Physics and DSNB

As it was discussed in section 2.1.2, the final state multiplicity of neutrons[1] is an important parameter in high energy neutrino interactions, since the number of neutrons is directly related to the inelasticity of the event and additionally hints towards FSI or nuclear correlations and can help with identifying event signatures. Therefore, the neutron multiplicity can be used to discriminate and exclude certain event topologies. A measurement of the number of final state neutrons has an impact on three main regions of interest that will be discussed in the following.

Background Reduction in Proton Decay Searches

A Grand Unified Theory (GUT) denotes a model, that unifies all fundamental forces into one overarching theory. In many of these theories the process of proton decay is predicted. This motivates the search for proton decay in WC detectors in order to either support in the occurrence of an observation or exclude the corresponding theories by limiting the available parameter space. The decay modes of

---

[1] The number of protons is in principle equally important but a WC detector has little to no option to measure protons due to their high mass and the corresponding high Cherenkov threshold.

interest are [176]

$$p \to e^+(\mu^+) + \pi^0 \to e^+(\mu^+) + \gamma + \gamma, \tag{5.1}$$

$$p \to K^+ + \overline{\nu}, \tag{5.2}$$

$$p \to \mu^+ + K^0, \tag{5.3}$$

to name a few of highest relevance. The first mode is expected to produce exactly three Cherenkov rings in a WC detector, one from the charged lepton and two from the π^0 decay gammas. Atmospheric neutrino events can mimic this event signature in many ways. First of all, single pion production[2]

$$\nu_l + n \to l^- + p + \pi^0, \quad \overline{\nu}_l + p \to l^+ + n + \pi^0, \tag{5.4}$$

has the same outgoing particles than the lepton/pion proton decay. Since the needed neutrino energy for CCRES processes is quite high, this process can be mostly excluded by cutting on the momentum. In the case of pure CCQE processes[3]

$$\nu_l + n \to l^- + p, \quad \overline{\nu}_l + p \to l^+ + n, \tag{5.5}$$

the momentum is more fitting and due to FSI the production of π^0s is possible. Additionally, FSI in single pion events can reduce the kinetic energy of CCRES events and can convert charged pions into π^0s. For most of these atmospheric background events, neutrons are part of the final state signature. Either they are produced directly in the neutrino interaction, in FSI, or the outgoing proton interacts hadronically generating neutrons. For the kaon decay modes, a similar case can be made, since the subsequent decay of the kaons yields pions that can also be produced by atmospheric neutrinos. For all the mentioned proton decay modes, neutrons do only occur very rarely in about 6% of events [141]. This means that neutron tagging is an excellent technique to reduce background for the proton decay search whilst maintaining a high event selection efficiency. This also motivates the Gadolinium loading of WC detectors, since the resulting gamma cascade of $8\,\mathrm{MeV}$ from neutron capture on Gadolinium is harder to miss than the $2.2\,\mathrm{MeV}$ gamma from a neutron capture by a proton.

Since atmospheric neutrinos are similar in energy and flavour to the accelerator neutrinos measured by ANNIE, a successful neutron multiplicity measurement would demonstrate the possibility to enhance background rejection capabilities of bigger WC detectors for proton decay searches by loading them with Gadolinium.

---

[2] This was introduced in equation (2.16) and is repeated here for comparison.

[3] This was introduced in equation (2.14) and is also repeated here for comparison.

Background Reduction in DSNB Searches

As it was already discussed in section 4.5.2, the main channel for supernova neutrino detection is the IBD. Atmospheric neutrinos pose the dominant background for the energy range above $20\,\mathrm{MeV}$ because they can produce invisible muons in the detector, that can decay under the emission of a Michel electron, so that together with an accidental neutron capture signal, the signature of the IBD is mimicked. It is therefore reasonable to dope the active medium of a WC detector with Gadolinium to use the advantages discussed in section 4.1.4. ANNIE aims not only to overcome the technological difficulties of Gadolinium loading and testing this technique, but also to measure the neutron multiplicity, because the neutron multiplicity can give insights about the behaviour of other backgrounds of e.g. spallation or radiogenic origin [3].

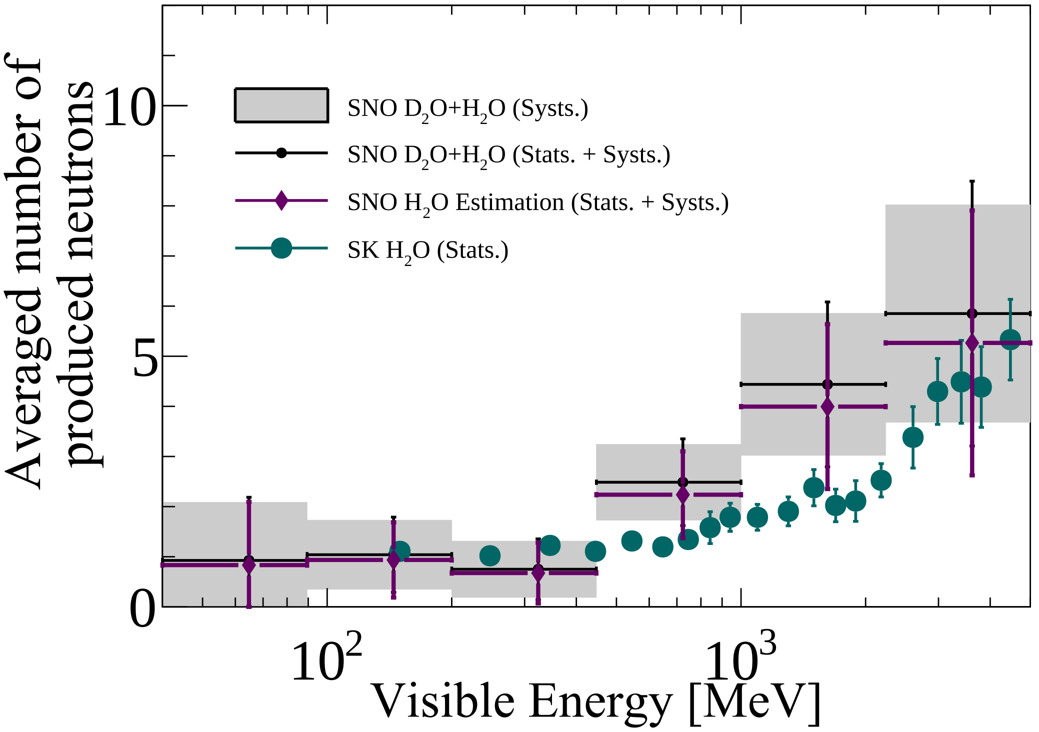

Figure 5.1.: Measurement of neutron multiplicity in (heavy) water from SNO and SK in relation to the visible energy [177].

In fact, the neutron multiplicity was already measured for atmospheric and accelerator neutrinos. The latter will be shown in the next section, whereas the first was conducted by SNO and SK and is shown in figure 5.1. Here, the neutron multiplicity is shown with respect to the visible energy as measured by SNO for H_2O and D_2O as grey boxes for systematic errors only, as black dots with systematic and statistical error and the estimation for light water only in purple diamonds. Additionally, the atmospheric neutrino neutron multiplicity for SK is shown as green dots with statistical uncertainties only. The data sets of both experiments are in good agreement and show indeed that with higher neutrino energy, the inelasticity of the event and therefore the number of neutrons increase.

Understanding of Nuclear Models for Future Long Baseline Neutrino Experiments

The accurate measurement of the neutrino energy is one of the key requirements for current and future long baseline neutrino experiments and is related to the sensitivity of these experiments to e.g. the MO or the CP violating phase. Ideally, clean CCQE interactions are happening without FSI or nuclear correlation leading to a clean single lepton event signature, so that the lepton's energy can be directly translated into the neutrino energy. Often, this is not the case and especially going to CCRES or CCDIS, the lepton energy is significantly lower than the neutrino energy because of the momentum transfer to other nucleons and e.g. pions. Measuring the number of neutrons can give a handle of the actual event signature and can be used to correct the neutrino energy.

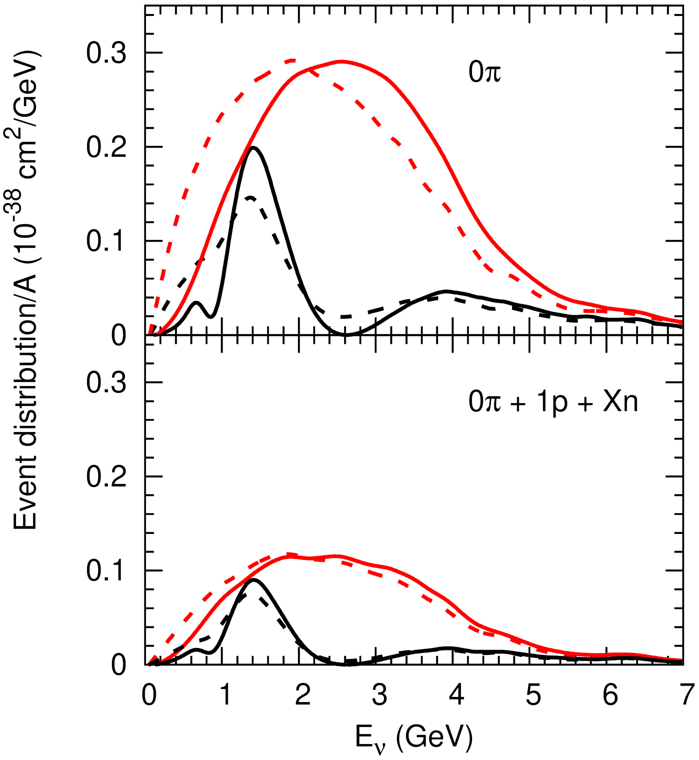

Figure 5.2.: Kinematic energy reconstruction for a 1 GeV muon neutrino beam with no further selection criteria except zero pions (top) and the additional selection of samples with exactly one proton (bottom) [178]. Red (black) lines show the spectrum without (with) oscillation, whilst the dotted (solid) lines correspond to the reconstructed (true) energy.

This is shown in figure 5.2 at the example of proton selection instead of neutron selection. The normalized flux times the cross section per nucleon is shown versus

the neutrino energy. The red (black) lines show the distribution without (with) oscillation at the near (far) detector. The dotted (solid) lines shows the reconstructed (true) energy. The energy reconstruction is based on equation 2.15, a beam of muon neutrinos with $1\,\mathrm{GeV}$ is assumed and the DUNE baseline is used. The top panel shows a zero pion selection, whereas the bottom panel shows the selection of exactly one proton, zero pions and X neutrons for a CCQE sample. It is to note that at these energies, as it was shown in figure 2.9, resonance production comes into play. Comparing both panels shows that the agreement of reconstructed and true energy is significantly better for the proton selection and hence motivates the tagging of neutrons/protons.
The neutron multiplicity in water was measured by T2K, which is shown in figure 5.3 for neutrino beam mode on the left side and antineutrino mode on the right side. The mean neutron multiplicity is displayed with respect to the transverse momentum of the muon as black dots for the data. The expected number of neutrons with regard to the different neutrino generators can be seen in the coloured bars with pink for NEUT [179], green for NuWro [180] and yellow for GENIE [181]. For both beam modes, the generators overestimate the number of neutrons for the first three data points. For the last data point to be interpreted correctly, more statistics are needed, since the error allows an agreement with all of the models. This figure demonstrates that more data on neutron multiplicity is needed for the tuning of neutrino generators, which is essential for the Monte Carlo (MC) simulations of high energy neutrino experiments. This is a task where ANNIE's measurements will help with.

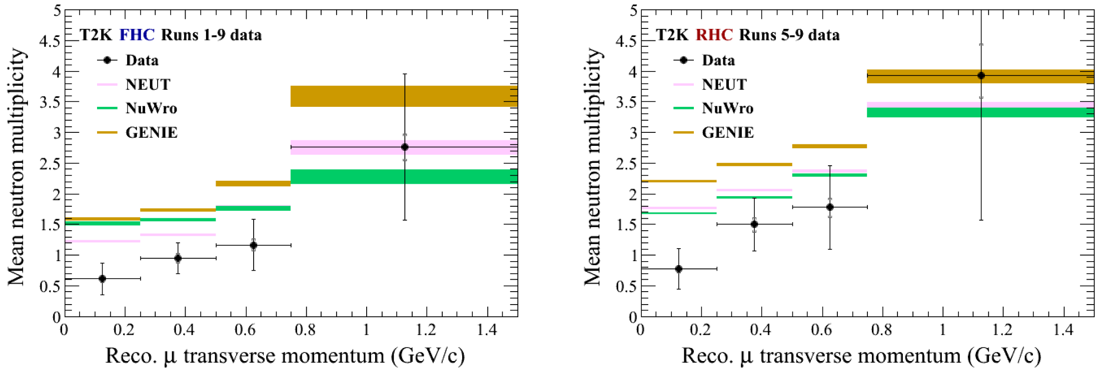

Figure 5.3.: Measurement of neutron multiplicity in water from T2K [182].

5.1.3. Research and Development for Future Experiments like Theia

Aside from the physics goals, ANNIE can also be viewed as testbed for two new technologies that can find application in future experiments like Theia [71]. The first technology is the LAPPD, that was covered in chapter 3. Currently, ANNIE aims to deploy five of these novel photodetectors. This process does not only include the designing of a water-proof housing and the readout electronics, that are capable of providing picosecond-timing, but also the development of algorithms for extracting hits from the raw data. Eventually, data taking and reconstructions with LAPPD data is planned in order to demonstrate the potential of these photosensors.

The second technology is the deployment of WbLS. The motivation and the theoretical aspects of this mixture of liquid scintillator and water was covered in chapter 4 and is together with LAPPDs the main feature of the simulated detector in chapter 6. ANNIE aims to deploy a vessel filled with WbLS into their tank to demonstrate the application of light separation and the improvement in reconstruction quality allowed by the simultaneous usage of Cherenkov and scintillation light.

5.2. Design

ANNIE's centerpiece is a neutrino detector located in the experiment hall, which was formerly used by the SciBar Booster Neutrino Experiment (SciBooNE) experiment [183]. As neutrino source the BNB is used. In the following, the beam is described followed by a discussion of the detector's design.

5.2.1. Booster Neutrino Beam (BNB)

The neutrino beam used by ANNIE as well as by SBND and MicroBooNE is the BNB. The functioning principle of a neutrino beam is shown in figure 5.4 and will be explained at the example of the BNB. The first step is the acceleration of protons. This happens in three stages for the BNB. The first step is a pre-accelerator that brings the protons to a kinetic energy of $750\,\mathrm{keV}$. This is followed by a linear accelerator for a kinetic energy of $400\,\mathrm{MeV}$, which is in turn followed by the booster, a synchrotron that accelerates the protons to $8\,\mathrm{GeV}$ [184].

This proton beam is send via the MI-8 Line on a fixed beryllium target. The subsequent interaction of protons within the target creates secondary particles, mostly in form of pions and kaons. These charged pions and kaons are focused via powerful magnets (so called magnetic horns) to filter into positively or negatively charged mesons. These horns can often be reversed to switch between discarding positive (negative) mesons for the production of an anti-muon (muon) neutrino beam, as it is also the case for the BNB.

The focusing magnets are followed by a decay vessel or pipe, in which the mesons decay via [130]

$$\pi^{+(-)} \rightarrow \mu^{+(-)} + \overset{(-)}{\nu}_\mu \qquad \mathrm{BR}: 99.99\,\%, \tag{5.6}$$

$$K^{+(-)} \rightarrow \mu^{+(-)} + \overset{(-)}{\nu}_\mu \qquad \mathrm{BR}: 63.6\,\%, \tag{5.7}$$

$$K^{+(-)} \rightarrow \pi^0 + e^{+(-)} + \overset{(-)}{\nu}_e \qquad \mathrm{BR}: 5.0\,\%, \tag{5.8}$$

$$K^{+(-)} \rightarrow \pi^0 + \mu^{+(-)} + \overset{(-)}{\nu}_\mu \qquad \mathrm{BR}: 3.4\,\%. \tag{5.9}$$

It needs to be stressed that only the relevant leptonic decay modes for neutrino production are shown with a branching ratio above $1\,\%$ and that the branching ratios are given in approximate values.
Most of these meson decays incorporate muons, that decay via

$$\mu^{+(-)} \rightarrow e^{+(-)} + \overset{(-)}{\nu}_e + \overline{\nu}_\mu(\nu_\mu). \tag{5.10}$$

Since it is necessary for oscillation experiments to have a neutrino beam that is as pure as possible, the decay pipe has to be simultaneously long enough for the mesons to decay and sufficiently short for the muons to be stopped before decaying. Muon decays would otherwise contaminate the muon neutrino beam with electron neutrinos that can fake electron neutrino appearance signals. When looking at the kaon decays, it becomes clear that a beam contamination is not avoidable, since roughly $5\,\%$ of kaons decay into an electron neutrino. Furthermore, there is a remaining contamination from muon and K_L^0 decays.

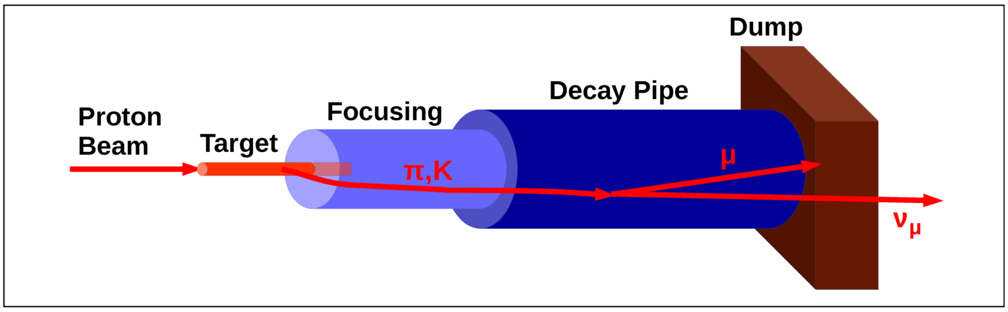

Figure 5.4.: Principle of a neutrino beam [185]. The proton beam is send on a beryllium target, creating a high number of mesons in the process. These mesons are focused by magnets into a decay pipe, selecting mesons of positive (negative) charge, which results in a neutrino (antineutrino) beam. The mesons decay in the decay pipe into mostly muons and muon neutrinos. The muons are stopped in a beam dump and the neutrinos travel to the detector.

The decay pipe is followed by a beam dump that absorbs the remaining decay products from the mesons, most importantly the muons, so that only the neutrinos travel further downstream.
The BNB's beam profile can be seen in figure 5.5 for the neutrino mode in (a) and

the antineutrino mode in (b), as they were calculated by the MiniBooNE collaboration in reference [186]. The solid (dashed) lines show the neutrino (antineutrino) fluxes for the electron flavour in red and the muon flavour in black. In both modes a considerable beam contamination can be seen. The beam composition for the neutrino mode amounts to $93.6\,\%$ ν_μ, $5.86\,\%$ $\overline{\nu}_\mu$, $0.52\,\%$ ν_e and $0.05\,\%$ $\overline{\nu}_e$. For the antineutrino mode the muon neutrino contamination is higher, whereas a lower electron (anti)neutrino flux is expected with $83.73\,\%$ $\overline{\nu}_\mu$, $15.71\,\%$ ν_μ, $0.4\,\%$ $\overline{\nu}_e$ and $0.2\,\%$ ν_e.

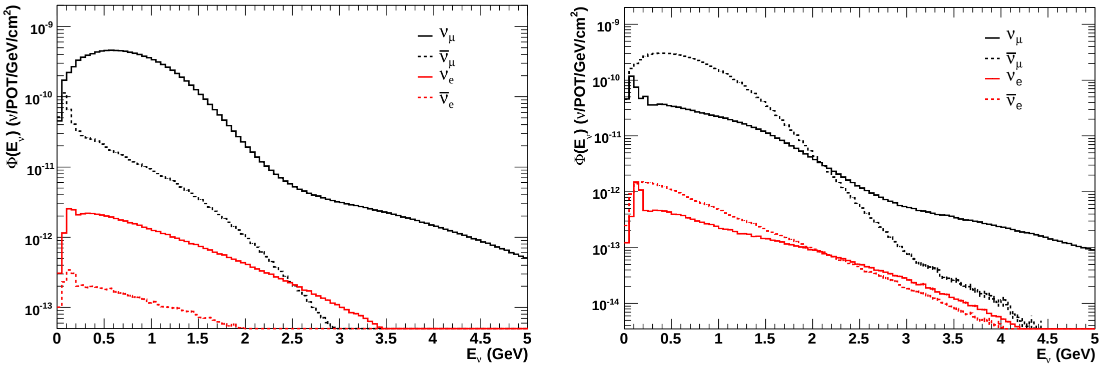

(a) (b)

Figure 5.5.: Predicted flux per neutrino type for the BNB in neutrino (a) and antineutrino (b) mode [186].

5.2.2. Detector

The ANNIE detector consists of three main components visualised in figure 5.6. The beam enters the detector from the left side and passes through the Front Anticoincidence Counter (FACC), the tank filled with gadolinium-loaded water and instrumented with PMTs and LAPPDs and the Muon Range Detector (MRD). The parts are described in the following based on reference [174].

Front Anti-coincidence Counter (FACC)

The FACC's purpose is to reject background events that come from the rock upstream of the detector, most predominantly particles originating from neutrino interactions within the rock. It consists of 26 scintillator paddles that are equipped via light guides with 2 inch PMTs. These paddles with a length of $322.0\,\mathrm{cm}$ and a height of $31.1\,\mathrm{cm}$ are placed in 13 rows, whereby always two paddles are overlapping for ensuring a coincidence measurement. In this way, the tank volume is sufficiently covered to exclude said background events.

Tank

ANNIE's water steel tank has a height and radius of about $4\,\mathrm{m}$ and $1.5\,\mathrm{m}$ and is equipped with 132 PMTs and three LAPPDs with two more to come in the future. The LAPPDs are installed on the downstream side of the tank in order to accurately measure the photons produced by the muons coming from the beam neutrino interactions. The tank is filled with roughly $26\,\mathrm{t}$ of gadolinium loaded water.

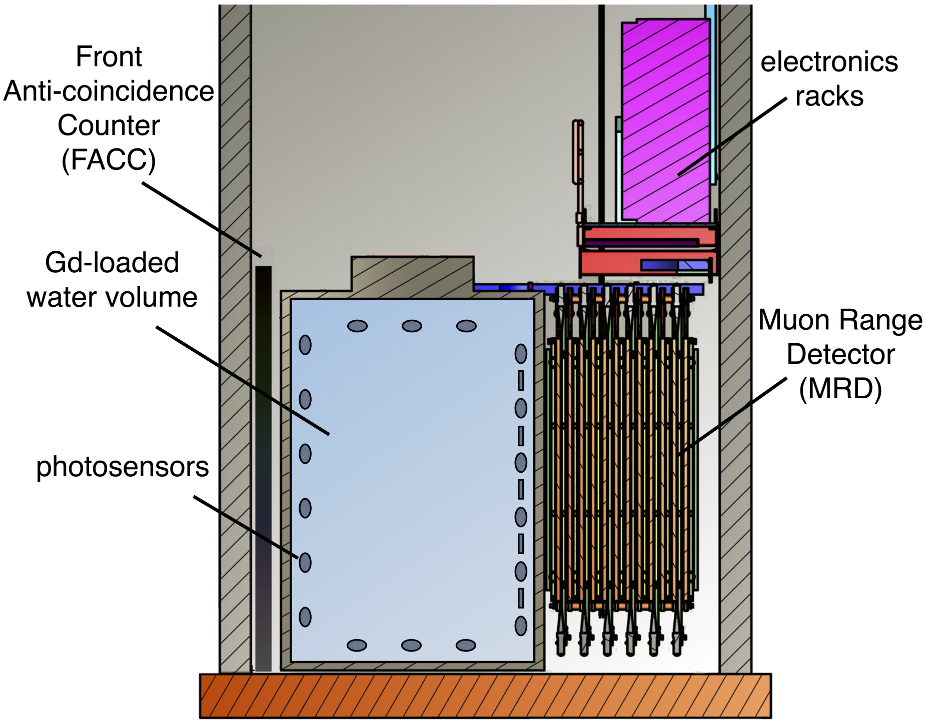

Figure 5.6.: Scheme of the ANNIE detector taken from reference [187]. The beam enters the hall from the left, traversing the FACC, the tank with the photodetectors and lastly the MRD.

Muon Range Detector (MRD)

Due to the small size of ANNIEs water tank, most of the muons from beam neutrino interactions within the water volume leave the tank with their remaining energy making an energy reconstruction based solely on the tank's photosensors impossible. Therefore, a sandwich calorimeter consisting of steel plates and scintillator paddles instrumented with PMTs is placed downstream of the tank to measure the energy of exiting muons. Furthermore, the positions of hit paddles allow to reconstruct the muon's direction/angle and their range. A part of the energy reconstruction problem persists though, when muons manage to exit the MRD.

5.3. Measurement Principle

The measurement principle for measuring the neutron multiplicity is shown in figure 5.7.

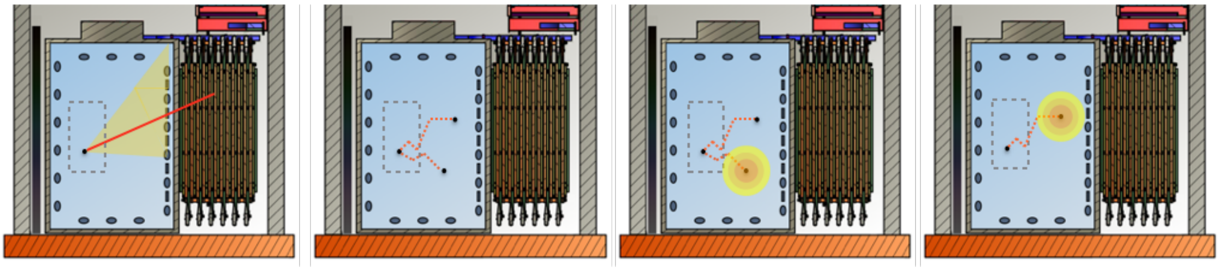

Figure 5.7.: Measurement scheme of ANNIE [188]. The first panel shows the neutrino interaction as black dot and the muon track as red line traversing the tank and stopping in the MRD. The Cherenkov emission from the muon is shown as yellow cone illuminating PMTs and LAPPDs. The second panel shows the neutron paths whilst thermalizing as red dashed lines. Panel three and four show the neutron capture and the following gamma cascade as orange-yellow circles.

The first panel shows the neutrino interaction (black dot) and the subsequent track of the charged lepton (red line). The Cherenkov radiation of the muon is measured by the PMTs and more importantly the LAPPDs, which allows to reconstruct the direction and vertex inside the tank and to find an energy estimate. The reconstruction of the direction and energy is heavily enhanced by the muon track in the MRD, where the hits in the scintillation panels allow to determine the angle of the muon and the track length. In addition, the structure and the number of Cherenkov rings can be reconstructed. This allows to distinguish between electron and muon events via the fuzziness of the rings and between events with different number of pions via the number of rings.

The next panel shows the thermalizing of the neutrons, that were created in the neutrino-nucleus interaction and whose paths are indicated by the dashed red line ending at black dots. The third panel shows the neutron capture by the gadolinium that is solved in the water. The capture releases a gamma cascade of $8\,\mathrm{MeV}$, that emits photons in different directions indicated by the orange-yellow circles around the black dots. This shows the necessity to have an even PMT coverage on all walls. The last panel shows the further delayed neutron capture of a second neutron.

The combination of a well-reconstructed muon track and the delayed signals of the neutrons allow to measure the neutron multiplicity of neutrino interactions with respect to the kinematics of the muon.

5.4. Status and First Results

ANNIE plans to measure in several phases, which will be discussed in the following, whereby already conducted results are presented. Currently, the experiment is in phase II, but recently there were advancements towards the phase II upgrade.

5.4.1. Phase I - Measurement of the Neutron Background

This section is based on reference [189]. In order to measure the neutron multiplicity of neutrino interactions accurately, the occurrences of background neutrons, that do not originate from neutrino interactions have to be known. This neutron background can be divided into two fractions. The first one is the neutron background, that is constant in time and comes from e.g. the natural radioactivity of the rock and that can be determined by measuring without beam. The second source of neutrons is beam-related, which in turn can be divided into so called sky-shine and dirt neutrons. Sky-shine neutrons are produced in the beam dump and are scattered into the atmosphere. The neutrons interact with the the molecules of the atmosphere and can - after multiple scatterings - reach the ANNIE detector. Dirt neutrons on the other hand originate from neutrino interactions in the rock upstream of the detector.

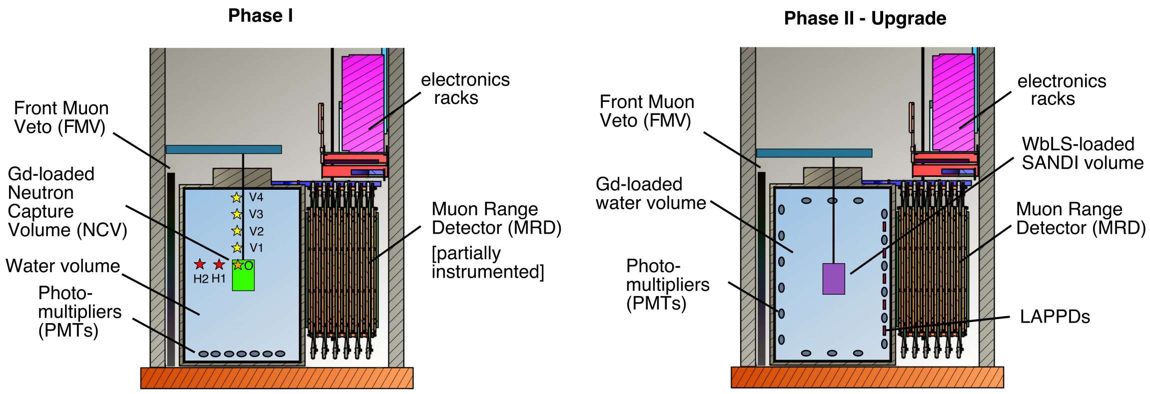

Figure 5.8.: The detector design for phase I (left) and the upgrade of phase II (right) [174].

For phase I, the ANNIE detector design differed from the phase II design, that was discussed above. The phase I design is shown in figure 5.8 on the left side. The tank was filled with 26 tons of ultra-pure deionized water and the bottom is instrumented with 58 PMTs with a size of eight inch. In the water volume the Neutron Capture Volume (NCV) was placed, which was an acrylic cylinder with a radius and height of $50\,\mathrm{cm}$ filled with gadolinium loaded liquid scintillator EJ-335. This vessel was instrumented with two PMTs with three inch in size to directly measure the $8\,\mathrm{MeV}$ gamma cascade from a neutron capture inside of the vessel. The measurement of the beam-related background was conducted in various positions of the NCV that is shown via the yellow and red stars with the original position in orange. In addition, six plastic scintillator paddles instrumented with a PMT were placed on top of the water tank as trigger for cosmic muon events. These paddles together with the bottom PMTs, the FACC and the first two layers of the MRD (the remaining layers of the MRD were not instrumented) are used as a veto in order to discard events from cosmic muons or from muons originating from neutrino interactions in the rock upstream of the detector.

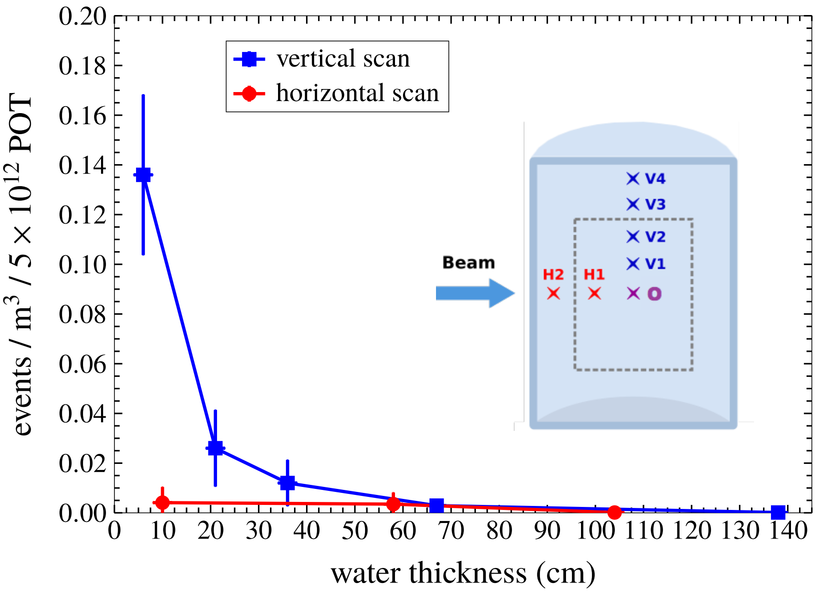

Figure 5.9.: Measurement of the beam-correlated neutron background with respect to the position of the NCV [189]

The results of phase I are shown in figure 5.9, where the number of neutron events per volume and beam spill is given with respect to the water thickness. The water thickness is hereby defined as the distance between the top of the NCV and the top of the tank for the vertical measurement points in blue and as the distance between the front of the NCV and the beam side of the tank for the horizontal points in red. The error bars show systematic and statistical errors. The sketch shows the position of the measurement points, as well as a fiducial volume cut in the dashed line.

It becomes clear, that sky-shine neutrons pose a relevant background, since the number of neutrons drastically decreases to roughly $20\,\%$ of the neutrons for V4 going to V3. Furthermore, the fiducial volume cut would allow V2 to be inside of the volume with 0.012 neutrons per m^3 and spill. After that, the rate basically drops to zero. The horizontal measurement points show only a very slightly decrease, which means that dirt neutrons are a minor background compared to the sky-shine neutrons.

5.4.2. Phase II - Neutron Multiplicity and Cross Section Measurements

While a cross section measurement is yet to be conducted and published, in 2022 a neutron multiplicity measurement was published in reference [174]. One of the results is to be presented here in figure 5.10. Shown is a comparison of the neutron multiplicity from simulation and measurements with respect to the angle (left) and the kinetic energy (right) of the outgoing lepton. The data is shown as solid markers, whereas the simulation is shown as dotted lines. The error bars and the shaded areas indicate the statistical errors. For these plots data of the 2021 beam year of ANNIE are used and for both measurements and simulations the same cuts are applied.

The expectation of the neutron multiplicity with respect to the angle is a flat distribution at around 0.5, whereas the data favours a flat distribution at around 0.25. For the energy plot a similar behaviour can be seen, where except the lowest energies with a value of about 0.37 a flat distribution at around 0.5 is expected and the data shows again a neutron multiplicity of roughly 0.25 except the highest energies, where it raises towards 0.4. With that, this result tells a similar story as the previously presented results from T2K in figure 5.3, in which the models overestimated the measured neutron multiplicity.

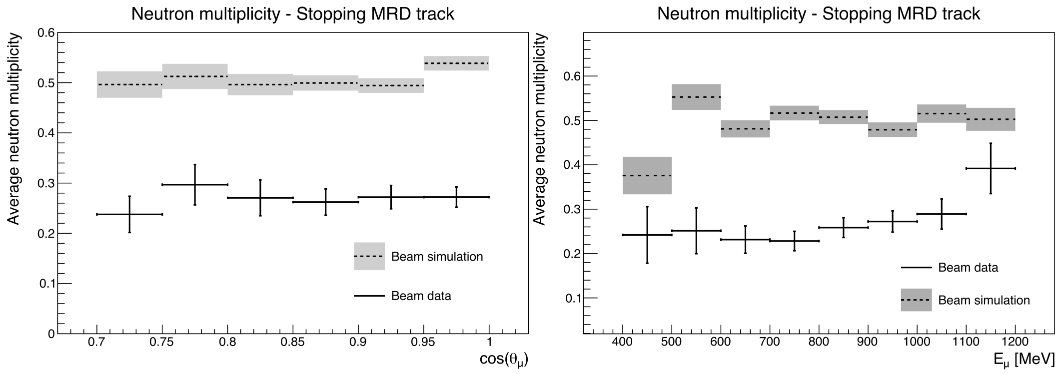

Figure 5.10.: Comparison of the neutron multiplicity measurement of ANNIE with the MC model with respect to the angle (left) and the kinetic energy (right) of the muon [174].

5.4.3. Phase II Upgrade - Water-based Liquid Scintillator (WbLS)

Although the second phase is not completed yet, advancements in the direction of the upgrade of the second phase are already in work. In fact, the WbLS filled volume labelled SANDI, that is shown in the detector scheme in figure 5.8 on the right side has already been deployed in the ANNIE detector for about two months. SANDI is a acrylic, cylindrical volume with a height of about $90\,\mathrm{cm}$ and a radius of approximately $0.45\,\mathrm{cm}$. The data that is taken with SANDI is currently being processed and analysed and future SANDI runs are planned.

6. Simulation of an Idealised Detector

For the event and LUT generation, a Geant4 (GEometry ANd Tracking (GEANT)) simulation of an idealised WbLS detector is developed from scratch. Geant4 [190, 191, 192] is widely used in high energy particle and neutrino physics experiments among others and is a toolkit designed for the simulation of particle interactions with matter. It was developed by Conseil Européen pour la Recherche Nucléaire (CERN) and is written in C++.

The simulation is meant to be ideal in order to have a best-case benchmark of the combination of WbLS and LAPPDs for light separation and the subsequent application of direction reconstruction and PID.

In the following sections, the implemented software is discussed starting with the properties of the detector including the material constants of the used water and the WbLS mixture. Lastly, the use of the simulation for event and LUT generation are covered.

Since this work is meant as a ideal case study, some simplifications and inaccuracies were accepted in the detector simulation. These will be noted and discussed throughout this chapter at the appropriate places.

6.1. Properties

Figure 6.1 shows the detector within the Geant4 display without the tank, so that the structure of the LAPPDs is visible.

A detailed discussion of the detector properties is given in the next sections divided in detector, LAPPDs, active volume and Physics Lists.

6.1.1. Detector

In Geant4 detector parts are defined as volumes with predefined forms, that consist of a material, which can be pulled from a database or defined by the user manually. The Ideal Detector Simulation (IDS) uses three volumes for the general structure. The world volume is a cube with $l_{\mathrm{world}} = 5\,\mathrm{m}$ edges filled with `G4_AIR` from the nist-database[1]. Unlike for most of the other used materials, which will be described in the following, the world material has no added properties like refractive index or absorption length, since no photon interaction outside of the tank is intended.

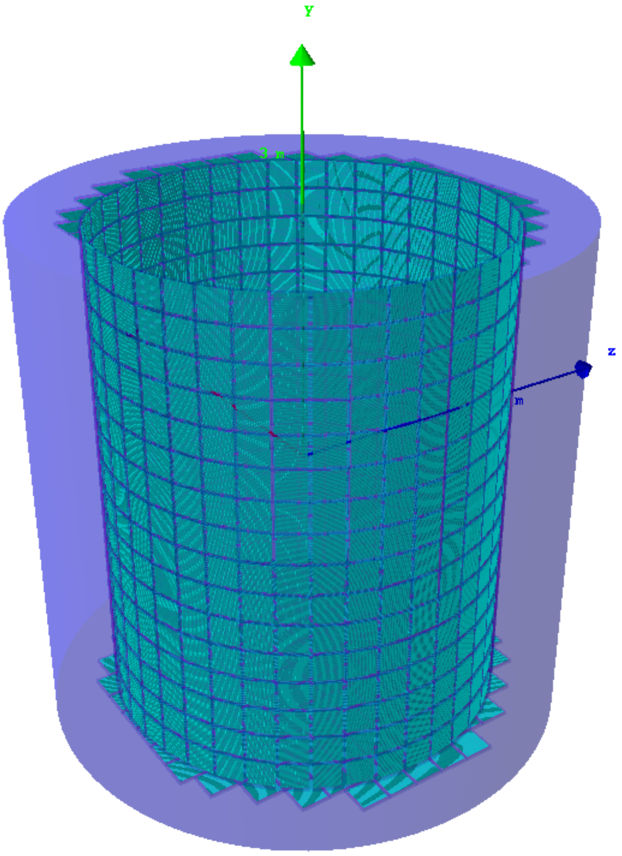

Figure 6.1.: Geant4 display of the IDS without the tank volume. The shown volume is the WbLS and the boxes represent the LAPPDs.

In the center of this cube, the tank cylinder is placed with a radius of $r_{\text{tank}} = 2.185\,\text{m}$ and a height of $h_{\text{tank}} = 4.285\,\text{m}$ consisting of `G4_STAINLESS-STEEL`. For the tank material, the absorption length is specified to be $10^{-9}\,\text{cm}$ for wavelengths between 80 and $800\,\text{nm}$ to ensure that photons are erased when hitting the tank wall. Furthermore, no refractive index is specified for the tank material to avoid reflections, since the probability for a photon to hit a gap between the active areas of the photodetectors, reflect off the tank wall and reach again the inner volume in the event time frame is negligible.

In Geant4 a newly placed smaller volume inside of a bigger volume automatically erases the old material in the respective area. For the active volume, another cylinder is used in the center of the world (and the tank) volume with a radius of $r_{\text{active}} = 1.985\,\text{m}$ and a height of $h_{\text{active}} = 3.885\,\text{m}$ meaning that the tank has a thickness of $d_{\text{tank}} = 0.2\,\text{m}$. This cylinder consists either of pure water or WbLS,

---

[1] In the following, materials in code blocks refer to the nist-database in Geant4 or to existing physics lists.

which were defined via property tables covered in section 6.1.3 and which erases the steel former in place for the active volume area.
The extent of the cylindrical volumes are calculated via a simple algorithm that is developed within this work and that uses the approximate detector size of ANNIE and the size of an LAPPD as input to find a detector size and LAPPD layout with the optimal optical coverage. This algorithm also leads to the number of LAPPDs of 936 and their arrangement of 148 LAPPDs in each of the endcaps and 640 barrel LAPPDs in 16 layers. Additionally, the placement causes LAPPDs in the end caps, which protrude in the x and z direction the barrel LAPPDs to ensure a maximum of optical coverage.
This detector design is unrealistic for various reasons. First of all, there is no support structure, on which the LAPPDs are mounted, including boxes for the readout electronics, since it is assumed that the support structure would be mostly located behind the photodetectors and therefore have only little to no influence on the particle and photon interactions. The tank has neither openings for cables and a liquid system nor a lid for opening. It is again assumed that the influence of these features, although they present engineering problems, is low enough to be neglected. At last, the placement of such a high number of LAPPDs is unreasonable due to exploding costs in reality. For this study, it is the declared goal to do a best-case benchmark so that the number of LAPPDs is justified as well as the aforementioned and still to be discussed simplifications.

6.1.2. LAPPDs

The LAPPD structure is modelled after the ANNIE implementation of the WCSim simulation [193]. It consists in essence of three box volumes. The mother LAPPD volume contains an interior volume at the bottom and a glass volume at the top, that have no overlap. In this work, the glass volume is further segmented, as it will be explained in the following. Furthermore, more details are now given to the dimensions of the volumes.
The LAPPD is defined to be in a mother box volume of length and width of $23.3\,\mathrm{cm}$ and height of about $2.85\,\mathrm{cm}$ with the same material as the chosen active volume meaning that this volume is needed for the orientation and the placement of the remaining volumes, which resemble the structure of one LAPPD. Furthermore, the mother volume ensures a appropriate spacing between the active areas of neighbouring LAPPDs to accommodate for the housing. Inside the mother volume is another box as LAPPD interior with length and width of $20.3\,\mathrm{cm}$ and height of about $1.57\,\mathrm{cm}$ placed with an offset so that the combination of interior and the glass volume is centered. The material of the interior volume is chosen to be a material with a very short absorption length of $10^{-9}\,\mathrm{cm}$ consisting of $70\,\%$ nitrogen and $30\,\%$ oxygen in order to ensure that the LAPPD does not measure photons hitting its back. For the same reason as for the tank material, no other properties

are specified.
On top of the internal volume, a grid of $41 \cdot 41 = 1681$ box volumes with an edge length of $5\,\mathrm{mm}$ and a height of $0.275\,\mathrm{cm}$ are placed directly adjacent to each other, so that an excess length of $1.4\mathrm{cm}$ is left at each side free of the mother volume symbolising the case of an LAPPD. The material of these boxes is specified to be borosilicate glass with 80.6% of silicon dioxide ($\mathrm{SiO_2}$), 13.0% Boron trioxide ($\mathrm{B_2O_3}$), 4.0% Sodium oxide ($\mathrm{Na_2O}$) and 2.4% Aluminium oxide ($\mathrm{Al_2O_3}$). The absorption length is set to be $10^9\,\mathrm{cm}$. Unlike for the tank or the internal box of the LAPPD the simulation of reflections off the glass face of the LAPPDs is necessary, since the possibility for the reflected light to hit another active area of a photodetector is sufficiently high, so that a refractive index table is specified for the glass material. This assumption will be discussed later in section 6.4.

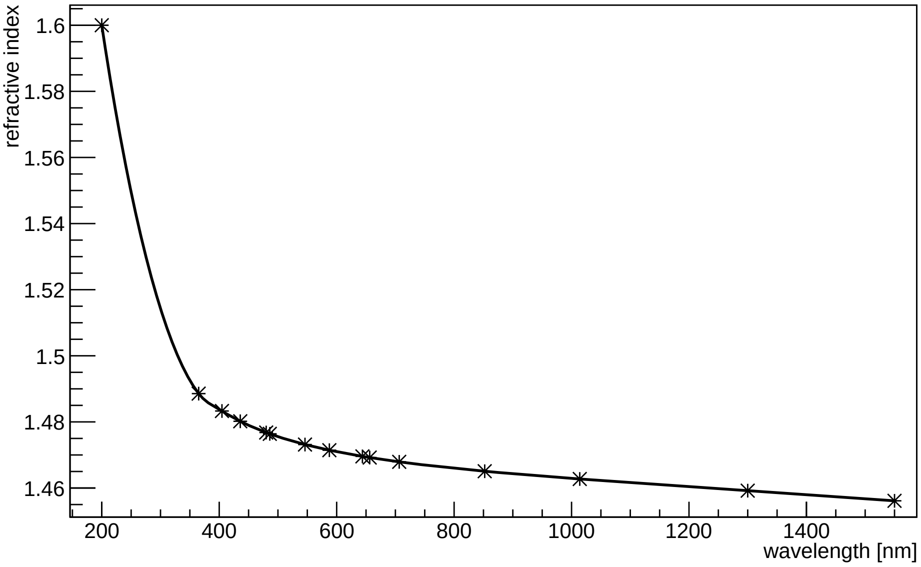

Figure 6.2.: Refractive index of borosilicate glass based on data from [194].

The refractive index for borosilicate glass is displayed in figure 6.2, in which the stars mark the values implemented in the properties table, whereas the line is the standard ROOT trend line for better readability[2]. All values except the one for roughly $200\,\mathrm{nm}$ come from [194], since according to [195] LAPPDs use borosilicate float glass as front and the company “SCHOTT” [196] develops this glass type and also provided the data in reference [194]. Because the provided table from said reference does not cover wavelengths below $365\,\mathrm{nm}$, the refractive index for the wavelength of $199.975\,\mathrm{nm}$ is set to 1.6, which is the value set across all wavelength points in the ANNIE simulation. It is assumed that this approach yields a slightly more realistic reflectivity behaviour than a constant value for all wave-

---

[2] This is the case for all the following property plots.

lengths, whereby the influence of the refractive index of the LAPPD glass plays if at all only a very minor role for this work.

The implementation differs from the ANNIE one in another point, since the ANNIE implementation uses one box volume instead of a lot of smaller ones and then in a later stage adds an electronic simulation on top of that to simulate the behaviour of the LAPPD realistically. For this work, an electronic simulation is not necessary in the best-case context, so that the pixel approach is used to simulate the spatial resolution of the LAPPD. With a pixel size of $5\,\mathrm{mm}$, it is safe to say that the assumed resolution is worse than the one listed in section 3.4.5 for a typical LAPPD. In principle, the pixel size could have been reduced to exactly fit the spatial resolution of a LAPPD but a higher pixel number directly increases the computation time of the TTR, so that the chosen pixel size is a good trade-off of accuracy and reconstruction time. Furthermore, the performance values of the LAPPDs might not be reachable when dealing with high photon numbers, so that slightly worse values for time and spatial resolution are assumed cautiously.

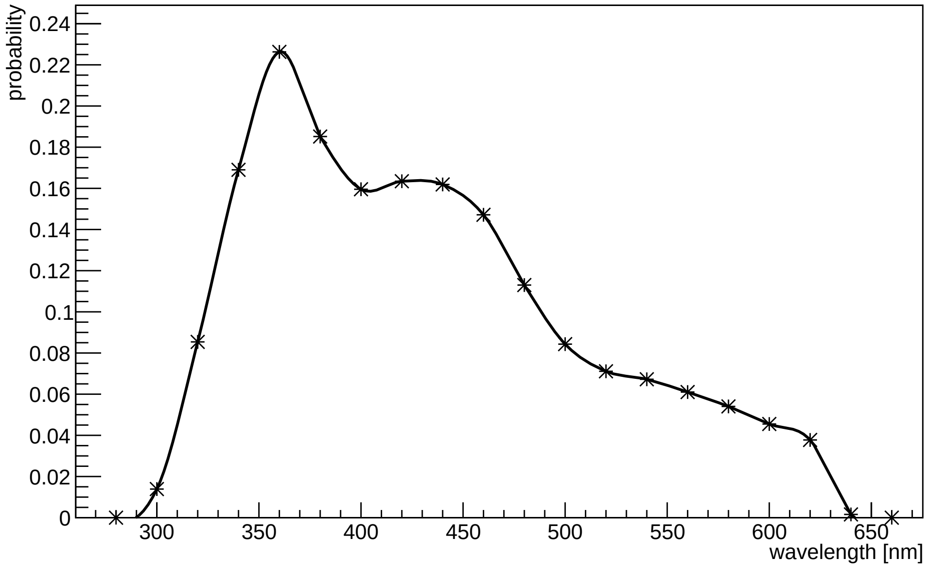

Figure 6.3.: QE of the LAPPDs with respect to the wavelength. The maximum efficiency is reached at $360\,\mathrm{nm}$ with a value of roughly $23\,\%$.

The time resolution or the TTS of the LAPPD is modelled by adding values following a Gaussian distribution with mean of $0\,\mathrm{ns}$ and sigma of $0.1\,\mathrm{ns}$ to the hit times measured by the sensitive detector in form of the LAPPD pixels. All hits after $100\,\mathrm{ns}$ are hereby ignored so that the event window is between 0 and $100\mathrm{ns}$. Furthermore, each hit is registered with a charge of exactly one PE.

The QE of the LAPPDs is also taken from the ANNIE WCSim implementation and is shown in figure 6.3 and, since the CE is set to $100\,\%$ for all angles, is equal to the PDE. Said figure shows the probability for a photon registered at a LAPPD pixel to be counted as a hit. The peak is at $360\,\mathrm{nm}$, which is in good agreement with the simulated scintillation emission wavelength spectrum, which will be shown in section 6.3.

6.1.3. Active Volume

The simulation works either with pure water or WbLS, whereby the focus of this thesis lies on the WbLS case. The possibility to simulate a pure Cherenkov detector is implemented to confirm in addition to reference [197] that the TTR is able to work with Cherenkov events, although it was initally developed to work in scintillation detectors.

The material properties for water are taken from the ANNIE implementation of WCSim [193], whereas the ones for WbLS are taken from the Theia Rat-Pac simulation [198]. Water is modelled as a combination of two elementary hydrogen atoms and one elementary oxygen atom with a density of $1.00\,\frac{\mathrm{g}}{\mathrm{cm}^3}$. WbLS on the other side is modelled as combination of $4.9835\,\%$ LAB, $0.0165\,\%$ PPO and $95\,\%$ water, whereby water is defined as the combination of $11.19\,\%$ hydrogen and $88.81\,\%$ oxygen with a density of $1.00\,\frac{\mathrm{g}}{\mathrm{cm}^3}$, which is also the density of the WbLS. PPO is specified to be $81.42\,\%$ carbon, $5.01\,\%$ hydrogen, $6.33\,\%$ nitrogen and $7.23\,\%$ oxygen with a density of $1.06\,\frac{\mathrm{g}}{\mathrm{cm}^3}$, while LAB consists of five different carbon and hydrogen combinations totalling to a composition with a density of $0.867\,\frac{\mathrm{g}}{\mathrm{cm}^3}$. This means that $5\,\%$ scintillator is solved in $95\,\%$ of water.

The refractive indices of water and WbLS are shown in figure 6.4 in blue and red. The graphs are very similar to each other, which is expected because of the low percentage of scintillator in the WbLS mixture.

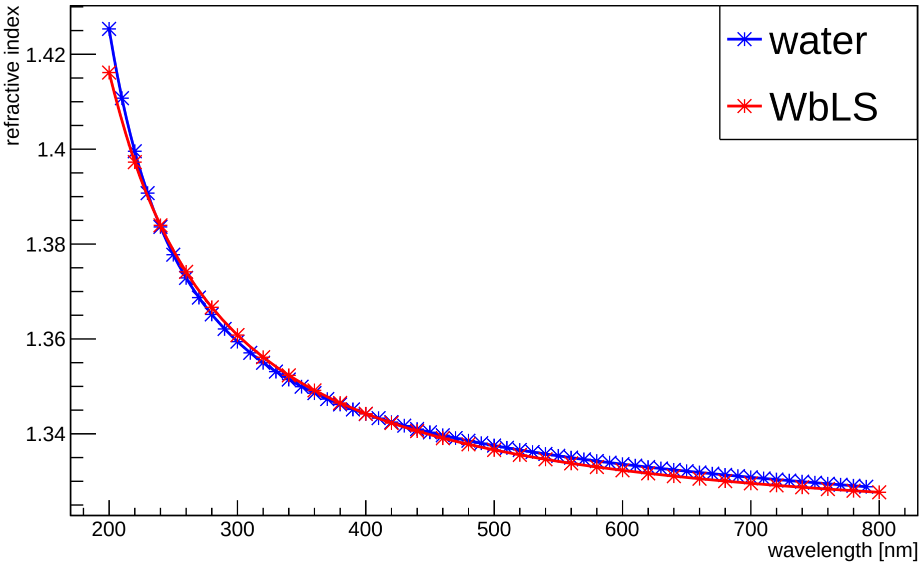

Figure 6.4.: Refractive index of the active media. The blue (red) line and markers refer to water (WbLS). Due to the small proportion of liquid scintillator in the WbLS only small differences are visible.

Figure 6.5 shows in the same colouring the graphs for the absorption length. Here, the distributions differ quite substantially, which can be explained via the wavelength-shifter contained in WbLS.

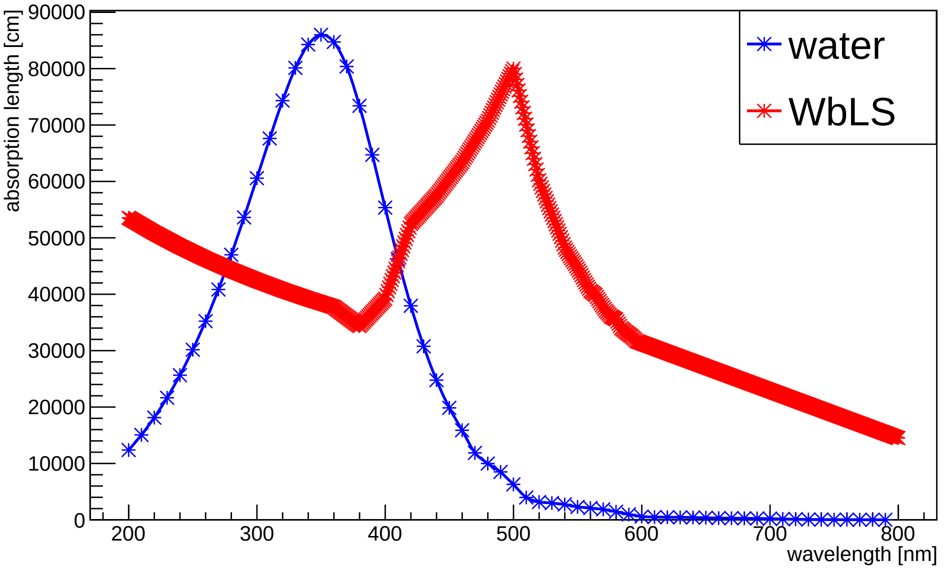

Figure 6.5.: Absorption length of the active media. The blue (red) line and markers refer to water (WbLS). Due to the different definitions of the property tables, the distance of the markers is higher for water than for WbLS.

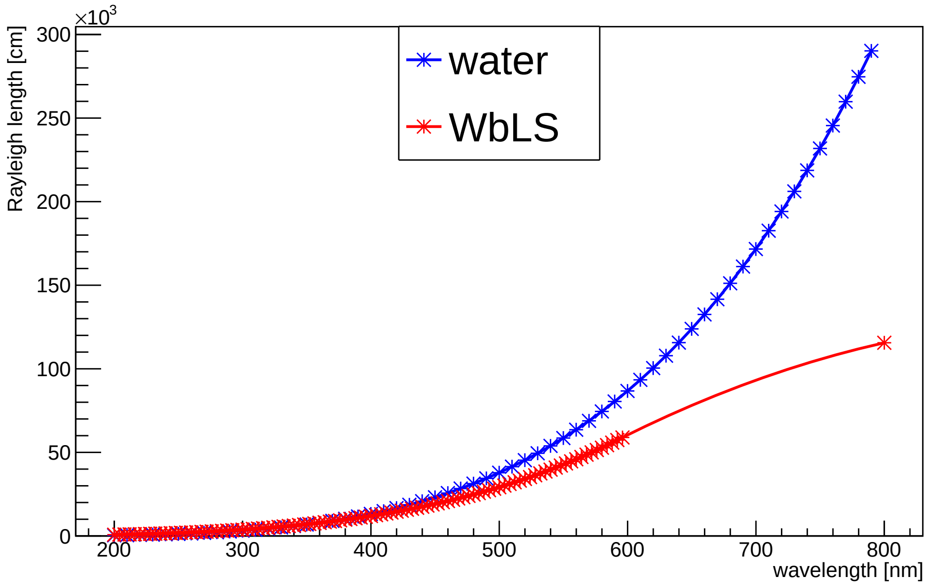

Figure 6.6.: Rayleigh length of the active media. The blue (red) line and markers refer to water (WbLS). Due to the different definitions of the property tables, the distance of the markers is higher for water than for WbLS. The gap in values for WbLS between 600 and $800\,\mathrm{nm}$ is also present in the Theia simulation.

The Rayleigh length is displayed in figure 6.6, again with the same colouring scheme. The graphs are very similar for wavelengths of up to about $450\,\mathrm{nm}$, where the Rayleigh length of water is rising stronger than the one for WbLS, which can be explained by the addition of atoms with a higher atomic number in WbLS. The gap in values for WbLS between 600 and $800\,\mathrm{nm}$ is also present in the Theia simulation.

It is to note that no Mie scattering length is defined for both media assuming that the effect is negligible following the model of the ANNIE and Theia simulation.

Additional to properties that were defined for both media, for WbLS scintillation properties are also added. In figure 6.7 the scintillation emission spectrum in terms of wavelength is shown. This emission spectrum is valid for both of the scintillator components, that are introduced in the following as fast and slow component. The graph illustrates the probability for a photon of a specific wavelength to be emitted after the deposition of energy in the scintillator. It will be described later when discussing figure 6.8.

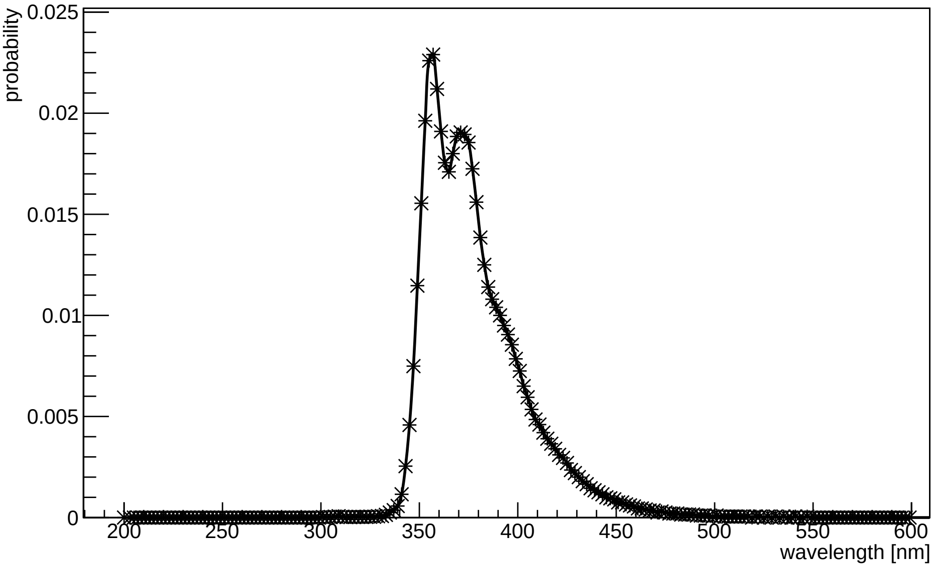

Figure 6.7.: Emission spectrum for the scintillation photons.

The scintillation yield or the number of emitted photons per deposited energy is defined to be $N_{\mathrm{LY}} = 500\,\mathrm{MeV}$ and the so called resolution scale is set to $R_{\mathrm{LY}} = 1.0$. This means according to reference [199], the scintillation yield follows a Gaussian distribution with a mean of

$$\mu_{\mathrm{LY}} = E_{\mathrm{dep}} \cdot N_{\mathrm{LY}} = E_{\mathrm{dep}}[\mathrm{MeV}] \cdot 500/\mathrm{MeV} \tag{6.1}$$

and a sigma of

$$\sigma_{\mathrm{LY}} = R_{\mathrm{LY}} \cdot \sqrt{E_{\mathrm{dep}} \cdot N_{\mathrm{LY}}} = 1.0 \cdot \sqrt{E_{\mathrm{dep}}[\mathrm{MeV}] \cdot 500/\mathrm{MeV}}. \tag{6.2}$$

The scintillator is modelled to consist of two components following equation 4.13, which demands two time constants and two weights. The time constant for the fast and the slow component is $\tau_{\text{fast}} = 3.8\,\text{ns}$ and $\tau_{\text{slow}} = 10.2\,\text{ns}$ with the weights of $\omega_{\text{fast}} = 0.58$ and $\omega_{\text{slow}} = 0.42$, since the yield ratio in Geant4 is defined to be 0.58 meaning that with a probability of $58\,\%$ a scintillation photon is emitted following the fast distribution. At last, Birks constant is set to $0.0121\,\frac{\text{cm}}{\text{MeV}}$, which is derived from the assumption that $\frac{E_{\text{dep}}}{E_{\text{vis}}} = 2$ [200] and the formulas from reference [201] and the data from reference [202].

With these medium properties, the amount of scattered, absorbed and reflected light can be extracted from the simulation. It is found that scattering is in the area of 1.3 to 1.5 percent for Cherenkov and scintillation light respectively. The reflection amounts to $1.3\,\%$ for both light types. The values for reflection and scattering can be explained with the smallness of the detector and the chosen materials. Absorption happens, but no reemission is modelled so that the respective photons are deleted.

6.1.4. Physics Lists

The underlying physics processes that are simulated in Geant4 are defined by the so called Physics Lists. Additional to the option of user-defined lists, Geant4 provides the user with a number of predefined list packages and the option to add individual lists.

The list package used for this simulation is called `FTFP_BERT`, which stands for the usage of the Fritiof model for high energies (above $4\,\text{GeV}$) with the `G4Precompound` model for deexcitation together with the Bertini intranuclear cascade model for the lower energy processes (below $5\,\text{GeV}$) [203, 204]. This choice is motivated by the Physics List used in ANNIE version of WCSim [193], which is `FTFP_BERT_HP`, whereby also a high precision neutron model for energies below $20\,\text{MeV}$ is used, since ANNIE focuses on neutron multiplicity and the capture of neutrons on Gadolinium. Neutrons are of less interest in this thesis so that the addition of the neutron model is omitted. Furthermore, the chosen Physics List is in accordance with the recommended use cases of the Geant4 development team [205].

In addition, the Physics List `G4OpticalPhysics` is loaded for all the optical photon processes, on which this work focuses.

6.2. Simulation Modes

There are two main modes in using the simulation in this work. The first one is for simulating the LUTs that are necessary for running the TTR and the second is for generating the events that can than be analysed by different programs.

6.3. Look-Up Table (LUT)

To reduce the computation time of the TTR, LUTs can be pre-calculated for the propagation time and the probability for the detection of a non-scattered photon, because without LUTs these properties would have to be calculated within the TTR for each hit individually. This will be further explained in section 7.2.3, where also the results are discussed. This section focuses on the technical side of producing the mean propagation time LUT as well as the direct light probability LUT with respect to the distance and angle between the LAPPD pixel and the emission point.
For each light type and medium, the two LUTs have to be generated, whereby the simulation only needs to run once for both tables meaning that three runs are needed. In each run, 10^6 events are generated with a randomly placed so-called photon bomb, which is a General Particle Source emitting photons, following a flat distribution in all three coordinates in order to cover the whole active volume inside of the LAPPD envelope. Each photon bomb consists out of 10^5 photons, which are emitted isotropically and following the wavelength spectra for the chosen light type.
For the Cherenkov emission spectrum in terms of wavelengths, equation (4.17) can be integrated for lambda when neglecting the wavelength dependency of the refractive index. This is a fair assumption because of the small wavelengths intervals in the refractive index tables of $10\,\mathrm{nm}$ for water and $20\,\mathrm{nm}$ for WbLS and in turn small maximum variations of the refractive index of about 0.019 for WbLS and 0.015 for water. Said integration yields

$$\frac{\mathrm{d}N}{\mathrm{d}x} = 2\pi\alpha z^2 \cdot \left(1 - \frac{1}{\beta^2 n^2(\lambda)}\right) \cdot \int\limits_{\lambda_0}^{\lambda_1} \frac{1}{\lambda'^2}\mathrm{d}\lambda'. \tag{6.3}$$

N is the number of emitted photons, x the travel length of the primary particle, α the fine-structure constant, z the charge of the particle, n the refractive index, λ the wavelength and β is the ratio of the group velocity to the speed of light.
Since the relation between refractive index and wavelength is given in a discrete table, for one wavelength on this table the differential number of emitted photons per path length can be calculated via

$$\frac{\mathrm{d}N}{\mathrm{d}x} = 2\pi\alpha z^2 \cdot \left(1 - \frac{1}{\beta^2 n^2(\lambda)}\right) \cdot \int\limits_{\lambda-\Delta\lambda}^{\lambda+\Delta\lambda} \frac{1}{\lambda'^2}\mathrm{d}\lambda', \tag{6.4}$$

in which $\Delta\lambda$ is half the binning interval of the refractive index table i.e. $\Delta\lambda_{\mathrm{water}} = 5\,\mathrm{nm}$ and $\Delta\lambda_{\mathrm{WbLS}} = 10\,\mathrm{nm}$. The probability for the emission of a photon at any of the wavelength for which a refractive index is specified in section 6.1.3 equals to one, so that the probability for the emission of a photon at a given wavelength can be calculated via

$$P(\lambda) = \frac{2\pi\alpha z^2 \cdot \left(1 - \frac{1}{\beta^2 n^2(\lambda)}\right) \cdot \int\limits_{\lambda-\Delta\lambda}^{\lambda+\Delta\lambda} \frac{1}{\lambda'^2} \mathrm{d}\lambda'}{\sum\limits_{i=0}^{n} 2\pi\alpha z^2 \cdot \left(1 - \frac{1}{\beta^2 n^2(\lambda_i)}\right) \cdot \int\limits_{\lambda_i-\Delta\lambda}^{\lambda_i+\Delta\lambda} \frac{1}{\lambda'^2} \mathrm{d}\lambda'} \tag{6.5}$$

$$= \frac{\left(1 - \frac{1}{\beta^2 n^2(\lambda)}\right) \cdot \int\limits_{\lambda-\Delta\lambda}^{\lambda+\Delta\lambda} \frac{1}{\lambda'^2} \mathrm{d}\lambda'}{\sum\limits_{i=0}^{n} \left(1 - \frac{1}{\beta^2 n^2(\lambda_i)}\right) \cdot \int\limits_{\lambda_i-\Delta\lambda}^{\lambda_i+\Delta\lambda} \frac{1}{\lambda'^2} \mathrm{d}\lambda'} \tag{6.6}$$

with n equals to the entries in the refractive index table.

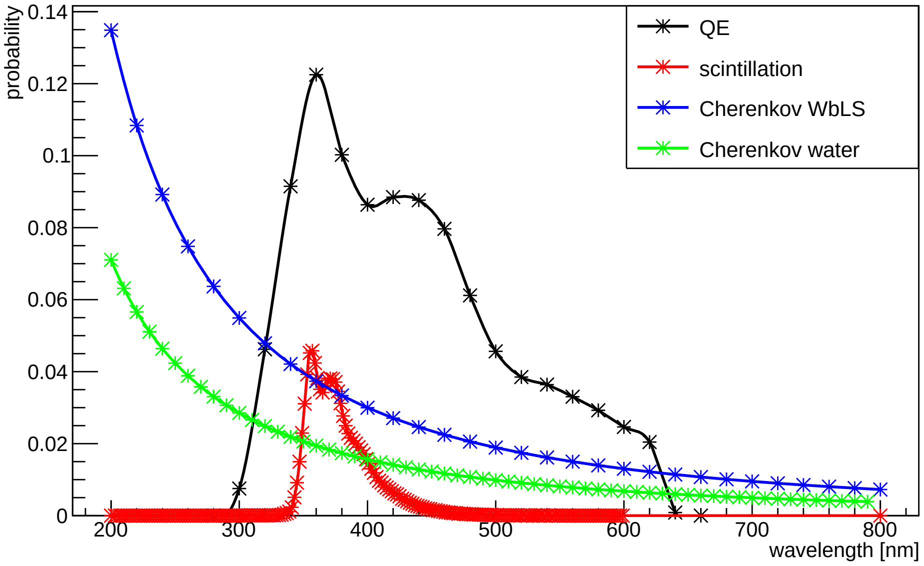

Figure 6.8.: Comparison of the QE (black) of the LAPPDs and the emission spectrum of Cherenkov radiation in water (green) and WbLS (blue) and scintillation light in WbLS (red). The QE spectrum is normalised to one for better comparison and the height difference in emission spectra of Cherenkov and scintillation light originates from the different number of values.

The scintillation emission spectrum with respect to the wavelength is given via a table as it was mentioned before, so that this table has to be normalised to one and can then be used for the simulation of the photon bombs. The used emission spectra for the generation of the LUTs are shown in figure 6.8. The Cherenkov emission spectrum is indicated in blue (green) for WbLS (water), whereas the scintillation emission spectrum is depicted in red. The black markers are again the QE of the LAPPDs, but normalised to one for better comparability and readability. The difference in the distribution heights originates from the difference in number of entries for the different medium property tables. It is clearly visible that the Cherenkov spectrum as well as the scintillation spectrum follows the expected behaviour described in section 4.2. Furthermore, the figure illustrates that the property tables and with that the calculated probabilities for photon emission per wavelength covers the entire sensitive wavelength interval of the LAPPDs with additional values at both ends. This is necessary to neither over- nor underestimate the measured number of photon hits, not only in the LUT but also in the general event generation. It can also be seen that the maximum of emission of scintillation light overlaps with the maximum of sensitivity of the LAPPDs at around $360\,\mathrm{nm}$. The second peak of the scintillation light at around $380\,\mathrm{nm}$ overlaps with a high QE of 0.1 as well.

Additionally, for every photon emitted, a Geantino[3] with the identical direction is also emitted for debugging purposes. This is the result of the reimplementation of several Geant4 classes and is a feature formerly implemented for the calculation of the LUTs, until another solution was found.

For the mean propagation time LUT, one histogram is filled with the hit time and one with the number of hits with respect to the distance and angle between the pixel and the emission point. Then a ROOT macro is used to divide the hit times with the number of photon hits, so that the average hit time can be written into the mean propagation time LUT.

The direct light probability table on the other hand needs additional postprocessing to be accurate. In the simulation only one histogram needs to be filled with a weight of $1/\mathrm{n}_{\mathrm{emitted}} = 1/10^5$ with respect to distance and angle to the pixel for every photon hit. This represents the probability for a direct photon hit for one photon bomb with the caveat that this can lead to an overestimation of the probability in the case that several pixel were hit, whose distance and angle falls into the same histogram bin. Especially for a high number of runs, this issue grows stronger. Therefore, the primary vertices of all photon bombs are written into a table so that in a ROOT macro the estimated number of events per histogram bin can be calculated via the computation of all distances and angles between the emission point and all LAPPD pixels, which is then filled in another histogram. The probability histogram from the simulation can the be divided by the events-per-bin histogram binwise to get the mean direct light probability LUT.

6.4. Event generation

The second simulation mode is used for the generation of the events, which are analysed in this thesis. In the simulation the event information are written into a binary data file, which is then in turn converted via a ROOT macro to the TTR data format. The resulting data is organised in a ROOT file containing the following information:

---

[3] A Geantino is a debug particle, which does behave like a photon without any interaction except with the sensitive detector.

- MC truth:
    - Particle IDs
    - Track IDs
    - Creator processes
    - Particle masses
    - Particle momenta
    - Particle energies
    - Particle end momenta
    - Particle end energies
    - Particle direction
    - Particle vertex
    - Particle endtex
    - Particle parent type
    - Particle start type
    - Particle stop type
- Hits:
    - Hit tube IDs
    - Hit times
    - Hit charges
    - Light flags

Except the light flags, which denotes whether a photon hit was from a Cherenkov or a scintillation photon, this is the regular TTR input data format. These ROOT files are then used as input for the TTR as well as for other analysing programs. Additionally, the positions of the LAPPD pixels are written into a text file together with their individual tube ID in the simulation, so that the geometry of the hits can be reconstructed with the combination of the event ROOT file and the LAPPD geometry text file. The splitting of the hit information into a geometry and an event file is excepted by the TTR, since the detector geometry does not change in between events so that the geometry file can be written and loaded only once reducing computation time and memory consumption.

7. Topological Track Reconstruction (TTR)

The idea of the Topological Track Reconstruction (TTR) was developed by Dr. Björn Wonsak and implemented in a C++ program by Dr. Sebastian Lorenz, in which the reconstruction was applied to LENA. Initially, the TTR was meant to reconstruct the energy loss per path length in unsegmented liquid scintillator detectors in order to improve veto cuts for muon induced backgrounds. This includes also the reconstruction of the particle track.

Nowadays, the reconstruction is adapted to several detectors and includes various new features e.g. the particle discrimination in JUNO by Dr. Henning Rebber in reference [206].

This chapter introduces the working principle in section 7.1[1], followed by a description of the steps necessary for the reconstruction to work with the simulation data generated by the Geant4 based program discussed in chapter 6. If not stated otherwise, this chapter is based on reference [2].

7.1. Working Principle

Liquid scintillator detectors generate data in the form of hits, which is the combination of the time the photon arrives at the photodetector and the position of this detector [2]. The TTR uses these hits in order to reconstruct the $\mathrm{d}E/\mathrm{d}x$ of the particle that transverses the detector. Since the number of emitted photons is proportional to the energy loss of the particle, the number of emitted photons is calculated per volume cell.

7.1.1. Basic Idea

The TTR works without any hypothesis of the particle type, energy or direction. Instead, four core assumptions are set to the event:

1. A reference point in time and space for the particle path is known.

---

[1] In this introduction, the TTR is explained for liquid scintillator detectors. The alteration to WC is discussed in section 7.2.

[2] In the case of a photodetector with a spatial resolution like an LAPPD or a SiPM the hit point on the photodetector added to the position is the second component of the hit information.

2. The particle travels in a straight line.
3. The velocity of the particle is equal to the speed of light in vacuum.
4. The optical photons travel in a straight line to the photodetectors without scattering or reflection.

The reference point can be given by an external vertex reconstruction or in the case of background muons via the response of veto detectors. With these assumptions, the basic idea of the TTR for **one** emitted photon and **one** photodetector can be formulated, which is depicted in figure 7.1.

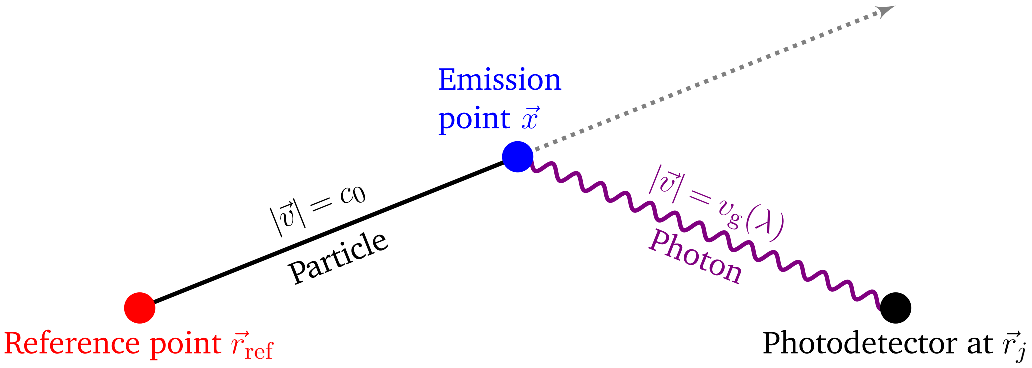

Figure 7.1.: Visualisation of the basic principle of the TTR based on reference [2]. The particle starts at the reference point (red dot), travels with the speed of light on a straight line (black line). At one point, a photon is emitted (blue dot), which travels unscattered (violet curly line) to the photodetector (black dot).

The particle travels in a straight line with the speed of light indicated via the black line. A reference point in time t_{ref} and space $\vec{r}_{\text{ref}}$ is given on the particle path shown as a red dot. In this visualisation, the reference point is at the beginning of the particle track i.e. the vertex of the event. Generally, the reference point can be at any position on the particle track before or after emitting a photon. At the blue dot or the emission point $\vec{x}$, a photon is emitted due to the scintillation effect, whereas the particle travels further along the gray line. The photon, indicated via the violet, curly line, travels unscattered on a straight path with the group velocity depending on the wavelength of the photon $v_g(\lambda)$ to the photodetector, shown as a black dot, and arrives at the simplified hit time $\hat{t}_j(x)$ on the jth photodetector located at the position $\vec{r}_j$.
This basic idea can be expressed via the following equation:

$$\hat{t}_j(\vec{x}) = t_{\text{ref}} \pm \underbrace{\frac{|\vec{x} - \vec{r}_{\text{ref}}|}{c_0}}_{t_{\text{particle}}} + \underbrace{\frac{|\vec{x} - \vec{r}_j|}{v_g(\lambda)}}_{t_{\text{photon}}} + t_s. \tag{7.1}$$

The hit time is the sum of the reference time t_{ref}, the time the particle needs to arrive at the emission point t_{particle} and the travel time of the photon to the detector

t_{photon}. Furthermore, a variable in form of t_s is added to incorporate the timing profile of the scintillation light and the time uncertainty of the photodetector. The $\pm$-sign in front of the particle time takes care of the fact, that the reference point can be reached by the particle before $(+)$ or after $(-)$ emitting the photon.

Inverting equation (7.1) and solving for $\vec{x}$ results in a set of possible emission points for one hit time. These emission points lie on the surface of a three-dimensional volume called an isochrone. Examples for isochrones are depicted in figure 7.2.

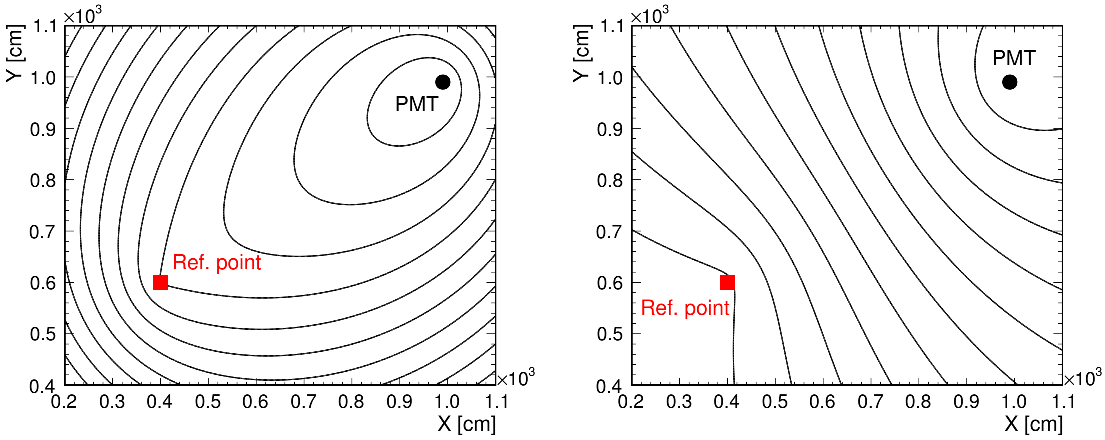

(a)

(b)

Figure 7.2.: Isochrones for different hit times with fixed PMT position and reference point taken from reference [2]. (a) respectively (b) is the result for reaching the reference point before respectively after the emission point.

The black lines each correspond to an isochrone and therefore for an individual hit time t_j at the photodetector. The photosensor is shown as a black dot labelled PMT and the red dot indicates the reference point. In figure 7.2 (a) respectively (b) the isochrones are shown for the case that the particle reaches the reference point before respectively after emitting the photon. In both cases, the isochrones are rotationally symmetric to the axis formed by the black and the red dot. For this visualisation, the time correction for scintillation profile and the time uncertainty of the photodetector is set to zero. Furthermore, a constant group velocity via

$$v_g = \frac{c_0}{n} \tag{7.2}$$

with the refractive index of $n = 1.484$ is used.

In order to go to a more realistic description, the Probability Density Function (PDF) $\Phi_{j,k}(\vec{x})$ has to be introduced, which corresponds to the probability that the kth photon on the jth photodetector was emitted at position $\vec{x}$. In contrast to the depiction in equation (7.1), t_s and t_{photon} are no fixed values but the PDFs $\Phi_{t_s}(t)$ and $\Phi_{t_{\text{photon}}}(t;\vec{x},\vec{r_j})$. $\Phi_{t_s}(t)$ includes the timing profile of the scintillation light and the time uncertainty of the photodetector, whereas $\Phi_{t_\text{photon}}(t;\vec{x},\vec{r_j})$ incorporates all possible photon flight paths, since the distance of emission point to photodetector differs depending on the exact hit coordinate on the surface of the photodetector. Furthermore, $\Phi_{t_\text{photon}}(t;\vec{x},\vec{r_j})$ also describes all possible emission wavelengths of the photon, which is directly related to the group velocity and in turn to the flight time. The relation between the aforementioned PDFs is given via

$$\Phi_{j,k}(\vec{x}) = w_{j,k}\varepsilon_j(\vec{x})\int\limits_0^\infty \Phi_{t_s}(\Delta t)\Phi_{t_\text{photon}}(t';\vec{x},\vec{r_j})\mathrm{d}t' \tag{7.3}$$

with

$$\Delta t = t_{j,k} - \hat{t}_j(\vec{x};t_\text{photon} = t', t_s = 0). \tag{7.4}$$

Equation (7.4) shows that $\Phi_{t_s}(\Delta t)$ depends on the difference of the measured hit time $t_{j,k}$ and the expected hit time $\hat{t}_j(\vec{x};t_\text{photon} = t', t_s = 0)$ and produces the probability that this difference can be explained by the scintillation time profile and the photodetector time uncertainty. $\Phi_{t_s}(\Delta t)$ is given via the convolution of the exponential scintillation decay function and a Gaussian representing the TTS of the photodetector. This will be discussed in more detail in section 7.2. In equation (7.3) $\varepsilon_j(\vec{x})$ is introduced, which is called spatial detection efficiency and represents three effects:

1. The attenuation due to reabsorbing or scattering of photons in the scintillator.
2. The angular acceptance of the photodetectors.
3. The probability that the isotropic emitted light hits the photosensitive surface of a photodetector, in following also called hit probability.
4. The PDE of the photodetectors.

$w_{j,k}$ denotes the weighting factor

$$w_{j,k} = \left(\int\limits_V \varepsilon_j(\vec{x})\int\limits_0^\infty \Phi_{t_s}(\Delta t)\Phi_{t_\text{photon}}(t';\vec{x},\vec{r_j})\mathrm{d}t'\mathrm{d}V\right)^{-1}, \tag{7.5}$$

which is needed to satisfy the normalisation condition

$$\int\limits_V \Phi_{j,k}(\vec{x})\mathrm{d}V \overset{!}{=} 1 \tag{7.6}$$

that the photon was emitted inside the detector volume V.

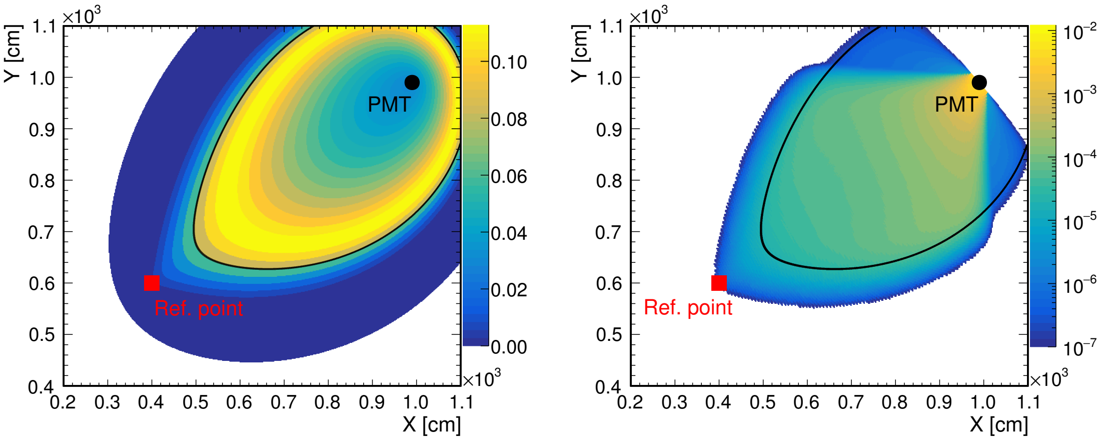

(a) (b)

Figure 7.3.: Unnormalised reconstruction result for one photon hit taken from [2]. (a) shows the result with the scintillation timing profile. (b) includes detector effects.

Going to PDFs from fixed values can be also be seen comparing figure 7.2 (a) to figure 7.3 (a). The latter one shows the unnormalised reconstruction result for one PMT and one photon without the detector effects ($\varepsilon_j(\vec{x}) = 1$) using equation (7.3). In contrast to figure 7.2 (a), the left side of figure 7.3 shows only one isochrone depicted as the black line showing again the exact solution of equation (7.1), whereas the red dot depicts the reference point and the black dot shows the photodetector. The color code represents the probability density function $\Phi_{j,k}(\vec{x})$, which means that in the yellow areas the probability for the photon origin is the highest. Because of the timing profile of the scintillation light the hit time is expected to be delayed, which leads to smearing the isochrone towards the PMT. The width of the smearing is additionally influenced by the time resolution of the photodetector. If the aforementioned detector effects are included and $\varepsilon_j(\vec{x}) \neq 1$, the right side of figure 7.3 is produced. Due to the attenuation and the hit probability the highest probability is now directly in front of the PMT and the angular acceptance of the photodetector is clearly visible.

In conclusion, a single photon results in an ambiguous event topology, in which the highest probability is directly in front of the photodetector, although the photon was emitted at another position. A particle traversing the detector volume produces tens of thousand photon hits though, which are correlated due to the particle path. This gives the possibility to superimpose the PDFs of every hit on every photodetector leading to low probabilities in front of the photodetectors, since only the photons on the corresponding photodetector yield high values in that area; all the hits on all other photodetectors produce low probabilities. High numbers of emitted photons in an area resulting in a high probability, since many photodetectors measure hits fitting to the emission point and a high number of low probabilities is added up. This superimposition can be expressed via

$$\Gamma_{\text{det}}(\vec{x}) = \sum_{j} \Gamma_{\text{det},j}(\vec{x}) = \sum_{j,k} \Phi_{j,k}(\vec{x}), \tag{7.7}$$

in which $\Gamma_{\text{det}}(\vec{x})$ is the spatial density distribution of all detected photons. This distribution, although able to describe the event topology roughly, is not able to correctly describe the differential energy loss per path length, since this variable is directly linked to the number of emitted photons, that is not equal to the number of detected photons. Due to the detector effects described by $\varepsilon_j(\vec{x})$, the number of detected photons underestimates the number of emitted photons drastically. In order to fight this, the global detection efficiency $\varepsilon(\vec{x})$ has to be calculated and can then be used to scale the spatial density distribution of detected photons via

$$\Gamma_{\text{em}}(\vec{x}) = \frac{\Gamma_{\text{det}}(\vec{x})}{\varepsilon(\vec{x})}. \tag{7.8}$$

With the spatial density distribution of emitted photons $\Gamma_{\text{em}}(\vec{x})$, the event topology can be characterised and the $\mathrm{d}E/\mathrm{d}x$ can be calculated.

It is to note, that the reconstruction can also be run as raw reconstruction in contrast to the detected and emitted light algorithm explained above. In the raw reconstruction, the number of detected photons is calculated based only on the timing of the hits and the angular acceptance of the photodetectors. This is a useful algorithm in case that the emitted light algorithm does not find a start topology at first due to the higher survival and detection probabilities for smaller distances to the photodetectors and is used in the light separation algorithm, that will be discussed in the next chapter.

7.1.2. Iterative Process

The superposition of the single photon PDFs, although assuming that the photons are part of the same event topology, does not use the correlation of the hits. This information can be used by introducing an iterative process, in which ideally the reconstruction result of all photodetectors but the $j\text{th}$ is used to reweigh the hit information of the $j\text{th}$ photodetector, since otherwise self-enhancing effects are introduced. Realistically, this is in terms of computation time and memory not possible, so that two different approaches are implemented.

1. The photodetectors are divided into two groups, one with even ID and one with odd ID numbers. The iterative process uses then these groups alternately to avoid using the probability mask of one group as starting point for the reconstruction of the same group. In the last iterations it is still useful to reconstruct with all photodetectors to use all available information,

since the usage of these information is more important than the small self-enhancement effects.

2. The photodetectors are randomly chosen for each iteration, which does not entirely prevent self-enhancement, but decreases the effect to a reasonable level.

A probability mask $M(\vec{x})$ is introduced, which can be $\Gamma_{\mathrm{det}}(\vec{x})$, $\Gamma_{\mathrm{em}}(\vec{x})$ or the result of the raw reconstruction. Furthermore, the probability mask can also be given via other PDFs, as long as they contain information of the event topology e.g. results of other reconstruction algorithms. In this thesis, only prior results of the TTR is used as mask.
The probability mask again has to satisfy

$$\int\limits_V M(\vec{x})\mathrm{d}V \overset{!}{=} 1, \tag{7.9}$$

so that the event topology is indeed inside of the detector volume. It can be applied to the PDF via

$$\Phi_{j,k}(\vec{x}) = w_{j,k} M(x)\varepsilon_j(\vec{x}) \int\limits_0^\infty \Phi_{t_s}(\Delta t)\Phi_{t_{\mathrm{photon}}}(t';\vec{x},\vec{r_j})\mathrm{d}t' \tag{7.10}$$

with the normalisation weight

$$w_{j,k} = \left(\int\limits_V M(x)\varepsilon_j(\vec{x}) \int\limits_0^\infty \Phi_{t_s}(\Delta t)\Phi_{t_{\mathrm{photon}}}(t';\vec{x},\vec{r_j})\mathrm{d}t'\mathrm{d}V \right)^{-1}. \tag{7.11}$$

In the $0\mathrm{th}$ iteration, the TTR runs without a probability mask in order to create the first probability mask for the $1\mathrm{th}$ iteration. The reconstruction result of the prior iteration is then used as probability mask for the following iteration. This can be repeated multiple times, whereas finding the number of iterations with the best result is still an issue. Furthermore, areas with a spatial number density below a threshold can be cut in between the iteration in order to reduce computation time. This is especially important, when the refinement is used to get a finer reconstruction result in the later iterations.
This iterative process is illustrated by figure 7.4 showing reconstruction results for a muon with a kinetic energy of $3\,\mathrm{GeV}$ starting at $(0, 1000, 0)\,\mathrm{cm}$ and travelling in direction of $(1, -1, 0)$ in the LENA detector. The top pictures represent the $0\mathrm{th}$ iteration, the middle ones the $8\mathrm{th}$ iteration and the bottom ones the $21\mathrm{th}$ iteration. In all pictures, the red line indicates the primary particle path of the muon, whereas the black lines show secondary particles. The color code represents the spatial number density of emitted photons projected along the z-axis[3] (left) and

---

[3] This is also the height of the cylindrical detector.

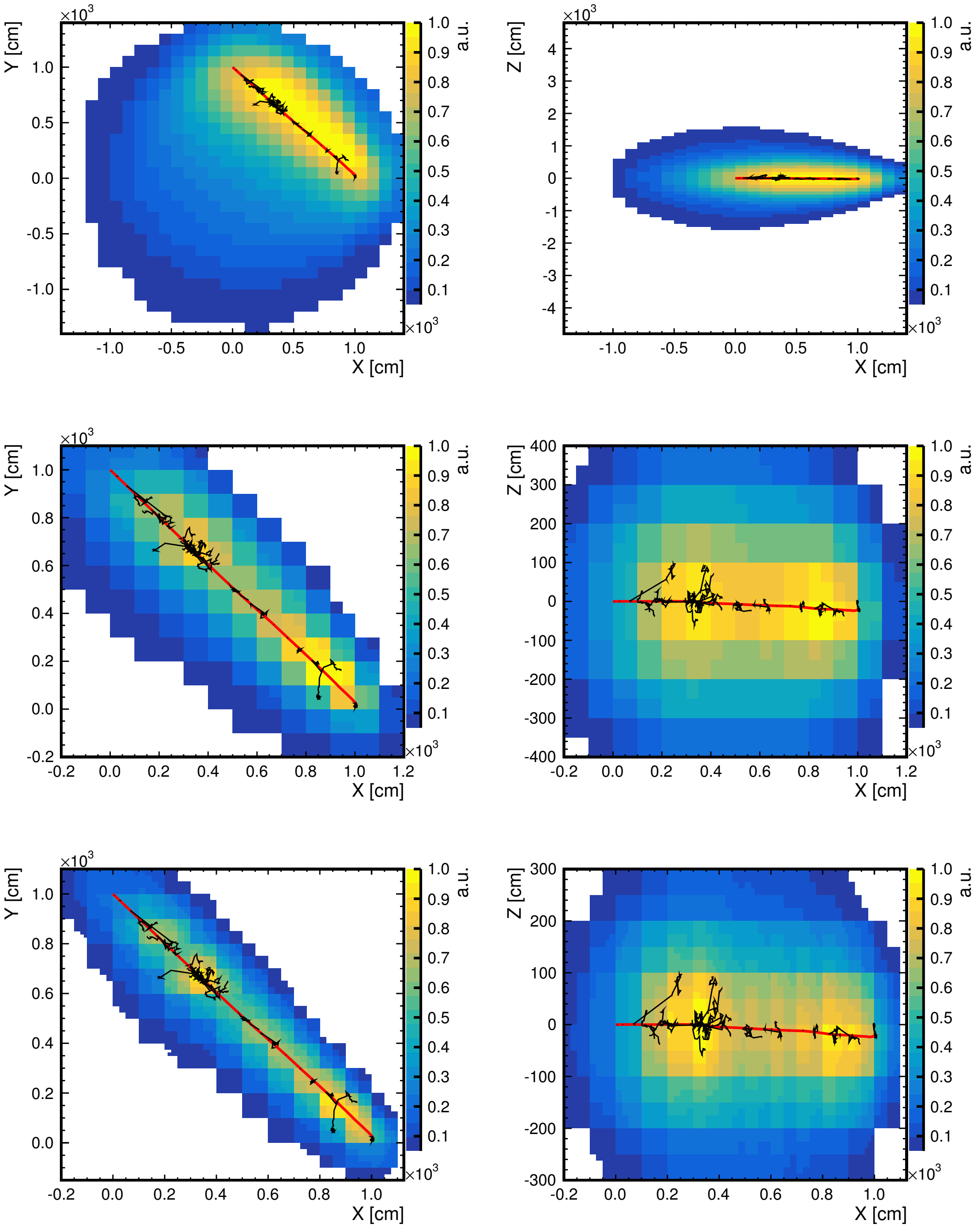

Figure 7.4.: Reconstruction results for a $3\,\mathrm{GeV}$ muon in LENA. The left (right) side shows the projection along the z-axis (y-axis). The shown iterations are 0 (top), 8 (middle) and 21 (bottom). The red line represents the primary particle path and the black lines correspond to the secondary particles. The color code shows the spatial number density of emitted photons. Taken from reference [2].

y-axis (right) in arbitrary units but normalised in a way that the highest entry is 1. The result for the $0\mathrm{th}$ iteration shows that the TTR is able to find the track. Going to iteration 8, the binning is getting finer and the reconstruction focuses on an area of interest, cutting everything below a threshold. Here, the color code shows that the areas with the highest activity of secondary particles are highlighted by the reconstruction. This effect is enhanced in the $21\mathrm{th}$ iteration, where the binning is even finer and the highest number densities are clearly matching the secondary particles and therefore the $\mathrm{d}E/\mathrm{d}x$.

7.2. Adaption Work

The TTR was developed for liquid scintillator detectors, in which good results were achieved. This thesis works with a simulated WbLS detector. As a first step, the TTR has to be adjusted to work with WC detectors as a proof of principle that the reconstruction can work with Cherenkov light. In the second step, modifications for reconstructing in WbLS detectors have to be implemented. Since it is necessary for understanding these modifications, this section starts with an explanation of some implementation details and the configuration parameters of the reconstruction, which is followed by a description of the changes for WC detectors. The focus of this section lies on the discussion of the modifications for WbLS detectors, that is concluding this section.

7.2.1. Implementation and Configurations

Ideally, the TTR would calculate the spatial number density of emitted photons for every point in the detector volume. In reality, the volume has to be segmented in smaller compartments in order to have a finite computing time and memory consumption. In the TTR, this problem is solved with the introduction of cells in a mesh. A cell is a cube defined via its position, its content corresponding to the spatial number density and its edge length. The size of the cells can be decreased in between the iterations in order to have a more detailed result in later iterations. The filling of the cell content happens within a loop over all cells, which in turn happens within a loop over all photodetectors applicable for the current iteration. In order to calculate the content, the so called signal function is evaluated depending on the cell position. For each photodetector a signal function is created using all hits detected by said detector. The signal function convolutes the exponential decay function of the scintillation light and the Gaussian distribution of the TTS of the photodetectors and is therefore the implementation of $\Phi_{t_s}(t)$.

In order to evaluate the signal function and to calculate the cell content added for the considered photodetector, an expected hit time has to be calculated. This expected time is the sum of the reference time, the time the particle would need to travel in a straight line from the reference point to the cell coordinate and the time the photon would travel from cell coordinate to the photodetector. Since the photon travel time is a statistical distribution depending on all possible flight paths, the wavelength and absorption and reemission, it is very time consuming to calculate this property for each cell and photodetector position. At this point, a

time Look-Up Table (LUT) is of use, which can be calculated or simulated outside of the reconstruction incorporating the aforementioned effects. In the reconstruction loop the corresponding time value depending of distance and angle between photodetector and cell can be called from the LUT to drastically decrease computation time at this point.
A second LUT is used within the reconstruction algorithm to describe the effects of $\varepsilon_j(\vec{x})$. The value of this LUT weights the added cell content of the photodetector incorporating the probability that an unscattered photon hits the photodetector.
The signal function as well as the LUTs will be discussed in more detail in section 7.2.3.

7.2.2. Water-Cherenkov (WC)

Since the TTR is implemented as a modular program, the adjustment to other detectors is possible without altering most of the code. Only the code depending the detector specifications have to be changed like the position of the photodetectors, the shape and size of the detector and the optical properties of the detector medium. Furthermore, LUTs have to be created for the new detector. To go from liquid scintillator detectors to a WC detectors, changing the signal function is the essential, additional step. The application of the TTR to ANNIE was done by Felix Benckwitz in his master thesis in reference [197]. His work is the fundament, the adjustments to the TTR in the next section and later chapters are build upon.

7.2.3. Water-based Liquid Scintillator (WbLS)

Starting with the aforementioned ANNIE-TTR-version, some changes are necessary to work with the ideal WbLS detector introduced in chapter 6. First of all, the detector specifications in the configuration file have to be changed. Since the ideal detector is cylindrical as well as ANNIE but with a different size, the values for radius r and height h of the fiducial target volume have to be modified instead of specifying another detector geometry. The chosen values are

$$r = 1.4\,\mathrm{m} \text{ and } h = 3.4\,\mathrm{m}, \tag{7.12}$$

which is an understatement of the simulated target volume discovered after producing the results of this thesis. The TTR is still able to work with events that occur outside of the specified range, as long as the position of the photosensors are specified correctly. This is confirmed by the results in the next chapters.
The position and the orientation of all LAPPD pixels are given to the TTR in a geometry file, that does not change in between events, when multiple events are reconstructed at once. For the light separation algorithm, each event gets its own geometry file, which will be explained in section 8.2. The geometry file includes a

list of photosensor ID, position, direction and type so that multiple different photodetectors can be specified with different characteristics. For the adjustment to the IDS, only one type in the form of a LAPPD pixel is needed. The half-length of the LAPPD pixels l_{LAPPD} and the TTS $\sigma_{\text{TTS}_{\text{LAPPD}}}$ are set to

$$l_{\text{LAPPD}} = 0.25\,\text{cm and } \sigma_{\text{TTS}_{\text{LAPPD}}} = 0.1\,\text{ns}. \tag{7.13}$$

Additionally, the decay constants τ_{fast}, τ_{slow} and their weights ω_{fast}, ω_{slow} have to be specified. For example, the values for $5\,\%$ LAB in water are

$$\tau_{\text{fast}} = 3.8\,\text{ns},\ \tau_{\text{slow}} = 10.2\,\text{ns and } \omega_{\text{fast}} = 0.58,\ \omega_{\text{slow}} = 0.42. \tag{7.14}$$

In order to use Cherenkov as well as scintillation light, the reconstruction is split up in a way, that in each iteration two reconstruction processes are running individually, one for scintillation and one for Cherenkov light. In principle, the splitting is not necessary and two different TTRs could have been used as well. This introduced two problems. The first one is that compiling and running two programs is more time consuming and the second and more important one is that there is no possibility to have the results and probability masks interact with each other in between the iterations, which is foreseen for the future.

In this work, the Cherenkov and scintillation part does not influence each other and, for simplicity, the parts are called Cherenkov and scintillation reconstruction in this thesis. The Cherenkov reconstruction treats all given hits as Cherenkov light, whereas the scintillation reconstruction assumes all given hits to be scintillation light. In the implementation, the difference is given by two factors. Firstly, the LUTs are different for the light types and secondly, the signal function differs.

LUTs

Four LUTs have to be created in order for the splitted reconstruction to work properly. For scintillation as well as Cherenkov light a mean propagation time and a direct light probability LUT has to be generated. In section 6.3, the simulation of these LUTs is explained in detail.

In figure 7.5 the mean propagation time LUT for Cherenkov light in (a) and scintillation light in (b) is displayed. The x-axis denotes the distance of the emission point of the photons to the LAPPD pixel, whereas the y-axis shows the angle between the normal vector of the pixel and the vector pointing towards the pixel from the emission point. It is important to note that the normal vectors of the pixels are pointing outwards of the detector volume, since this is the definition used in the TTR. The z-axis shows a color code corresponding to the propagation time.

The two maxima at large distances at roughly 0.7 and 0.9 can be explained by the following: The maximum distance is reached, when the emission point is in one corner of the tank, while the hit is registered by a LAPPD pixel at the opposing corner e.g. emission at $(-r, 0, -h/2)$ and detection at $(+r, 0, +h/2)$. In the corner of detection, the photon can be seen by a LAPPD pixel in the lid or by a pixel in the barrel resulting in two different normal vectors for the angle calculation. Detection in the barrel leads to the bigger angle of 0.9 and detection in the lid gives 0.7, since the height of the detector is larger than its radius. Because the angle between the two normal vectors is $\pi/2$, the sum of the angles at the maximum length also approximates this value.

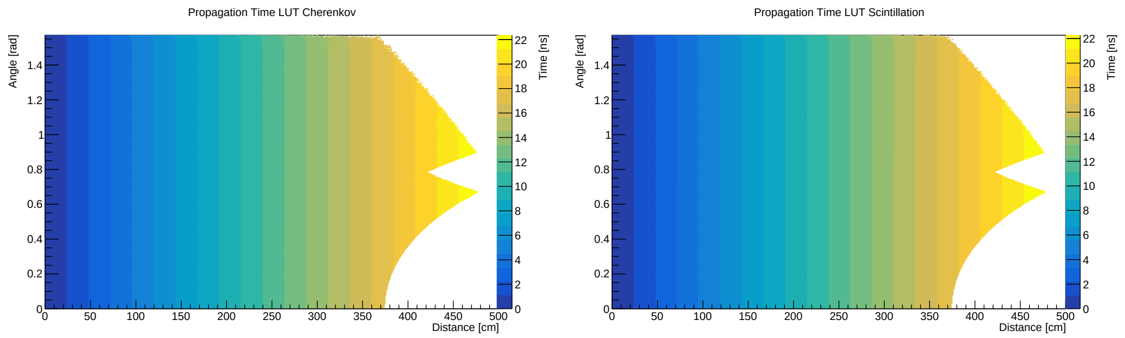

(a) (b)

Figure 7.5.: Mean propagation time LUTs for (a) Cherenkov and (b) scintillation light.

Comparing the mean propagation time tables for Cherenkov and scintillation light shows no obvious difference. In both tables, the propagation time increases with the distance to the photodetector in the same manner and no influence of the angle is visible, because the angular acceptance of the LAPPD is modelled to be $100\,\%$ for all angles. These tables can be easily approximated by averaging the photon group velocities with respect to the refractive indices for the different photon wavelengths and then divide the mean velocity with the distance whilst taking the PDE of the LAPPDs into account.

This approximation compared to the mean values of the LUTs per distance bin can be seen in figure 7.6. The blue (red) line corresponds to the Cherenkov (scintillation) LUT values, whereas the black (green) line shows the approximation for Cherenkov (scintillation) light. The difference between the individual lines in the LUT set is barely visible, which is also true for the approximation set. This is expected, since all wavelengths are averaged in this plot and the difference of group velocities due to dispersion[4] is eliminated by applying the PDE. The difference in velocity from the LUT and the approximation can be explained by uncertainties

---

[4] In general, the emission wavelength spectrum for Cherenkov and scintillation photons differs as shown in figure 4.4, so that the Cherenkov photons are faster than the scintillation photons. Applying the PDE leads to a very similar average wavelength for the different light types.

and interpolations in the calculation leading to a slightly higher velocity for the approximation. Nevertheless, the approximation can confirm that there are no significant errors in the time LUT calculation. The cutoff of the simulated LUTs at around $480\,\mathrm{cm}$ is due to the detector dimensions.

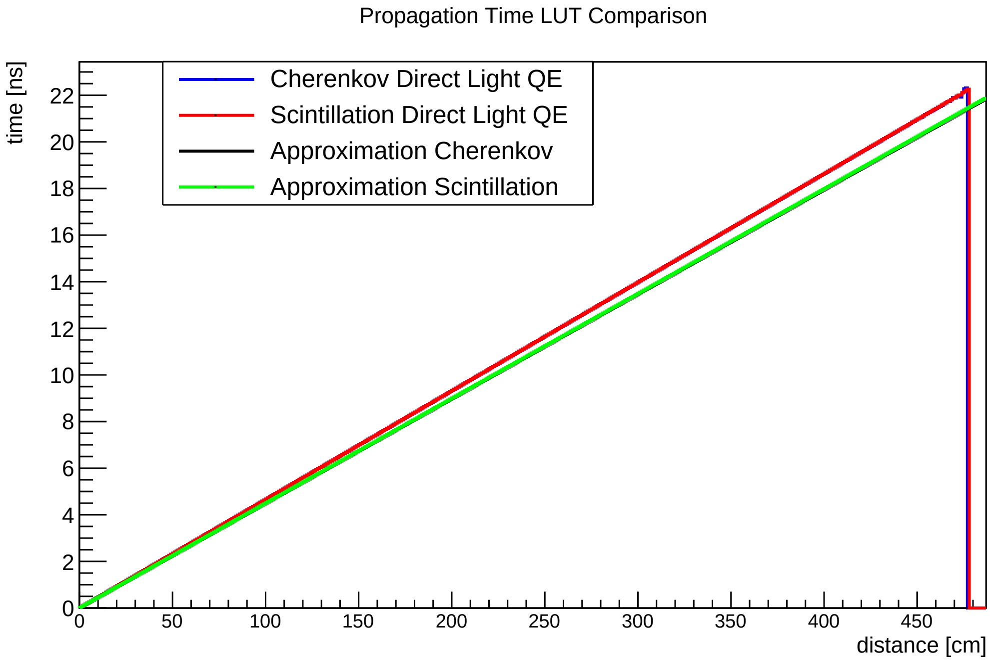

Figure 7.6.: Comparison of mean propagation times. Blue (red) shows the Cherenkov (scintillation) light LUT values averaged over all angles. Black (green) displays the approximated propagation times for Cherenkov (scintillation) light.

The direct light probability LUTs are displayed with a logarithmic $x-$ and z-axis in figure 7.7. The color code shows the probability for an emitted photon at a distance and an angle to the LAPPD to travel towards the pixel in a straight line without scattering effects and to be detected there. The probability shows the expected decline towards higher distances and due to reflection, the probability for direct light is slightly decreasing with higher angle.

For larger distance (above roughly $55\,\mathrm{cm}$) the probability is displayed as 0, which is plainly wrong. This is why another depiction is necessary for visualising and verifying this LUTs. Similar to the plot in figure 7.6, the mean value per distance bin for all angles is calculated and compared to an approximation in figure 7.8 with a logarithmic y-axis. Here, only scintillation light is depicted. The red line shows only direct light with including the QE of the photodetectors, whereas the black line also includes scattered light. The blue line shows only direct light without taking the QE into account. The green line shows a very rough approximation only including geometrical effects assuming that this is the dominating effect in these distributions, which will be explained in the following.

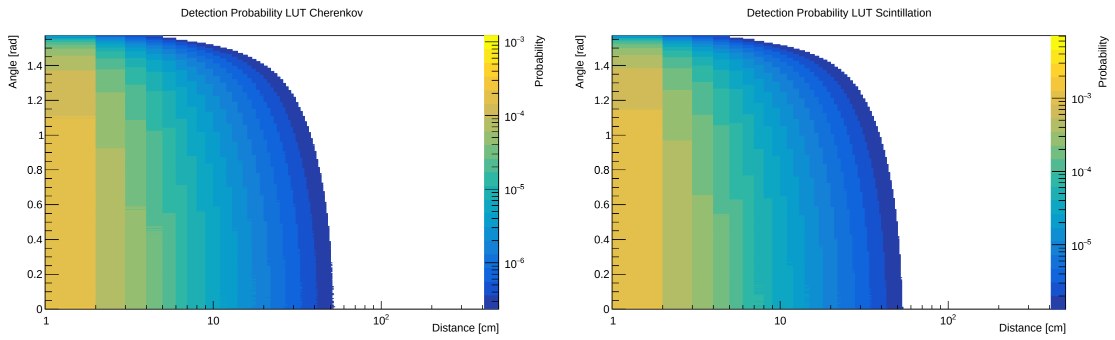

(a) (b)

Figure 7.7.: Direct light probability LUTs with logarithmic x and z-axis for (a) Cherenkov and (b) scintillation light.

There are several possibilities for calculating the probability that isotropic emitted photons hit a certain LAPPD pixel:

1. Run the simulation in the LUT generating mode but with geantinos[5] instead of photons. This is a dangerous approach without any other method of verification, since an error in the simulation would influence both the photon and the geantino result leading to a self-confirmation.

2. Create an evenly distributed point cloud at the surface of a sphere around the emission point with a radius equally to the distance of photodetector to emission point and calculate the amount of points hitting a LAPPD pixel. Repeat this for every distance bin. With this method, the geometrical properties could be approximated very well if a high number of points is calculated, since at large distances at least one point should lie within the pixel. The necessary amount of points then increases the run time and the memory consumption substantially.

3. Analytically calculate the projection of the pixel unto a sphere around the emission point to find the percentage of the pixel area with respect to the sphere's surface. This is a non-trivial mathematical problem.

4. Approximate the geometrical coverage of a LAPPD pixel as seen by the emission point. The probability for a photon of an isotropic emission to hit a pixel is equal to the percentage of the surface of a sphere around the emission point with a radius equal to the distance between pixel and emission, that is covered by said pixel. This can be calculated by dividing the area of a pixel by the surface of the sphere. On the one hand, this is a very rough approximation, which systematically overestimates the proportion of pixel area to sphere surface area. On the other hand, the implementation and run time of this approximation is very short and it should be able to explain the

---

[5] A geantino is a virtual particle in Geant4 meant for debugging. It behaves like a photon without any reflection or scattering.

shape of the distribution.

Of these four options, the last one is chosen, since the first one has a dangerous self-confirmation potential, whereas the second and third option are too time consuming to apply in the scope of this thesis. The approximation can be expressed via

$$P = \frac{0.25\,\mathrm{cm}^2}{4\pi r^2}, \tag{7.15}$$

where r is the radius of the sphere and $0.25\,\mathrm{cm}^2$ is the area of a LAPPD pixel. This approximation shows a very similar behaviour compared to the other distributions shown in figure 7.8 but shifted to higher values due to the systematic overestimation, which explains the gap between the green and the blue line. This means that the geometrical properties is indeed the dominating effect in the direct light probability LUTs. The difference between the blue and the red line shows the influence of the LAPPD's QE. Comparing the black and the red line shows the influence of scattered light in the detector simulation, which is very small due to the size of the detector.

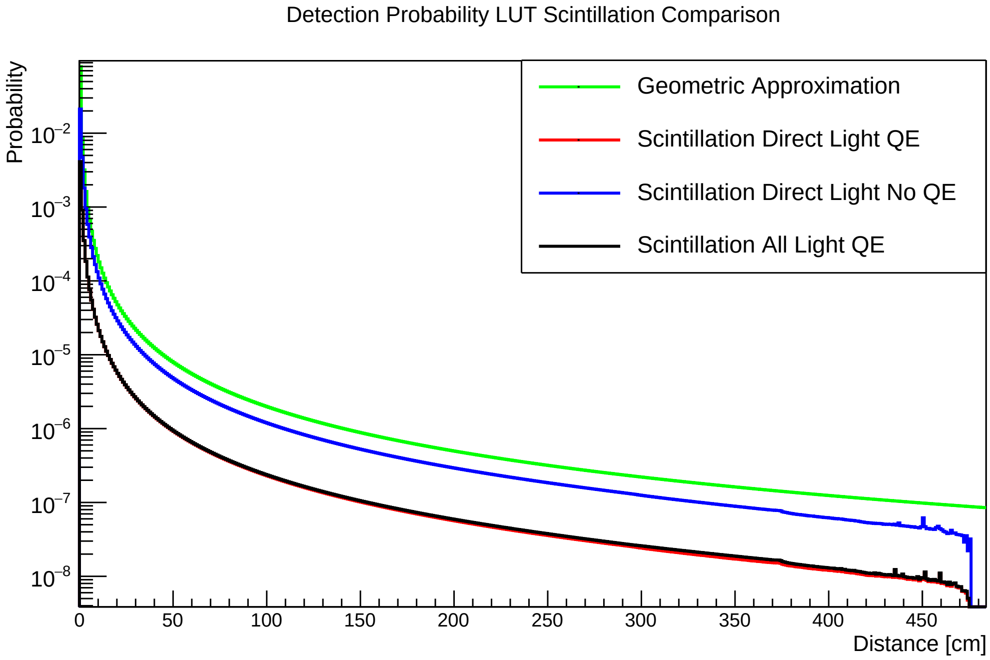

Figure 7.8.: Comparison of light probabilities for scintillation light. Green shows a geometrical approximation. Blue shows the direct light probability without the influence of the QE. Red shows the direct light probability including the QE and black shows the light probability including scattered light and the QE. Red, blue and black lines correspond to the mean LUT values averaged over all angles.

In figure 7.9 a comparison of the mean values averaged over all angles between Cherenkov (blue line) and scintillation (red line) is shown including the influence of the QE, again with a logarithmic y-axis. Additionally, the probability for direct light for Cherenkov (scintillation) light is shown without the influence of the QE in black (green). In this depiction (and also in figure 7.8), all simulated graphs show fluctuating values at very high distances ($> 430\,\mathrm{cm}$), which come from the low statistics at the very edge of the detector, since flat distributions for all three coordinates were used for the photon bomb positions. Since the distributions without the QE are almost indistinguishable, the difference in the red and blue line comes solely from the inclusion of the QE, that filters out more Cherenkov photons than scintillation photons. This is because the used emission spectra shown in section 6.3 shows a complete overlap with the QE for scintillation light, whereas the maximum of Cherenkov emission is towards smaller wavelengths outside of the QE.

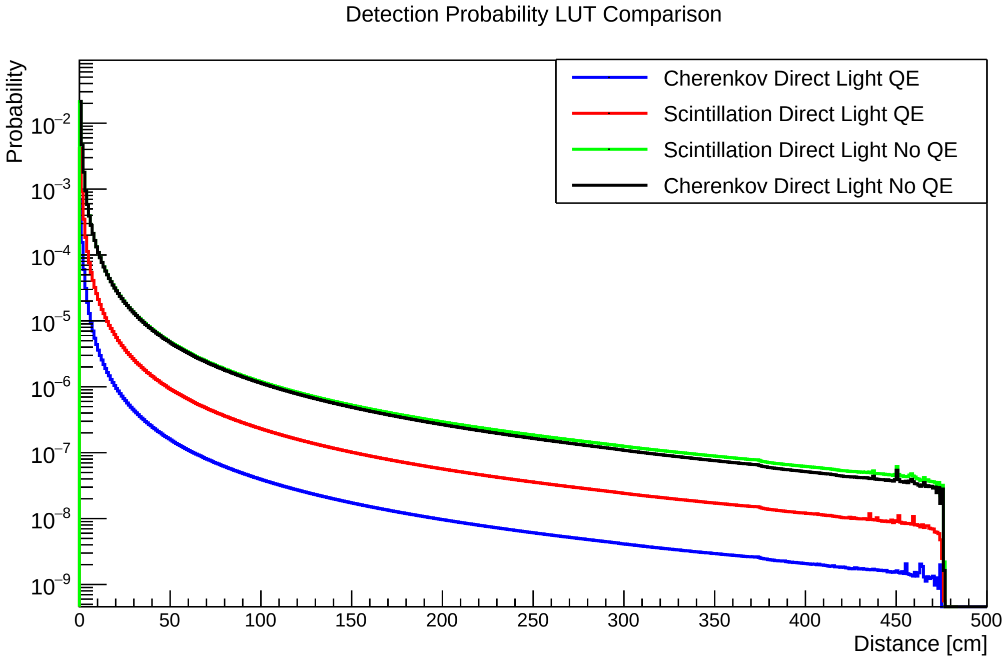

Figure 7.9.: Comparison of direct light probabilities. Blue (red) shows the Cherenkov (scintillation) light LUT values averaged over all angles.

Signal function

The difference in the signal functions is illustrated in figure 7.10. The signal function for the Cherenkov light can be seen on the left side, while the right side shows the signal function for the scintillation light. For both pictures, a single hit at $100\,\mathrm{ns}$ is used, which is chosen for vividness like all other hit times in this segment. It is to note, that the x-axis is not identical, since a higher zoom is chosen for the Cherenkov signal function. Because of the instantaneous emission of Cherenkov photons, the Cherenkov signal function resembles a Gaussian

$$f_{\mathrm{Cherenkov}}(t) = \frac{1}{\sigma_{\mathrm{TTS}}\sqrt{2\pi}} \cdot \exp\left(-\frac{1}{2}\frac{(t-\mu_{\mathrm{hit}})^2}{\sigma_{\mathrm{TTS}}^2}\right) \tag{7.16}$$

with the time resolution of the LAPPD $\sigma_{\mathrm{TTS}} = 0.1\,\mathrm{ns}$ and the time of the hit $\mu_{\mathrm{hit}} = 100\,\mathrm{ns}$. For the scintillation signal function, the Cherenkov signal function has to be convoluted with the exponential decay function of the scintillation light emission profile, which was introduced in equation (4.13) and is expanded here to include the hit time

$$d_{\mathrm{scintillation}}(t) = \sum_{i=1}^{n} \frac{\omega_i}{\tau_i} \exp\left(-\frac{t-\mu_{\mathrm{hit}}}{\tau_i}\right). \tag{7.17}$$

Here, the scintillation time constants of the components are $\tau_1 = 3.8\,\mathrm{ns}$, $\tau_2 = 10.2\,\mathrm{ns}$, whereas their weights correspond to $\omega_1 = 0.58$, $\omega_2 = 0.42$. The scintillation signal function is given by

$$\begin{aligned} f_{\mathrm{scintillation}}(t) = c \cdot \sum_{i=1}^{n} \frac{\omega_i}{2\tau_i} \exp\left[\frac{1}{\tau_i} \cdot \left(t - \mu_{\mathrm{hit}} + \frac{\sigma_{\mathrm{TTS}}^2}{2\tau_i}\right)\right] \\ \cdot \left\{1 + \mathrm{erf}\left[\frac{1}{\sqrt{2}\omega_i} \cdot \left(\mu_{\mathrm{hit}} - t - \frac{\sigma_{\mathrm{TTS}}^2}{\tau_i}\right)\right]\right\} \end{aligned} \tag{7.18}$$

with the charge of the hit c. In this thesis, all hits are assumed to have a charge of one PE. This assumption is also used to create the visualisation of the signal functions in figure 7.10 and 7.11.

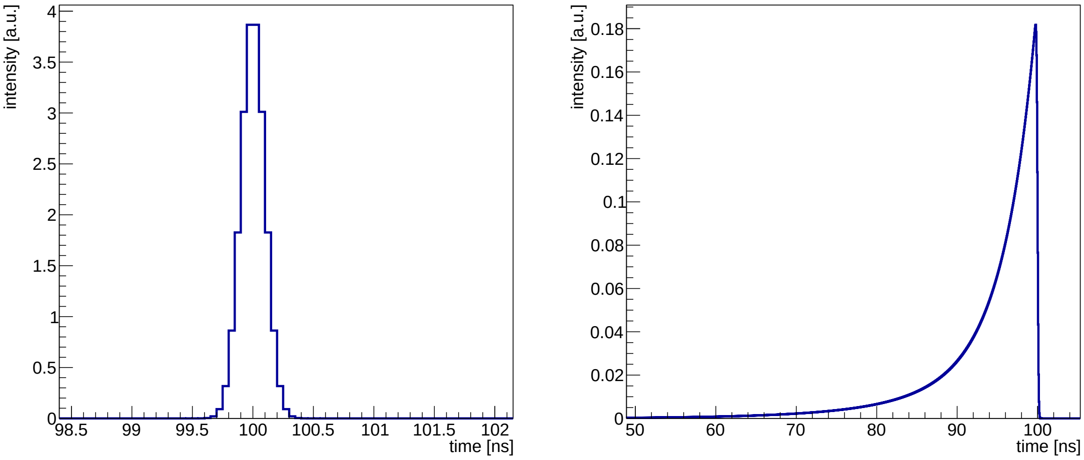

(a) (b)

Figure 7.10.: Unnormalised signal function for a single hit in (a) the Cherenkov part and (b) the scintillation part of the TTR.

As it can be seen in the right side of figure 7.10, the exponential decay functions are dominating the scintillation signal function due to the excellent time resolution of the LAPPDs. In comparison to the sharp peak of the Cherenkov signal function, the scintillation timing profile introduces a substantial uncertainty. At the first look, the fact that the tail of the scintillation function goes to lower times may seem unintuitive. The reason for this shape shall be illustrated via an example.

Assuming a delayed emission of a scintillation photon at the position $\vec{x}_{\text{delay}}$ with the hit time $t_{\text{delayed}} = 100\,\text{ns}$. The emission point is then in a cell with a distance to the photodetector registering the hit, that the expected time for an instantaneous emission is e.g. $t_{\text{expected}} = 90\,\text{ns}$, so that the scintillation signal function is evaluated at that time, giving a small cell content of roughly $0.02\,\text{a.u.}$. A cell with a higher distance to the photodetector, so that the expected hit time is indeed $100\,\text{ns}$ would get the maximum cell content. Cells with an even higher distance to the photodetector get a cell content of 0, since otherwise the photon has to be emitted faster than instantaneous or has to travel with a velocity higher than the speed of light.

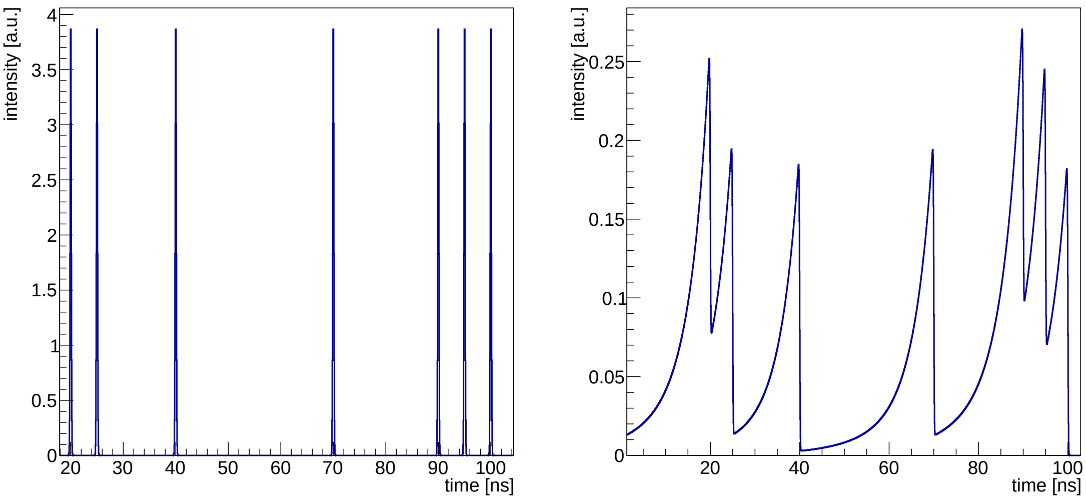

(a)

(b)

Figure 7.11.: Unnormalised signal function for multiple hits in (a) the Cherenkov part and (b) the scintillation part of the TTR.

If a photodetector detects multiple hits, the signal functions resembles the combination of single hit signal functions as it is illustrated in figure 7.11. Here, again the left side shows the Cherenkov and the right side the scintillation signal function. As expected, the Cherenkov signal function shows sharp peaks around the hit times of $20\,\text{ns}$, $25\,\text{ns}$, $40\,\text{ns}$, $70\,\text{ns}$, $90\,\text{ns}$, $95\,\text{ns}$ and $100\,\text{ns}$ without any overlap. The scintillation signal function on the other hands, shows indeed overlaps leading for the highest peak at the hit time of $90\,\text{ns}$ due to the near hits at $95\,\text{ns}$ and $100\,\text{ns}$.

7.2.4. Example events

Two example events will be presented in this section to illustrate that the reconstruction is able to produce results in WbLS and to show the advantages and disadvantages of the two light types. In order to avoid possible difficulties with reconstructing Cherenkov photons in the scintillation reconstruction and vice versa, which could be misinterpreted that the implementation is not working as intended,

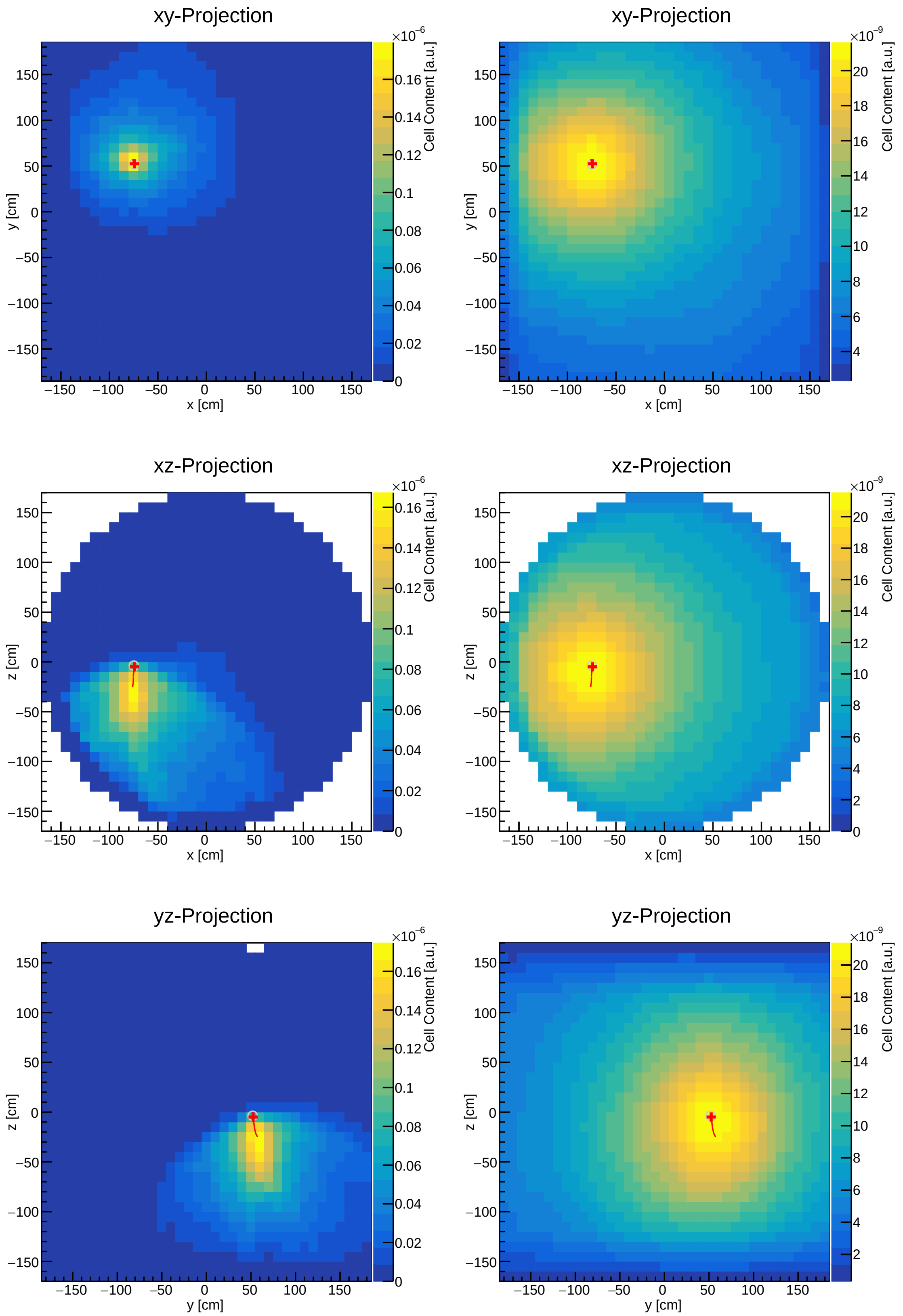

Figure 7.12.: Raw reconstruction result of the left (right) Cherenkov (scintillation) reconstruction in the first iteration.

these example results are produced with a perfect ordering of hits. This means, Cherenkov photons are reconstructed only in the Cherenkov reconstruction and the other way around. It is to note, that this ordering is, as it will be shown in later chapters, not obtainable and the reconstruction is in fact part of the mechanism to order the hits.

Both events are reconstructed starting with one iteration with a cell size of $10\,\mathrm{cm}$ with the raw algorithm, followed by four iterations with the same cell size with the emitted light algorithm and concluded by another emitted light iteration with a cell size of $5\,\mathrm{cm}$. The hit time information is smeared with a Gaussian with $\sigma_{\mathrm{LAPPD}} = 0.1\,\mathrm{ns}$. The vertex position is assumed to have an uncertainty of $1.0\,\mathrm{cm}$ in position and $0.2\,\mathrm{ns}$ in time. Only hits with a time less than $100\,\mathrm{ns}$ are taken into account.

In figure 7.12, the first iteration with the raw algorithm is shown. The primary particle is a electron with $56.32\,\mathrm{MeV}$ starting at $(-74, 52, -4)\,\mathrm{cm}$ in approximately $(0, 0, -1)$ direction. The left (right) side shows the Cherenkov (scintillation) reconstruction's result. The first row shows the xy-projection, the second one the xz-projection and the last row displays the yz-projection. Since the xz-projection is the top view of the cylindrical detector, the reconstructed results resembles a circle. This description is true for all the following pictures.

The Cherenkov reconstruction is sharper and confined to a smaller area than the scintillation reconstruction in all projections showing the advantage of the fast emission timing of Cherenkov photons. This is clearly visible comparing the left side to the right side. Furthermore, it is shown that both reconstructions are able to find the track in all directions.

Figure 7.13 displays the fourth iteration of the same event with the emitted light algorithm. Again, the timing of the Cherenkov photons helps the Cherenkov reconstruction to have a better contrast. This result can be improved upon with the next iterations. This is shown in figure 7.14, where the sixth iteration for the same event is shown. Here, the confinement of the high probability areas of the detector is even closer to the track.

In figure 7.15 the sixth iteration of a second event is shown with a electron with $37.11\,\mathrm{MeV}$ starting at $(81, 160, 50)\,\mathrm{cm}$ in $(0.61, -0.62, -0.50)$ direction. In all projections it is visible in the scintillation reconstruction that the emitted light algorithm tends to show high values towards the detector edge, when the event happens in proximity to the detector wall. This is a known issue for the emitted light algorithm. Nevertheless, the result shows an similar confinement to the track than the previous event. The high values towards the detector edge are not happening in the Cherenkov reconstruction.

This events show that the splitting of the reconstruction works like intended and that with perfect ordering both parts yield good results. It is to note that there can be problems in the emitted light algorithm, when the reference time is shifted near $1\,\mathrm{ns}$ with respect to the true vertex time. This is one of the reasons for the light separation algorithm to work with the raw reconstruction mode, for which one example event is shown in the next chapter.

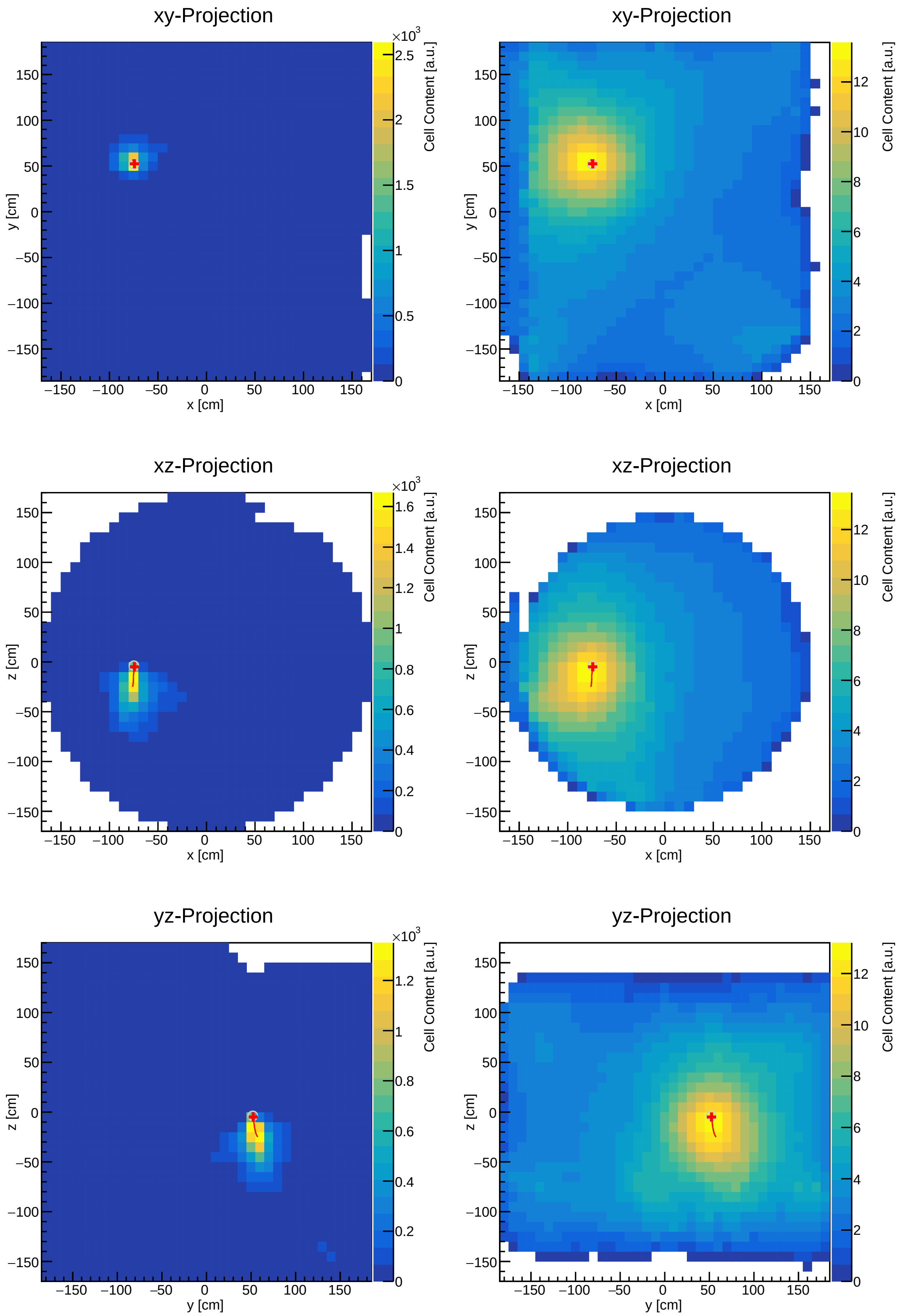

Figure 7.13.: Emitted light reconstruction result of the left (right) Cherenkov (scintillation) reconstruction for the fourth iteration.

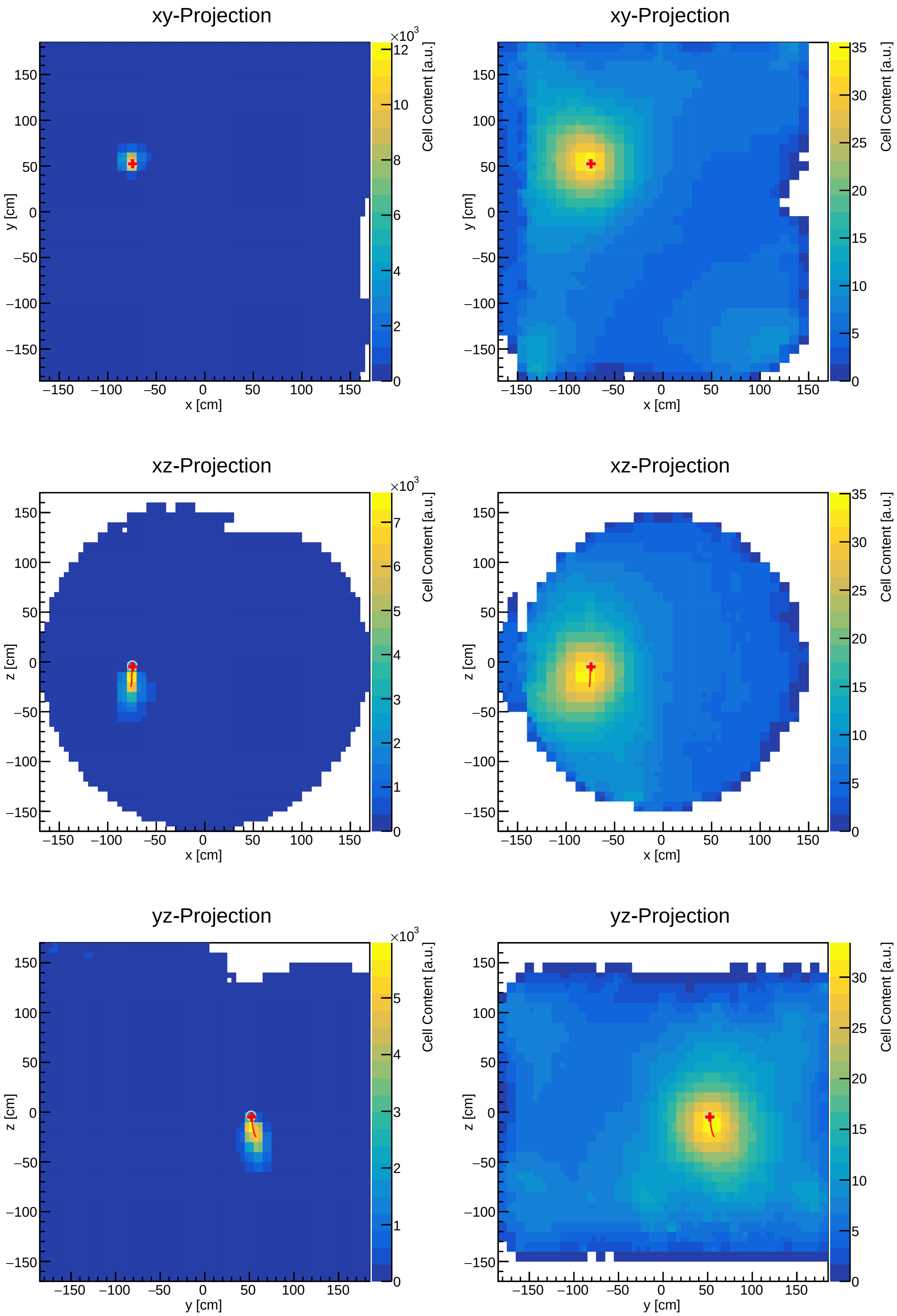
xy-Projection

xy-Projection

xz-Projection

xz-Projection

yz-Projection

yz-Projection

Figure 7.14.: Emitted light reconstruction result of the left (right) Cherenkov (scintillation) reconstruction for the sixth iteration.

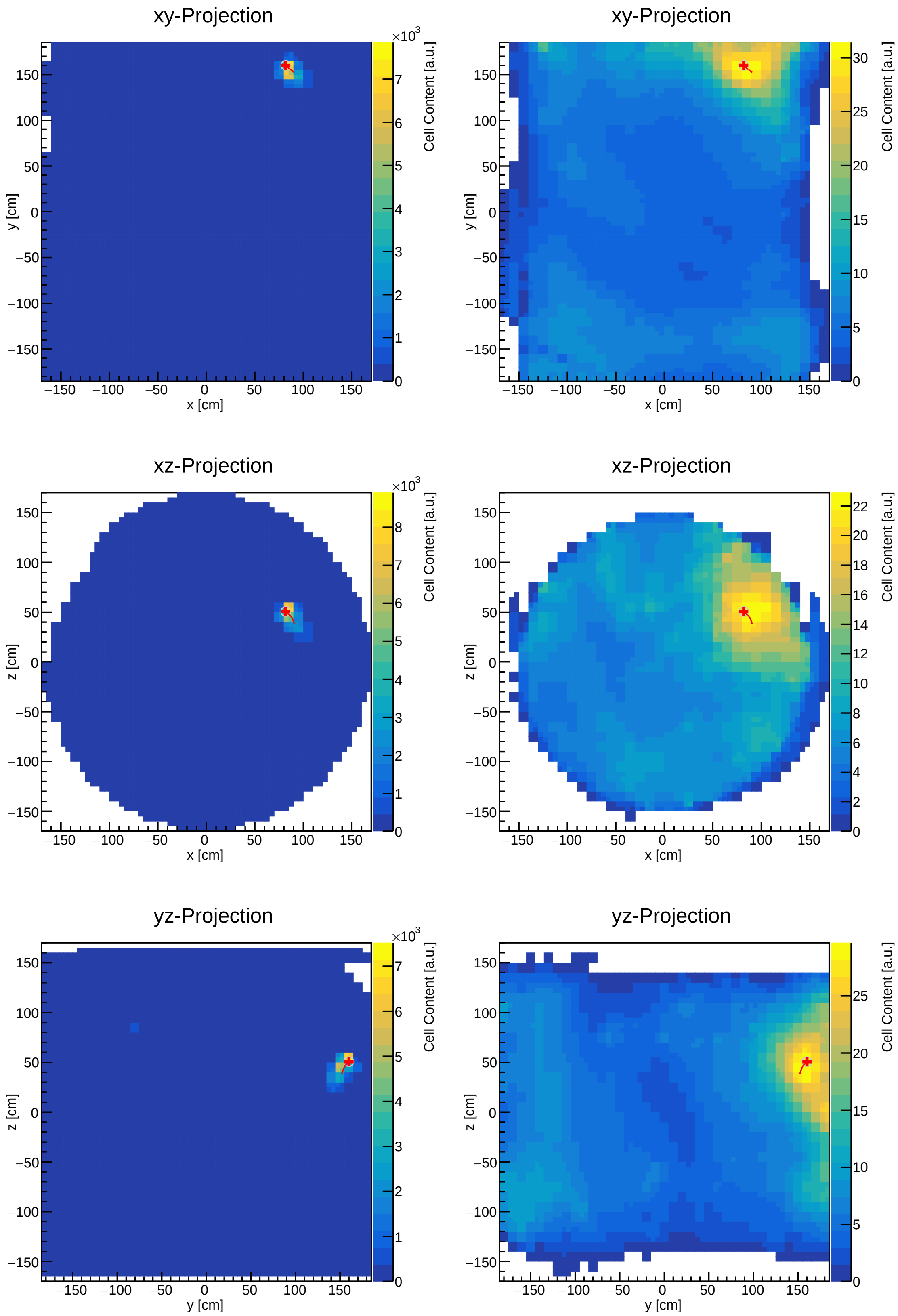

Figure 7.15.: Emitted light reconstruction result of the left (right) Cherenkov (scintillation) reconstruction for the sixth iteration of a second example event.

8. Light Separation

The development of a light separation algorithm based on timing is the focus of this work. Such an algorithm is a vital step to access the advantages of Cherenkov and scintillation light and to develop subsequent applications like direction reconstruction and PID. In the following, the used datasets are shown, followed by an introduction of the used method for light separation. Section 8.3 shows the results for the different samples, which are then discussed in section 8.4.

8.1. Datasets

The light separation algorithm is developed for two different applications. The first application is PID, for which $12,000$ electron, muon and gamma events in the energy range of $0.5\,\mathrm{MeV}$ to $120\,\mathrm{MeV}$ are simulated with the IDS (see chapter 6) in the WbLS mode. Furthermore, $14,000$ protons are simulated in the energy range of $0.5\,\mathrm{MeV}$ to $140\,\mathrm{MeV}$. The energy range for protons is chosen in that way since quenching effects lead to less scintillation photon emission for protons than for the other particles, so that for higher energies the proton background would be missing when simulating to $120\,\mathrm{MeV}$. The number of events is chosen to have an equal coverage of events per energy interval. The threshold of $0.5\,\mathrm{MeV}$ is set to avoid zero photon events. Furthermore, for a direction reconstruction approach $10,000$ events of electrons with energies between 0.5 and $10\,\mathrm{MeV}$ are simulated and reconstructed, since this is the energy range relevant for $0\nu\beta\beta$, where a direction reconstruction of solar neutrinos can help with background reduction.
For all events, the direction and vertex of the primary particles is chosen at random to reach a big coverage of possible reconstruction scenarios.

8.2. Method

The first step in the light separation process is the TTR used in the **raw** reconstruction mode. The raw reconstruction instead of the emitted light reconstruction is used for two reasons. First of all, the emitted light algorithm normalises the added cell content so that all hits add the exact same summed cell content. Secondly, it was discovered that the emitted light algorithm has issues with tracks that are too close to the detector wall and the production of artifacts in the Cherenkov reconstruction for unsorted hits.

As it was explained in the last chapter, the TTR is able to work with both light types simultaneously by assuming all given hits Cherenkov (scintillation) for the Cherenkov (scintillation) reconstruction. It is expected that the TTR is able to produce good results for sorted hits in that mode for track finding and measuring the deposited energy, but the analysis of the performance of the TTR in that mode is outside of the scope of this thesis. Rather, the ability of the TTR to separate the light types is investigated.

Every hit is evaluated twice, once in the Cherenkov part and once in the scintillation part of the TTR and adds a certain Cherenkov and scintillation cell content amount to the cells, in which the detector volume is divided. This is visualised by the following example, that does not reflect the exact working method of the TTR but is suitable to explain the idea in the three figures 8.1, 8.2 and 8.3. The first figure shows the xy-projection, the second one the xz-projection and the third one the yz-projection. Hereby, the left side shows always the Cherenkov part and the right side the scintillation part of the TTR. The top row shows the reconstruction result for a single Cherenkov hit, while the bottom row shows the same for a single scintillation hit. The middle row shows the TTR result of the fourth iteration, that can be used as probability mask for the next iteration. In the reconstruction process the single hit isochrones are weighted by the probability mask. It is expected that the nature of the photon influences the overlap of the probability mask and the single hit isochrones, so that the result of the weighting is higher (lower) for Cherenkov photons in the Cherenkov (scintillation) reconstruction and vice versa. The example event shown is an electron with about $74.4\,\mathrm{MeV}$ starting at $(-102, -75, 93)\,\mathrm{cm}$ and travelling in the $(0.57, -0.82, -0.09)$ direction, whereby the reference point is the primary MC truth vertex smeared with $1\,\mathrm{cm}$ in space and $0.2\,\mathrm{ns}$ in time. This is assumed to be the resolution of a vertex reconstruction in such a detector and is an assumption that is used in the following results as well. It is further to note that the single hit pictures are from randomly chosen hits for illustration purposes only.

It can be observed for all three pictures that the Cherenkov part of the TTR on the left side shows sharper isochrones for the single hit cell content and a more confined probability mask, because only the TTS of the LAPPDs is taken into account. The scintillation part on the other hand shows smeared isochrones due to the inclusion of the exponential decay of the scintillation light emission, that is also reflected in the probability mask. Whether the hit is a true direct Cherenkov or scintillation hit can also be seen based on the position and shape of the isochrones. This is more clearly visible in the Cherenkov reconstruction due to the sharper isochrones. The position of the hit photodetector can be assumed to sit roughly at the point on the detector wall that is opposite to the tip of the isochrone and that is centered within the isochrone.

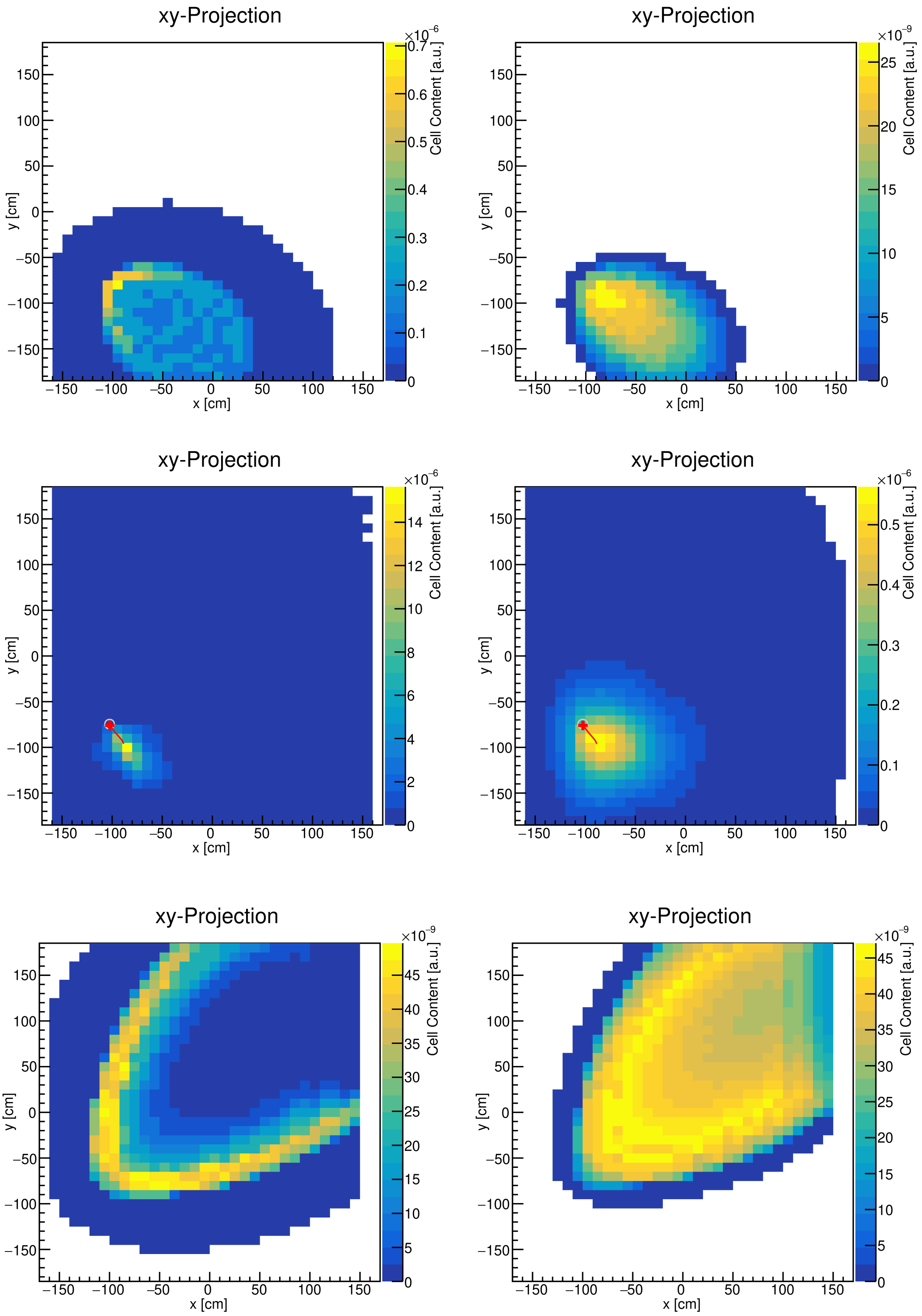

Figure 8.1.: Example event for the working principle of the light separation in the TTR in the xy-projection. Left (right) shows the Cherenkov (scintillation) part of the TTR. Top (bottom) show the added cell content for a single true Cherenkov (scintillation) hit; middle shows the probability mask used for evaluating top and bottom.

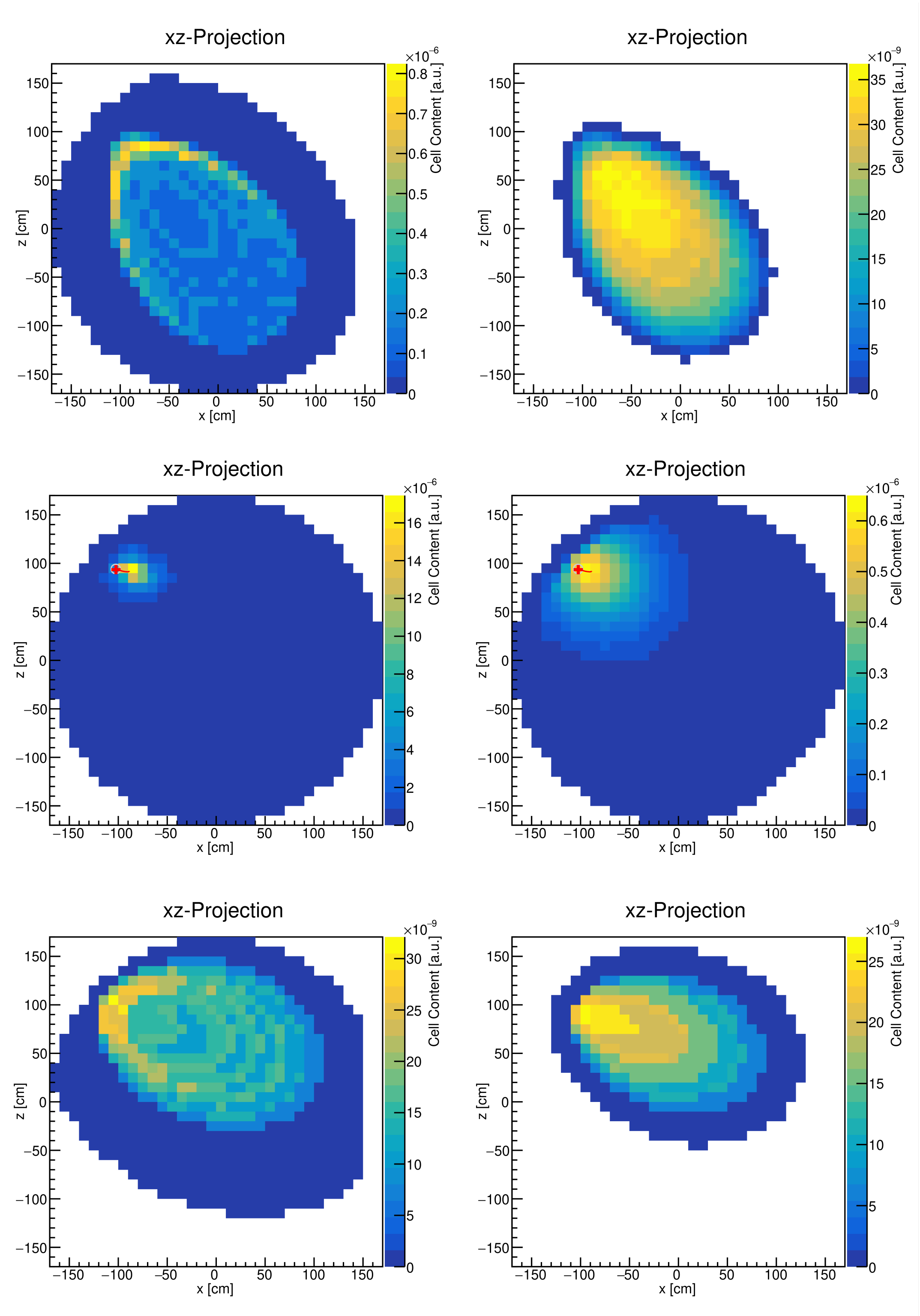

Figure 8.2.: Example event for the working principle of the light separation in the TTR in the xz-projection. Left (right) shows the Cherenkov (scintillation) part of the TTR. Top (bottom) show the added cell content for a single true Cherenkov (scintillation) hit; middle shows the probability mask used for evaluating top and bottom.

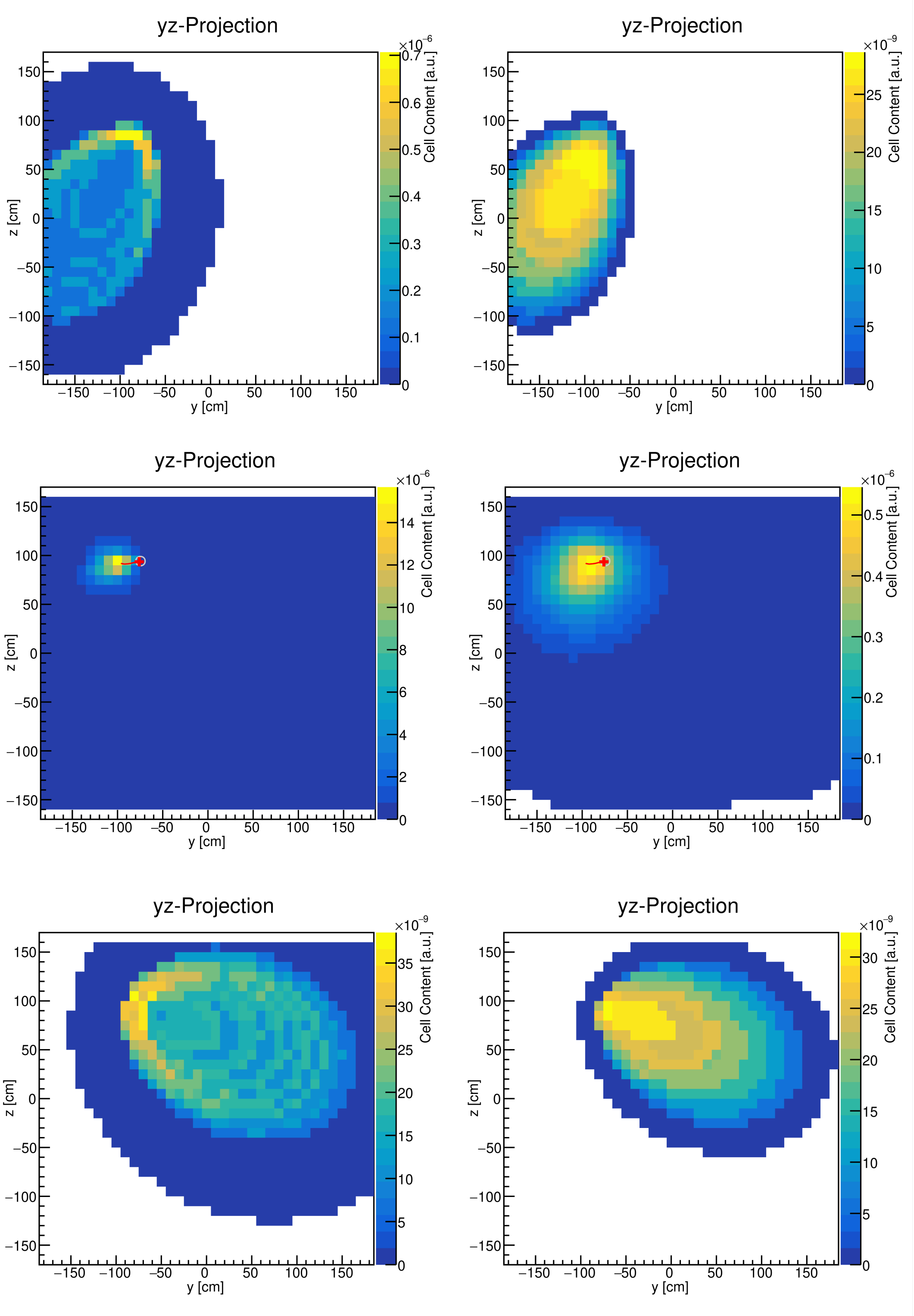

Figure 8.3.: Example event for the working principle of the light separation in the TTR in the yz-projection. Left (right) shows the Cherenkov (scintillation) part of the TTR. Top (bottom) show the added cell content for a single true Cherenkov (scintillation) hit; middle shows the probability mask used for evaluating top and bottom.

For the xy-projection in figure 8.1 the true Cherenkov hit is measured at roughly $x = 0\,\mathrm{cm}$ and $y = -175\,\mathrm{cm}$. The pixel detecting the scintillation hit is located roughly at $x = y = 150\,\mathrm{cm}$. Comparing the assumed hit position to the true electron direction indicated by the red line in the middle pictures shows that the position of the pixel measuring the Cherenkov hit is in the direction of the flight path of the electron, whilst the pixel detecting the scintillation photon is not. It is to note that the position does not perfectly match with the particle path due to the Cherenkov angle. This behaviour can also be seen in figure 8.3. Here, for the scintillation hit to come from Cherenkov radiation, the particle has to travel roughly in the opposite direction. In the xz-projection (figure 8.2) both hit position would be compatible for a Cherenkov photon.

The added cell content for single hits has no separation power by itself since is is normalised for the individual hits, but the addition of the probability mask does the trick by modifying the cell content of the single hits with the established track from the probability mask. The difference in expected time and sharpness of the hits leads to a difference of summed cell content[1] over the whole detector per hit. The reason for that is that the very early timing of a Cherenkov hit does not match the expected time correction in the scintillation reconstruction and the overlap of the added cell content with the distribution of the probability mask is reduced. The same situation is expected for the scintillation photons in the Cherenkov reconstruction. The delay of the hit puts the added cell content too far outwards of the hit LAPPD pixel, so that the track in the probability mask is matched to a lesser degree than for a Cherenkov hit. This can be imagined with help of the three aforementioned figures. In most cases the cells with high contents for the true Cherenkov hit match the cells with high contents of the probability mask better than for the scintillation hit. For the Cherenkov part of the TTR it can be observed, that the isochrones for the Cherenkov hit are more concentrated on the track in the probability mask, whereas the isochrone for the scintillation hit has comparatively higher contents in cells that do not match the track. The same observation can be made for the Cherenkov hit in the scintillation part of the TTR.

The calculation of the **summed cell content** is a central aspect of the light separation method and demands for a more detailed explanation.

The TTR evaluates every photosensor individually and calculates, how much content is added to each cell of the detector volume. Adding all of the cell contents, that a photodetector adds to the detector mesh, results in the so called summed cell content.

Since the calculation of the contribution of a photodetector is based on the signal function that is constructed from the individual hits on this photosensor, this method gives the summed cell content only for the photodetectors, but not for the individual hits. In order to assign each hit a summed cell content, a ROOT

---

[1] This term is explained later in this section.

macro is used before the TTR to duplicate the pixels that have seen multiple hits in the geometry file, that is expected by the TTR specifying the type, position and direction of all photosensors. Furthermore, pixels are eliminated in the geometry file that did not see a single hit to reduce computation time. This results in a geometry file that contains one pixel for every hit with a number of pixels occurring multiple times to assure that the summed cell content for one LAPPD pixel also corresponds to exactly one photon hit.

With this method, the TTR assigns every hit a summed cell content in the Cherenkov and in the scintillation part of the reconstruction regardless of the true nature of the photon.

It can be shown with five iterations of $10\,\mathrm{cm}$ and one final iteration of $5\,\mathrm{cm}$ binning, that the distributions are pulled apart and a separation of Cherenkov and scintillation photons is possible. Further iterations did not show significant improvement and in regard of computation time, this number of iterations appeared to be a sweet spot. Nevertheless, it cannot be excluded that there is a better performing reconstruction configuration.

The principle of the light separation algorithm for the example event introduced above is shown in figure 8.4. In the first three panels the summed Cherenkov cell content versus the summed scintillation cell content as scatter plot are shown. The red (blue) hits are true scintillation (Cherenkov) hits. In the 0th iteration (8.4 (a)), the hits are not separable yet, although a slight hint towards higher summed Cherenkov cell contents is visible. This improves, as in iteration 4 (8.4 (b)) the Cherenkov hits are moved towards higher summed Cherenkov cell content values. For the last iteration (8.4 (c)), a clear separation is visible, as most of the Cherenkov hits are located in the low scintillation and high Cherenkov cell content area. The improved performance in the last iteration can be explained, because a binning of $5\,\mathrm{cm}$ reaches roughly the spatial and time resolution of the LAPPDs and therefore the limit of the photosensors, whilst being able to resolve the fine time differences of the light types.

It is notable that the scintillation hits form an empty spot below 0.0006 summed scintillation cell content and below 0.002 summed Cherenkov cell content. It appears that hits either do not fit the Cherenkov reconstruction at all shown with hits at the y-axis or there is a minimum of summed scintillation cell content assigned to a hit, if it fits the Cherenkov reconstruction considerably well. Since the binning is finer and therefore the summed cell content is higher, this minimum increases, forming a visible spot. It is also to note that the separation in even and odd hit IDs for the iterations lead to less hits in (a) and (b), whilst (c) shows all hits.

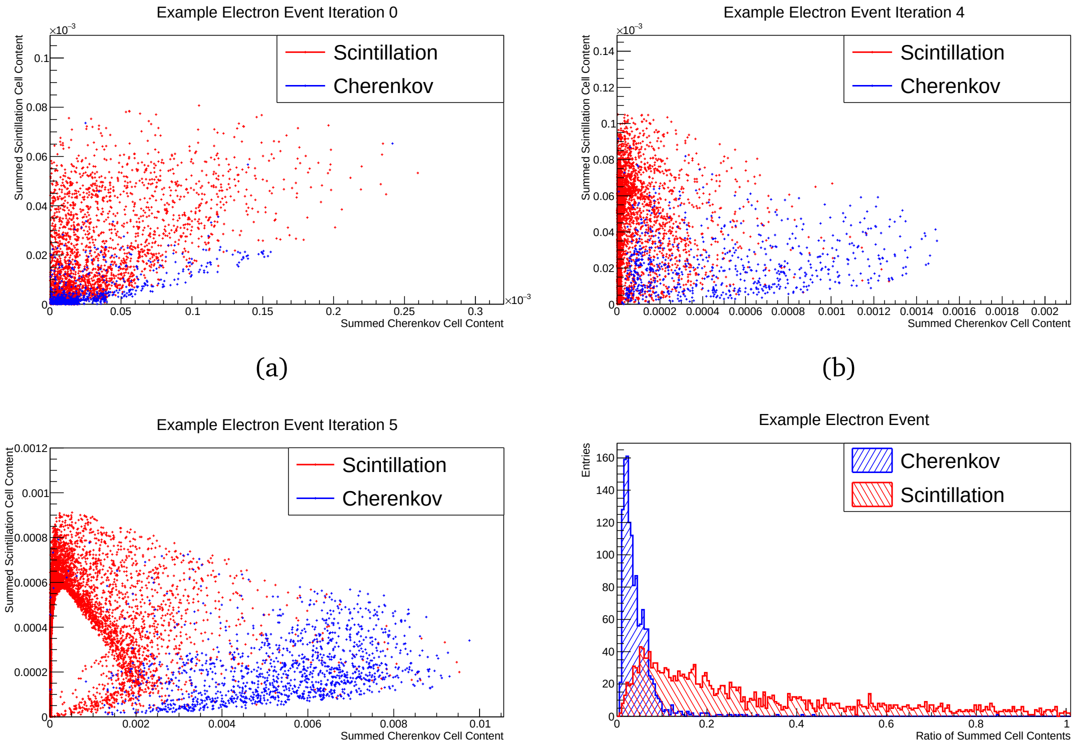

(a) (b)

(c) (d)

Figure 8.4.: Influence of the iterations on the light separation power of the TTR for iteration 0 in (a), iteration 4 in (b) and iteration 5 in (c) in terms of the added summed Cherenkov (x-axis) and scintillation cell content (y-axis). Towards the later iterations the distributions of true Cherenkov in blue and scintillation hits in red are pulled apart. (d) shows the ratio of the summed scintillation cell content to the Cherenkov cell content, where a clear separation can be seen.

The last panel shows the ratio of the summed scintillation content to the summed Cherenkov content so that the true Cherenkov hits are expected to have a low ratio. On this distribution a cut can now be defined to gain a Cherenkov sample with hits below the chosen cut value and a scintillation sample with hits above the chosen cut value. The chosen cut value on this summed cell content ratio are referred to as C_{Sep} in the following to avoid confusion with other cut values.

8.3. Results

For all Cherenkov radiation producing particles, the quality of the light separation can be investigated in terms of efficiency, purity and Matthew's Correlation Coefficient (MCC). The efficiency is defined as the ratio of number of Cherenkov photons in the cut window to the number of Cherenkov photons in the event. The purity is defined as the ratio of Cherenkov photons in the cut window to the number of all photons in the cut window. Furthermore, MCC is used throughout this thesis for evaluating cuts in binary datasets. It is defined as [207]

$$\mathrm{MCC} = \frac{\mathrm{TP}\cdot\mathrm{TN} - \mathrm{FP}\cdot\mathrm{FN}}{\sqrt{(\mathrm{TP}+\mathrm{FP})\cdot(\mathrm{TP}+\mathrm{FN})\cdot(\mathrm{TN}+\mathrm{FP})\cdot(\mathrm{TN}+\mathrm{FN})}}, \tag{8.1}$$

where TP is the number of true positives, TN the number of true negatives, FP the number of false positives and FN the number of false negatives. In the light separation picture, TP is the number of Cherenkov photons in the Cherenkov sample, TN the number of scintillation photons in the scintillation sample, FP the number of scintillation photons in the Cherenkov sample and FN the number of Cherenkov photons in the scintillation sample.

The advantage of the MCC against the purity and efficiency is that the MCC takes into account the number of events of the different classes in a test sample and yields comparable results for non-balanced sample sizes. The MCC ranges between -1 and $+1$, where $+1$ shows the best cut and 0 is an equal number of true and false values. Negative values for the MCC show that there is discrimination potential, but the hypothesis needs adjustment.

The purity p can be expressed as

$$p = \frac{\mathrm{TP}}{\mathrm{TP}+\mathrm{FP}} \tag{8.2}$$

also known as precision or positive predictive value and the efficiency e as

$$e = \frac{\mathrm{TP}}{\mathrm{TP}+\mathrm{FN}} \tag{8.3}$$

also known as sensitivity, recall or true positive rate.

The results are in the following shown for four samples starting with the electron sample. This is followed by the low energy electron, the gamma and the muon sample. The proton sample is ignored in this analysis, since no Cherenkov photon emission is expected from the protons directly and the only Cherenkov photon emission in proton events can come from secondary particles.

8.3.1. Electron

Figure 8.5 shows the results for the light separation for the electron sample with energies between 0.5 and $120\,\mathrm{MeV}$. (a) shows the ratio of the scintillation to the Cherenkov summed cell contents for all hits in the sample for true Cherenkov (scintillation) photons in blue (red). For ratios below 0.07, the number Cherenkov photons raises significantly in regard to the number of scintillation photons. The ratio plot also shows that a contamination of the Cherenkov sample cannot be avoided regardless of chosen cut and that a higher cut value than 0.07 would decrease the purity whilst increasing the efficiency. The cut value of $C_{\mathrm{Sep}} = 0.09$ is shown as purple dotted line.

It is important to note that in all the following plots of these metrics, the MCC values in black are placed exactly on the values of the x-axis in question, whilst the purity in blue and the efficiency in red is slightly shifted for better visibility. The markers for the efficiency and purity still correspond to the value on the x-axis, that is shown by the MCC marker. The same is done for the number of photons, but here the number of scintillation photon marker in red shows the exact value, whereas the blue marker for number of Cherenkov photons and the black marker for the total number of photons is shifted. In order to show the influence of different event topologies, the metrics as well as the number of photons are calculated for every event individually and filled into histograms. The mean of these histograms correspond to the markers, whilst the standard deviation of said histograms correspond to the error bars. This can lead to error bars reaching unrealistic values above 1.0 for the metrics, since events without Cherenkov hits in the cut window or without Cherenkov hits at all contribute as low values or zero, increasing the standard deviation. Furthermore, the scala of y-axis changes often also in between neighbouring plots.

The interpretation of (a) can be confirmed by (b), where the influence of the chosen cut value on the purity, efficiency and MCC is shown. Hereby, the cut ranges between 0.02 and 0.15 in 0.01 steps in order to show the development of the metrics for all the different samples. As the cut value is moved towards higher values, the purity decreases, while the efficiency increases as expected. The MCC increases to a maximum at 0.09 and is stable for the following cut values until it decreases again. Furthermore, the variance in the events displayed by the error bars decreases for higher cut values for all three metrics. This means that there is a substantial variance in the ratio distributions for the Cherenkov photons, since low cut values contain highly varying number of Cherenkov photons.

The variance in purity and MCC is comparatively stable starting at cut values of 0.09 and above, whilst the variance in efficiency still decreases significantly to a minimum at the highest cut value. This can be explained by the fact that nearly all Cherenkov photons are now contained in the Cherenkov sample leading to a high efficiency for a high number of events. From this figure, a cut value can be chosen which can then be investigated in terms of energy and distance to the detector wall. In the electron sample, the chosen cut value is $C_{\text{Sep}} = 0.09$ to get the maximum value for MCC of 0.76 ± 0.12, a purity of 0.76 ± 0.11 and an efficiency of 0.87 ± 0.16.

(c) shows the influence of energy on the metrics, whereby the visible energy is shown in terms of true number of scintillation photons. This representation is chosen instead of the true energy of the primary particle, since particles that leave the detector deposit only a fracture of their energy in the detector. Furthermore, secondary particles can influence the visible energy so that the true energy and the observed event topology does not match hindering the interpretation.

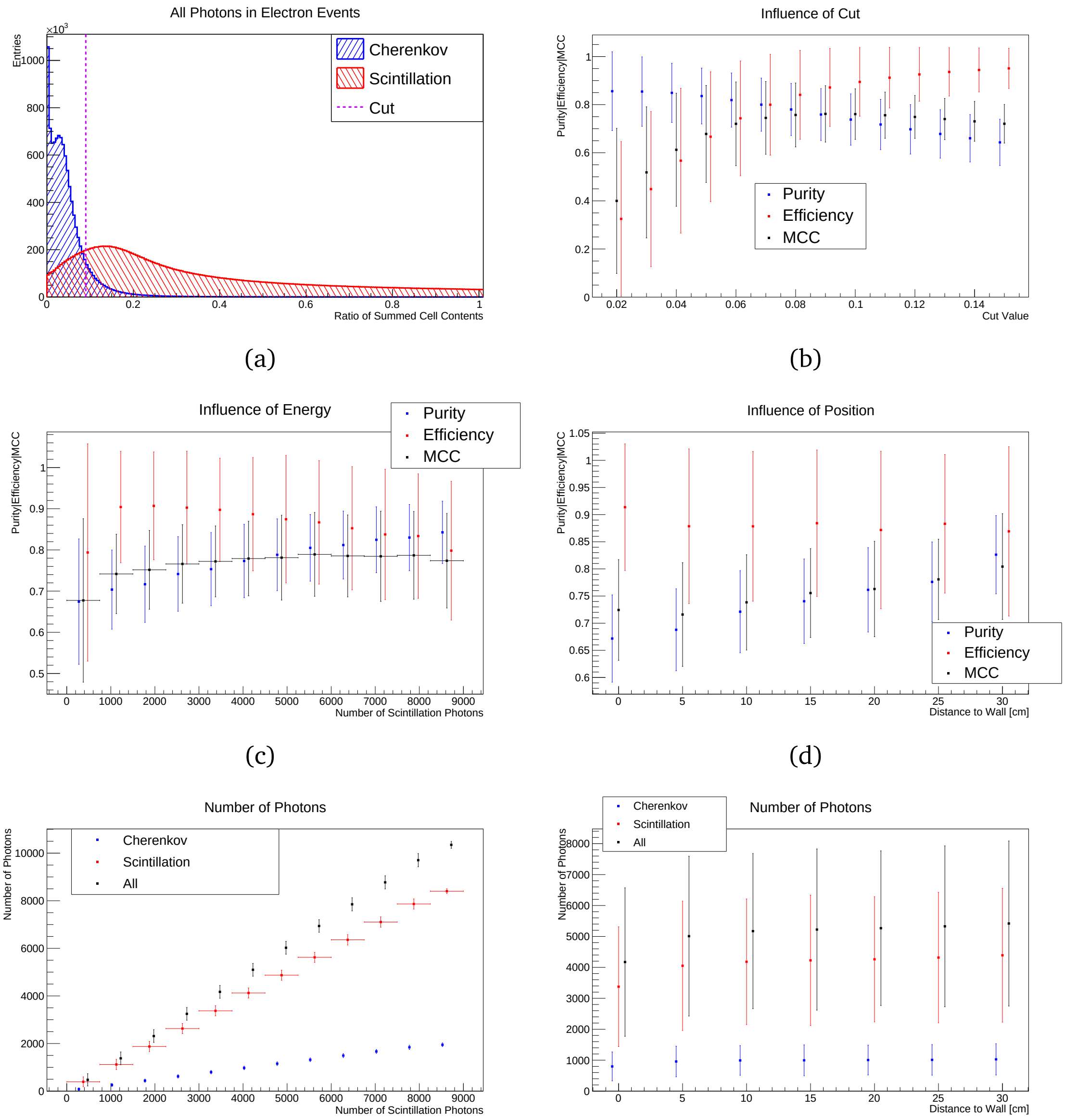

(a) (b) (c) (d) (e) (f)

Figure 8.5.: Light separation results for the electron sample. (a) shows the ratio of the summed cell content for all photons with the indication of the chosen cut value based on the maximum MCC, that is shown together with the purity and efficiency with respect to the cut value in (b). (c) shows the influence of the energy in terms of the true number of scintillation photons. The number of events in relation to the energy in terms of photon intervals is shown in (e). (d) shows the influence of the position of the event on the performance; (f) is the same as (e) but for the position of the event.

Nevertheless, the number of scintillation photons is linearly linked to the primary energy of the particle so that the depicted range corresponds roughly to energies of 0 to $120\,\mathrm{MeV}$. The intervals are of the size of 750 photons (shown by the horizontal error bars of the MCC values) starting at 0 and going up to 9000 photons so that the first interval shows all events with less than 750 scintillation photons, the second intervals shows events with a number of scintillation photons between 750 and 1500 and so on. The intervals are chosen in that way, so that they roughly correspond to $10\,\mathrm{MeV}$. To help with the interpretation (e) shows the number of scintillation (red), Cherenkov (blue) and all photons (black) in the intervals. Here, the expected linear increase for all photon types is visible, whilst the vertical error bars show that the variance in photon number is small.

(c) shows that the step from the first photon interval to the second one shows the best improvement. After that, the performance stays roughly on one level in terms of MCC, whilst the purity increases towards higher energies with a decrease of efficiency. The best performance is reached at the 5625 photon interval with a MCC of 0.79 ± 0.10, a purity of 0.81 ± 0.08 and an efficiency of 0.87 ± 0.15.

(d) shows the influence of the event position on the metrics with (f) being equivalent to (e) but in terms of the distance to the wall. All events that have a minimum distance as shown on the x-axis to the detector wall in their primary vertex and the end position of the primary particle track are contained in the corresponding marker. Thereby, the events that are already included in a higher distance point are excluded for the next nearer point. This means, the e.g. $10\,\mathrm{cm}$ marker includes all events with a distance higher than $10\,\mathrm{cm}$, that are not already included in the $15\,\mathrm{cm}$ point. The marker at $0\,\mathrm{cm}$ includes also the events, which are not contained. For this plot, the first photon interval is excluded to decrease the dependence of the performance on the event's visible energy, since all other photon intervals show similar performance. For electron events, the MCC and purity increases with a higher distance to the wall, while the efficiency stays on the same level. For the $0\,\mathrm{cm}$ marker the efficiency is highest, while the purity is lowest. The high variance of photon numbers in (f) and the metrics in (d) is due to the fact that all energies are displayed at once and in (f) it can be seen that events, that exit the detector, at the $0\,\mathrm{cm}$ marker decrease the overall number of photons.

The results for the other samples is shown in the same manner so that the general description of the figures is valid for the following sections as well.

The performance of the light separation can be increased in terms of purity with a loss in efficiency, when incorporating the **angle criterium**. For the angle criterium, the direction of the primary particle is reconstructed according to the first hits directional sum, that is explained in the next chapter. This direction is used to calculate the angle between the reconstructed direction and the difference vector of pixel position and reference point. All hits, of which the angle is greater than 45° are considered as scintillation photons. The remaining photons are separated via the light separation method described previously.

Results for the light separation with angle criterium are shown in figure 8.6. The influence of the cut value in (a) in comparison to figure 8.5 (b) shows that the purity decreases and the efficiency increases slower for higher cut values than for the method without the angle criterium. The MCC shows that the angle criterium worsens the performance, because the decline in efficiency is not compensated for with the rise in purity. The cut value of $C_{\mathrm{Sep}} = 0.09$ is chosen for the plots in (b) and

(c) to be comparable with the plots in figure 8.5 (c) and (d). This results in overall values for MCC of 0.69 ± 0.13, purity of 0.87 ± 0.08 and efficiency of 0.64 ± 0.18. The cut value of 0.12 would perform slightly better in terms of MCC with a difference of 0.005 in the mean values and a smaller standard deviation of 0.01. The number of photons plots shown in figure 8.5 stay also valid for the angle criterium.

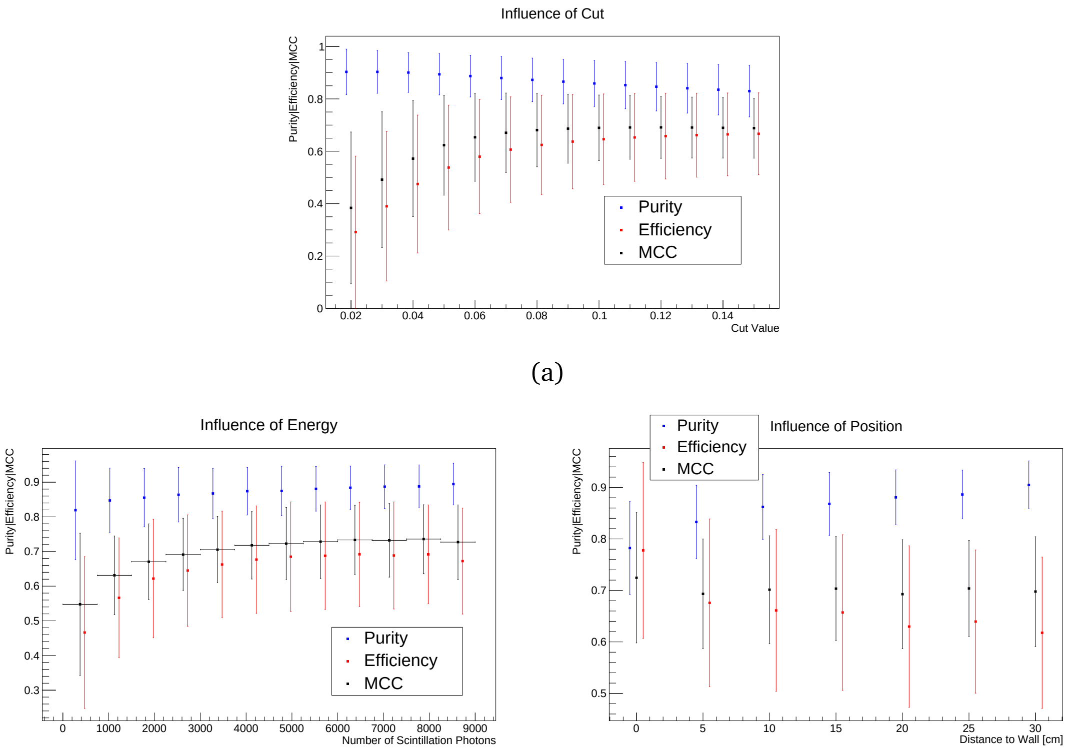

(a)

(b)

(c)

Figure 8.6.: Light separation results for the electron sample with angle criterium. (a) shows the influence of the cut values, (b) the influence of energy and (c) the influence of the event's position on the performance.

The influence of energy in (b) shows that the purity stays on a high level with rising energy, but the variation declines shown by smaller error bars. Comparing (b) to 8.5 (c) shows that the behaviour of the metrics is opposite for the angle criterium than for the regular method, since the efficiency rises for higher energies, whilst for the regular method the efficiency stays rather stable and the purity shows a rise. This can be explained by the increasing performance of the direction reconstruction for higher energies. Thus, less of the Cherenkov photons are excluded due to the angle between the true direction and the reconstructed angle of the electron so that the efficiency rises.

The influence of position in (c) can be compared to figure 8.5 (d). The rise of the purity and the decline in efficiency is observable for both methods. For the angle criterium the overall purity is again higher. The difference in efficiency between the $0\,\mathrm{cm}$ and the $5\,\mathrm{cm}$ marker is higher than for the regular method. This is due to the Cherenkov disk that occurs, when the particle exits the detector or the pri-

mary particle path ends close to the detector wall. A difference in the direction of the primary particle and the reconstructed direction excludes more photons in the ring than in the disk case.
The angle criterium for the other samples are not discussed here, but can be found in the appendix A.

8.3.2. Low energy electron

The results for the low energy electron sample with energies between 0.5 and $10\,\mathrm{MeV}$ is shown in figure 8.7. Since this sample is the first energy interval of the regular electron sample with more statistics, comparable results are expected. The ratio plot of (a) shows a very similar distribution to the full electron sample, but with a higher scintillation distribution even for low values of ratio. The metrics versus cut value plot in (b) shows again the expected increase of efficiency with the simultaneous decrease of purity and a maximum of MCC at $C_{\mathrm{Sep}} = 0.1$, which is chosen as cut value. Comparing figure 8.5 (b) to 8.7 (b) shows that the overall metrics for the low electron sample are slightly worse than for the full electron sample. This is also expected when taking figure 8.5 (c) into account, where it was shown that the first energy interval performs the worst in the full electron sample.
Figure 8.7 (c) tells a similar story than for the full electron sample, as again the lowest energy interval shows the worst results, reaching values of less than $50\,\%$ for all metrics. It is to note that here the intervals have a size of 82 photons roughly corresponding to $1\,\mathrm{MeV}$. The second photon interval for example goes from 82 to 164 and therefore roughly from 1 to $2\,\mathrm{MeV}$, whilst the first interval covers $< 1\,\mathrm{MeV}$. As it will be discussed in section 9.1.2, the energy intervals are not perfectly aligned with the energy and have to be viewed as an inaccurate assumption. Going to higher energies improves the situation notably and in the third interval a performance is reached that stays stable for the higher energies. Expressing this in energy means that starting at roughly $2\,\mathrm{MeV}$ the light separation algorithm performs good with the best values at the photon interval of 697 with a MCC of 0.73 ± 0.09, a purity of 0.67 ± 0.09 and an efficiency of 0.92 ± 0.12. (e) shows again the linear increase of all photon distributions.
(d) shows that the influence of the distance to the detector wall is again a minor one and that the purity and MCC increases slightly with greater distance whilst the efficiency stays on a stable level. Here, the first two photon intervals are excluded. The number of photons in (f) shows a very similar behaviour to the full electron sample and can be viewed as nearly constant, but due to the lower energy the number of events leaving the detector is smaller so that no substantial decrease in photon number for the $0\,\mathrm{cm}$ marker can be seen. Overall the performance of the light separation for the full low electron sample can be viewed as good with values of 0.69 ± 0.16 for MCC, 0.65 ± 0.14 for purity and 0.84 ± 0.22 for efficiency.

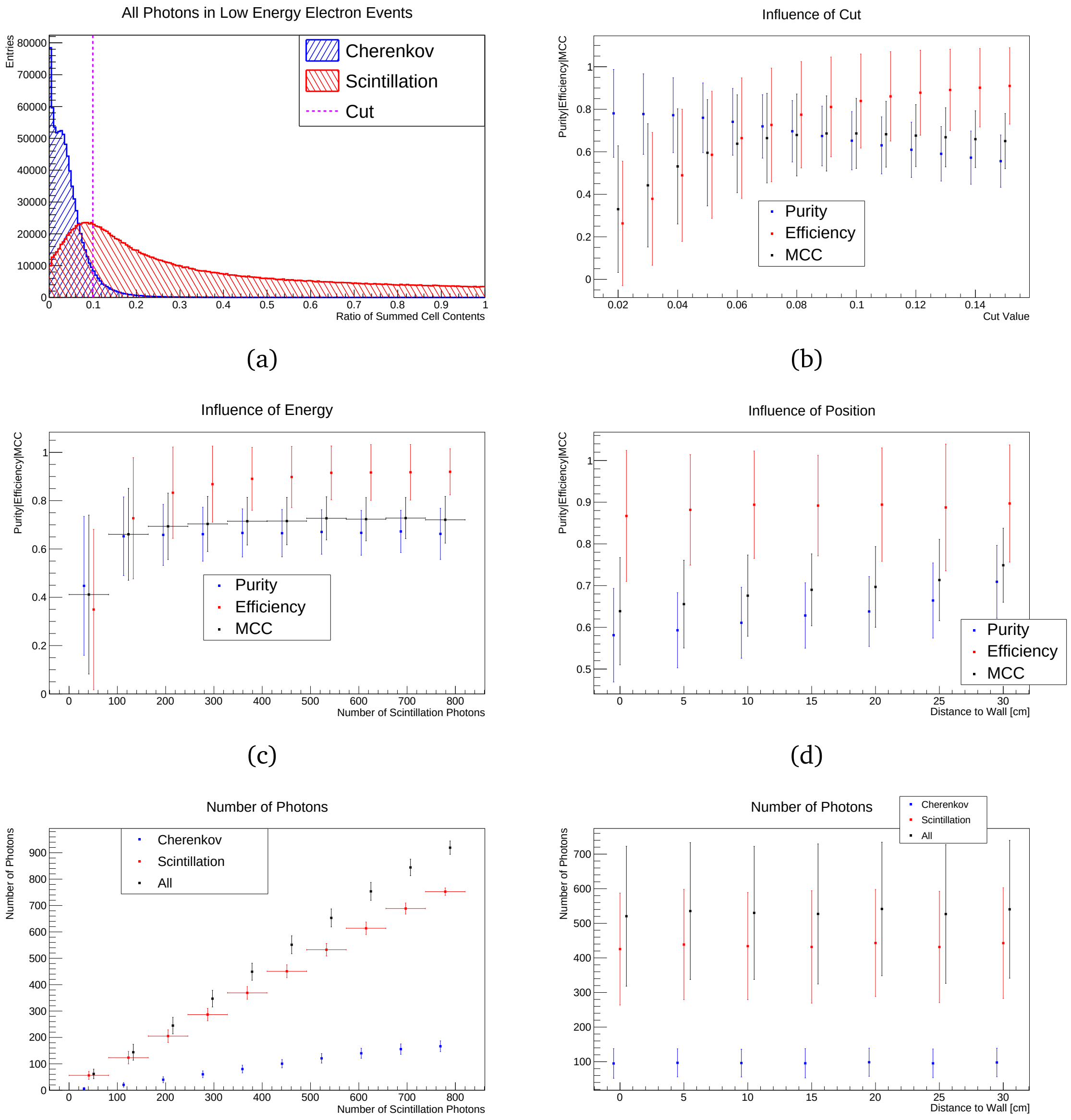

(a) (b) (c) (d) (e) (f)

Figure 8.7.: Light separation results for the low energy electron sample. (a) shows the ratio of the summed cell content for all photons with the indication of the chosen cut value based on the maximum MCC, that is shown together with the purity and efficiency with respect to the cut value in (b). (c) shows the influence of the energy in terms of the true number of scintillation photons. The number of events in relation to the energy in terms of photon intervals is shown in (e). (d) shows the influence of the position of the event on the performance; (f) is the same as (e) but for the position of the event.

8.3.3. Gamma

For the gamma sample, the results are shown in figure 8.8. Since gammas are expected to produce an electromagnetic shower that is very similar to the event characteristics of electrons, the results for the gamma sample can be best compared to the results of the full electron sample in figure 8.5. Comparing the ratio plots of both sample in (a) shows that for gammas a high number of scintillation photons contribute at the lowest ratio values and overlap there with the Cherenkov photons. This can be explained with the Compton scattering of the gammas, which leads to low energy electrons and to an overall higher event expansion. This in turn leads to scintillation photons that have a high Cherenkov cell content contribution, because the Cherenkov isochrone of e.g. a low energy electron can match accidentally the probability mask content of a different electron or positron. In addition, the reference point for the TTR is set to the smeared primary vertex position. A vertex reconstruction would likely not find the vertex at that position for a Compton scattering gamma, especially when the gamma exits without a significant photon emission the detector, since a vertex reconstruction pins down the position of highest photon emission. Going to higher ratio values, the contribution of scintillation photons is lower than for the electron sample.

The influence of the cut value in (b) is as expected similar to the other two samples, although the purity does not decrease as fast and stays comparatively high, since the number of scintillation photons towards higher ratio values in (a) is lower than for the other samples. The cut value of $C_{\mathrm{Sep}} = 0.13$ is chosen for the further analysis, as it has the highest value for the MCC of 0.61 ± 0.32. The purity for this cut value is 0.69 ± 0.25 and the purity amounts to 0.70 ± 0.32.

An interesting observation can be made in (c), since the lowest photon interval has drastically lower performance compared to the remaining photon intervals. This behaviour was also observed for the other two samples, but for gammas the effect is stronger. This can be explained by the Compton scattering nature of the gamma that leads to low emission of photons and a higher number of events, for which the primary particle leaves the detector. This means on one hand that in the lowest photon interval there is a higher number of gamma events than electron events, which will be shown and discussed in the next chapter. On the other hand there is also a higher number of gamma events that emits only singular Cherenkov photons, for which the performance of the light separation algorithm suffers. Comparing figure 8.5 (e) to figure 8.8 (e) shows that the photon emission in the first photon interval for gammas is lower than for electrons.

Whilst gammas emit 25.69 ± 41.85 Cherenkov and 206.35 ± 192.30 scintillation photons, electrons emit 83.23 ± 53.26 Cherenkov and 391.06 ± 207.07 scintillation photons. Going to the higher photon intervals, the number of photons equalizes to the ones seen for the electron sample and the performance of the light separation algorithm stays on a high level. Nevertheless, the outlier at the lowest photon interval explains the higher variances for the metrics for the total sample in comparison to the previously discussed samples. The peak performance is reached at 5625 scintillation photons with a MCC of 0.78 ± 0.14, a purity of 0.77 ± 0.13 and an efficiency of 0.89 ± 0.13.

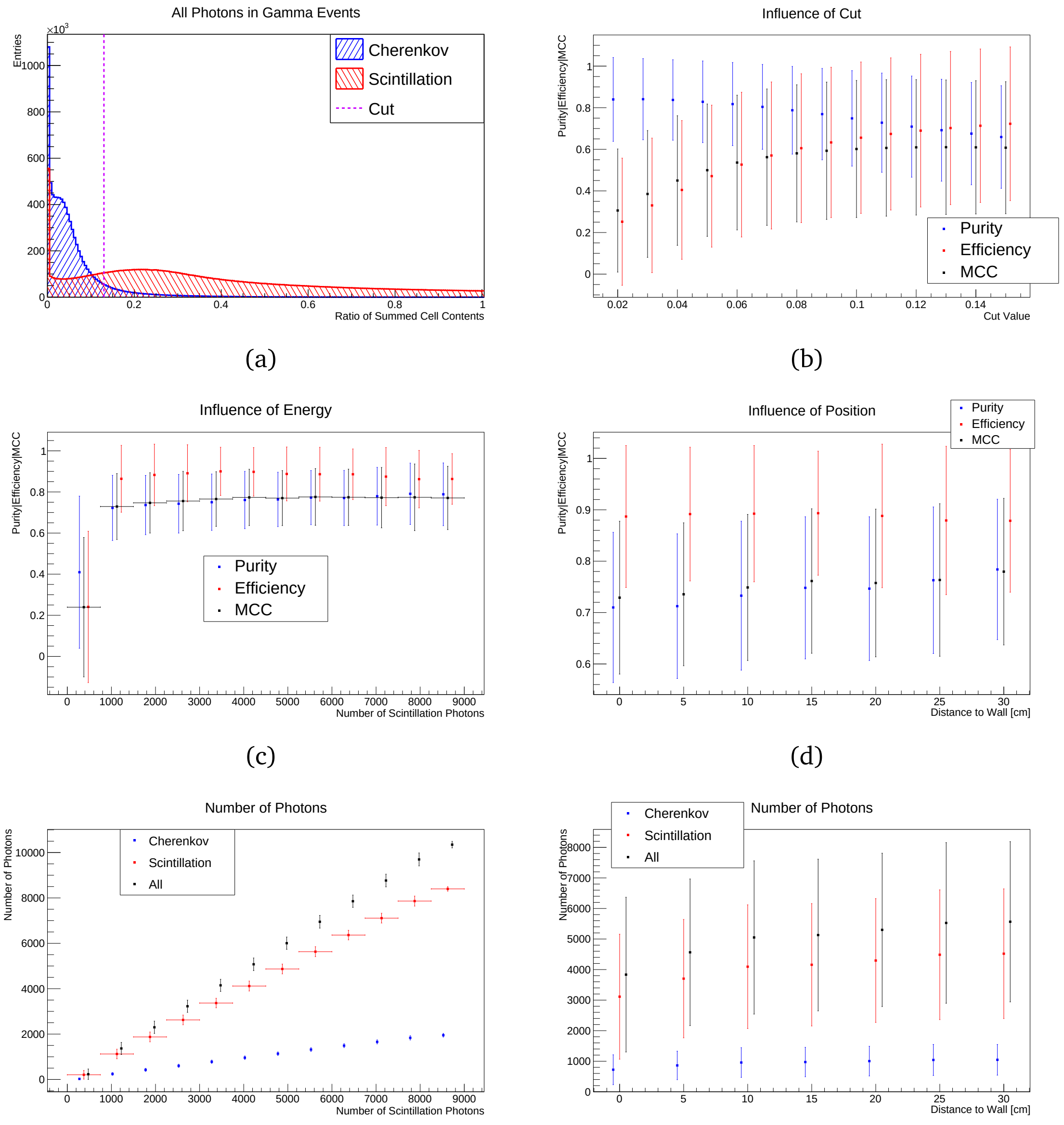

(a) (b)

(c) (d)

(e) (f)

Figure 8.8.: Light separation results for the gamma sample. (a) shows the ratio of the summed cell content for all photons with the indication of the chosen cut value based on the maximum MCC, that is shown together with the purity and efficiency with respect to the cut value in (b). (c) shows the influence of the energy in terms of the true number of scintillation photons. The number of events in relation to the energy in terms of photon intervals is shown in (e). (d) shows the influence of the position of the event on the performance; (f) is the same as (e) but for the position of the event.

The influence of the position on the performance is shown in (d), while the number of photons is shown in (f). Hereby, the first photon interval is excluded to extract the influence of the position. With that, a similar result like for the already discussed samples can be observed with a small rise in purity and MCC and a stable efficiency. In (f) it is notable that the first distance marker shows a considerable lower amount of photons.

For the gamma sample it is sensible to show the influence of the position plot for the whole sample to support the assumption that the performance decrease in terms of visible energy comes from the events, in which the primary particle leaves the detector. The influence of the event position for all events in figure 8.9 in (a) reflects that events leaving the detector happen more often for gammas and pose a higher difficulty for the algorithm, as the first point shows significantly worse performance compared to the other two samples and also compared to the remaining points, for which the performance is similar to the other samples on a consistently high level. The number of photons in (b) shows that the first point has also a lower number of emitted photons compared to the other data points. This behaviour is exclusive to the gamma sample and is not observed in the electron samples and is again the result of Compton scattering and the higher number of gamma events that leave the detector without emitting a substantial number of photons.

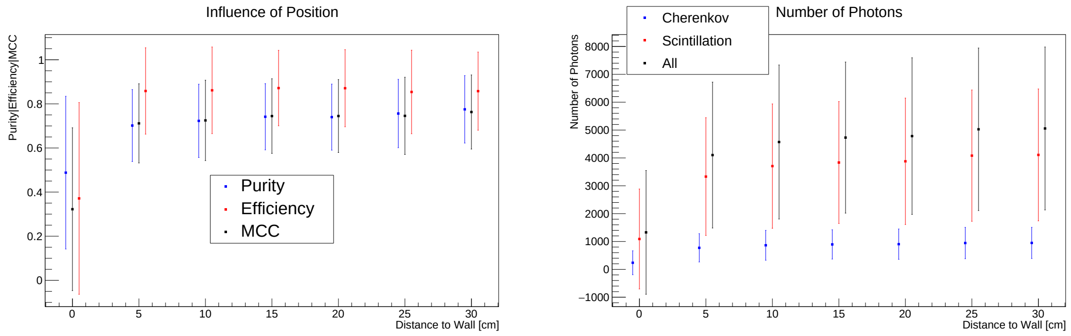

(a) (b)

Figure 8.9.: Influence of the position on the performance in (a) and the number of photons in (b) for the whole gamma sample.

8.3.4. Muon

The muon sample is different compared to the previous samples because of the Cherenkov threshold of about $52\,\mathrm{MeV}$ (compare table 4.2), which has a high influence on all of the result plots. In (a) it is visible that the total number of Cherenkov photons is small in comparison to the scintillation photons, since about half of the non-decaying muons only emit scintillation photons. Nevertheless, a Cherenkov sample can be found with a cut on the ratio value that contains more Cherenkov than scintillation photons. (b) shows again the influence of the cut and it is visible that the variance of the events is higher than for the previous samples, since many of the events do not contain Cherenkov photons at all. This also leads to low mean values for all metrics. In this case, a cut at $C_{\text{Sep}} = 0.14$ is chosen, as it was also confirmed that this value would be a good compromise looking at only the Cherenkov emitting muons. This leads for the whole sample to poor values for the metrics of a MCC of 0.32 ± 0.32, a purity of 0.29 ± 0.32 and an efficiency of 0.41 ± 0.43, since the low energy events without Cherenkov radiation decrease the overall performance.

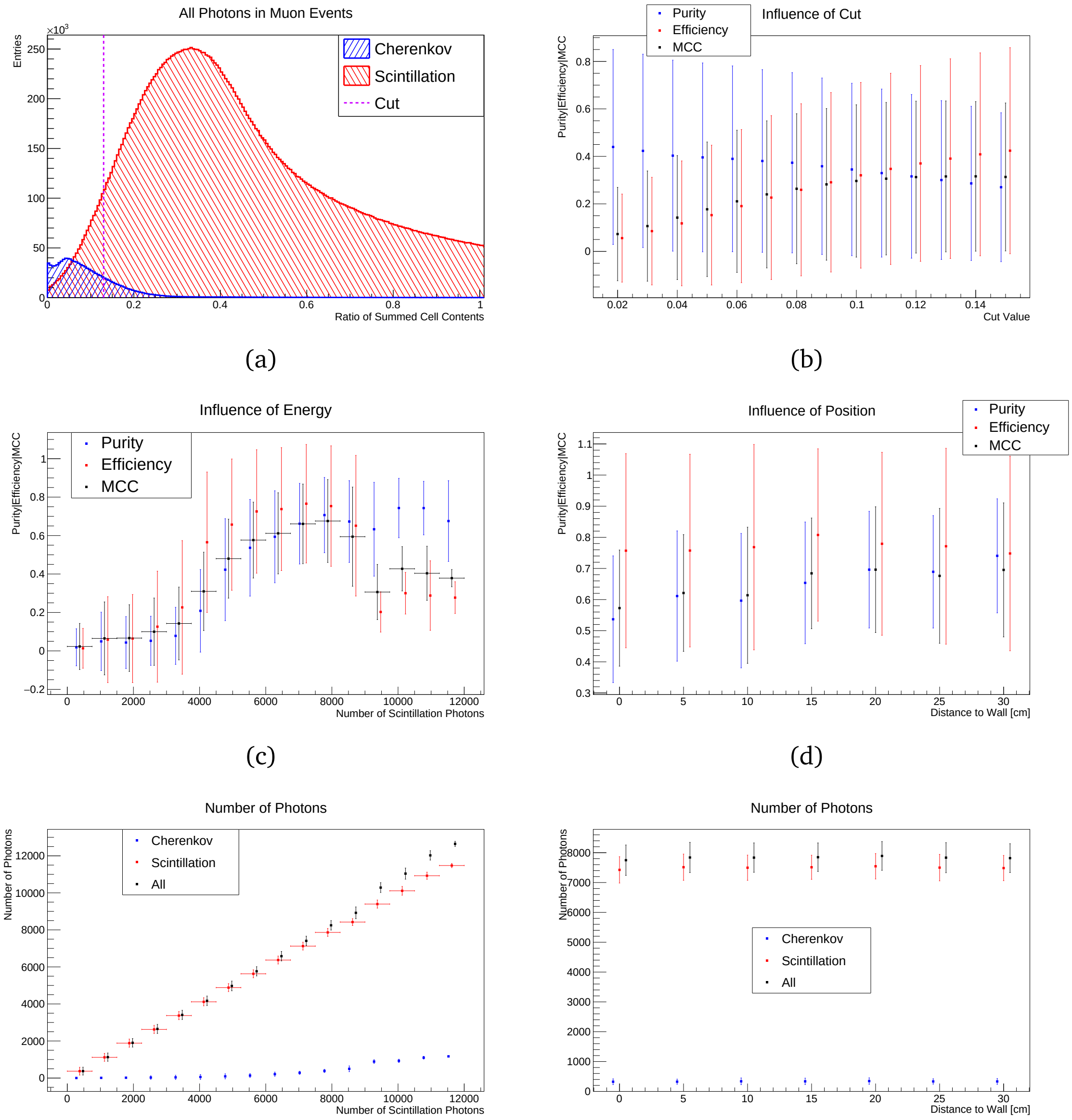

(a) (b)

(c) (d)

(e) (f)

Figure 8.10.: Light separation results for the muon sample. (a) shows the ratio of the summed cell content for all photons with the indication of the chosen cut value based on the maximum MCC, that is shown together with the purity and efficiency with respect to the cut value in (b). (c) shows the influence of the energy in terms of the true number of scintillation photons. The number of events in relation to the energy in terms of photon intervals is shown in (e). (d) shows the influence of the position of the event on the performance; (f) is the same as (e) but for the position of the event.

For the influence of energy plots, it needs to be stressed that the x-axis displays a wider range due to the higher maximum number of scintillation photons emitted due to Michel electrons. The number of photon plot in (e) with respect to the number of scintillation photons shows that aside of the decaying muons the Cherenkov photon emission starts at the 4125 photon interval. This is also reflected in the influence of energy plot in (c), where the metrics are marginally above zero, before they rise at said interval. The performance rises further to the 7875 photon interval, before it drops down and reaching worse efficiencies and MCC values below 0.45 starting at the 9375 interval. This decrease is because only the decaying muons contribute to these high number of scintillation photons, for which the emission time of the photons from the Michel electron do not match the muon's track. The influence of energy shows also that the metrics can be used to estimate the number of Cherenkov photons due to very poor results for no Cherenkov radiation at all and then increasing values for higher scintillation photon numbers. For the future, this behaviour might be usable to identify muons that decay in the event window.

For these muons the TTR seems to perform poorly, since the photons from the Michel electron can come with a substantial delay up to the length of the readout window of $100\,\mathrm{ns}$, whilst the reference point is set to a smeared primary vertex time. The peak performance of the light separation algorithm for muons is at 7875 with a MCC of 0.68 ± 0.22, a purity of 0.71 ± 0.20 and an efficiency of 0.75 ± 0.31.

For the influence of position plot in (d) and (f) the photon intervals below 6750 and above 8250 are excluded to again eliminate the substantial influence of the energy on the discrimination's performance. The number of photon plot in (f) shows no influence of the event position, whilst the purity and MCC shows a mild increase towards higher distance, while the efficiency stays on roughly the same level. The high variance on efficiency originates from the chosen cut value from (b).

8.4. Discussion

The chosen method for the separation of Cherenkov and scintillation light works well for all particles. For context the main assumptions that lead to the results are here summarised:

- The simulated detector is completely covered with LAPPDs.
- Reflection, scattering and absorption is simulated; reemission is not.
- Perfect reconstruction of the hits on the LAPPDs is assumed meaning that no readout nor electronics are simulated.
- Time and spatial resolution of $0.1\,\mathrm{ns}$ and $> 1\,\mathrm{mm}$ with a pixel size of $5\,\mathrm{mm}$ is assumed for the LAPPDs.
- The primary vertex is assumed to be reconstructed with an uncertainty of $1\,\mathrm{cm}$ in space and $0.2\,\mathrm{ns}$ in time.
- Hits below $100\,\mathrm{ns}$ after the start of the primary particles are considered.

Of these assumptions, the reconstruction of the vertex in space and time deserves further discussion. First of all, it is unlikely that a vertex reconstruction performs on the same level for different visible energies and the topology of the event. Secondly, it was found in Borexino with $\approx 0.4\%$ Cherenkov photons that the reconstructed vertex is systematically shifted towards the flight direction of the particle by about $2\,\mathrm{cm}$ for energies between 0.5 and $0.8\,\mathrm{MeV}$ due to the Cherenkov photons [208]. This systematic shift has to be investigated in the future for all results presented in this thesis. Furthermore, it is questionable how the systematic shift is correlated to the percentage of Cherenkov photons and the overall event energy.

One option to correct for a shifted vertex in the light separation algorithm is given here: The reconstructed vertex is used as reference point for the TTR. A shift in reference point does not harm the TTR per se, since any point on the track can be used as reference point[2]. The issue arises with the corresponding reference time, that would be too early to fit the hits on the photosensors. In consequence, the systematic shift on the vertex reconstruction can be investigated and a time correction can be applied to the reference time. For that, knowledge of the particle direction is not necessary, so that it should be possible for nearly all energies. At the lowest energies of a few MeV, the track length can be smaller than the shift, which can lead to additional difficulties.

Furthermore, it is imaginable that a coarse light separation can help with filtering out Cherenkov photons and hence reduce the shift in reconstructed vertex. Following that, an iterative approach can be used to improve the vertex resolution, which in turn improves the performance of the light separation algorithm and so on.

The peak performance with respect to the visible energy of the particles is summarised in table 8.1 for the different presented samples. First of all, it has to be taken into account that the values are in general taken with different cut values that reflect a difference in the balancing of purity to efficiency and that in case of the low energy electron also a completely different energy range is assumed. Nevertheless, the values can give a hint on the performance of the light separation algorithm. The best metric for comparison is the MCC, since it reflects the purity as well as the efficiency and the relative population of Cherenkov and scintillation photon in the tested sample. It can be seen that the electron and gamma sample performed best with very similar results in MCC while for the chosen cut the purity (efficiency) for gamma (electron) is better. As it was discussed the overall performance is better for the electron sample taking all energies into account due to the Compton scattering nature of the gamma and therefore the difficulties of the algorithm for the lowest visible energies. The low electron performance is slightly worse than the electron and gamma performance, which is due to the

---

[2] The TTR has methods to deal with reference points that are towards the end of the track by calculating in the so called “backwards in time” mode.

general slight visible energy dependence of the performance. The muon sample performs the worst and has also the highest variance, which is due to the decaying muons.

Table 8.1.: Summary of the light separation peak performance.

Sample	MCC	Purity	Efficiency
Electron	0.79 ± 0.10	0.81 ± 0.08	0.87 ± 0.15
Low Energy Electron	0.73 ± 0.09	0.67 ± 0.09	0.92 ± 0.12
Gamma	0.78 ± 0.14	0.77 ± 0.13	0.89 ± 0.13
Muon	0.68 ± 0.22	0.71 ± 0.20	0.75 ± 0.31

The influence of the event's position can be viewed as a minor one, since the performance shows only slight increase for higher distances to the detector wall for all samples except the gamma sample. For the gamma sample, as shown in figure 8.9 the influence of the position for all events is high due to the gamma events, in which the primary particle leaves the detector, and/or gamma events that start and end near the detector edge. This means that the performance can be increased with a fiducial volume cut, especially for the gamma sample.

The achieved purities can be compared to the results of reference [173], where the combination of WbLS and a LAPPD is used for light separation on the MeV level based on a timing cut. For 5% WbLS a purity of 68.8% is reached in that work, which is comparable to the results shown for the low energy sample in figure 8.7. It is to note, that the LAPPD in that paper has a worse TTS and that the timing constants of the scintillation model differ from the values assumed in this thesis. In reference [172] a similar experiment was conducted using PMTs for measuring cosmic muons reaching a purity of $(81 \pm 2)\%$ and an efficiency of $(84 \pm 4)\%$ for 5% WbLS, which are better results than shown in this thesis. Both of these works are based on the CHESS experiment [171]. It can be assumed, that the event topologies considered in these papers are more constrained than the ones in this thesis, which might explain the difference in performance.

It needs to be stressed that the purity and efficiency values can be finetuned by the cut value depending on the desired application and that the presented results reflect only one choice of parameters for the TTR as well as for the light separation algorithm optimised for MCC. For the tuning also the angle criterium can be taken into account. Since this criterium depends on the reconstructed direction, it is questionable how this method will perform with a vertex reconstruction, as it will be discussed in section 9.1.2. Furthermore, the high variance of the metrics shows that the events even at similar energies and distances can have quite different ratio distributions. A dynamic cut that takes for example the number of photons and the position of the track as well as the shape of the ratio distribution into account is desirable for the future. Finally, it is vital to develop and apply a vertex reconstruction to evaluate the shown results in the future.

9. Applications of the Light Separation

In this chapter, the two applications of the successful light separation of the previous chapter are discussed. Firstly, the direction reconstruction of low energy electrons and secondly, the PID of particles is shown.

9.1. Direction Reconstruction of Low Energy Electron Events

As it was discussed in section 4.5.1, the direction of low energy electrons can be used to discriminate between solar neutrinos and $0\nu\beta\beta$ signals. In this section, the method for the direction reconstruction of low energy electrons is discussed, the results are shown and then discussed.

9.1.1. Method

Two methods in different configurations are used for the reconstruction of the electron's direction. The first method uses the result of the 5th raw iteration of the TTR, that was used for the light separation algorithm of the previous chapter. Finding the position of the maximum bin of these results and subtracting the position of the reference point yields a direction vector. These results are labelled as **TTR Cherenkov** and **TTR Scintillation**.

The second method is a directional sum s. The directional sum is calculated by using the difference vectors of the reference point $\vec{r}_{\mathrm{ref}}$ to the pixel position $\vec{r}_i$ of the ith hit. These difference vectors are normalised to one and summed up. This can be expressed as

$$s = \sum_{i=1}^{n} \frac{\vec{r}_i - \vec{r}_{\mathrm{ref}}}{|\vec{r}_i - \vec{r}_{\mathrm{ref}}|} \tag{9.1}$$

with n as the number of hits in the event. The directional sum with all hits is called **Directional Sum All Hits**.

Since the scintillation hits are emitted isotropically, only the Cherenkov hits should have a high impact on the directional sum vector, so that the directional sum should point in the direction of the true particle direction. Since scintillation hits can still impose a perturbation on the performance of the directional sum, the directional sum is also calculated for the Cherenkov sample using a cut of $C_{\mathrm{Sep}} = 0.08$ on the ratio of summed cell contents. This will be called **Cherenkov Directional Sum** in the following. Additionally, only the first $30\,\%$ percent of hits sorted by the ratio of summed cell content is used to calculate a third directional sum. In the case that the first $30\,\%$ are less than 10 hits, the first 10 hits are used and events with less than 10 detected photons overall use the conventional directional sum for all photons. This directional sum will be referred to as **First Hits Directional Sum**.

It is to note that not only the direction of a directional sum, but also the length is of interest. The length increases when the hit distribution favours one direction. Hence, a higher number of Cherenkov photons leads to a greater length. In other words, the length of the directional sum could be used to estimate the number of Cherenkov photons in an event.

9.1.2. Results

The results for the different methods for all events are shown in figure 9.1, where the angle between the reconstructed direction and the MC truth direction is displayed. The left side shows the distributions without any weighting, whilst the right side shows the number of events divided by the sinus of the angle that corresponds to the respective bin center to approximately account for the solid angle. (a) and (b) show the distributions across all possible angles and (c) and (d) are zoomed in to only show the range to about $90°$.

The first observation is that the method using the TTR (dark green for Cherenkov and yellow for scintillation reconstruction) performs worse than the directional sum. Comparing both TTR approaches shows little difference. This means that treating all photons as Cherenkov or scintillation photons yields similar results for finding the direction of the electron with the TTR.

The directional sum results show also similar results, whereby using the first hits sorted by ratio seems to perform best (black), followed by the directional sum only using the hits in the Cherenkov window (red) and the regular directional sum with all hits (blue). This is especially good visible in looking at (b) and (d), where the height of peak for the smallest angle differs for the three directional sum methods. Nevertheless, it needs to be stressed that the distributions all peak at $12°$ in (a) and (c), meaning that for most events a significant deviation from the MC truth direction is reconstructed. This deviation is even higher for the TTR method, where the distribution is broader and reaches high values for $15°$ to $25°$.

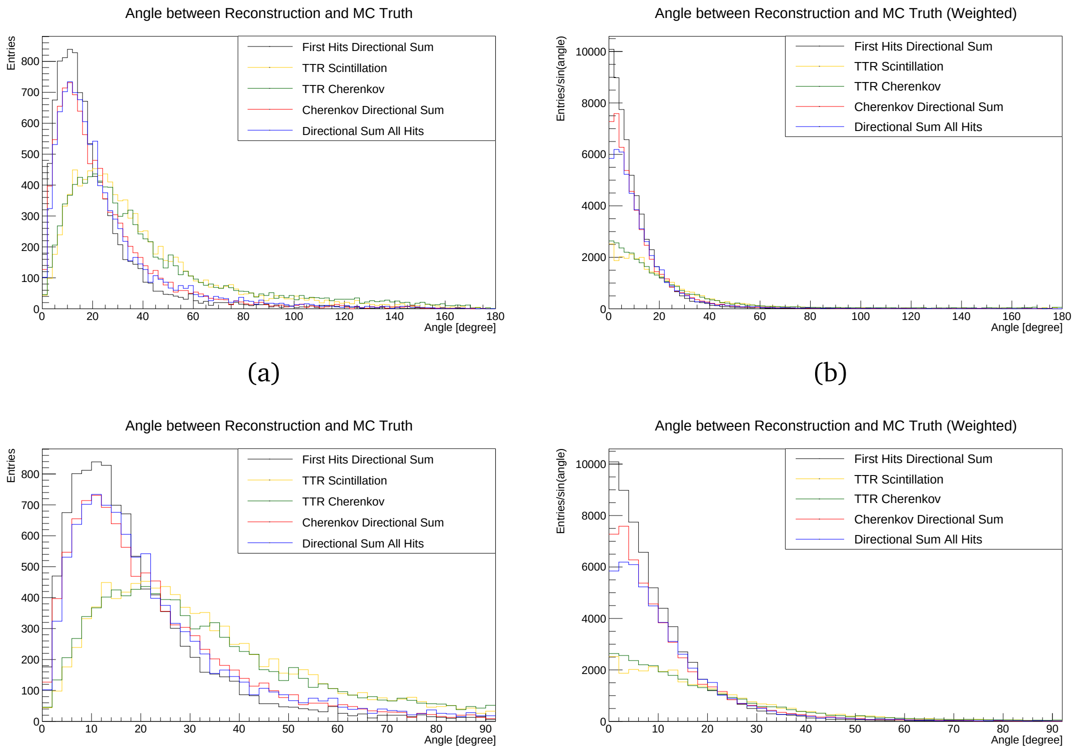

(a) (b)

(c) (d)

Figure 9.1.: Results for the direction reconstruction for all events. (a) shows the results for different methods; (c) shows the same but zoomed to only show angles below $90°$. (b) and (d) show the results in the same manner but here the number of events is weighted by the sinus of the angle corresponding to the bin center to account for the solid angle.

The three best methods are further investigated in terms of energy and distance to the wall of the event. The angle between reconstructed and MC truth direction is filled in histograms for the number of scintillation photons or the distance in question. In figure 9.2, the mean of these histograms are shown as markers, whereas the error bars show the standard deviation. In (a) the influence of energy in terms of number of scintillation photons is shown in that manner, where the horizontal error bars for the red markers show the width of the intervals. (c) displays the number of events in the intervals to show the underlying statistics again with horizontal error bars for the width of the intervals. Notable is that the lowest photon interval has about 750 events, since this is the energy interval of roughly lower than $1\,\mathrm{MeV}$, where only a little more than $10,000/20 = 500$ events are expected. The translation of energy to scintillation photon number is not exact though, which can be explained with exiting events, in which the electron deposits only part of its energy in the detector. This is also the reason for the low number of events for the two highest photon interval, since for higher energy events the probability for exiting the detector is higher. Furthermore, the highest point corresponds only to the highest energies near $10\,\mathrm{MeV}$ yielding only about roughly 50 events. This means, the lower intervals roughly cover already the range of 0.5 to nearly $\approx 10\,\mathrm{MeV}$ and the intervals therefore correspond to approximately $1.1\,\mathrm{MeV}$.

As it is shown in (a) the performance of the direction reconstruction increases for all methods with rising visible energy (number of scintillation photons). Furthermore, it becomes clear that all three directional sum methods perform very similar, whereby the first hits directional sum (black) performs best for all photon intervals. In the first four intervals the Cherenkov directional sum (red) performs slightly better than the regular directional sum (blue). Towards higher energies, the regular directional sum performs then slightly better than the Cherenkov one. The biggest increase in performance is going from the first photon interval with e.g. $(57.84 \pm 38.12)^\circ$ for the Cherenkov directional sum to the second photon interval with $(34.01 \pm 26.55)^\circ$. The highest overall performance is reached for the first hits directional sum in the last photon interval with $(13.49 \pm 13.02)^\circ$. The increase in performance is also clearly visible in the standard deviation. The variance is also the lowest for the first hit directional sum. Notably, the variance of the Cherenkov directional sum is higher towards higher energies, even compared to the regular directional sum. This can be explained by the loss of Cherenkov photons and their directional information due to the efficiency of the cut, whilst keeping scintillation photons in the cut window that hinder the reconstruction of the direction. As it was discussed, the light separation algorithm can perform differently depending on the event topology, so that an additional variance is brought into the Cherenkov directional sum. Using the first hits sorted by ratio seems to overcome this problem.

The influence of the distance to the wall of the events is shown in (b) with the number of events displayed in (d). To decrease the influence of the energy, only events with a number of scintillation photons above 328 are shown. The number is chosen in that way to be in accordance to the last six photon interval markers. It can be seen that the performance increases towards higher distances. The most notable gap is between the $0\,\mathrm{cm}$ and the $5\,\mathrm{cm}$ markers because of the inclusion of exiting events and the general edge effects of the TTR and therefore the light separation. Whilst the directional sum with all hits and the first hits directional sum shows a rather stable performance, the Cherenkov window directional sum shows a more notable increase in performance, which is due the dependence of the light separation algorithm on the distance as well. It is to note that (d) shows a flat distribution of event numbers except for the $30\,\mathrm{cm}$ marker, where a higher number of events is located. This is due to the fact that, the last marker covers more of the detector's volume.

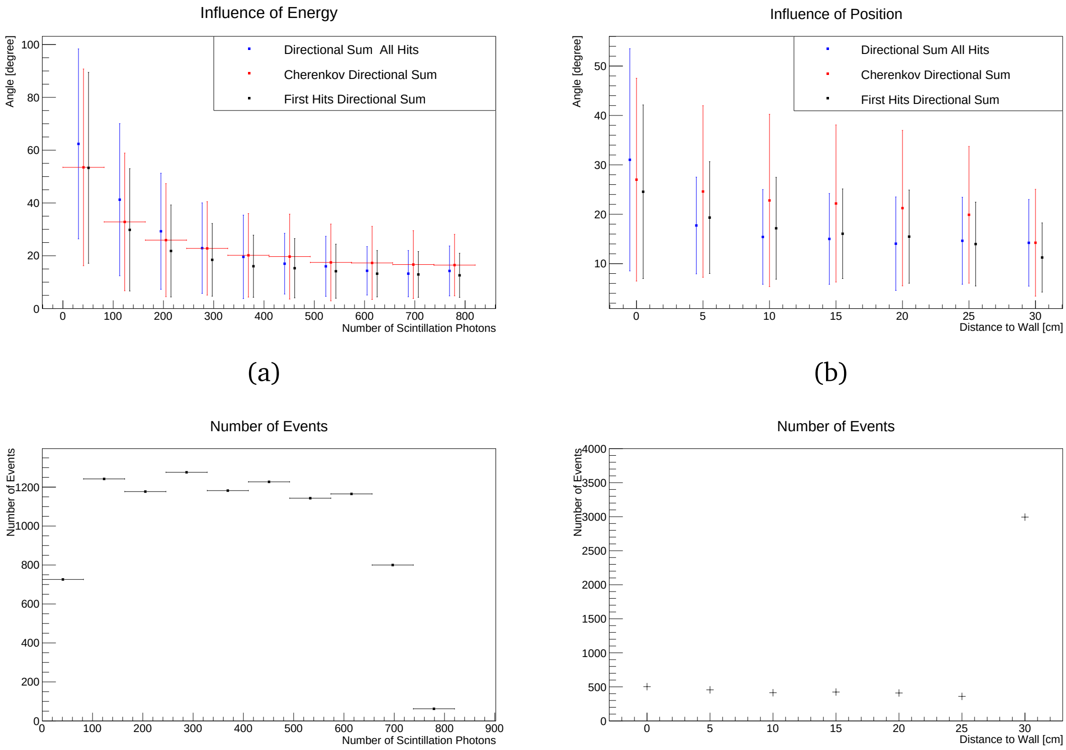

(a) (b)

(c) (d)

Figure 9.2.: Influence of the energy in (a) and the distance to the detector wall in (b) on the direction reconstruction results. For (b) only events with more than 328 scintillation photons are accepted. The number of events is shown in (c) for the photon intervals and in (d) for the events in the respective distance to the wall. In (a) the last interval corresponds to the highest energies near $10\,\mathrm{MeV}$ meaning that the intervals before that roughly show 0.5 to $\approx 10\,\mathrm{MeV}$, so that each interval corresponds to roughly $1.1\,\mathrm{MeV}$.

9.1.3. Discussion

Additionally to the preconditions discussed in section 8.4, a few more assumptions have to be made clear for the direction reconstruction. First of all, the direction of a solar neutrino does not perfectly coincide with the direction of the subsequent electron so that an additional angle would have to be taken into account. Furthermore, again a primary vertex has to be reconstructed for the discussed methods to work. As previously discussed, a systematic shift on the reconstructed vertex towards the direction of the electron is expected. This shift can cancel out the direction information of the Cherenkov photons, so that a directional sum would be completely random and would have a length of nearly $0\,\mathrm{cm}$. Furthermore, the correction proposed earlier for this problem in the context of the light separation algorithm does not apply here, because the directional sum does not rely on the timing at all [1]. This means, the results here should be viewed with caution and

---

[1] The selection methods to achieve the directional sum for a Cherenkov enriched sample rely on timing though.

a vertex reconstruction is needed in the future to accurately evaluate the shown methods.
Because the angle is determined between the primary direction that originates from the primary vertex and the reconstructed direction that comes from the reference point, the reconstructed angle is not to be viewed as exact, since the difference of the assumed primary position has also an influence. Since the smearing is a minor one, this effect is neglected here.
The results show that to higher energies, the direction reconstruction with the best three methods works quite well, whereas the TTR method is substantially worse. The regular directional sum shows already comparable results to the methods that make use of the light separation algorithm showing that a WbLS detector can reconstruct low energy electrons quite well without sophisticated algorithms, if the vertex is reconstructed with the assumed precision. This is due to the directionality of the Cherenkov photons. These results can be improved upon though, when a light separation algorithm is in place.
It can also been shown that events at the edge of the detector pose a difficulty for the direction reconstruction and the performance increases with higher distances to the detector wall.
Nevertheless, even for the best method at highest energy a difference of $(13.45 \pm 11.22)^\circ$ between the MC truth and the reconstructed direction is seen. Depending on the application and the desired background rate, the shown direction reconstruction can still be used to veto particle tracks, that are in agreement to the sun's position.
In the future, a vertex reconstruction has to be build to investigate the influence of Cherenkov photons on the mentioned systematic shift. Furthermore, the light separation algorithm can be improved, which should also lead to an improvement of the direction reconstruction. Additionally, other direction reconstruction algorithms like a circular Hough transform or a likelihood method can be implemented.

9.2. Particle Identification Using the Cherenkov to Scintillation Ratio

It was shown in section 4.5.2 that PID with the ratio of Cherenkov to scintillation photons is a valid option to improve the background reduction in the search for supernova neutrinos. In this section, the method for finding and improving the PID based on said ratio and the subsequent results are presented for the discrimination between e^-, μ^-, γ and p, followed by a discussion of the results.

9.2.1. Method

Based on the light separation algorithm shown in the last chapter, a Cherenkov and a scintillation sample can be defined, whereby all photons below the cut value are counted as reconstructed Cherenkov photons and all photons above the cut value are treated as scintillation photons regardless of the MC truth flag. This means that true scintillation photons can be labelled as Cherenkov photons and vice versa, when the ratio assigned to the hit lies in the respective sample. Then, the ratio of the number of reconstructed Cherenkov photons to the number of reconstructed scintillation photons is calculated to find another cut to discriminate between particles. The cut on the ratio of Cherenkov to scintillation photons will be labelled C_{Ratio}.

For the muon/proton and the gamma against muon and proton discrimination it has been found that including the angle criterium enhances the performance, on which the cut is denoted as C_{Angle}. This angle criterium overall improves the purity of the Cherenkov sample, when the direction can be reconstructed based on the first hits directional sum. This direction reconstruction performs best for events with a high number of Cherenkov photons so that for gammas a higher percentage of Cherenkov hits lay within the assumed Cherenkov cone than for muons and protons. Therefore, the number of hits in the Cherenkov window increases more for gammas than for muons and protons, when comparing the regular light separation with the inclusion of the angle criterium. The same happens when comparing muons above Cherenkov threshold to protons.

Additionally, the product of the length of the directional sum obtained by the first hits directional sum and the ratio with angle criterium shows even better results for selecting muons against protons. The length of the directional sum increases when there is a direction favoured in the distribution of hits. The Cherenkov photons of the muons above Cherenkov threshold therefore lead to a greater length of the directional sum in contrast to the purely isotropic scintillation hit distribution of the protons. The cut on the product of ratio and directional sum is called C_{DirSum}.

Furthermore, it has been found that for selecting electrons (gammas) against a background of muons and protons the shape of the summed cell content ratio distribution can be used, that is displayed e.g. in figure 8.5 (a) for the electron sample. Such a distribution for all photons regardless of type is achieved for each event. Since the electron and gamma events feature a high emission of Cherenkov photons, many of the hits have a small ratio in contrast to the muon and proton events where little to no Cherenkov emission is expected. This leads to a peak towards low ratios for gammas and electrons and towards higher ratios for muons and protons. This peak position correlates with the mean of the histogram, so that the mean value can be used for separation. This is done by filling only hits with a ratio of less than 0.5 in a histogram for each event individually and calculate the mean of these histograms[2]. These values are then filled in another histogram (see 9.4 (f) for example), on which a cut value can be defined that will be called C_{Mean}.

9.2.2. Results

Figure 9.3 shows the number of Cherenkov and scintillation photons as scatter plot (top) and the subsequent ratio (bottom) of the number of Cherenkov photons divided by the number of scintillation photons. The left side shows the MC truth and the right side shows the reconstruction, whereby a cut value of $C_{\text{Sep}} = 0.08$ is chosen for the light separation algorithm.

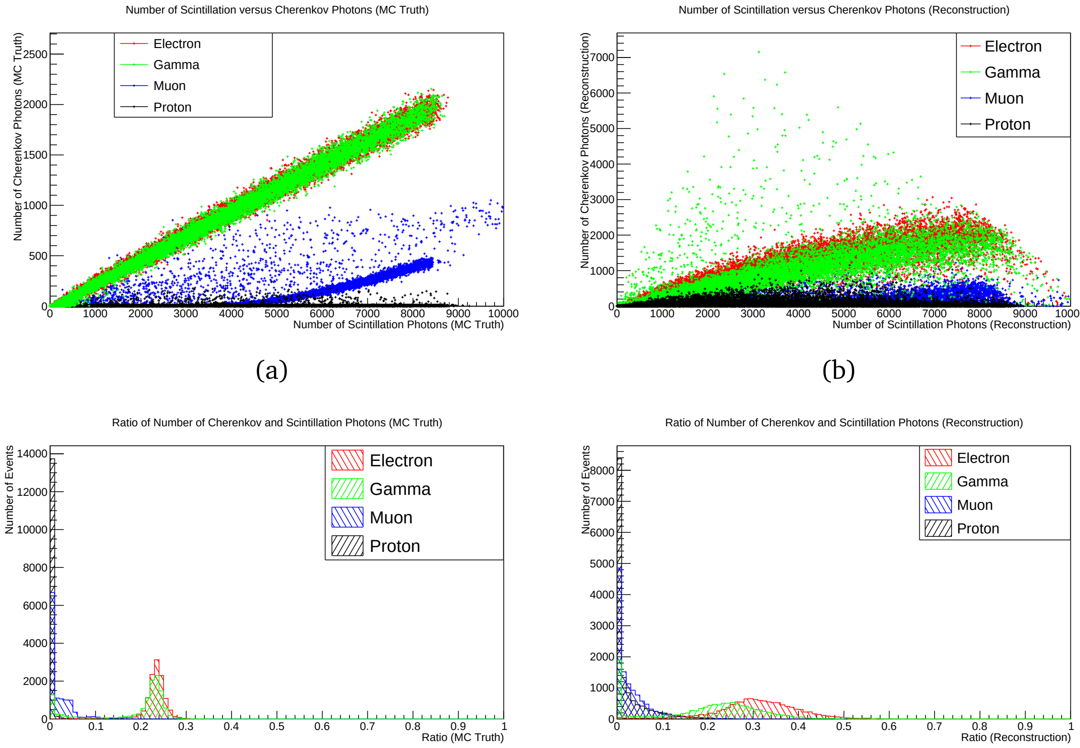

(a) (b) (c) (d)

Figure 9.3.: Scatter and ratio plots for the number of Cherenkov photons versus the number of scintillation photons for MC truth and reconstruction. (a) shows the MC truth as scatter and (c) as ratio plot. (b) shows the reconstruction as scatter and (d) as ratio plot.

(a) shows clearly that for the MC truth, the electron (red) and gamma (green) events are completely overlapping due to the fact that both particles create electromagnetic showers and therefore emit the same amount of Cherenkov photons. As expected most of the proton (black) events lay directly on the x-axis because no Cherenkov radiation is expected in the chosen energy range (below $140\,\text{MeV}$ for protons). Some proton events show a small number of Cherenkov photons (< 100) due to proton-electron scattering that leads to electrons with a kinetic energy above Cherenkov threshold. Nevertheless, these events are still separated

---

[2] Figure 9.4 (e) shows such a histogram for all events simultaneously.

from the electron and gamma events. For muons (blue), two populations have to be taken into account. The first one is the non-decaying muon population that shows below roughly 4000 scintillation photons no Cherenkov emission or only Cherenkov emission due to excited electrons. Towards higher energies, the muon exceeds the Cherenkov threshold leading to the linear rise resulting in about 400 Cherenkov photons at 8000 scintillation photons. The second population for muons are the decaying muons, leading to a Michel electron that contributes to the number of Cherenkov photons. These are the events that are visible between the regular muon events and the electron events with some occasional events reaching even into the electron events or above. It needs to be stressed that for low deposited energies and therefore low numbers of scintillation photons (below 500), the difference between the particles starts to vanish.

Translating the scatter plot into the ratio plot (b) confirms the observations made above: The proton events are mostly located in the first bin with a high amount of muon events, which are non-decaying muons below Cherenkov threshold. It is notable that also a significant number of gamma events are located in the first bins. This is due to the Compton scattering behaviour of the gamma and in turn the higher probability for gammas to exit the detector without emission of Cherenkov photons. Going towards higher ratios shows the contribution of the non-decaying muons above Cherenkov threshold and the Michel electron events. Starting at a ratio of 0.2 the overlaying peaks for the electron and gamma events emerge, whereby the number of events for electrons is higher due to the gamma contribution in the first bins.

(c) shows the reconstructed scatter plot, where all distributions are smeared out and the scale of the y-axis is chosen higher to show the gamma events with a high reconstructed number of Cherenkov photons. This is due to the fact that for some gamma events a significant number of scintillation hits have a low ratio of summed cell contents assigned (see figure 8.8 (a)), that are now counted as Cherenkov photons. For a high number of gamma events, the reconstructed number of Cherenkov photons is lower compared to that of the electron events. Both of these effects are assumed to be due to the higher expansion of gamma events. The proton and muon events both show a higher contribution towards a higher number of Cherenkov photons, which means that here again scintillation photons are misidentified as Cherenkov photons visible by the purity that was discussed in the last chapter. Towards higher deposited energies (> 5000 scintillation photons) the muon events are more prominent for a higher number of Cherenkov photons compared to the proton events. Finally, a clear discrimination between muon/proton and electron/gamma events is also visible in the reconstruction.

The reconstructed ratio in (d) shows that still a high number of proton and muon events are located in the first bin with a contribution of gamma events. In contrast to the MC truth, the proton events show a high contribution towards higher ratio overlapping the muon events and the electron and gamma events seem to be separable. It is also to note that the electron and gamma events have a broader distribution in the reconstruction reaching higher ratio values and that the gamma events with a high reconstructed number of Cherenkov photons are not visible, since they have a ratio higher than 1.0.

In the following, results for the particle discrimination for four different cases will be presented. The metrics already introduced in section 8.3 are used again to evaluate the results. Firstly, the selection of electron (gamma) events against muons and protons will be shown. This is followed by the results for discriminating electrons and gammas and finally muons and protons.

It is to note that the influence of energy is in the following displayed in terms of the reconstructed number of scintillation photons, that is for most events similar to the true number of scintillation photons. This is done to be able to interpret the resulting graphs with help of the scatter histograms like figure 9.3 (b).

The metrics values shown in the following are provided with error values that were estimated following the method for the MCC from reference [209]: $25\,\%$ of the events included in the respective data point are chosen at random with replacement (i.e. events can occur multiple times in the sample) and the metrics are calculated for that subsample. This is repeated one hundred times and the mean and the standard deviation of the resulting MCC, purity and efficiency distributions are calculated. The mean is then the position of the marker and the standard deviation resembles the size of the vertical error bars. The errors are therefore purely statistical and can be seen as an estimate to show the influence of beneficial and disadvantageous event distributions. It needs to be stressed that with this method variations of the mean and the standard deviation values can occur in the order of a few 10^{-3}.

Electron vs. Muon and Proton

In figure 9.4, the MC truth as scatter in (a) and as ratio plot in (c) as well as the reconstructed result as scatter in (b) and ratio plot in (d) is shown, whereas red shows the electron events and black muon and proton events. The cut value for the summed cell content ratio plots is chosen to be $C_{\text{Sep}} = 0.11$, at which the maximum of MCC is reached for the whole sample.

Additional to the observations made above concerning figure 9.3, a few remarks have to be pointed out. Firstly, without the gamma events it is visible that in the MC truth scatter plots in (a) the overlap of muon and proton events with the electron events is low for low visible energies. This can also be said for the reconstruction in (b), although there the overlap is comparatively high to the MC truth. In the ratio plots, the MC truth in (c) as well as the reconstruction in (d) show a clear separation between the samples. In (d) the chosen cut value of $C_{\text{Ratio}} = 0.19$

is displayed (purple dotted line), for which the MCC is highest.

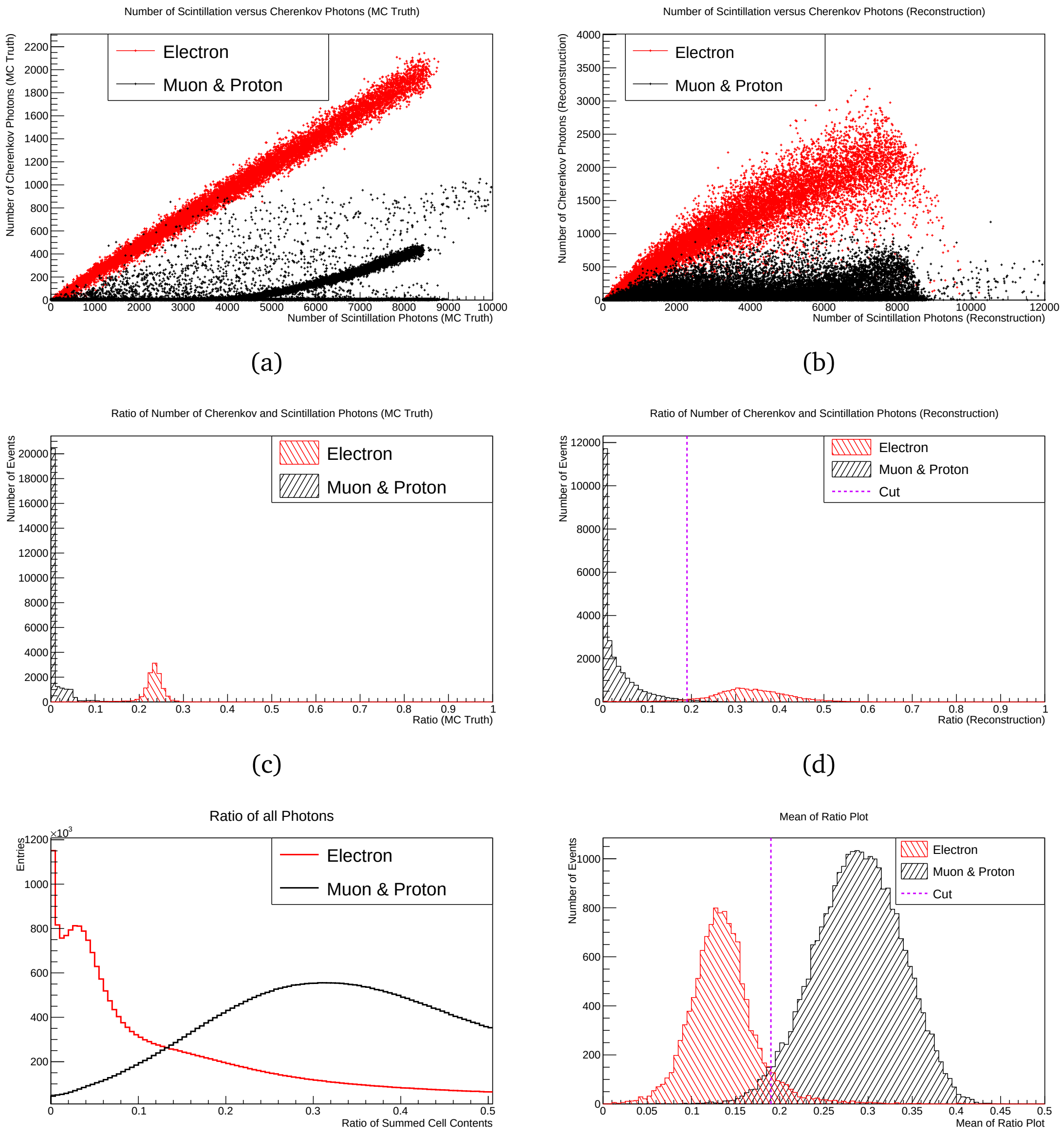

(a) (b) (c) (d) (e) (f)

Figure 9.4.: Scatter and ratio plots for the number of Cherenkov photons versus the number of scintillation photons for MC truth and reconstruction for electron versus muon and proton. (a) shows the MC truth as scatter and (c) as ratio plot. (b) and (d) are the same for the reconstruction. (e) shows the ratio of summed cell contents for all photons in electron and muon & proton events and (f) shows the distribution of mean values, that are extracted from the ratio of summed cell contents for the individual events.

In (e) the ratio of the summed scintillation to the Cherenkov cell content is shown for all photons in the samples in question. Due to the low (high) number of Cherenkov photons the mean of this distribution is high (low) for muons and protons (electrons). This observation is applicable to individual events as well. With that, for each event the ratio of summed cell contents for all hits is filled into a histogram, of which the mean is extracted. In (f) the mean of the ratio of summed cell content for all events in the respective samples is shown. The electron distribution peaks at around 0.13, whereas the muon and proton distribution shows high values in the area of 0.3. An overlap of both distributions between 0.15 and 0.25 is clearly visible. Here, the chosen cut value of $C_{\mathrm{Mean}} = 0.19$ for the highest MCC is shown. The fact that the cut value for both methods is identical is assumed to be purely accidental.

The results for the discrimination between electrons and muons & protons for both methods are shown in figure 9.5. (a) and (b) show the influence of the cut value on the metrics for the ratio and the mean method. As it is shown, the influence of the cut value is contrary for both methods. For the ratio method in (a) the purity rises towards higher cut values, whilst the efficiency decreases. For the mean method in (b) the purity decreases for higher cut values, whilst the efficiency rises. The reason lies in the distributions, on which the cuts are defined, since for the ratio the electron (muon-like) events tend towards higher (lower) values, whereas for the mean method the electron (muon-like) events tend towards lower (higher) values.

In (c) the influence of the deposited energy in terms of reconstructed number of scintillation photons is shown for the ratio method. In (e) the same is shown for the mean method and in (g) the number of events in the respective photon interval is shown. Because electron events are compared to muon and proton events simultaneously, the sample sizes are heavily balanced towards the latter. Both samples show a decline of event number towards higher number of scintillation photons, which is due to the higher number of exiting events for higher energies and therefore to less deposited energy in the detector. It is to note that the last photon interval also includes all hits with a higher number of scintillation photons. The rapid decline of events for the last interval cannot be explained by the increasing number of events, that are not contained in the detector alone. The decline hints that only the highest of energies near $120\,\mathrm{MeV}$ for electron and muons and $140\,\mathrm{MeV}$ for protons is located in that interval. Except the lowest photon interval, the difference in event number in the samples stays roughly the same. Comparing (c) and (e) shows that the ratio method and the mean method produce very similar results. Both methods perform worst for the lowest and the highest photon interval, whereby it has to be noted that the purity stays high for the highest photon interval. For the low photon interval this can be explained with the visible overlap in figure 9.4 (b) for low scintillation photon numbers. For the highest photon interval the efficiency and therefore the MCC drops, since there are low number of electron events in that interval and of these events some are overlapping with the muon-like events (see figure 9.4 (b)). This is a behaviour that is also observed for the following discrimination cases meaning that the choice of photon intervals is not ideal.

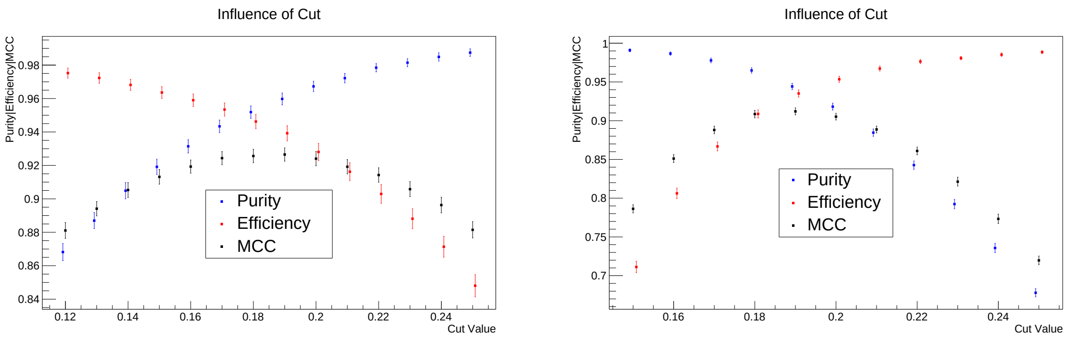

(a) Ratio method (b) Mean method

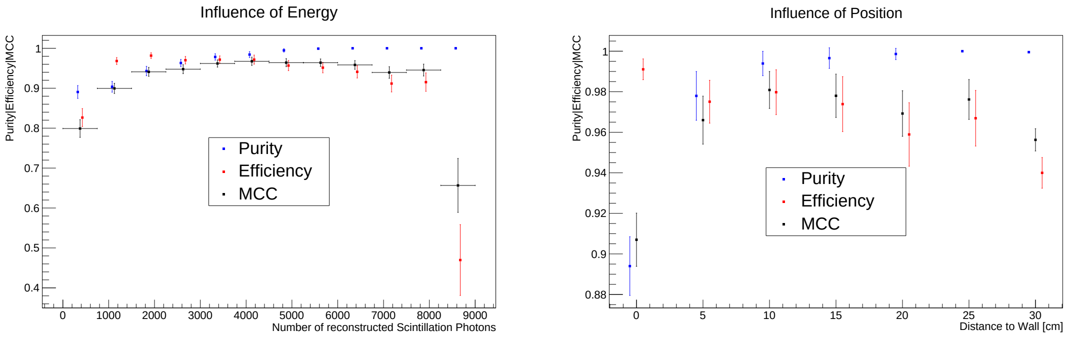

(c) Ratio method (d) Ratio method

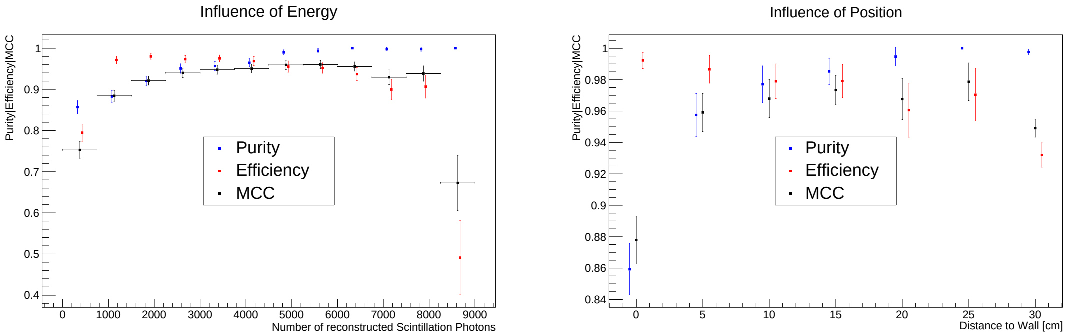

(e) Mean method (f) Mean method

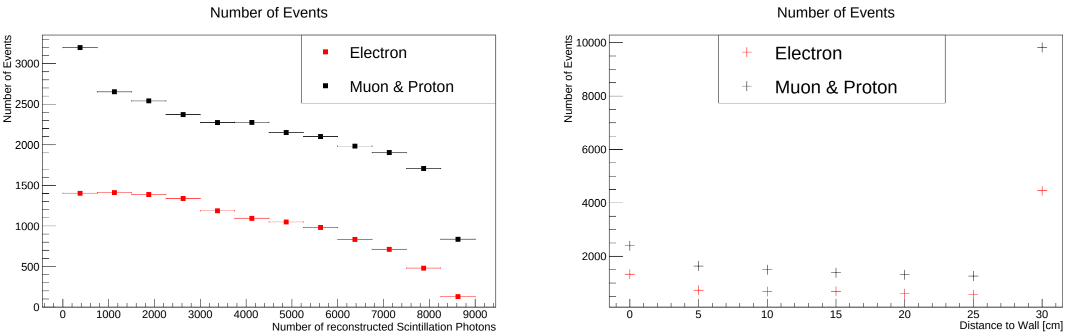

(g) (h)

Figure 9.5.: Particle discrimination results for selecting electron events versus muon and proton events. (a) and (b) show the influence of the cut value for the ratio and mean method. (c) and (e) show the influence of energy for the ratio and mean method and (d) and (f) show the influence of the event's position for the ratio and mean method. (g) and (h) shows the number of events in terms of reconstructed number of scintillation photons and in terms of the event's position.

The best performing interval for the ratio [mean] method is at 4125 $[5625]$ with a MCC of $(96.8 \pm 0.9) \cdot 10^{-2}$ $[(96.1 \pm 1.0) \cdot 10^{-2}]$, a purity of $(98.5 \pm 0.8) \cdot 10^{-2}$ $[(99.3 \pm 0.6) \cdot 10^{-2}]$ and an efficiency of $(97.1 \pm 1.0) \cdot 10^{-2}$ $[(95.4 \pm 1.3) \cdot 10^{-2}]$, which means that the peak performance is comparable as well, but a slightly worse performance for the mean method can be seen for the lowest photon interval.
The influence of the event's position for the events with a reconstructed number of scintillation photons between 1500 and 8250 can be seen in (d) for the ratio method and in (f) for the mean method with the number of events shown in (h). The number of events show a flat distribution with the exception of the highest distance, which is due to the higher available volume. (d) and (f) show that the position of the event has no real influence on both methods except for the inclusion of events that leave the detector at the $0\,\mathrm{cm}$ marker, where a decrease in purity and MCC is shown. A hint for a increasing purity (decreasing efficiency) can be seen towards higher distance for both methods and for the $30\,\mathrm{cm}$ marker a slight decrease in efficiency and MCC can be seen. Lastly, the overall performance of the methods can be compared for all events. The ratio [mean] method reaches values of $(92.7 \pm 0.3) \cdot 10^{-2}$ $[(91.2 \pm 0.4) \cdot 10^{-2}]$ for MCC, $(96.0 \pm 0.3) \cdot 10^{-2}$ $[(94.4 \pm 0.4) \cdot 10^{-2}]$ for purity and $(94.0 \pm 0.4) \cdot 10^{-2}$ $[(93.5 \pm 0.4) \cdot 10^{-2}]$ for efficiency.
In conclusion, both methods perform excellent whilst the ratio method seems to be slightly better. The mean method on the other hand has the advantage that no cut value on the ratio has to be defined eliminating one optimisation step. As both methods use essentially the same event characteristics, a combination of these methods is not foreseen for the future.

Gamma vs. Muon and Proton

It is expected that the discrimination between gamma and muon-like events performs in a similar way than the electron selection. The results are discussed in a similar manner, starting with figure 9.6, in which the MC truth is shown as scatter (a) and ratio (c) plot together with the reconstruction as scatter (b) and ratio (d) plot. The MC truth scatter plot is very similar to the previous one for the electron selection with the only difference being the higher contribution of gamma events towards very low scintillation photon numbers. This is more apparent in the MC truth ratio plot, where a significant number of gamma events have a ratio of less than 0.1.
For the reconstruction plots a cut value of $C_{\mathrm{Sep}} = 0.11$ on the summed cell content ratio is chosen. Due to the overall lower ratio of the number of reconstructed Cherenkov to scintillation photons, the overlap of the muon-like and the gamma events is higher than for the electron case. This is especially the case for events with a number of reconstructed scintillation photons less than 2000. As discussed previously, some gamma events have a ratio that is higher than 1.0 visible in the scatter plot.

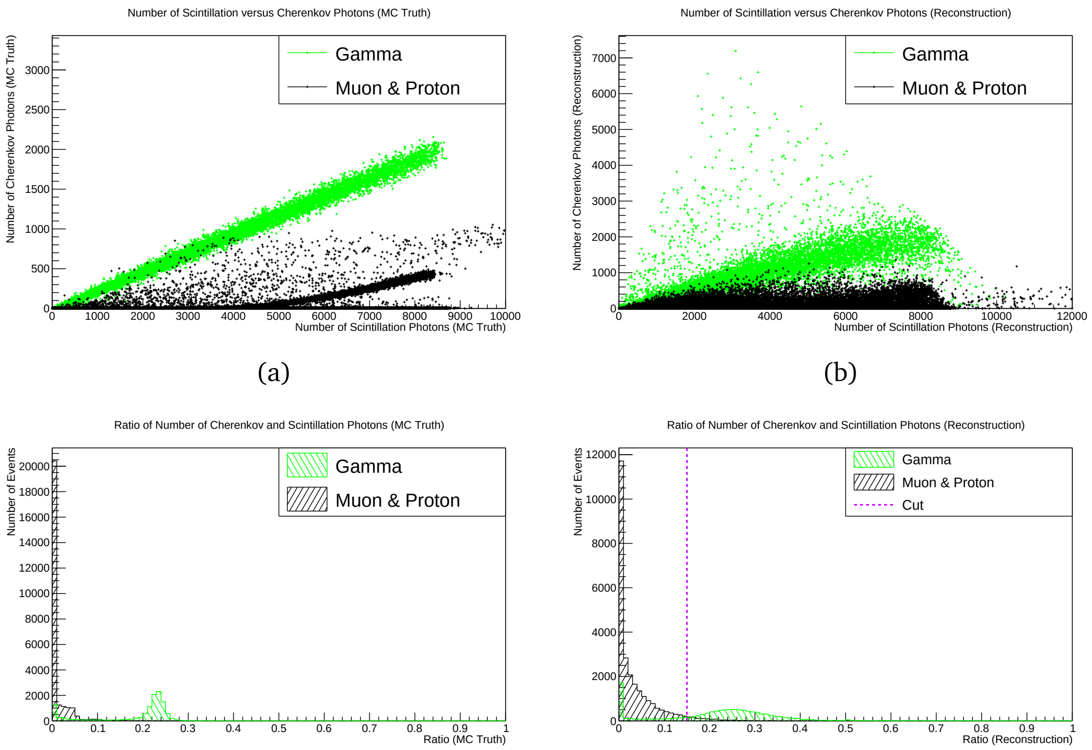

(a)

(b)

(c)

(d) Ratio method

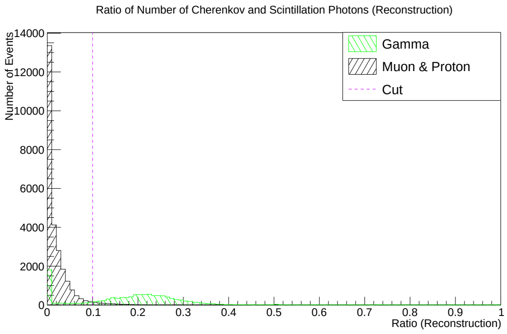

(e) Ratio method with angle criterium

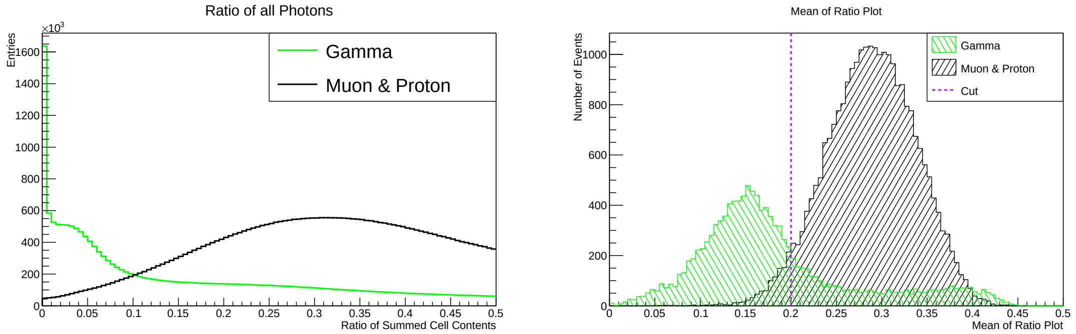

(f)

(g) Mean method

Figure 9.6.: Scatter and ratio plots for the number of Cherenkov photons versus the number of scintillation photons for MC truth and reconstruction for electron versus muon and proton. (a) shows the MC truth as scatter and (c) as ratio plot. (b) and (d) are the same for the reconstruction. The ratio for the angle criterium is shown in (e). (f) shows the ratio of summed cell contents for all photons in electron and muon & proton events and (g) shows the distribution of mean values, that are extracted from the ratio of summed cell contents for the individual events.

The reconstructed ratio shows that the ratio for both samples is smeared out compared to the MC truth and that the contribution towards very low ratios is also still visible for the gamma events. The cut of $C_{\mathrm{Ratio}} = 0.16$ is displayed as the purple dotted line.

(e) shows the ratio plot when incorporating the angle criterium. In comparison to (d) it can be observed that the distributions are shifted towards lower ratio values for all events. This means, this method underestimates the ratio, which becomes clear when comparing to the MC truth in (c). The overlap of muon-like and gamma events is decreased though. Furthermore the chosen cut value for the light separation algorithm is here $C_{\mathrm{Sep}} = 0.13$ and the cut value on the ratio is $C_{\mathrm{Angle}} = 0.1$ indicated by the purple line.

In (f) the ratio of the summed cell contents is shown for all photons in gamma and proton & muon events. For the gamma events it is notable that the decrease from the first bin to the second bin is very high compared to the same distribution for electron events (see figure 9.4 (e)), because as it is shown in figure 8.8 (a) for gamma events a considerable amount of scintillation hits also get a low ratio assigned (See also section 8.3.3). Nevertheless, the mean of this distribution for all events is low (high) for gamma (muon & proton) events. This is also to some degree applicable for the individual events, as it is shown in the mean of the summed cell content ratio plot in (g), that shows that the gamma events have a low mean compared to the muon-like events. Compared to the electron case in figure 9.4 (f), it is clearly visible that there is a higher contribution of gamma events with higher means. This can be explained with the Compton scattering events that only emit negligible amounts of Cherenkov photons, before leaving the detector. Additionally the cut value of $C_{\mathrm{Mean}} = 0.2$ on the mean distribution is shown.

The results for the gamma and muon-like discrimination are displayed in figure 9.7. (a) and (b) show the influence of the cut value on the performance for the ratio and the mean method. Again, the contrary behaviour is visible that was discussed previously for the electron selection, that the purity (efficiency) rises (declines) for higher cut values for the ratio method and vice versa for the mean method. It is also visible that the chosen cut values of 0.16 for the ratio and 0.2 for the mean method yield the best MCC values of $(74.5 \pm 0.6) \cdot 10^{-2}$ and $(72.4 \pm 0.8) \cdot 10^{-2}$.

(c) and (e) show the influence of the visible energy on the performance for the ratio and the mean method, whereas (g) shows the distribution of sample sizes. It is notable that the number of gamma events for the lowest photon interval is highest and surpasses the number of the muon-like events. This can be explained by the Compton scattering nature of gammas and the higher tendency to leave the detector without notable Cherenkov emission i.d. before creating an electromagnetic shower. This leads also to the higher gap in event number for all other photon intervals compared to the gap between electron and muon-like event number in

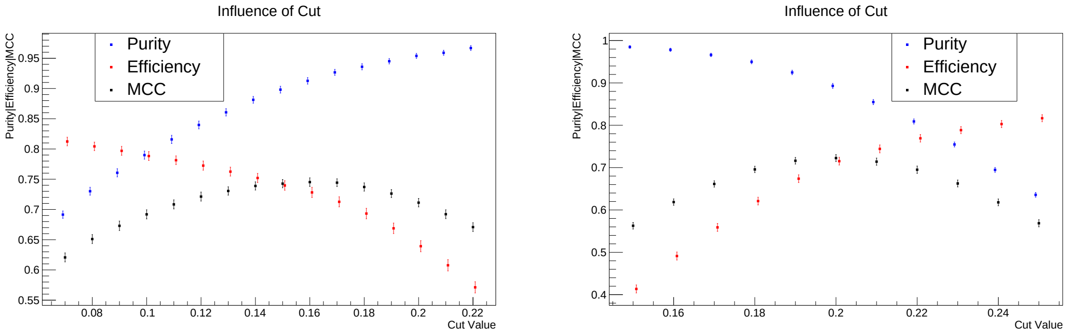

(a) Ratio method (b) Mean method

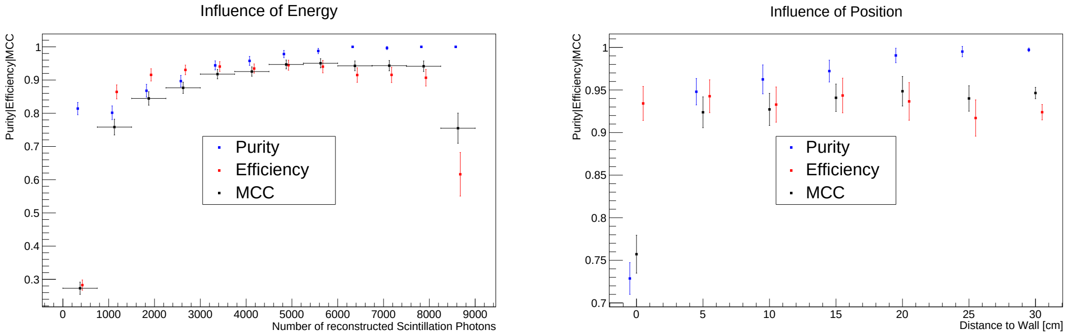

(c) Ratio method (d) Ratio method

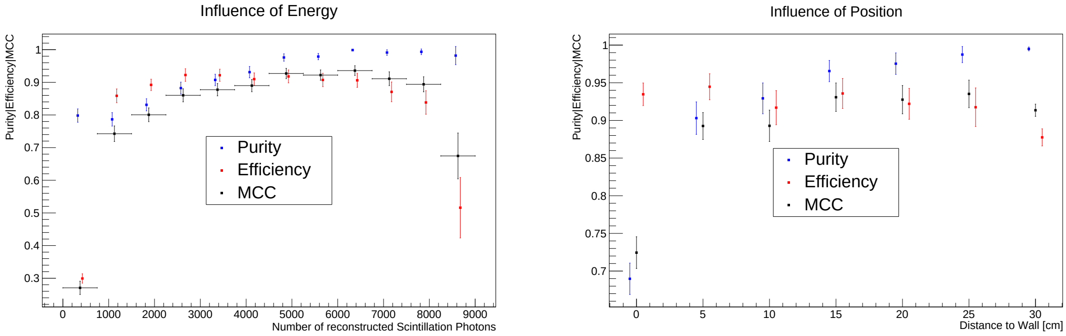

(e) Mean method (f) Mean method

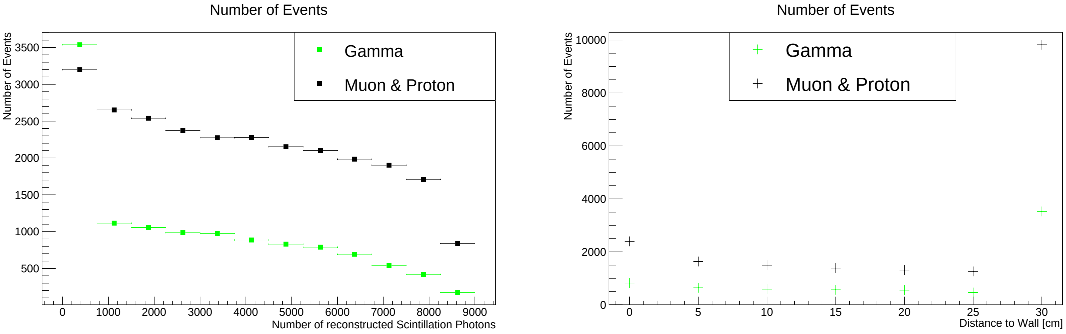

(g) (h)

Figure 9.7.: Particle discrimination results for selecting gamma events versus muon and proton events for the ratio and mean method. (a) and (b) show the influence of the cut value for the ratio and mean method. (c) and (e) show the influence of the energy, (d) and (f) the influence of the event's position and (f) and (g) show the number of events for the different intervals.

figure 9.5 (g).

The influence of the visible energy on the performance of the ratio and mean method is, similar to the previous electron case, almost indistinguishable. For the lowest and the highest photon interval the performance is worst, for which an explanation was given previously, and a rise in performance towards higher energies can be seen. Starting at the 4875 interval the performance can be considered as stable in terms of MCC. The peak performance for the ratio [mean] method is at 5625 [6375] with a purity of $(98.8 \pm 0.7) \cdot 10^{-2}$ [$(99.9 \pm 0.3) \cdot 10^{-2}$] efficiency of $(93.9 \pm 1.6) \cdot 10^{-2}$ [$(90.1 \pm 2.1) \cdot 10^{-2}$] and a MCC of $(95.0 \pm 1.2) \cdot 10^{-2}$ [$(93.3 \pm 1.4) \cdot 10^{-2}$] showing comparable results with a hint of better performance for the ratio method.

For the influence of position plots, only events with a reconstructed number of scintillation photons between 1500 and 8250 are considered. This is done to reduce the variation in performance due to the difference in visible energy and to eliminate the outliers. With that, it is ensured that a variation of performance with respect to the event's position originates from the position and not from a correlation of energy and position. (h) shows the number of events with respect to the event's position, which is very similar to figure 9.5 (h).

(d) and (f) shows the influence of the position on the performance of the particle discrimination for the ratio and the mean method. The trend of both methods is very similar and a real performance increase can only be seen going from $0\,\mathrm{cm}$ to $5\,\mathrm{cm}$. Overall, the performance of the ratio method is superior as seen comparing (d) and (f). For all events the ratio [mean] method reaches a purity of $(91.3 \pm 0.5) \cdot 10^{-2}$ [$(89.4 \pm 0.6) \cdot 10^{-2}$] an efficiency of $(72.8 \pm 0.7) \cdot 10^{-2}$ [$(71.6 \pm 0.8) \cdot 10^{-2}$] and a MCC of $(74.5 \pm 0.6) \cdot 10^{-2}$ [$(72.4 \pm 0.8) \cdot 10^{-2}$].

When incorporating the angle criterium, the results in figure 9.8 are obtained. (a) shows the influence of the cut value, which is comparable with figure 9.7 (a), but shows a higher MCC at the chosen cut value of $(79.2 \pm 0.7) \cdot 10^{-2}$, which is an increase of $4.7 \cdot 10^{-2}$ to the ratio method. Here, a purity of $(93.2 \pm 0.5) \cdot 10^{-2}$ and efficiency of $(77.6 \pm 0.8) \cdot 10^{-2}$ is reached.

The influence of the energy in (b) shows overall a better performance than the other methods. This is also true for the first and especially for the last photon interval. The best performing interval is here at 7875 with a MCC of $(97.3 \pm 1.2) \cdot 10^{-2}$, a purity of $(97.6 \pm 1.3) \cdot 10^{-2}$ and an efficiency of $(98.1 \pm 1.3) \cdot 10^{-2}$. This means the angle criterium has a better MCC by $2.3 \cdot 10^{-2}$ in comparison to the ratio method.

The influence of the position in (c), for which only events with a number of reconstructed scintillation photons between 1500 and 8250 are considered, shows excellent results for all contained events. For the contained events, all metrics are clearly above 0.95 with small errors, whilst the purity and MCC suffers for events that are near the detector edge or exit the detector.

(d) and (e) are very similar to the plots for the ratio method and are therefore not discussed.

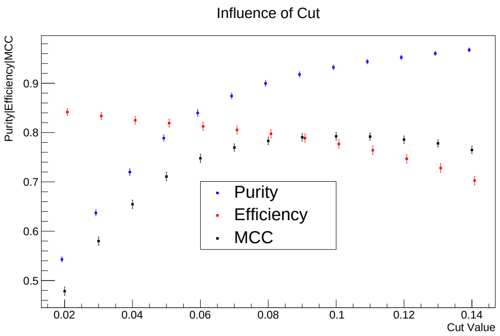

(a) Ratio method with angle criterium

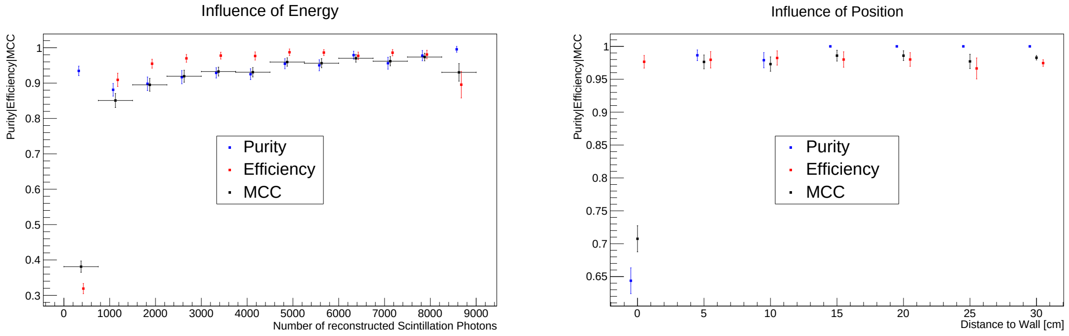

(b) Ratio method with angle criterium

(c) Ratio method with angle criterium

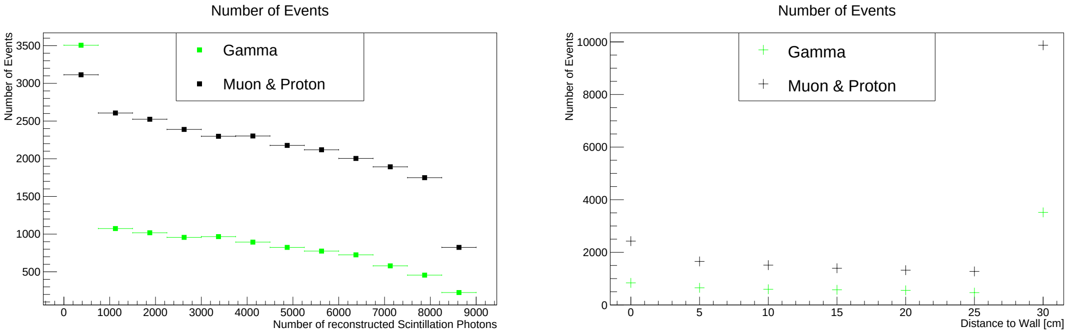

(d)

(e)

Figure 9.8.: Particle discrimination results for selecting gamma events versus muon and proton events for the ratio method with angle criterium. (a) shows the influence of the cut value, (b) the influence of the energy and (c) the influence of the position. (d) and (e) show the number of events for the respective intervals.

The discrimination of gammas from the muon-like events works therefore well for these methods, but due to the different event characteristics of the gamma, the overall performance with a MCC of $(79.2 \pm 0.7) \cdot 10^{-2}$ is worse than the electron selection with a MCC of $(92.7 \pm 0.3) \cdot 10^{-2}$. The peak performance in the best photon interval is comparable though with a MCC of $(96.8 \pm 0.9) \cdot 10^{-2}$ for electron and $(97.3 \pm 1.2) \cdot 10^{-2}$ for gamma selection.

Electron vs. Gamma

The electron/gamma discrimination is a special case, as it is not obtainable in the MC truth of the number of Cherenkov to scintillation photons, that is shown in figure 9.9 in (a) as scatter and in (c) as ratio plot. In the scatter plot, both distributions occupy the same diagonal, which in turn results in the overlaying distributions in the ratio plot. The only application visible in the MC truth would be a selection of gamma events via their low ratio.

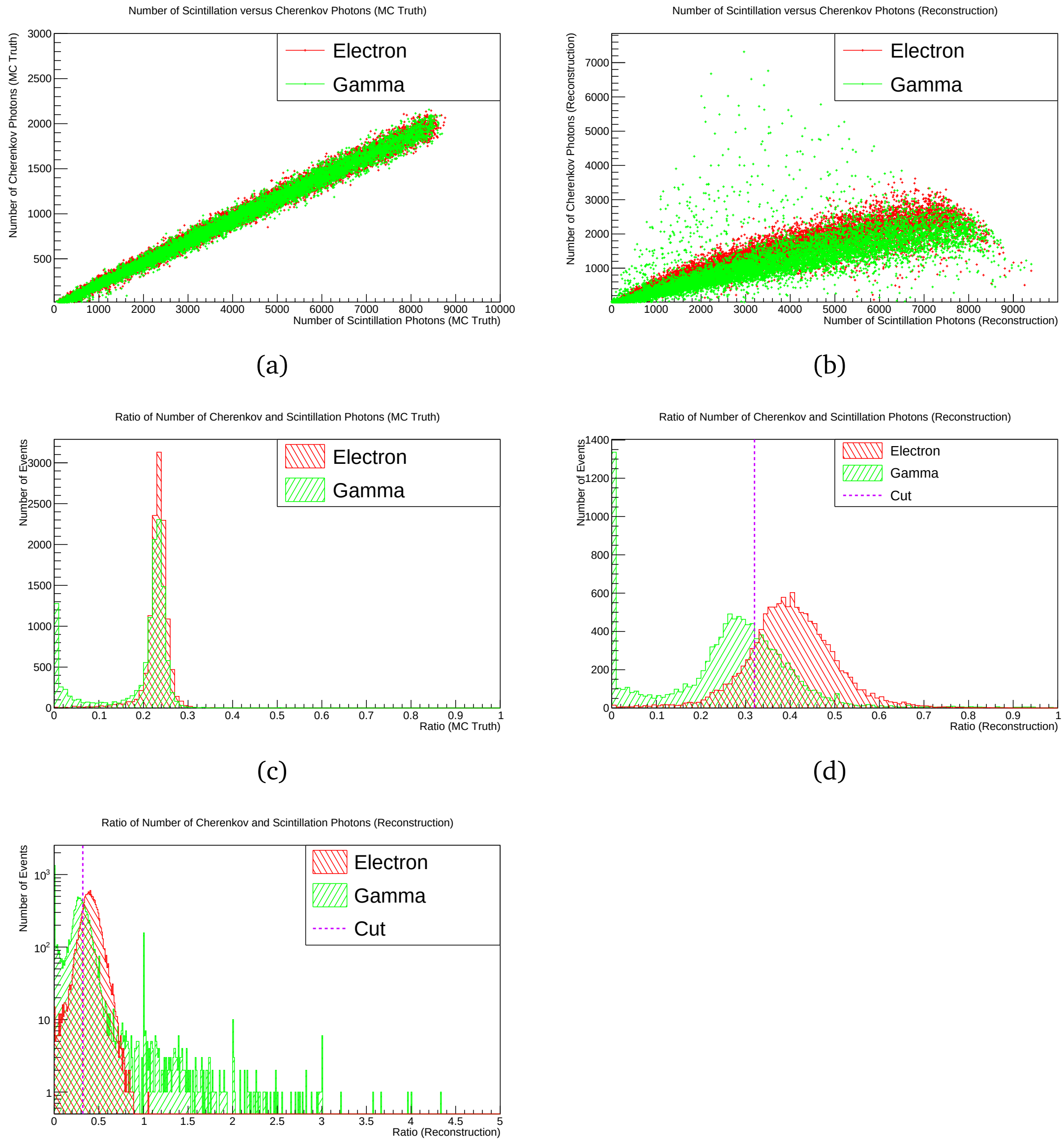

(a) (b)

(c) (d)

(e)

Figure 9.9.: Scatter and ratio plots for the number of Cherenkov photons versus the number of scintillation photons for MC truth and reconstruction for electron versus gamma. (a) and (c) show the MC truth as scatter and ratio plot. (b) and (d) is the same for the reconstruction. (e) is the reconstructed ratio with a logarithmic y-axis and a higher range in x-axis.

The situation changes going to the reconstruction displayed as scatter in (b) and ratio in (d). Due to the higher expansion of gamma events and the therefore changed distributions of the summed cell content ratio, the cut on said ratio underestimates the number of Cherenkov photons for a majority of gamma events. Furthermore, the difference between gammas and electrons can also originate from the assumed reference point, that is not necessarily in agreement with the position of the highest photon emission for gammas. This has to be investigated in the future and it is possible that this discrimination is no longer possible with a vertex reconstruction. At the same time, a small number of gamma events get a unrealistically high number of Cherenkov photons assigned to. This can be seen in (e), where the reconstructed ratio plot is extended up to 5.0 with a logarithmic y-axis. A considerable amount of gamma events can be seen with a ratio higher than 1.0. These high ratio gamma events can be interpreted as Compton scattering gammas that result in a low number of scintillation photons and a primary vertex that is not in near proximity to the points of high photon emission.

The distribution of gamma events in the ratio plot opens up the option to exclude all hits above a ratio of 0.9 for the electron selection to reach a slightly higher purity, whilst only losing one single electron event and 442 gamma events. In both ratio plots the possibility of discrimination can be seen and in both the chosen cut value of $C_{\text{Sep}} = 0.32$ is shown as purple dotted line.

Figure 9.10 displays the influence of the cut value on the metrics for all events in (a) and only the events with a ratio less than 0.9 in (b). The behaviour of the metrics are essentially the same with the maximum of MCC at the same cut value of $C_{\text{Ratio}} = 0.32$ with $(47.9 \pm 1.1) \cdot 10^{-2}$ for all events and $(50.2 \pm 1.3) \cdot 10^{-2}$ for the pre-selected events. Since only one electron event is eliminated, the efficiency stays essentially the same and the improvement in MCC originates from an improvement in purity.

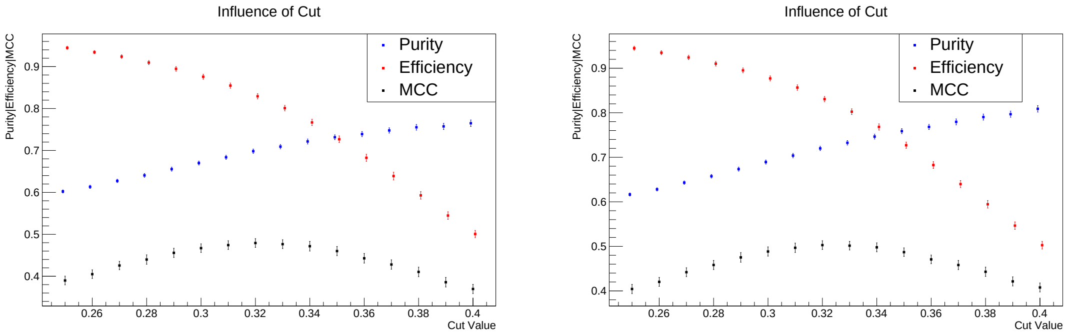

(a) All events

(b) Events with ratio < 0.9

Figure 9.10.: Influence of the cut value on metrics for electron selection against gamma for the whole sample in (a) and for the pre-selected events in (b).

The results for the electron/gamma discrimination can be seen in figure 9.11. On the left side the influence of the energy on the performance and on the right side the influence of the position is displayed. (e) and (g) show the number of events with respect to the reconstructed number of scintillation photons for all events and for the events with a ratio of less than 0.9. Since only one electron event is missing, there is no difference in the electron distributions. For the gamma events on the other hand a decrease can be seen of 254 events for the lowest photon interval. For the next photon interval the difference is 59 excluded events. The number of events that are discarded declines towards higher energies, so that for the photon interval at 4875 only 3 events are excluded. For the following photon intervals, no events have a ratio of above 0.9 so that no gamma events are missing here. This means that the probability for a gamma event to yield a ratio above threshold decreases towards a higher number of reconstructed scintillation number and hence towards higher deposited energies.

The performance of the discrimination in terms of visible energy in (a) for all events and (c) for the pre-selected events shows therefore no difference for the photon intervals following 4875. Before that an increase in purity and therefore in MCC can be seen, whilst the efficiency stays the same. Thereby, the effect is bigger the more events were excluded so that it is at an maximum of 0.08 MCC increase for the lowest photon interval to reach a MCC of $(61.2 \pm 2.7) \cdot 10^{-2}$. In contrast to the previous discrimination results, the peak performance is reached at the lowest photon interval for the full [reduced] sample with a MCC of $(53.2 \pm 2.4) \cdot 10^{-2}$ $[(61.2 \pm 2.7) \cdot 10^{-2}]$, a purity of $(62.1 \pm 1.8) \cdot 10^{-2}$ $[(72.3 \pm 2.1) \cdot 10^{-2}]$ and efficiency of $(74.3 \pm 2.1) \cdot 10^{-2}$ $[(74.1 \pm 2.5) \cdot 10^{-2}]$. After that the performance decreases in terms of MCC, whilst the purity stays stable and the efficiency even rises. This is due to the unbalanced sample size for all photon intervals except the first one, where the number of electron events is higher than the number of gamma events. For example, at the second photon interval there are 1484 electron events against 1090 gamma events for the pre-selected sample. Towards even higher visible energies, the efficiency starts also to decline, which is a behaviour that was also seen for the previous discrimination cases. At the highest photon interval, the discrimination fails completely as there is a total overlap in figure 9.9 (b) for events with a number of reconstructed scintillation photons above 8250. This overlap might vanish when taking particles with energies above $120\,\mathrm{MeV}$ into account.

For the influence of position (f) and (h) show the event numbers for the full sample and the pre-selected sample. Here again, the events with less than 8250 and more than 1500 reconstructed scintillation photons are considered to be in the stable range of the metrics whilst being comparable to the previously discussed influence of position plots for the other discrimination cases. Since the higher difference in event numbers is at the lowest energy markers, the number of events in relation to the distance show no difference.

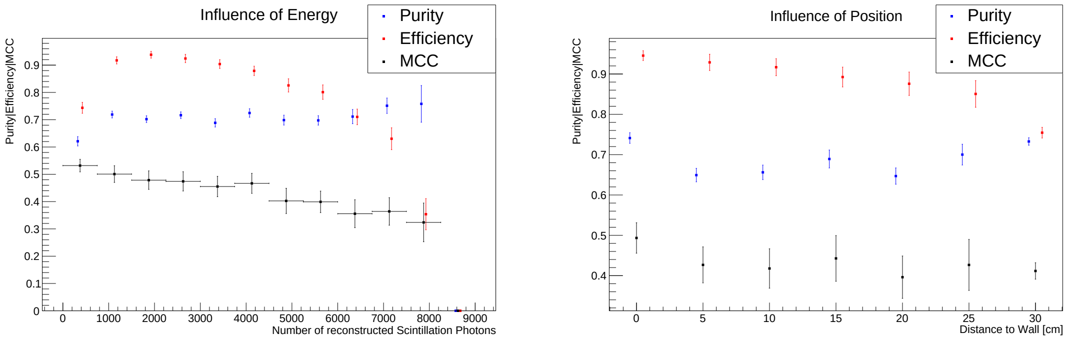

(a) All events (b) All events

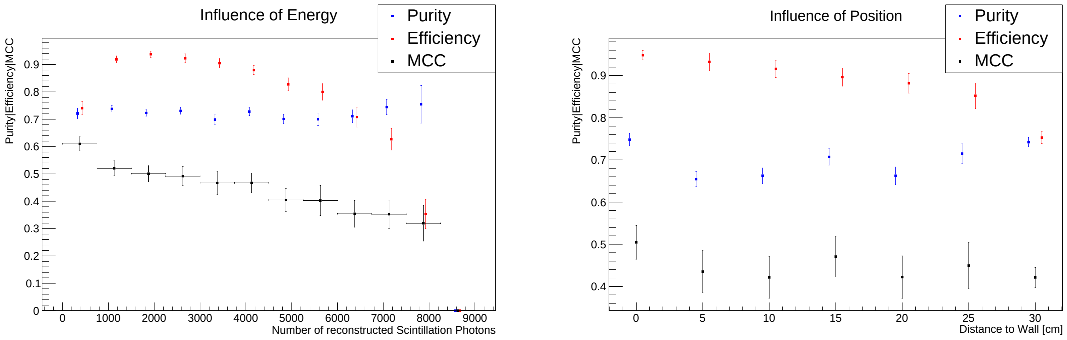

(c) Events with ratio < 0.9 (d) Events with ratio < 0.9

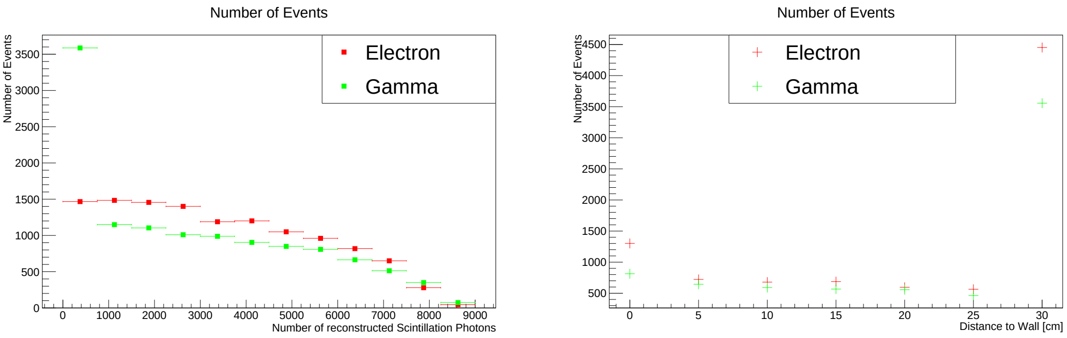

(e) All events (f) All events

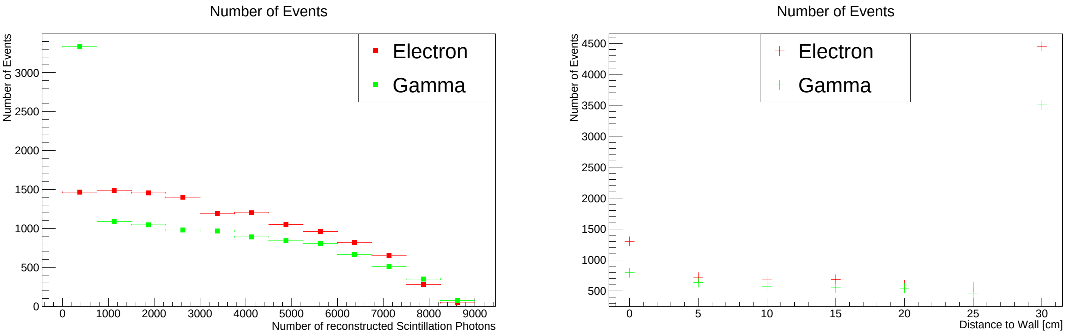

(g) Events with ratio < 0.9 (h) Events with ratio < 0.9

Figure 9.11.: Particle discrimination results for selecting electron events versus gamma events. (a) and (c) show the influence of energy for the whole and the pre-selected sample. (e) and (g) show the number of events in terms of reconstructed scintillation photons for the full and pre-selected sample. (b) and (d) show the influence of the event's position in the same manner and (f) and (h) show the number of events for the influence of the event's position plots.

This leads to an influence of the position on the performance of the discrimination, that is for both samples the same, as seen in (b) and (d). For both plots, all metrics appear to be stable. This is surprising, since many of the previous plots showed a decline of performance going from the $5\,\mathrm{cm}$ marker to the $0\,\mathrm{cm}$ marker.
For all events in the pre-selected sample a MCC of $(50.4 \pm 1.2) \cdot 10^{-2}$ a purity of $(72.1 \pm 0.6) \cdot 10^{-2}$ and an efficiency of $(83.0 \pm 0.6) \cdot 10^{-2}$ is reached, whilst for the full sample $(47.9 \pm 1.1) \cdot 10^{-2}$, $(69.8 \pm 0.5) \cdot 10^{-2}$ and $(83.0 \pm 0.7) \cdot 10^{-2}$ (MCC, purity and efficiency) is achieved.
Although no electron/gamma discrimination is at first expected from the MC truth, the underestimation of Cherenkov emission in the reconstruction leads to a working electron selection. Due to the high overlap of both samples, for electron/gamma the separation method does not perform as well as the electron/muon-like or gamma/muon-like discrimination. Furthermore, it needs to be investigated how the assumption of the vertex position influences these results and whether the discrimination is for a more realistic case possible at all.

Muon vs. Proton

The discrimination of muon and proton is different from the former cases, since a discrimination should only be possible at higher energies, when the muons start to emit Cherenkov photons due to the exceeding of the Cherenkov threshold in kinetic energy. This is shown in the MC truth as scatter plot in (a), where the non-decaying muons start to emit Cherenkov photons at around 4000 scintillation photons in visible energy. The decaying muons resulting in Michel electrons show a higher number of Cherenkov photons than the majority of muon events. Most of the proton events emit no Cherenkov photons at all and a few individual proton events show Cherenkov photons due to the excitation of electrons. This is also shown in the MC truth ratio plot, where the overwhelming majority of proton events are located in the first bin. It is to note that the ratio plots here has a logarithmic y-axis and the binning is finer, which is also true for the reconstruction plots, because both muon and proton events are mostly located towards low ratio values less than 0.1. The optimisation of the cut value therefore demands a finer binning, because the values are located in a smaller interval compared to the previous discrimination cases.
The reconstruction, for which a cut of $C_{\mathrm{Sep}} = 0.11$ is chosen on the summed cell content ratio, is shown as scatter in (b) and as ratio in (d). In the scatter plot a high overlap of proton and muon events for low number of scintillation photons can be seen that starts to vanish at around 6000 scintillation photons. Since the reconstructed ratio plot shows events of all energies, no real separation is visible, although a hint for a higher number of muon events can be seen. Nevertheless, even for all events at once a separating cut can be found of $C_{\mathrm{Ratio}} = 0.008$ visible as purple line.

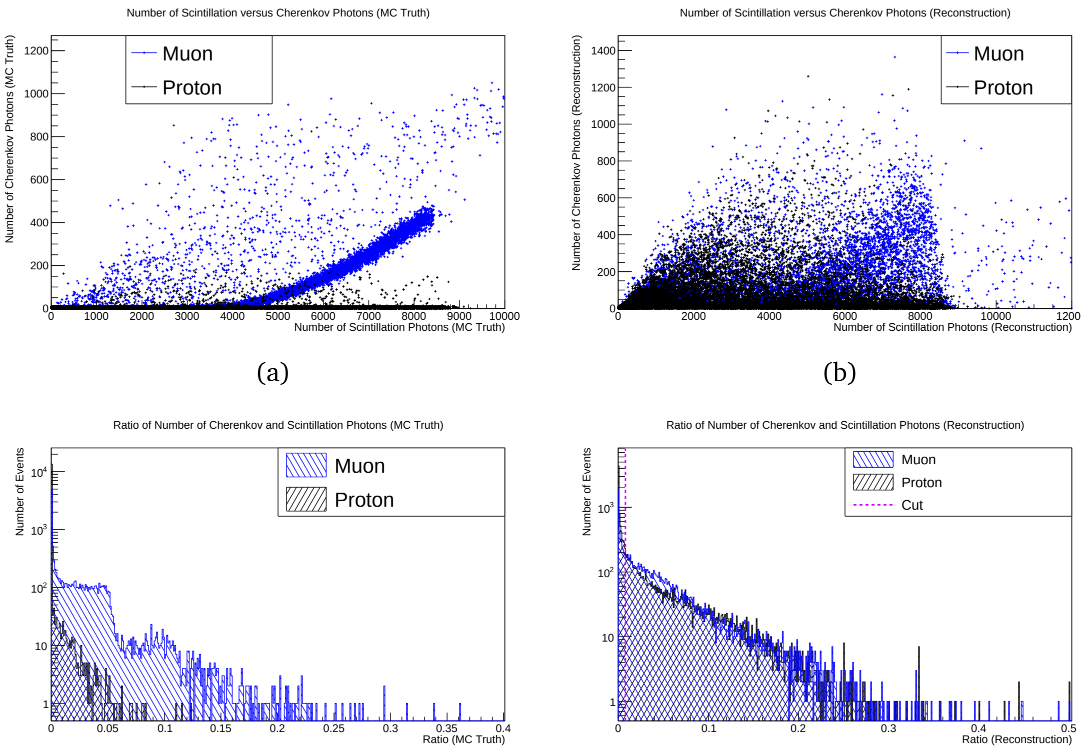

(a)

(b)

(c)

(d) Ratio method

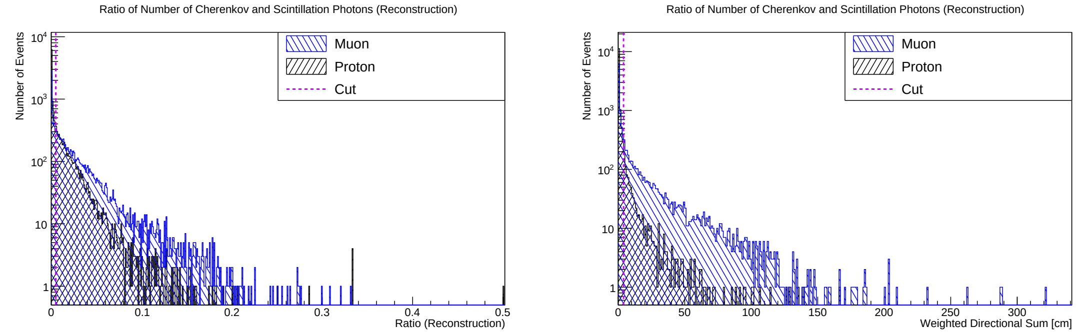

(e) Ratio method with angle criterium

(f) Directional sum method with angle criterium

Figure 9.12.: Scatter and ratio plots (all with logarithmic y-axis) for the number of Cherenkov photons versus the number of scintillation photons for MC truth and reconstruction for muon versus proton. (a) and (c) show the MC truth as scatter and ratio plot . (b) and (d) show the reconstruction as scatter and ratio plot. (e) and (f) show the ratio with the angle criterium and the weighted ratio with the length of the directional sum.

In (e) the ratio plot is shown, whereby the angle criterium is used as well to increase the purity of the light separation algorithm. This leads to a higher number of muon events towards higher ratios and the chosen cut value is $C_{\text{Angle}} = 0.005$. In (f) the angle criterium is used for the computation of the ratio, which is then multiplied with the length of the directional sum, that only takes the first hits into account, as described in the section 9.1.1. For further optimization a cut of $C_{\text{Sep}} = 0.1$ is used for the directional sum method on the summed cell content ratio. Here, the population of muon events stays roughly the same for high values of the weighted directional sum, but the number of proton events decreases. At the same time, a higher number of muon events is shifted towards very low weighted directional sum values that are below the cut value, which should lead to a decrease in efficiency. The cut value for this method is set to be $C_{\mathrm{DirSum}} = 4$.

The influence of the cut value on the metrics is shown in figure 9.13 (a) for the ratio method, (b) for the ratio method with the angle criterium and (c) for the directional sum method with angle criterium. Since these metrics are evaluated on all events, the values are in general rather low, which is especially true for the MCC values. For all methods the purity rises for higher cut values, whilst the efficiency declines and the MCC stays on a stable level. When comparing the methods, some observations can be made. First of all, the overall purity increases from the ratio method to the ratio method with the angle criterium and reaches it maximum in the directional sum method. For the efficiency the opposite behaviour can be seen, whilst the level of MCC develops similar to the purity with a lower increase meaning that the regular ratio method reaches the best efficiency, but worst purity and MCC, while the directional sum method reaches best purity and MCC but worst efficiency.

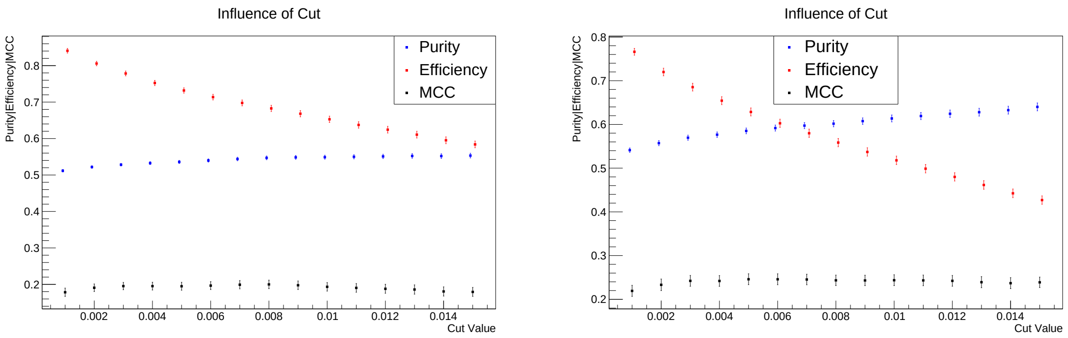

(a) Ratio method

(b) Ratio method with angle criterium

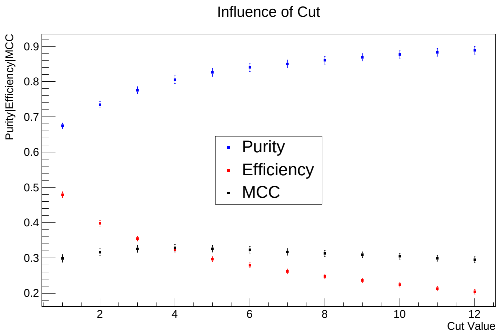

(c) Directional sum method

Figure 9.13.: Influence of the cut value on metrics for muon selection against proton. (a) shows the ratio, (b) the ratio method with angle criterium and (c) the directional sum method.

The results for the regular ratio method are shown in figure 9.14. In (b) the number of events per photon interval is displayed. Since $14,000$ proton events and $12,000$ muon events are used for this analysis, the number of proton events is

higher across all energies. The highest difference is in the lowest interval, which can be explained by the quenching effect on protons leading to a lower emission of scintillation photons. In (a) the performance of the discrimination with respect to the number of reconstructed scintillation photons is shown. Since the non-decaying muons are not expected to yield Cherenkov photons before the 4125 photon interval, the performance for lower visible energies is very low with MCC values at around 0, while the purity does not exceed 0.5 meaning that more than half of the events in the muon sample are protons.
Towards higher visible energies, the performance increases reaching a maximum at 7875 with a MCC of $(71.0 \pm 3.3) \cdot 10^{-2}$, a purity of $(86.1 \pm 2.0) \cdot 10^{-2}$ and an efficiency of $(81.3 \pm 2.8) \cdot 10^{-2}$.

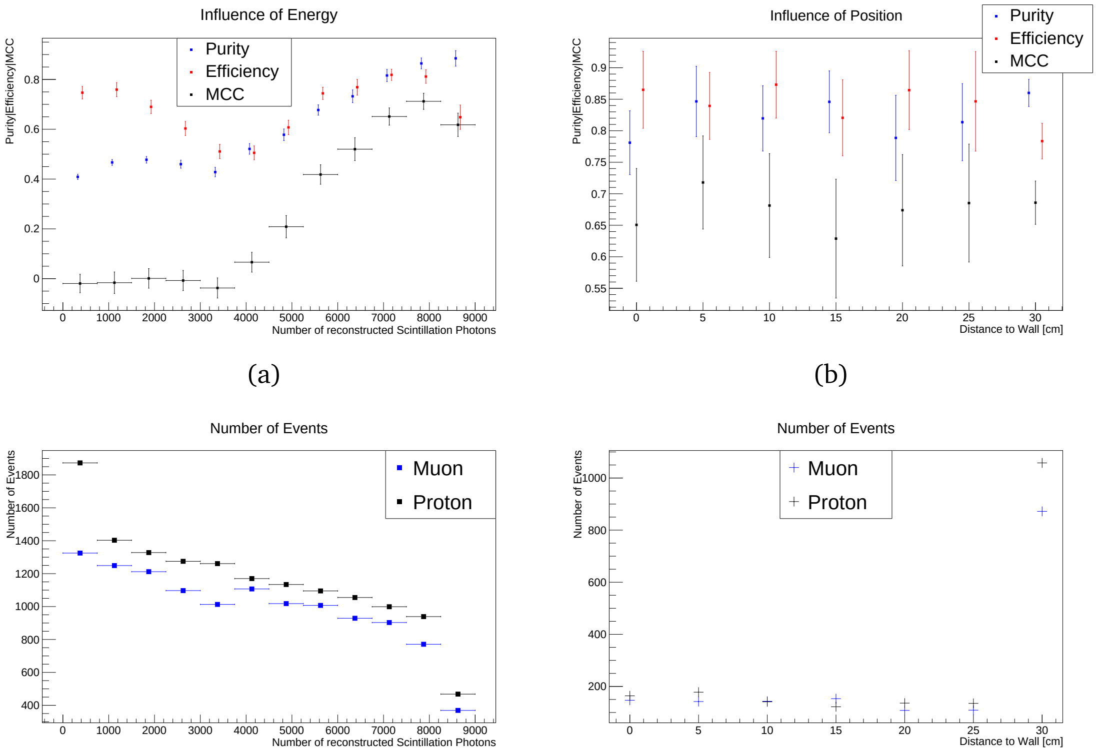

(a) (b)

(c) (d)

Figure 9.14.: Particle discrimination results for selecting muon events versus proton events for the ratio method. (a) shows the influence of energy and (b) the influence of the event's position. (c) and (d) show the number of events for the respective intervals.

In (d) the number of events in relation to the distance of the events to the detector wall is shown, while (b) shows the influence of the position on the performance. Here as well as for the following plots of that manner only the two best performing photon intervals are shown in the influence of position plots to minimize the influence of the event's visible energy. This leads to poor statistics, as it is shown in (d) and therefore to fluctuating values for all metrics and high error bars. For the future a higher number of events is needed to accurately investigate the influence of the event's position for this discrimination case.

For the other two methods the results can be found in figure 9.15. In (e) the number of events with respect to the reconstructed visible energy is shown for the angle criterium. This picture is very comparable to figure 9.14 (c) with only slight changes, that comes due to the fact that the angle criterium changes the light separation algorithm and hence the number of reconstructed scintillation photons. In (g) the same plot is shown for the directional sum method. The difference between (e) and (g) originates from a different cut value C_{Sep} in the light separation algorithm. Comparing (a) to figure 9.14 (a) shows that the purity and MCC slightly increases, whilst the efficiency decreases when including the angle criterium. The overall shape of the distribution stays the same. The peak performance is reached again at 7875 with a MCC of $(77.0 \pm 3.0) \cdot 10^{-2}$, a purity of $(90.2 \pm 1.9) \cdot 10^{-2}$ and an efficiency of $(84.2 \pm 2.6) \cdot 10^{-2}$ showing an increase in purity, efficiency and MCC of 0.041, 0.029 and 0.06 compared to the regular ratio method. For the directional sum method in (c) this evolution is continued further increasing purity and MCC, but decreasing in efficiency, whereby the difference is comparatively bigger then going from the regular ratio method to the ratio method with angle criterium. It is notable that the purity already is on a high level above 0.7 for low reconstructed visible energies, whilst the efficiency and MCC is below 0.2 meaning that most of the muons are discarded. This gives reason for the assumption that the decaying muons are here separated from the protons. The peak performance for this method is again at 7875 with a MCC of $(77.6 \pm 2.6) \cdot 10^{-2}$, a purity of $(95.3 \pm 1.5) \cdot 10^{-2}$ and an efficiency of $(78.8 \pm 2.9) \cdot 10^{-2}$, further increasing the purity and the MCC by 0.051 and 0.006 while losing 0.054 in efficiency.

The dip in efficiency at the last marker can be explained by the low number of muon events, that have a high number of Cherenkov photons starting at 8250 scintillation photons in figure 9.12 (b). Furthermore, all events with more than 8250 scintillation photons are incorporated in that interval so that also the events with more than $10,000$ scintillation hits are included, that have a low number of Cherenkov photons.

The influence of position in (b) and (d) shows fluctuating behaviour due to the low statistics shown in (f) for the angle criterium and (h) for the directional sum method.

It is notable that the purity is overall higher in (d) than in (b), which is expected when comparing (a) to (c).

The muon/proton discrimination yields good results at higher visible energies for all methods. The overall performance in terms of MCC and purity is best for the directional sum method at the cost of efficiency.

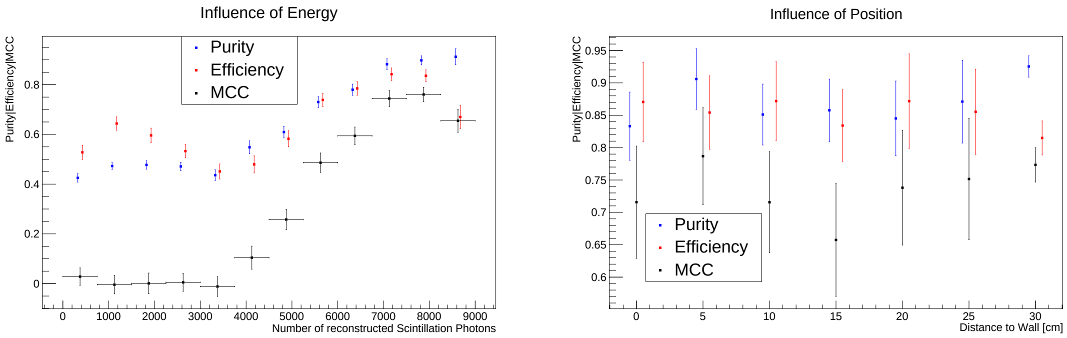

(a) Ratio method with angle criterium (b) Ratio method with angle criterium

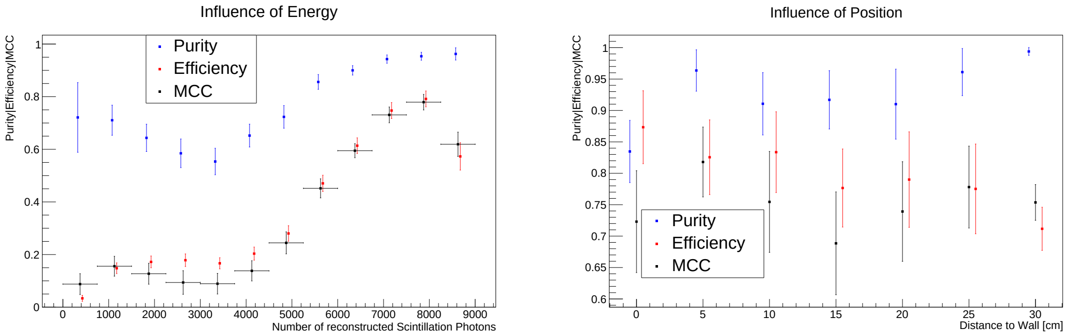

(c) Directional sum method (d) Directional sum method

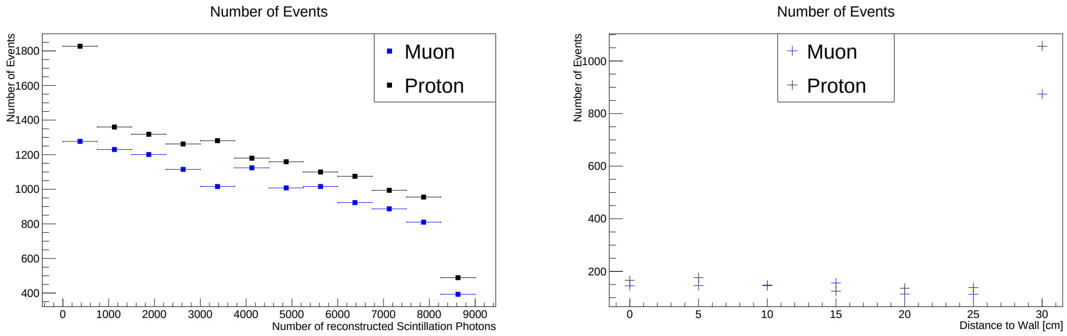

(e) Ratio method with angle criterium (f) Ratio method with angle criterium

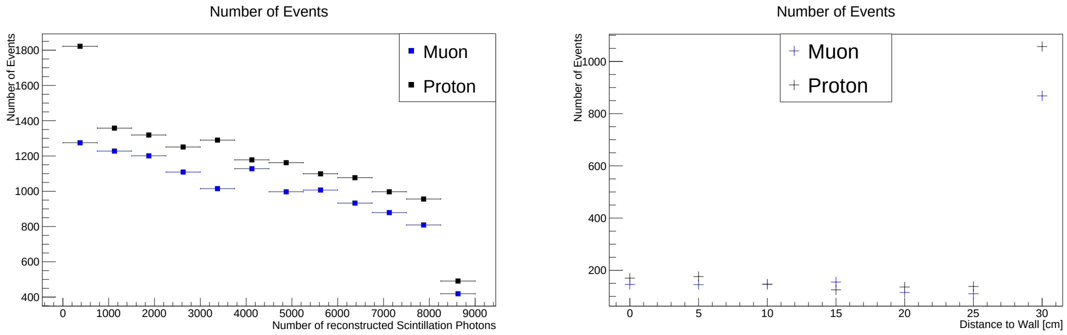

(g) Directional sum method (h) Directional sum method

Figure 9.15.: Particle discrimination results for selecting muon events versus proton events with the ratio method including the angle criterium and the directional sum method. (a) and (c) shows the influence of energy for the angle and the directional sum method. (b) and (d) is the same for the influence of the event's position and (e) and (f) [(g) and (h)] shows the number of events for the intervals for the angle criterium [directional sum method].

9.2.3. Discussion

Again, it is important to view the achieved results in context of the preconditions that were discussed in section 8.4. In comparison to the direction reconstruction, the influence of the vertex reconstruction is expected to have a lower impact, because the light separation algorithm depends not that heavily on the reference point. As the PID with the ratio method follows directly from the light separation algorithm, the suggested approaches to deal with the shifted vertex can also apply here. For the angle criterium and the directional sum method, the situation differs because both methods use the reference point and a subsequent direction reconstruction.

In table 9.1 the peak performance in terms of best photon interval for the different discrimination cases and methods is summarized. As it is expected from the MC truth, the best discrimination cases are selecting electrons and gammas against a background of muons and protons. For the electron selection all metrics are above 0.95 whereby the ratio (mean) method achieves a slightly better efficiency (purity). The gamma selection performs slightly worse for the ratio and mean method, but the ratio method with angle criterium reaches a slightly higher MCC. Again the ratio method has the higher efficiency, while the mean method achieves a higher purity, that reaches rounded even 1.0. These high values of purity imply that the majority of Michel electrons from muon decays are also suppressed. This is a point, that can be investigated by a follow-up study.

The electron/gamma discrimination is not achievable in the MC truth and is only possible in the reconstruction due to a worse performance of the light separation algorithm for gammas leading to a lower number of reconstructed Cherenkov photons than expected. It is therefore not surprising that the performance for the electron selection against a gamma background is significantly worse than the performance of the previously discussed discrimination cases. The ratio method for all events in the peak energy range sees a decrease of about 0.4, 0.3 and 0.2 in MCC, purity and efficiency compared to the previous cases. This can be improved upon when discarding all events with a ratio of summed cell contents above 0.9, so that the MCC increases by 0.08 and the purity is brought to a similar level than the efficiency with an increase of about 0.10. As a side note: This discrimination case was also investigated with help of the TTR in reference [206], where the expansion of the events in the MeV area was used for a successful electron/gamma discrimination.

The muon/proton discrimination sits performance-wise in the middle of the electron/gamma and the other discrimination cases for the peak performance. It needs to be stressed though that the performance of the muon selection against a proton background is heavily dependent on the reconstructed number of scintillation photons, as it can be seen in figure 9.15 (a) and (c) for example. This strong dependence is not seen for the other discrimination cases and can be explained by the fact that the non-decaying muons need to first reach the Cherenkov threshold for emitting Cherenkov photons and the gap between muon and proton events in the MC truth as well as the reconstruction scatter plot in 9.12 increases with higher visible energies. The purity, efficiency and MCC can be increased by incorporating the angle criterium by 0.041, 0.029 and 0.06. When weighting the ratio with the directional sum, another increase in MCC of 0.006 and purity of 0.049 can be achieved, whilst the efficiency suffers by 0.054.

This means that depending on the application one has to chose carefully, which method and cut values are used. For highest purity, the weighted ratio is best, while the ratio method with angle criterium excels at the efficiency. This is of course also true for the other discrimination cases.

The electron selection versus muons and protons also performs well in the intervals that are in the area of 8 to $30\,\mathrm{MeV}$ and therefore important for DSNB detection. For the first three photon intervals, that are roughly below $30\,\mathrm{MeV}$ purities of $(88.7 \pm 1.7) \cdot 10^{-2}$, $(90.6 \pm 1.4) \cdot 10^{-2}$ and $(94.4 \pm 1.2) \cdot 10^{-2}$ with efficiencies of $(82.5 \pm 2.1) \cdot 10^{-2}$, $(96.7 \pm 1.0) \cdot 10^{-2}$ and $(98.3 \pm 0.6) \cdot 10^{-2}$ are obtained for the intervals of 375, 1125 and 1875 reconstructed scintillation photons without a fiducial volume cut.

Table 9.1.: Summary of the particle discrimination peak performance.

Case	Method	MCC/10^{-2}	Purity/10^{-2}	Efficiency/10^{-2}
$e^-/\mu^- p$	Ratio	96.8 ± 0.9	98.5 ± 0.8	97.1 ± 1.0
	Mean	96.1 ± 1.0	99.3 ± 0.6	95.4 ± 1.3
$\gamma/\mu^- p$	Ratio	95.0 ± 1.2	98.8 ± 0.7	93.9 ± 1.6
	Ratio (Angle)	97.3 ± 1.2	97.6 ± 1.3	98.1 ± 1.3
	Mean	93.3 ± 1.4	99.9 ± 0.3	90.1 ± 2.1
e^-/γ	Ratio all events	53.2 ± 2.4	62.1 ± 1.8	74.3 ± 2.1
	Ratio pre-selection	61.2 ± 2.7	72.3 ± 2.1	74.1 ± 2.5
μ^-/p	Ratio	71.0 ± 3.3	86.1 ± 2.0	81.3 ± 2.8
	Ratio (Angle)	77.0 ± 3.0	90.2 ± 1.9	84.2 ± 2.6
	Weighted Ratio	77.6 ± 2.6	95.3 ± 1.5	78.8 ± 2.9

In the future, the presented methods can be finetuned, as the presented cuts are optimised for MCC, which is not necessarily the best cut for a desired background rate for example. Furthermore, improvements on the light separation algorithm are also expected to reflect in the performance of the particle identification. The performance of the PID could also profit from a dynamic cut value on the ratio of Cherenkov to scintillation photons based for example on the number of photons. As already discussed, it is necessary to evaluate the presented results when incorporating a vertex reconstruction to investigate the influence of the systematic shift in reconstructed vertex position. This is especially true for the electron/gamma separation, since it is questionable whether the underestimation of the number of

Cherenkov photons vanishes with a reference point located at the position of the highest photon emission. If the discrimination power vanishes in that case, it is also imaginable that a correction on the vertex reconstruction can be applied to yield comparable results.

10. Summary

The field of neutrino physics is in rapid development. LS detectors have already been proven to be successful in measuring solar and reactor neutrinos. Borexino and Double-Chooz for example enabled to conduct precise measurements of the respective oscillation parameters. In the near future they will be accompanied by the JUNO experiment, that is expected to improve the precision on the solar oscillation parameters and to contribute heavily to the determination of the MO. At the same time, HK as the new state-of-the art WC detector will set out to improve the atmospheric oscillation parameters. As part of the T2HK experiment, HK will also help with the determination of the MO and the CP violation in the leptonic sector. In addition, the LArTPC detector DUNE as a third technology is expected to have an impact on the determination of the CP violating phase. Complementary to DUNE, the Theia experiment is proposed to be brought in to the LBNF. Theia, which is in one configuration planned to use WbLS and LAPPDs, is not only expected to help with the measuring of δ_{CP}, but could also measure DSNB neutrinos for the first time.

This is possible, since a WbLS detector combines the advantages of Cherenkov radiation and scintillation light. Cherenkov radiation excels in direction reconstruction, because of the directionality of Cherenkov photons in the Cherenkov cone, whilst scintillation light is great for calorimetry with its low energy threshold and the number of scintillation photons, that is proportional to the deposited energy. Furthermore, the ratio of Cherenkov to scintillation photons can be used for PID and event identification, which is of great use for reducing the background in DSNB neutrino searches.

To access the Cherenkov to scintillation photon ratio, a light separation algorithm is necessary to sort the measured photon hits into a Cherenkov and a scintillation sample. This can be done e.g. via the timing characteristics - Cherenkov photons are emitted quasi-instantaneous, whereas the emission of scintillation photons happens delayed. This approach profits from photodetectors with a great time resolution, which makes LAPPDs a perfect choice with a TTS of less than $100\,\mathrm{ps}$. Additionally, LAPPDs are also suited to resolve the difference in directionality due to their spatial resolution of below $1\,\mathrm{mm}$. This can be for example used in the future to precisely reconstruct Cherenkov rings.

This thesis can be viewed as a feasibility study for the combination of LAPPDs as photosensors and WbLS as active medium in an ideal detector. These are two technologies that are currently investigated by the ANNIE experiment at the Fermilab, which is the associated experiment of this thesis. ANNIE is an accelerator neutrino experiment at Fermilab, that additionally to the LAPPD and WbLS R&D aims to measure the cross-section and the neutron multiplicity of neutrino-nucleus interactions. Currently, three LAPPDs are in use in ANNIE's water tank and first data was taken with a volume filled with WbLS.

In this work, first a Geant4 based simulation was developed to model an ideal detector filled with WbLS and completely covered with LAPPDs with a radius of about $2.2\,\mathrm{m}$ and a height of about $4.3\,\mathrm{m}$. This simulation was then not only used to simulate the event samples in form of $12,000$ $(14,000)$ muon, gamma and electron (proton) events with energies from $0.5\,\mathrm{MeV}$ to $120\,\mathrm{MeV}$ $(140\,\mathrm{MeV})$ and $10,000$ electron events with energies from $0.5\,\mathrm{MeV}$ and $10\,\mathrm{MeV}$ but also to generate LUTs for the propagation time and the direct light probability for both Cherenkov and scintillation photons separately.

These LUTs are necessary to operate the TTR, which was developed in this group for the reconstruction of the deposited energy of muons in LS detectors like LENA and JUNO. The TTR uses an iterative process to reconstruct a track and the $\mathrm{d}E/\mathrm{d}x$ based on an reference point in time and space. In this work, the TTR was splitted up to have a Cherenkov and a scintillation part, that run the regular reconstruction steps enclosed in parallel. Hereby, the Cherenkov part assumes every hit to be a Cherenkov photon and vice versa. With that, the TTR assigns every hit a weight to be originally a Cherenkov or scintillation photon. It has been shown that with five iterations of $10\,\mathrm{cm}$ binning and one iteration with $5\,\mathrm{cm}$ binning, the hits are sufficiently sorted by weights, so that the ratio of weights can be used to separate between Cherenkov and scintillation photons. With this methods purities for the best performing energies ranging from $(68 \pm 22)\,\%$ for the muon sample to $(81 \pm 8)\,\%$ for the electron sample can be reached. Thereby, the efficiency values are $(75 \pm 31)\,\%$ for muons and $(87 \pm 15)\,\%$ for electrons are achieved. Comparable results were shown for the low energy electron and the gamma sample.

These results and the following as well have to be viewed in the context of the underlying assumptions. First of all, the used Geant4 simulation is idealised ignoring reemission and the detector completely covered with LAPPDs, that have the characteristics mentioned above. Furthermore, perfect reconstruction of the photon hits are assumed without electronics and readout simulation. At last, the vertex is assumed to be reconstructed with an uncertainty of $1\,\mathrm{cm}$ in space and $0.2\,\mathrm{ns}$ in time. This assumption is known to be too ideal, because the Cherenkov light introduces a systematic shift of the vertex position towards the particle's flight direction.

For the low energy electron sample several approaches for a direction reconstruction were presented based on a directional sum and the TTR. The directional sum already produced good results in contrast to the TTR based method without taking the light separation algorithm into account due to the sufficient number of Cherenkov photons. Nevertheless, it has been shown that a slight improvement can be reached by incorporating the light separation to reach a peak performance of $(13.45 \pm 11.22)^\circ$ for the highest visible energies. It is to note though that for the lowest visible energies, the direction reconstruction is only capable of vetoing half of the detector.

Additionally, particle discrimination was achieved based on the reconstructed ratio of Cherenkov to scintillation photons. Here, excellent results for the e^-/μ^-p [γ/μ^-p] discrimination were achieved with purities of $(98.5 \pm 0.8) \cdot 10^{-2}$ [$(97.6 \pm 1.3) \cdot 10^{-2}$], efficiencies of $(97.1 \pm 1.0) \cdot 10^{-2}$ [$(98.1 \pm 1.3) \cdot 10^{-2}$] and MCC values of $(96.8 \pm 0.9) \cdot 10^{-2}$ [$(97.3 \pm 1.2) \cdot 10^{-2}$] in the best visible energy interval. With that the atmospheric muon neutrino background can be suppressed that is relevant for DSNB neutrino searches. Due to an underestimation of Cherenkov photons, a e^-/γ discrimination was also possible that reached in the best energy interval a purity of $(72.3 \pm 2.1) \cdot 10^{-2}$ and an efficiency of $(74.1 \pm 2.5) \cdot 10^{-2}$ with a MCC of $(61.2 \pm 2.7) \cdot 10^{-2}$. At last, a μ^-/p discrimination was conducted that for the best visible energy achieved values like $(77.6 \pm 2.6) \cdot 10^{-2}$ for MCC, $(95.3 \pm 1.5) \cdot 10^{-2}$ for purity and $(78.8 \pm 2.9) \cdot 10^{-2}$ for efficiency when also incorporating directional information to the ratio of Cherenkov to scintillation photons.

To conclude, it has been shown that the combination of WbLS and LAPPDs in the ideal case is feasible for accessing the advantages of Cherenkov and scintillation light in form of direction reconstruction and PID in the energy range below $120\,\mathrm{MeV}$. This makes these results not applicable to ANNIE, which operates with accelerator neutrino with higher energies. Furthermore, the direction of neutrinos is known in ANNIE. Therefore, it is reasonable to investigate the presented light separation algorithm in the future not only in terms of other particles, but also in terms of higher energies up to the GeV regime. Other methods of light separation can be investigated e.g. likelihood-based approaches and the existing methods can be further optimised, whilst bringing the underlying simulation to more realism. Speaking of realism, it is essential to evaluate the presented results with a vertex reconstruction due to the discussed shift in reconstructed vertex. Furthermore, other WbLS mixtures and photodetectors can be tested in regard to the light separation quality. Lastly, remaining applications like ring counting and PID via the ring structure are a sensible progression to the applications shown in this thesis.

A. Additional Light Separation Plots

In this chapter the light separation results with the angle criterium are shown for the remaining samples. Figure A.1 shows the results for the low energy electron sample. For (b) a cut value of $C_{\mathrm{Sep}} = 0.14$ is set and (c) includes only events with more than 164 scintillation photons (excluding the first two intervals).

Figure A.2 shows the results for the gamma sample. For (b) a cut value of $C_{\mathrm{Sep}} = 0.15$ is set and (c) includes only events with more than 750 scintillation photons (excluding the first interval).

Figure A.3 shows the results for the muon sample. For (b) a cut value of $C_{\mathrm{Sep}} = 0.14$ is set and (c) includes only events with more than 6750 and less than 8250 scintillation photons (including only the two best performing intervals).

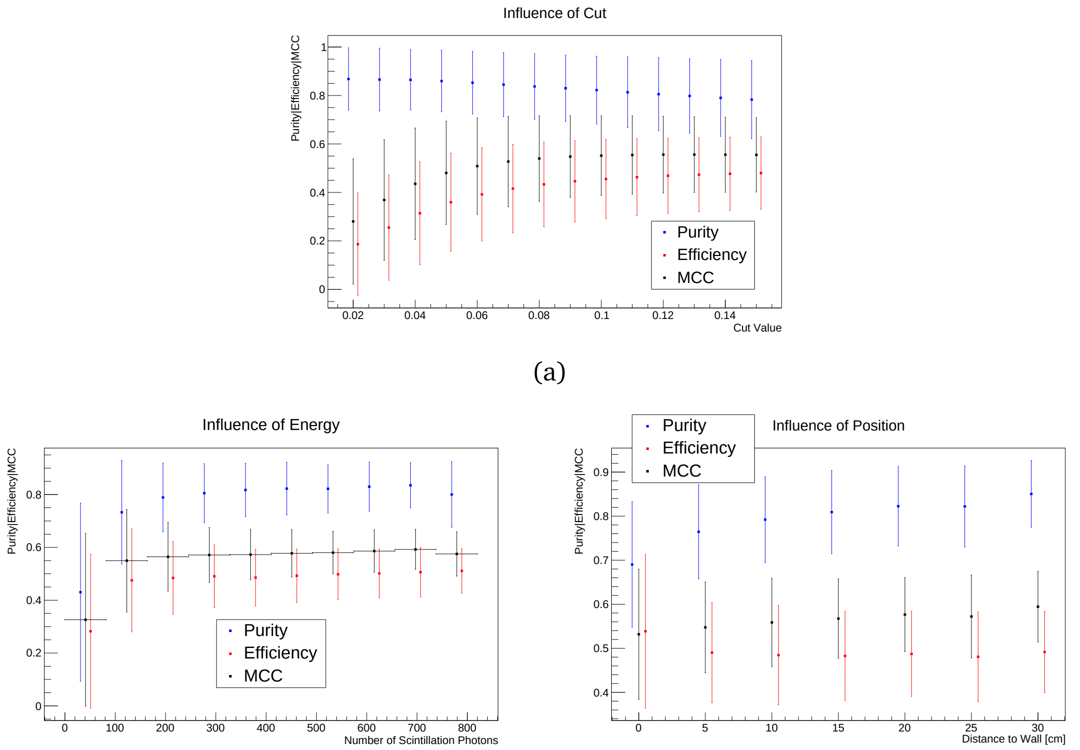

(a)

(b) (c)

Figure A.1.: Performance of the light separation for the low energy electron sample with angle criterium. (a) shows the influence of the cut value, (b) the influence of energy and (c) the influence of the event's position.

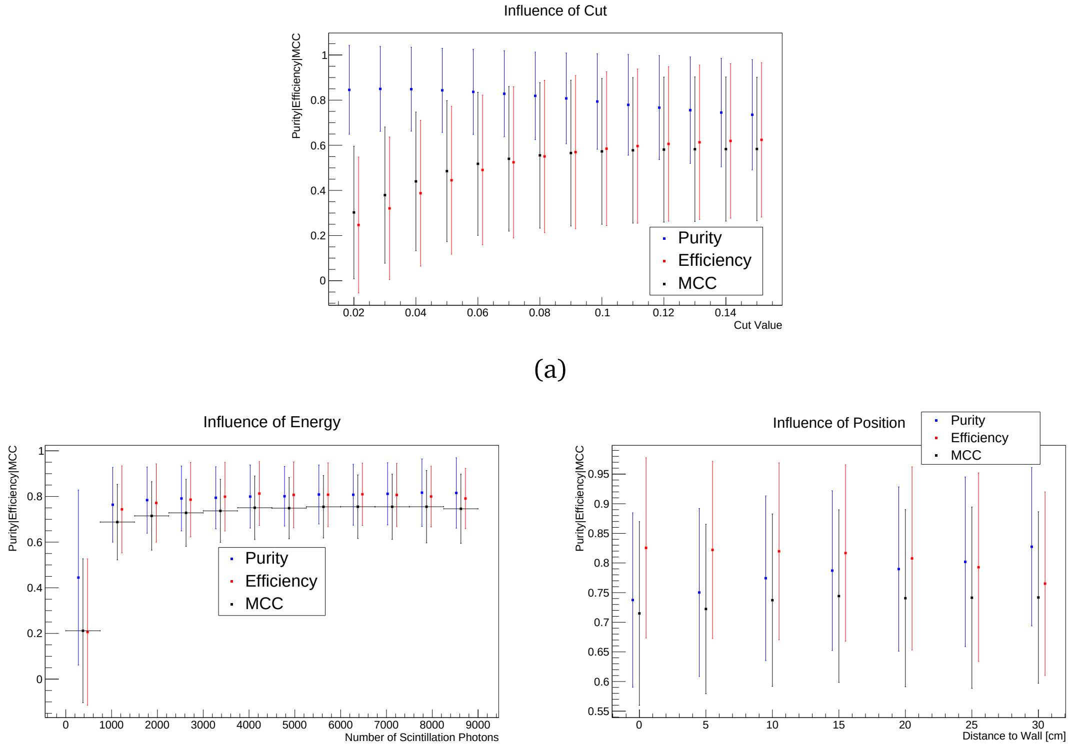

(a)

(b)

(c)

Figure A.2.: Performance of the light separation for the gamma sample with angle criterium. a) shows the influence of the cut value, (b) the influence of energy and (c) the influence of the event's position.

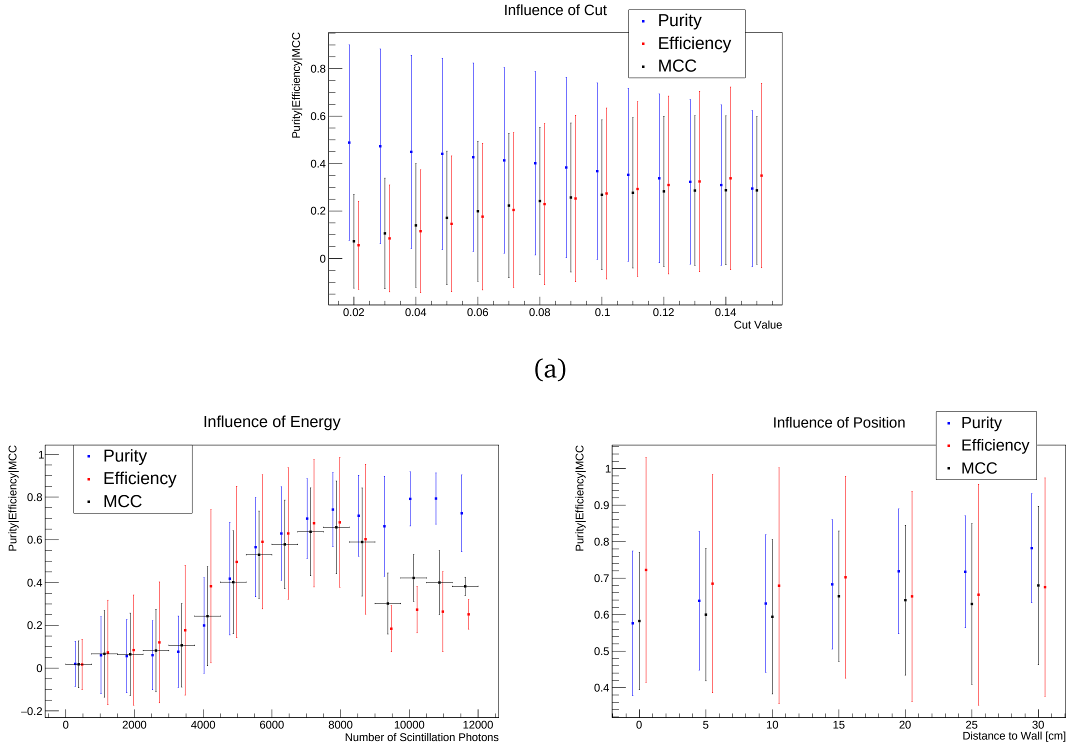

(a)

(b)

(c)

Figure A.3.: Performance of the light separation for the muon sample with angle criterium. a) shows the influence of the cut value, (b) the influence of energy and (c) the influence of the event's position.

List of Figures

List of Tables

List of Acronyms

$0\nu\beta\beta$ Neutrinoless Double Beta Decay

ANNIE Accelerator Neutrino Neutron Interaction Experiment

APD Avalanche PhotoDiode

BEST Baksan Experiment on Sterile Transitions

bis-MSB 1,4-Bis-(2-methylstyryl)-benzol

BBN Big Bang Nucleosynthesis

BNB Booster Neutrino Beam

CC Charge Current

CCDIS Charge Current Deep Inelastic Scattering

CCQE Charge Current Quasi-Elastic

CCRES Charge Current Resonant

CE Collection Efficiency

CERN Conseil Européen pour la Recherche Nucléaire

CEvNS Coherent Elastic Neutrino-Nucleus Scattering

CHESS CHErenkov/Scintillation Separation

CMB Cosmic Microwave Background

CNB Cosmic Neutrino Background

CNGS CERN Neutrinos to Gran Sasso

CNO Carbon–Nitrogen–Oxygen

CP Charge Parity

CUORE Cryogenic Underground Observatory for Rare Events

CUPID-Mo CUORE Upgrade with Particle Identification in Molybdenum

DCR Dark Count Rate

DSNB Diffuse Supernova Neutrino Background

DUNE Deep Underground Neutrino Experiment

ECHo The Electron Capture in $^{163}\mathrm{Ho}$ experiment

ESSνSB European Spallation Source neutrino Super Beam

FACC Front Anti-coincidence Counter

Fermilab Fermi National Accelerator Laboratory

FHC Forward Horn Current

FSI Final State Interactions

FWHM Full Width at Half Maximum

GALLEX Gallium Experiment

GEANT GEometry ANd Tracking

GERDA The GERmanium Detector Array

GUT Grand Unified Theory

HK Hyper-Kamiokande

IBD Inverse Beta Decay

IDS Ideal Detector Simulation

INGRID Interactive Neutrino GRID

IO Inverse Ordering

JUNO Jiangmen Underground Neutrino Observatory

KamLAND Kamioka Liquid Scintillator Antineutrino Detector

KamLAND-Zen KamLAND Zero-Neutrino Double-Beta Decay

KATRIN Karlsruhe Tritium Neutrino Experiment

LAB Linear AlkylBenzene

LAPPD Large Area Picosecond Photodetector

LArTPC Liquid Argon Time Projection Chamber

LBNF Long-Baseline Neutrino Facility

LEGEND The Large Enriched Germanium Experiment for Neutrinoless $\beta\beta$ Decay

LENA Low Energy Neutrino Astronomy

LEP Large Electron-Positron Collider

LMA Large Mixing Angle

LS Liquid Scintillator

LSND Liquid Scintillator Neutrino Detector

LSS Large Scale Structures

LUT Look-Up Table

MC Monte Carlo

MCC Matthew’s Correlation Coefficient

MCP MicroChannel Plate

MiniBooNE Mini Booster Neutrino Experiment

MINOS Main Injector Neutrino Oscillation Search

MO Mass Ordering

MPPC Multi-Pixel Photon Counter

MRD Muon Range Detector

MSW Michejew-Smirnow-Wolfenstein

NC Neutral Current

NCQE Neutral Current Quasi-Elastic

NCV Neutron Capture Volume

NEOS Neutrino Experiment for Oscillation at Short baseline

NO Normal Ordering

NOνA NuMI Off-Axis ν_e Appearance

PC PseudoCumene

PDE Photon Detection Efficiency

PDF Probability Density Function

PE Photoelectron

PID Particle Identification

PINGU Precision IceCube Next Generation Upgrade

PMT PhotoMultiplier Tube

PMNS Pontecorvo-Maki-Nakagawa-Sakata

pp proton-proton

PPO 2,5-diphenyloxazole

PROSPECT Precision Reactor Oscillation and SPECTrum Experiment

PXE Phenylxylylethane

QE Quantum Efficiency

RAA Reactor Antineutrino Anomaly

RENO Reactor Experiment for Neutrino Oscillation

RFG Relativistic Fermi Gas

RHC Reverse Horn Current

SAGE The Soviet-American Gallium solar neutrino Experiment

SBND Short-Baseline Near Detector

SciBooNE SciBar Booster Neutrino Experiment

SiPM Silicon PhotoMultiplier

SR Spatial Resolution

SK Super-Kamiokande

SM Standard Model of particle physics

SN SuperNova

SNO Sudbury Neutrino Observatory

SPAD Single Photon Avalanche Diode

SPS Super Proton Synchrotron

SPTR Single Photon Time Resolution

SSM Standard Solar Model

T2K Tokai-to-Kamioka

T2HK Tokai-to-Hyper-Kamiokande

TAO Taishan Antineutrino Observatory

TTR Topological Track Reconstruction

TTS Transit Time Spread

WbLS Water-based Liquid Scintillator

WC Water-Cherenkov

Bibliography

[1] M. Askins et al. "THEIA: an advanced optical neutrino detector". In: *Eur. Phys. J. C* 80.5 (2020), p. 416. DOI: `10.1140/epjc/s10052-020-7977-8`. arXiv: `1911.03501 [physics.ins-det]`.

[2] B.S. Wonsak et al. "Topological track reconstruction in unsegmented, large-volume liquid scintillator detectors". In: *Journal of Instrumentation* 13.07 (July 2018), P07005–P07005. DOI: `10.1088/1748-0221/13/07/p07005`. URL: `https://doi.org/10.1088/1748-0221/13/07/p07005`.

[3] I. Anghel et al. *Letter of Intent: The Accelerator Neutrino Neutron Interaction Experiment (ANNIE)*. 2015. arXiv: `1504.01480 [physics.ins-det]`.

[4] M. J. Minot et al. "Large Area Picosecond Photodetector (LAPPD TM) - Pilot production and development status". In: *Nuclear Instruments and Methods in Physics Research. Section A, Accelerators, Spectrometers, Detectors and Associated Equipment* 936 (Dec. 2018). DOI: `10.1016/j.nima.2018.11.137`.

[5] Edoardo Vitagliano, Irene Tamborra, and Georg Raffelt. "Grand unified neutrino spectrum at Earth: Sources and spectral components". In: *Reviews of Modern Physics* 92.4 (Dec. 2020). DOI: `10.1103/revmodphys.92.045006`. URL: `https://doi.org/10.1103%2Frevmodphys.92.045006`.

[6] James Alvey et al. "Cosmic neutrino background detection in large-neutrino-mass cosmologies". In: *Physical Review D* 105.6 (Mar. 2022). DOI: `10.1103/physrevd.105.063501`. URL: `https://doi.org/10.1103%2Fphysrevd.105.063501`.

[7] Alexandre V. Ivanchik and Vlad Yu. Yurchenko. "Relic neutrinos: Antineutrinos of primordial nucleosynthesis". In: *Physical Review D* 98.8 (Oct. 2018). DOI: `10.1103/physrevd.98.081301`. URL: `https://doi.org/10.1103%2Fphysrevd.98.081301`.

[8] Edoardo Vitagliano, Javier Redondo, and Georg Raffelt. "Solar neutrinos at keV energies: thermal flux". In: *J. Phys. Conf. Ser.* 1342.1 (2020). Ed. by Ken Clark et al., p. 012050. DOI: `10.1088/1742-6596/1342/1/012050`. arXiv: `1709.02811 [hep-ph]`.

[9] Liudmila Lukyanchenko. "Study of Diffuse Supernova Neutrino Background with Modern and Future Detectors". In: *Physics of Atomic Nuclei* 80 (Nov. 2017), pp. 1153–1156. DOI: `10.1134/S1063778817060084`.

[10] S. Fukuda et al. “The Super-Kamiokande detector”. In: *Nuclear Instruments and Methods in Physics Research Section A: Accelerators, Spectrometers, Detectors and Associated Equipment* 501.2 (2003), pp. 418–462. ISSN: 0168-9002. DOI: `https://doi.org/10.1016/S0168-9002(03)00425-X`. URL: `https://www.sciencedirect.com/science/article/pii/S016890020300425X`.

[11] Fengpeng An et al. “Neutrino physics with JUNO”. In: *Journal of Physics G: Nuclear and Particle Physics* 43.3 (Feb. 2016), p. 030401. DOI: `10.1088/0954-3899/43/3/030401`. URL: `https://doi.org/10.1088%2F0954-3899%2F43%2F3%2F030401`.

[12] K. Abe et al. “Letter of Intent: The Hyper-Kamiokande Experiment — Detector Design and Physics Potential —”. In: (Sept. 2011). arXiv: `1109.3262 [hep-ex]`.

[13] M. Sajjad Athar et al. “Status and perspectives of neutrino physics”. In: *Progress in Particle and Nuclear Physics* 124 (2022), p. 103947. ISSN: 0146-6410. DOI: `https://doi.org/10.1016/j.ppnp.2022.103947`. URL: `https://www.sciencedirect.com/science/article/pii/S0146641022000084`.

[14] Julia Sawatzki, Michael Wurm, and Daniel Kresse. “Detecting the Diffuse Supernova Neutrino Background in the future Water-based Liquid Scintillator Detector Theia”. In: *Phys. Rev. D* 103.2 (2021), p. 023021. DOI: `10.1103/PhysRevD.103.023021`. arXiv: `2007.14705 [physics.ins-det]`.

[15] J. A. Formaggio and G. P. Zeller. “From eV to EeV: Neutrino cross sections across energy scales”. In: *Reviews of Modern Physics* 84.3 (Sept. 2012), pp. 1307–1341. DOI: `10.1103/revmodphys.84.1307`. URL: `https://doi.org/10.1103%2Frevmodphys.84.1307`.

[16] F. Vannucci. “Interactions of neutrinos with matter”. In: *Progress in Particle and Nuclear Physics* 95 (2017), pp. 1–47. ISSN: 0146-6410. DOI: `https://doi.org/10.1016/j.ppnp.2017.03.003`. URL: `https://www.sciencedirect.com/science/article/pii/S0146641017300340`.

[17] Masaru Doi. “Inverse Muon Decay in the Gauge Theory”. In: *Progress of Theoretical Physics* 84.6 (Dec. 1990), pp. 1036–1041. ISSN: 0033-068X. DOI: `10.1143/ptp/84.6.1036`. eprint: `https://academic.oup.com/ptp/article-pdf/84/6/1036/5407013/84-6-1036.pdf`. URL: `https://doi.org/10.1143/ptp/84.6.1036`.

[18] B. Abi et al. *Deep Underground Neutrino Experiment (DUNE), Far Detector Technical Design Report, Volume I: Introduction to DUNE*. 2020. arXiv: `2002.02967 [physics.ins-det]`.

[19] Solveig Skadhauge and Renata Zukanovich Funchal. “Determining neutrino and supernova parameters with a galactic supernova”. In: *Journal of Cosmology and Astroparticle Physics* 2007.04 (Apr. 2007), pp. 014–014. DOI: `10.1088/1475-7516/2007/04/014`. URL: `https://doi.org/10.1088%2F1475-7516%2F2007%2F04%2F014`.

[20] D. Akimov et al. “Measurement of the Coherent Elastic Neutrino-Nucleus Scattering Cross Section on CsI by COHERENT”. In: *Physical Review Letters* 129.8 (Aug. 2022). DOI: `10.1103/physrevlett.129.081801`. URL: `https://doi.org/10.1103%2Fphysrevlett.129.081801`.

[21] D. Akimov et al. “Observation of coherent elastic neutrino-nucleus scattering”. In: *Science* 357.6356 (Sept. 2017), pp. 1123–1126. DOI: `10.1126/science.aao0990`. URL: `https://doi.org/10.1126%2Fscience.aao0990`.

[22] Kate Scholberg. “Observation of Coherent Elastic Neutrino-Nucleus Scattering by COHERENT”. In: *PoS* NuFact2017 (2018), p. 020. DOI: `10.22323/1.295.0020`. arXiv: `1801.05546 [hep-ex]`.

[23] Michael Wurm et al. “The next-generation liquid-scintillator neutrino observatory LENA”. In: *Astropart. Phys.* 35 (2012), pp. 685–732. DOI: `10.1016/j.astropartphys.2012.02.011`. arXiv: `1104.5620 [astro-ph.IM]`.

[24] Luis Alvarez-Ruso and Eduardo Saul-Sala. “Neutrino interactions with matter and the MiniBooNE anomaly”. In: *The European Physical Journal Special Topics* 230.24 (Oct. 2021), pp. 4373–4389. DOI: `10.1140/epjs/s11734-021-00293-9`. URL: `https://doi.org/10.1140%2Fepjs%2Fs11734-021-00293-9`.

[25] L. Alvarez-Ruso et al. “NuSTEC White Paper: Status and challenges of neutrino–nucleus scattering”. In: *Progress in Particle and Nuclear Physics* 100 (May 2018), pp. 1–68. DOI: `10.1016/j.ppnp.2018.01.006`. URL: `https://doi.org/10.1016%2Fj.ppnp.2018.01.006`.

[26] Kai Zuber. *Neutrino Physics*. 3rd ed. URL: `https://doi.org/10.1201/9781315195612`. CRC Press, 2020.

[27] S.M. Bilenky, C. Giunti, and W. Grimus. “Phenomenology of neutrino oscillations”. In: *Progress in Particle and Nuclear Physics* 43 (Jan. 1999), pp. 1–86. DOI: `10.1016/s0146-6410(99)00092-7`. URL: `https://doi.org/10.1016%2Fs0146-6410%2899%2900092-7`.

[28] Fumihiko Suekane. “Neutrino Oscillation”. In: *Neutrino Oscillations: A Practical Guide to Basics and Applications*. Tokyo: Springer Japan, 2015, pp. 45–75. ISBN: 978-4-431-55462-2. DOI: `10.1007/978-4-431-55462-2_4`. URL: `https://doi.org/10.1007/978-4-431-55462-2_4`.

[29] Carlo Giunti and Chung W. Kim. *Fundamentals of Neutrino Physics and Astrophysics*. Oxford University Press, Mar. 2007. ISBN: 9780198508717. DOI: `10.1093/acprof:oso/9780198508717.001.0001`. URL: `https://doi.org/10.1093/acprof:oso/9780198508717.001.0001`.

[30] Claudio Giganti, Stéphane Lavignac, and Marco Zito. "Neutrino oscillations: The rise of the PMNS paradigm". In: *Prog. Part. Nucl. Phys.* 98 (2018), pp. 1–54. DOI: `10.1016/j.ppnp.2017.10.001`. arXiv: `1710.00715 [hep-ex]`.

[31] NuFIT. *NuFIT 5.2 (2022)*. Accessed 25.04.2023, URL: `www.nu-fit.org`.

[32] Ivan Esteban et al. "The fate of hints: updated global analysis of three-flavor neutrino oscillations". In: *Journal of High Energy Physics* 2020.9 (Sept. 2020). DOI: `10.1007/jhep09(2020)178`. URL: `https://doi.org/10.1007%2Fjhep09%282020%29178`.

[33] K. Abe et al. "Atmospheric neutrino oscillation analysis with external constraints in Super-Kamiokande I-IV". In: *Physical Review D* 97.7 (Apr. 2018). DOI: `10.1103/physrevd.97.072001`. URL: `https://doi.org/10.1103%2Fphysrevd.97.072001`.

[34] Aldo Ianni. "Solar neutrinos and the solar model". In: *Physics of the Dark Universe* 4 (2014). DARK TAUP2013, pp. 44–49. ISSN: 2212-6864. DOI: `https://doi.org/10.1016/j.dark.2014.06.002`. URL: `https://www.sciencedirect.com/science/article/pii/S2212686414000211`.

[35] Mariia Redchuk. "Solar neutrino analysis with the Borexino detector". In: *Journal of Physics: Conference Series* 1056.1 (July 2018), p. 012050. DOI: `10.1088/1742-6596/1056/1/012050`. URL: `https://dx.doi.org/10.1088/1742-6596/1056/1/012050`.

[36] Andrea Gallo Rosso et al. "Introduction to neutrino astronomy". In: *Eur. Phys. J. Plus* 133.7 (2018), p. 267. DOI: `10.1140/epjp/i2018-12143-6`. arXiv: `1806.06339 [astro-ph.HE]`.

[37] Raymond Davis. "A review of the homestake solar neutrino experiment". In: *Progress in Particle and Nuclear Physics* 32 (1994), pp. 13–32. ISSN: 0146-6410. DOI: `https://doi.org/10.1016/0146-6410(94)90004-3`. URL: `https://www.sciencedirect.com/science/article/pii/0146641094900043`.

[38] V.N. Gavrin et al. "Sage: The Soviet-American gallium solar neutrino experiment". In: *Nuclear Physics B - Proceedings Supplements* 28.1 (1992), pp. 75–81. ISSN: 0920-5632. DOI: `https://doi.org/10.1016/0920-5632(92)90149-M`. URL: `https://www.sciencedirect.com/science/article/pii/092056329290149M`.

[39] D. Vignaud. “The GALLEX solar neutrino experiment”. In: *Nuclear Physics B - Proceedings Supplements* 60.3 (1998), pp. 20–29. ISSN: 0920-5632. DOI: `https://doi.org/10.1016/S0920-5632(97)00498-2`. URL: `https://www.sciencedirect.com/science/article/pii/S0920563297004982`.

[40] K. S. Hirata et al. “Real-time, directional measurement of $^{8}\mathrm{B}$ solar neutrinos in the Kamiokande II detector”. In: *Phys. Rev. D* 44 (8 Oct. 1991), pp. 2241–2260. DOI: `10.1103/PhysRevD.44.2241`. URL: `https://link.aps.org/doi/10.1103/PhysRevD.44.2241`.

[41] Christopher W. Walter. “The Super-Kamiokande Experiment”. In: (Feb. 2008), pp. 19–43. DOI: `10.1142/9789812771971_0002`. arXiv: `0802.1041 [hep-ex]`.

[42] J Boger et al. “The Sudbury Neutrino Observatory”. In: *Nuclear Instruments and Methods in Physics Research Section A: Accelerators, Spectrometers, Detectors and Associated Equipment* 449.1 (2000), pp. 172–207. ISSN: 0168-9002. DOI: `https://doi.org/10.1016/S0168-9002(99)01469-2`. URL: `https://www.sciencedirect.com/science/article/pii/S0168900299014692`.

[43] Masayuki Nakahata. “History of solar neutrino observations”. In: *PTEP* 2022.12 (2022), 12B103. DOI: `10.1093/ptep/ptac039`. arXiv: `2202.12421 [hep-ex]`.

[44] G. Alimonti et al. “The Borexino detector at the Laboratori Nazionali del Gran Sasso”. In: *Nuclear Instruments and Methods in Physics Research Section A: Accelerators, Spectrometers, Detectors and Associated Equipment* 600.3 (Mar. 2009), pp. 568–593. DOI: `10.1016/j.nima.2008.11.076`. URL: `https://doi.org/10.1016%2Fj.nima.2008.11.076`.

[45] G. Settanta et al. “First detection of CNO neutrinos with Borexino”. In: *55th Rencontres de Moriond on Electroweak Interactions and Unified Theories*. May 2021. arXiv: `2105.09211 [hep-ex]`.

[46] M. Agostini et al. “Comprehensive measurement of pp-chain solar neutrinos”. In: *Nature* 562.7728 (2018), pp. 505–510. DOI: `10.1038/s41586-018-0624-y`.

[47] F. Suekane et al. *An Overview of the KamLAND 1-kiloton Liquid Scintillator*. 2004. arXiv: `physics/0404071 [physics.ins-det]`.

[48] L.J. Wen, J. Cao, and Y.F. Wang. “Reactor Neutrino Experiments: Present and Future”. In: *Annual Review of Nuclear and Particle Science* 67.1 (2017), pp. 183–211. DOI: `10.1146/annurev-nucl-101916-123318`. eprint: `https://doi.org/10.1146/annurev-nucl-101916-123318`. URL: `https://doi.org/10.1146/annurev-nucl-101916-123318`.

[49] F. Ardellier et al. "Double Chooz: A Search for the neutrino mixing angle theta(13)". In: (June 2006). arXiv: `hep-ex/0606025`.

[50] J. K. Ahn et al. "RENO: An Experiment for Neutrino Oscillation Parameter θ_{13} Using Reactor Neutrinos at Yonggwang". In: (Mar. 2010). arXiv: `1003.1391 [hep-ex]`.

[51] Jun Cao and Kam-Biu Luk. "An overview of the Daya Bay reactor neutrino experiment". In: *Nuclear Physics B* 908 (2016). Neutrino Oscillations: Celebrating the Nobel Prize in Physics 2015, pp. 62–73. ISSN: 0550-3213. DOI: `https://doi.org/10.1016/j.nuclphysb.2016.04.034`. URL: `https://www.sciencedirect.com/science/article/pii/S0550321316300724`.

[52] A. Achterberg et al. "First Year Performance of The IceCube Neutrino Telescope". In: *Astropart. Phys.* 26 (2006), pp. 155–173. DOI: `10.1016/j.astropartphys.2006.06.007`. arXiv: `astro-ph/0604450`.

[53] K. Abe et al. "The T2K Experiment". In: *Nucl. Instrum. Meth. A* 659 (2011), pp. 106–135. DOI: `10.1016/j.nima.2011.06.067`. arXiv: `1106.1238 [physics.ins-det]`.

[54] I. Ambats et al. "The MINOS Detectors Technical Design Report". In: (Oct. 1998). DOI: `10.2172/1861363`.

[55] D S Ayres et al. "The NOvA Technical Design Report". In: (Oct. 2007). DOI: `10.2172/935497`. URL: `https://www.osti.gov/biblio/935497`.

[56] R. Abbasi et al. "The Design and Performance of IceCube DeepCore". In: *Astropart. Phys.* 35 (2012), pp. 615–624. DOI: `10.1016/j.astropartphys.2012.01.004`. arXiv: `1109.6096 [astro-ph.IM]`.

[57] Olga Mena and Stephen J. Parke. "Unified graphical summary of neutrino mixing parameters". In: *Phys. Rev. D* 69 (2004), p. 117301. DOI: `10.1103/PhysRevD.69.117301`. arXiv: `hep-ph/0312131`.

[58] R. N. Cahn et al. "White Paper: Measuring the Neutrino Mass Hierarchy". In: *Snowmass 2013: Snowmass on the Mississippi*. July 2013. arXiv: `1307.5487 [hep-ex]`.

[59] Thomas Schwetz-Mangold. *Accelerator Neutrino I - Three neutrino phenomenology and global analyses*. June 2022. DOI: `10.5281/zenodo.6683818`.

[60] Anatael Cabrera et al. "Synergies and prospects for early resolution of the neutrino mass ordering". In: *Sci. Rep.* 12.1 (2022), p. 5393. DOI: `10.1038/s41598-022-09111-1`. arXiv: `2008.11280 [hep-ph]`.

[61] K. Abe et al. "Atmospheric neutrino oscillation analysis with external constraints in Super-Kamiokande I-IV". In: *Phys. Rev. D* 97.7 (2018), p. 072001. DOI: `10.1103/PhysRevD.97.072001`. arXiv: `1710.09126 [hep-ex]`.

[62] M. G. Aartsen et al. “Determining neutrino oscillation parameters from atmospheric muon neutrino disappearance with three years of IceCube DeepCore data”. In: *Phys. Rev. D* 91.7 (2015), p. 072004. DOI: `10.1103/PhysRevD.91.072004`. arXiv: `1410.7227 [hep-ex]`.

[63] M. G. Aartsen et al. “PINGU: A Vision for Neutrino and Particle Physics at the South Pole”. In: *J. Phys. G* 44.5 (2017), p. 054006. DOI: `10.1088/1361-6471/44/5/054006`. arXiv: `1607.02671 [hep-ex]`.

[64] Stefano Gariazzo et al. “Neutrino mass and mass ordering: no conclusive evidence for normal ordering”. In: *JCAP* 10 (2022), p. 010. DOI: `10.1088/1475-7516/2022/10/010`. arXiv: `2205.02195 [hep-ph]`.

[65] Cora Dvorkin et al. “Neutrino Mass from Cosmology: Probing Physics Beyond the Standard Model”. In: (Mar. 2019). arXiv: `1903.03689 [astro-ph.CO]`.

[66] Andrei D Sakharov. “Violation of CP invariance, C asymmetry, and baryon asymmetry of the universe”. In: *Soviet Physics Uspekhi* 34.5 (May 1991), p. 392. DOI: `10.1070/PU1991v034n05ABEH002497`. URL: `https://dx.doi.org/10.1070/PU1991v034n05ABEH002497`.

[67] “Direct CP violation in charmless three-body decays of $B^{\pm}$ mesons”. In: (June 2022). arXiv: `2206.07622 [hep-ex]`.

[68] G.D. Barr et al. “A new measurement of direct CP violation in the neutral kaon system”. In: *Physics Letters B* 317.1 (1993), pp. 233–242. ISSN: 0370-2693. DOI: `https://doi.org/10.1016/0370-2693(93)91599-I`. URL: `https://www.sciencedirect.com/science/article/pii/037026939391599I`.

[69] M. Bauer. “Matter-antimatter Asymmetry, CP Violation and the Time Operator in Relativistic Quantum Mechanics”. In: (Aug. 2022). arXiv: `2208.13864 [hep-ph]`.

[70] B. Abi et al. “Long-baseline neutrino oscillation physics potential of the DUNE experiment”. In: *Eur. Phys. J. C* 80.10 (2020), p. 978. DOI: `10.1140/epjc/s10052-020-08456-z`. arXiv: `2006.16043 [hep-ex]`.

[71] M. Askins et al. “Theia: Summary of physics program. Snowmass White Paper Submission”. In: *Snowmass 2021*. Feb. 2022. arXiv: `2202.12839 [hep-ex]`.

[72] A. Alekou et al. “The European Spallation Source neutrino Super Beam”. In: (Mar. 2022). arXiv: `2203.08803 [physics.acc-ph]`.

[73] M. Aker et al. “The design, construction, and commissioning of the KATRIN experiment”. In: *JINST* 16.08 (2021), T08015. DOI: `10.1088/1748-0221/16/08/T08015`. arXiv: `2103.04755 [physics.ins-det]`.

[74] M. Aker et al. “Direct neutrino-mass measurement with sub-electronvolt sensitivity”. In: *Nature Phys.* 18.2 (2022), pp. 160–166. DOI: `10.1038/s41567-021-01463-1`. arXiv: `2105.08533 [hep-ex]`.

[75] Christian Weinheimer. *Direct search for the neutrino mass scale with the KATRIN experiment*. Talk, accessed 12.06.2023, URL: `https://indico.gsi.de/event/17443/`. Apr. 2023.

[76] M. Aker et al. “KATRIN: status and prospects for the neutrino mass and beyond”. In: *J. Phys. G* 49.10 (2022), p. 100501. DOI: `10.1088/1361-6471/ac834e`. arXiv: `2203.08059 [nucl-ex]`.

[77] A. Ashtari Esfahani et al. “The Project 8 Neutrino Mass Experiment”. In: *Snowmass 2021*. Mar. 2022. arXiv: `2203.07349 [nucl-ex]`.

[78] L. Gastaldo et al. “The Electron Capture ^{163}Ho Experiment ECHo: an overview”. In: *J. Low Temp. Phys.* 176.5-6 (2014). Ed. by Erik Skirokoff, pp. 876–884. DOI: `10.1007/s10909-014-1187-4`. arXiv: `1309.5214 [physics.ins-det]`.

[79] Jean, P. and Guessoum, N. “Neutron-capture and 2.22 MeV emission in the atmosphere of the secondary of an X-ray binary”. In: *A&A* 378.2 (2001), pp. 509–521. DOI: `10.1051/0004-6361:20011201`. URL: `https://doi.org/10.1051/0004-6361:20011201`.

[80] J. Schechter and J. W. F. Valle. “Neutrinoless double-β decay in SU(2)$\times$U(1) theories”. In: *Phys. Rev. D* 25 (11 June 1982), pp. 2951–2954. DOI: `10.1103/PhysRevD.25.2951`. URL: `https://link.aps.org/doi/10.1103/PhysRevD.25.2951`.

[81] Michelle J. Dolinski, Alan W.P. Poon, and Werner Rodejohann. “Neutrinoless Double-Beta Decay: Status and Prospects”. In: *Annual Review of Nuclear and Particle Science* 69.1 (Oct. 2019), pp. 219–251. DOI: `10.1146/annurev-nucl-101918-023407`. URL: `https://doi.org/10.1146%5C%2Fannurev-nucl-101918-023407`.

[82] E. Armengaud et al. “New Limit for Neutrinoless Double-Beta Decay of $^{100}\mathrm{Mo}$ from the CUPID-Mo Experiment”. In: *Phys. Rev. Lett.* 126 (18 May 2021), p. 181802. DOI: `10.1103/PhysRevLett.126.181802`. URL: `https://link.aps.org/doi/10.1103/PhysRevLett.126.181802`.

[83] C. Augier et al. “Final results on the $0\nu\beta\beta$ decay half-life limit of ^{100}Mo from the CUPID-Mo experiment”. In: *Eur. Phys. J. C* 82.11 (2022), p. 1033. DOI: `10.1140/epjc/s10052-022-10942-5`. arXiv: `2202.08716 [nucl-ex]`.

[84] O. Azzolini et al. “Final Result of CUPID-0 Phase-I in the Search for the $^{82}\mathrm{Se}$ Neutrinoless Double-β Decay”. In: *Phys. Rev. Lett.* 123 (3 July 2019), p. 032501. DOI: `10.1103/PhysRevLett.123.032501`. URL: `https://link.aps.org/doi/10.1103/PhysRevLett.123.032501`.

[85] D. Q. Adams et al. “Improved Limit on Neutrinoless Double-Beta Decay in $^{130}\mathrm{Te}$ with CUORE”. In: *Phys. Rev. Lett.* 124 (12 Mar. 2020), p. 122501. DOI: `10.1103/PhysRevLett.124.122501`. URL: `https://link.aps.org/doi/10.1103/PhysRevLett.124.122501`.

[86] O. Azzolini et al. “Final Result on the Neutrinoless Double Beta Decay of ^{82}Se with CUPID-0”. In: *Phys. Rev. Lett.* 129.11 (2022), p. 111801. DOI: `10.1103/PhysRevLett.129.111801`. arXiv: `2206.05130 [hep-ex]`.

[87] D. Q. Adams et al. “Search for Majorana neutrinos exploiting millikelvin cryogenics with CUORE”. In: *Nature* 604.7904 (2022), pp. 53–58. DOI: `10.1038/s41586-022-04497-4`. arXiv: `2104.06906 [nucl-ex]`.

[88] Anastasiia Zolotarova. “Bolometric Double Beta Decay Experiments: Review and Prospects”. In: *Symmetry* 13.12 (2021). ISSN: 2073-8994. DOI: `10.3390/sym13122255`. URL: `https://www.mdpi.com/2073-8994/13/12/2255`.

[89] M. Agostini et al. “Final Results of GERDA on the Search for Neutrinoless Double-β Decay”. In: *Phys. Rev. Lett.* 125 (25 Dec. 2020), p. 252502. DOI: `10.1103/PhysRevLett.125.252502`. URL: `https://link.aps.org/doi/10.1103/PhysRevLett.125.252502`.

[90] S. Abe et al. “Search for the Majorana Nature of Neutrinos in the Inverted Mass Ordering Region with KamLAND-Zen”. In: *Phys. Rev. Lett.* 130.5 (2023), p. 051801. DOI: `10.1103/PhysRevLett.130.051801`. arXiv: `2203.02139 [hep-ex]`.

[91] A. Gando et al. “Search for Majorana Neutrinos Near the Inverted Mass Hierarchy Region with KamLAND-Zen”. In: *Phys. Rev. Lett.* 117 (8 Aug. 2016), p. 082503. DOI: `10.1103/PhysRevLett.117.082503`. URL: `https://link.aps.org/doi/10.1103/PhysRevLett.117.082503`.

[92] N. Abgrall et al. “The Large Enriched Germanium Experiment for Neutrinoless $\beta\beta$ Decay: LEGEND-1000 Preconceptual Design Report”. In: (July 2021). arXiv: `2107.11462 [physics.ins-det]`.

[93] W. R. Armstrong et al. “CUPID pre-CDR”. In: (July 2019). arXiv: `1907.09376 [physics.ins-det]`.

[94] C. Adams et al. “Neutrinoless Double Beta Decay”. In: (Dec. 2022). arXiv: `2212.11099 [nucl-ex]`.

[95] Patrick Janot and Stanisław Jadach. “Improved Bhabha cross section at LEP and the number of light neutrino species”. In: *Phys. Lett. B* 803 (2020), p. 135319. DOI: `10.1016/j.physletb.2020.135319`. arXiv: `1912.02067 [hep-ph]`.

[96] Jack J. Bennett et al. “Towards a precision calculation of N_{eff} in the Standard Model II: Neutrino decoupling in the presence of flavour oscillations and finite-temperature QED”. In: *JCAP* 04 (2021), p. 073. DOI: `10.1088/1475-7516/2021/04/073`. arXiv: `2012.02726 [hep-ph]`.

[97] Sebastian Böser et al. “Status of Light Sterile Neutrino Searches”. In: *Prog. Part. Nucl. Phys.* 111 (2020), p. 103736. DOI: `10.1016/j.ppnp.2019.103736`. arXiv: `1906.01739 [hep-ex]`.

[98] Feng Peng An et al. “Improved Measurement of the Reactor Antineutrino Flux and Spectrum at Daya Bay”. In: *Chin. Phys. C* 41.1 (2017), p. 013002. DOI: `10.1088/1674-1137/41/1/013002`. arXiv: `1607.05378 [hep-ex]`.

[99] Y. Abe et al. “Improved measurements of the neutrino mixing angle θ_{13} with the Double Chooz detector”. In: *JHEP* 10 (2014). [Erratum: JHEP 02, 074 (2015)], p. 086. DOI: `10.1007/JHEP02(2015)074`. arXiv: `1406.7763 [hep-ex]`.

[100] A. Letourneau et al. “Origin of the Reactor Antineutrino Anomalies in Light of a New Summation Model with Parametrized β^- Transitions”. In: *Phys. Rev. Lett.* 130 (2 Jan. 2023), p. 021801. DOI: `10.1103/PhysRevLett.130.021801`. URL: `https://link.aps.org/doi/10.1103/PhysRevLett.130.021801`.

[101] P. Anselmann et al. “GALLEX solar neutrino observations: complete results for GALLEX II”. In: *Physics Letters B* 357.1 (1995), pp. 237–247. ISSN: 0370-2693. DOI: `https://doi.org/10.1016/0370-2693(95)00897-T`. URL: `https://www.sciencedirect.com/science/article/pii/037026939500897T`.

[102] C. Giunti et al. “Gallium Anomaly: critical view from the global picture of ν_e and $\overline{\nu}_e$ disappearance”. In: *JHEP* 10 (2022), p. 164. DOI: `10.1007/JHEP10(2022)164`. arXiv: `2209.00916 [hep-ph]`.

[103] V. V. Barinov et al. “Search for electron-neutrino transitions to sterile states in the BEST experiment”. In: *Phys. Rev. C* 105.6 (2022), p. 065502. DOI: `10.1103/PhysRevC.105.065502`. arXiv: `2201.07364 [nucl-ex]`.

[104] A. Aguilar et al. “Evidence for neutrino oscillations from the observation of $\bar{\nu}_e$ appearance in a $\bar{\nu}_\mu$ beam”. In: *Phys. Rev. D* 64 (2001), p. 112007. DOI: `10.1103/PhysRevD.64.112007`. arXiv: `hep-ex/0104049`.

[105] A. A. Aguilar-Arevalo et al. “Updated MiniBooNE neutrino oscillation results with increased data and new background studies”. In: *Phys. Rev. D* 103.5 (2021), p. 052002. DOI: `10.1103/PhysRevD.103.052002`. arXiv: `2006.16883 [hep-ex]`.

[106] P. Abratenko et al. "First Constraints on Light Sterile Neutrino Oscillations from Combined Appearance and Disappearance Searches with the MicroBooNE Detector". In: *Phys. Rev. Lett.* 130.1 (2023), p. 011801. DOI: `10.1103/PhysRevLett.130.011801`. arXiv: `2210.10216 [hep-ex]`.

[107] Y. J. Ko et al. "Sterile Neutrino Search at the NEOS Experiment". In: *Phys. Rev. Lett.* 118.12 (2017), p. 121802. DOI: `10.1103/PhysRevLett.118.121802`. arXiv: `1610.05134 [hep-ex]`.

[108] Z. Atif et al. "Search for sterile neutrino oscillations using RENO and NEOS data". In: *Phys. Rev. D* 105 (11 June 2022), p. L111101. DOI: `10.1103/PhysRevD.105.L111101`. URL: `https://link.aps.org/doi/10.1103/PhysRevD.105.L111101`.

[109] A. P. Serebrov et al. "NEUTRINO4 experiment: preparations for search for sterile neutrino at 100 MW Reactor SM-3 at 6-12 Meters". In: (May 2012). arXiv: `1205.2955 [hep-ph]`.

[110] A. P. Serebrov et al. "Search for sterile neutrinos with the Neutrino-4 experiment and measurement results". In: *Phys. Rev. D* 104 (3 Aug. 2021), p. 032003. DOI: `10.1103/PhysRevD.104.032003`. URL: `https://link.aps.org/doi/10.1103/PhysRevD.104.032003`.

[111] I. Alekseev et al. "Search for sterile neutrinos at the DANSS experiment". In: *Physics Letters B* 787 (2018), pp. 56–63. ISSN: 0370-2693. DOI: `https://doi.org/10.1016/j.physletb.2018.10.038`. URL: `https://www.sciencedirect.com/science/article/pii/S0370269318308098`.

[112] Mikhail Danilov. "New results from the DANSS experiment". In: *PoS* ICHEP2022 (Nov. 2022), p. 616. DOI: `10.22323/1.414.0616`. arXiv: `2211.01208 [hep-ex]`.

[113] J. Ashenfelter et al. "PROSPECT - A Precision Reactor Oscillation and Spectrum Experiment at Short Baselines". In: *Snowmass 2013: Snowmass on the Mississippi*. Sept. 2013. arXiv: `1309.7647 [physics.ins-det]`.

[114] Hamamatsu Photonics K.K. Editorial Committee. *Photomultiplier Tubes - Basics and Applications -*. Manual, Fourth Edition, URL: `https://www.hamamatsu.com/resources/pdf/etd/PMT_handbook_v4E.pdf`. April 2017.

[115] M.G. Aartsen et al. "The IceCube Neutrino Observatory: instrumentation and online systems". In: *Journal of Instrumentation* 12.03 (Mar. 2017), P03012–P03012. DOI: `10.1088/1748-0221/12/03/p03012`. URL: `https://doi.org/10.1088%2F1748-0221%2F12%2F03%2Fp03012`.

[116] Hamamatsu Photonics K.K. *About PMTs | Photomultiplier tubes (PMTs)*. Accessed 23.08.2021, URL: `https://www.hamamatsu.com/eu/en/product/optical-sensors/pmt/about_pmts/index.html`.

[117] Semiconductor Components Industries. *Introduction to the Silicon Photomultiplier (SiPM)*. Publication Order Number: AND9770/D, Revision 8, URL: `https://www.onsemi.com/pub/Collateral/AND9770-D.PDF`. July 2021.

[118] K. Kobayashi A. Ghassemi K. Sato. *MPPC*. Technical Note, URL: `https://hub.hamamatsu.com/sp/hc/resources/TN0014/mppc_kapd9005e.pdf`. March 2017.

[119] Binhao Wang and Jifang Mu. “High-speed Si-Ge avalanche photodiodes”. In: *PhotoniX* 3 (Mar. 2022), p. 8. DOI: `10.1186/s43074-022-00052-6`.

[120] M. Otani et al. “Design and construction of INGRID neutrino beam monitor for T2K neutrino experiment”. In: *Nuclear Instruments and Methods in Physics Research Section A: Accelerators, Spectrometers, Detectors and Associated Equipment* 623.1 (2010). 1st International Conference on Technology and Instrumentation in Particle Physics, pp. 368–370. ISSN: 0168-9002. DOI: `https://doi.org/10.1016/j.nima.2010.02.251`. URL: `https://www.sciencedirect.com/science/article/pii/S016890021000536X`.

[121] K. Abe et al. *T2K ND280 Upgrade – Technical Design Report*. 2020. arXiv: `1901.03750 [physics.ins-det]`.

[122] JUNO Collaboration et al. *TAO Conceptual Design Report: A Precision Measurement of the Reactor Antineutrino Spectrum with Sub-percent Energy Resolution*. 2020. arXiv: `2005.08745 [physics.ins-det]`.

[123] Frank Simon. “Silicon photomultipliers in particle and nuclear physics”. In: *Nuclear Instruments and Methods in Physics Research Section A: Accelerators, Spectrometers, Detectors and Associated Equipment* 926 (2019). Silicon Photomultipliers: Technology, Characterisation and Applications, pp. 85–100. ISSN: 0168-9002. DOI: `https://doi.org/10.1016/j.nima.2018.11.042`. URL: `https://www.sciencedirect.com/science/article/pii/S0168900218316176`.

[124] Inc. Incom. *LAPPD™*. Accessed 20.09.2021, URL: `https://incomusa.com/lappd/`.

[125] Inc. Incom. URL: `https://incomusa.com/`.

[126] M.V. Nemallapudi et al. “Single photon time resolution of state of the art SiPMs”. In: *Journal of Instrumentation* 11.10 (Oct. 2016), P10016–P10016. DOI: `10.1088/1748-0221/11/10/p10016`. URL: `https://doi.org/10.1088/1748-0221/11/10/p10016`.

[127] Narongkiat Rodphai et al. “20-inch photomultiplier tube timing study for JUNO”. In: *Journal of Physics: Conference Series* 2145.1 (Dec. 2021), p. 012017. DOI: `10.1088/1742-6596/2145/1/012017`. URL: `https://doi.org/10.1088/1742-6596/2145/1/012017`.

[128] Haiqiong Zhang et al. “Tested Performance of JUNO 20” PMTs”. In: *Journal of Physics: Conference Series* 1468.1 (Feb. 2020), p. 012197. DOI: `10.1088/1742-6596/1468/1/012197`. URL: `https://doi.org/10.1088/1742-6596/1468/1/012197`.

[129] A. V. Lyashenko et al. “Performance of Large Area Picosecond Photo-Detectors (LAPPD^{TM})”. In: *Nucl. Instrum. Meth. A* 958 (2020). Ed. by Manfred Krammer et al., p. 162834. DOI: `10.1016/j.nima.2019.162834`. arXiv: `1909.10399 [physics.ins-det]`.

[130] R. L. Workman et al. “Review of Particle Physics”. In: *PTEP* 2022 (2022), p. 083C01. DOI: `10.1093/ptep/ptac097`.

[131] Hermann Kolanoski and Norbert Wermes. “3 Wechselwirkungen von Teilchen mit Materie”. In: *Teilchendetektoren: Grundlagen und Anwendungen*. Berlin, Heidelberg: Springer Berlin Heidelberg, 2016, pp. 27–90. ISBN: 978-3-662-45350-6. DOI: `10.1007/978-3-662-45350-6_3`. URL: `https://doi.org/10.1007/978-3-662-45350-6_3`.

[132] J. Lindhard and M. Scharff. “Energy Dissipation by Ions in the kev Region”. In: *Phys. Rev.* 124 (1 Oct. 1961), pp. 128–130. DOI: `10.1103/PhysRev.124.128`. URL: `https://link.aps.org/doi/10.1103/PhysRev.124.128`.

[133] Jens Lindhard, Morten Scharff, and H. E. Schioett. “RANGE CONCEPTS AND HEAVY ION RANGES (NOTES ON ATOMIC COLLISIONS, II)”. In: 1963.

[134] Hermann Kolanoski and Norbert Wermes. “11 Cherenkov-Detektoren”. In: *Teilchendetektoren: Grundlagen und Anwendungen*. Berlin, Heidelberg: Springer Berlin Heidelberg, 2016, pp. 437–474. ISBN: 978-3-662-45350-6. DOI: `10.1007/978-3-662-45350-6_11`. URL: `https://doi.org/10.1007/978-3-662-45350-6_11`.

[135] William R. Leo. “Passage of Radiation Through Matter”. In: *Techniques for Nuclear and Particle Physics Experiments: A How-to Approach*. Berlin, Heidelberg: Springer Berlin Heidelberg, 1994, pp. 17–68. ISBN: 978-3-642-57920-2. DOI: `10.1007/978-3-642-57920-2_2`. URL: `https://doi.org/10.1007/978-3-642-57920-2_2`.

[136] Chr. Møller. “Zur Theorie des Durchgangs schneller Elektronen durch Materie”. In: *Annalen der Physik* 406.5 (1932), pp. 531–585. DOI: `https://doi.org/10.1002/andp.19324060506`. eprint: `https://onlinelibrary.wiley.com/doi/pdf/10.1002/andp.19324060506`. URL: `https://onlinelibrary.wiley.com/doi/abs/10.1002/andp.19324060506`.

[137] H. J. Bhabha. “The scattering of positrons by electrons with exchange on Dirac’s theory of the positron”. In: *Proc. Roy. Soc. Lond. A* 154 (1936), pp. 195–206. DOI: `10.1098/rspa.1936.0046`.

[138] Konrad Kleinknecht. "Physikalische Grundlagen". In: *Detektoren für Teilchenstrahlung*. Wiesbaden: Vieweg+Teubner Verlag, 2005, pp. 1–42. ISBN: 978-3-322-82205-5. DOI: `10.1007/978-3-322-82205-5_1`. URL: `https://doi.org/10.1007/978-3-322-82205-5_1`.

[139] K. Abe et al. "First gadolinium loading to Super-Kamiokande". In: *Nuclear Instruments and Methods in Physics Research Section A: Accelerators, Spectrometers, Detectors and Associated Equipment* 1027 (Mar. 2022), p. 166248. DOI: `10.1016/j.nima.2021.166248`. URL: `https://doi.org/10.1016%2Fj.nima.2021.166248`.

[140] David M. Webber. "An Improved Measurement of Electron Antineutrino Disappearance at Daya Bay". In: *Nuclear Physics B - Proceedings Supplements* 233 (2012). Proceedings of the 10th International Conference on Beauty, Charm and Hyperons in Hadronic Interactions, pp. 96–101. ISSN: 0920-5632. DOI: `https://doi.org/10.1016/j.nuclphysbps.2012.12.061`. URL: `https://www.sciencedirect.com/science/article/pii/S0920563212005865`.

[141] I. Anghel et al. *Expression of Interest: The Atmospheric Neutrino Neutron Interaction Experiment (ANNIE)*. 2014. DOI: `10.48550/ARXIV.1402.6411`. URL: `https://arxiv.org/abs/1402.6411`.

[142] Hermann Kolanoski and Norbert Wermes. "13 Szintillationsdetektoren". In: *Teilchendetektoren: Grundlagen und Anwendungen*. Berlin, Heidelberg: Springer Berlin Heidelberg, 2016, pp. 495–536. ISBN: 978-3-662-45350-6. DOI: `10.1007/978-3-662-45350-6_13`. URL: `https://doi.org/10.1007/978-3-662-45350-6_13`.

[143] Christel M. Marian. "Understanding and Controlling Intersystem Crossing in Molecules". In: *Annual Review of Physical Chemistry* 72.1 (2021). PMID: 33607918, pp. 617–640. DOI: `10.1146/annurev-physchem-061020-053433`. eprint: `https://doi.org/10.1146/annurev-physchem-061020-053433`. URL: `https://doi.org/10.1146/annurev-physchem-061020-053433`.

[144] Napy1kenobi. *Electronic energy levels of an organic molecule*. Accessed 16.06.2022, URL: `https://commons.wikimedia.org/wiki/File:Pistates.svg`.

[145] A. Abusleme et al. "Optimization of the JUNO liquid scintillator composition using a Daya Bay antineutrino detector". In: *Nucl. Instrum. Meth. A* 988 (2021), p. 164823. DOI: `10.1016/j.nima.2020.164823`. arXiv: `2007.00314 [physics.ins-det]`.

[146] Xianfei Wen and Andreas Enqvist. "Measuring the scintillation decay time for different energy deposited by γ-rays and neutrons in a Cs2LiYCl6:Ce3+ detector". In: *Nuclear Instruments and Methods in Physics Research Sec-*

tion A: Accelerators, Spectrometers, Detectors and Associated Equipment 853 (2017), pp. 9–15. ISSN: 0168-9002. DOI: `https://doi.org/10.1016/j.nima.2017.02.019`. URL: `https://www.sciencedirect.com/science/article/pii/S0168900217302036`.

[147] S. Kasuga et al. "A study on the eμ identification capability of a water Ĉerenkov detector and the atmospheric neutrino problem". In: *Physics Letters B* 374.1 (1996), pp. 238–242. ISSN: 0370-2693. DOI: `https://doi.org/10.1016/0370-2693(96)00138-4`. URL: `https://www.sciencedirect.com/science/article/pii/0370269396001384`.

[148] Juan Jose Gomez-Cadenas, José María Benlloch-Rodríguez, and Paola Ferrario. "Monte Carlo study of the Coincidence Resolving Time of a liquid xenon PET scanner, using Cherenkov radiation". In: *JINST* 12.08 (2017), P08023. DOI: `10.1088/1748-0221/12/08/P08023`. arXiv: `1706.07629 [physics.ins-det]`.

[149] Derek J. Gardiner. "Introduction to Raman Scattering". In: *Practical Raman Spectroscopy*. Ed. by Derek J. Gardiner and Pierre R. Graves. Berlin, Heidelberg: Springer Berlin Heidelberg, 1989, pp. 1–12. ISBN: 978-3-642-74040-4. DOI: `10.1007/978-3-642-74040-4_1`. URL: `https://doi.org/10.1007/978-3-642-74040-4_1`.

[150] M. Wurm et al. "Optical scattering lengths in large liquid-scintillator neutrino detectors". In: *Review of Scientific Instruments* 81.5 (2010), p. 053301. DOI: `10.1063/1.3397322`. eprint: `https://doi.org/10.1063/1.3397322`. URL: `https://doi.org/10.1063/1.3397322`.

[151] Gilbert N. Plass. "Mie Scattering and Absorption Cross Sections for Absorbing Particles". In: *Appl. Opt.* 5.2 (Feb. 1966), pp. 279–285. DOI: `10.1364/AO.5.000279`. URL: `http://opg.optica.org/ao/abstract.cfm?URI=ao-5-2-279`.

[152] G Alimonti et al. "Light propagation in a large volume liquid scintillator". In: *Nuclear Instruments and Methods in Physics Research Section A: Accelerators, Spectrometers, Detectors and Associated Equipment* 440.2 (2000), pp. 360–371. ISSN: 0168-9002. DOI: `https://doi.org/10.1016/S0168-9002(99)00961-4`. URL: `https://www.sciencedirect.com/science/article/pii/S0168900299009614`.

[153] P. Kampmann, Y. Cheng, and L. Ludhova. "A semi-analytical energy response model for low-energy events in JUNO". In: *Journal of Instrumentation* 15.10 (Oct. 2020), P10007–P10007. DOI: `10.1088/1748-0221/15/10/p10007`. URL: `https://doi.org/10.1088%2F1748-0221%2F15%2F10%2Fp10007`.

[154] Tanner Kaptanoglu et al. “Spectral photon sorting for large-scale Cherenkov and scintillation detectors”. In: *Physical Review D* 101.7 (Apr. 2020). DOI: `10.1103/physrevd.101.072002`. URL: `https://doi.org/10.1103%2Fphysrevd.101.072002`.

[155] L. Agostino et al. “Future large-scale water-Cherenkov detector”. In: *Phys. Rev. ST Accel. Beams* 16 (6 June 2013), p. 061001. DOI: `10.1103/PhysRevSTAB.16.061001`. URL: `https://link.aps.org/doi/10.1103/PhysRevSTAB.16.061001`.

[156] Y. Itow et al. “The JHF-Kamioka neutrino project”. In: *3rd Workshop on Neutrino Oscillations and Their Origin (NOON 2001)*. June 2001, pp. 239–248. arXiv: `hep-ex/0106019`.

[157] Josephine Paton. *Neutrinoless Double Beta Decay in the SNO+ Experiment*. 2019. DOI: `10.48550/ARXIV.1904.01418`. URL: `https://arxiv.org/abs/1904.01418`.

[158] Y. Gando et al. “The nylon balloon for xenon loaded liquid scintillator in KamLAND-Zen 800 neutrinoless double-beta decay search experiment”. In: *Journal of Instrumentation* 16.08 (Aug. 2021), P08023. DOI: `10.1088/1748-0221/16/08/p08023`. URL: `https://doi.org/10.1088%2F1748-0221%2F16%2F08%2Fp08023`.

[159] Henning Rebber. “Event Discrimination with Topological 3D Reconstruction at MeV Energies in the JUNO Experiment”. PhD thesis. Universität Hamburg, 2019.

[160] B. J. Land et al. “MeV-scale performance of water-based and pure liquid scintillator detectors”. In: *Phys. Rev. D* 103.5 (2021), p. 052004. DOI: `10.1103/PhysRevD.103.052004`. arXiv: `2007.14999 [physics.ins-det]`.

[161] M. Agostini et al. “First Directional Measurement of Sub-MeV Solar Neutrinos with Borexino”. In: *Phys. Rev. Lett.* 128.9 (2022), p. 091803. DOI: `10.1103/PhysRevLett.128.091803`. arXiv: `2112.11816 [hep-ex]`.

[162] Edoardo Vitagliano, Irene Tamborra, and Georg Raffelt. “Grand Unified Neutrino Spectrum at Earth: Sources and Spectral Components”. In: *Rev. Mod. Phys.* 92 (2020), p. 45006. DOI: `10.1103/RevModPhys.92.045006`. arXiv: `1910.11878 [astro-ph.HE]`.

[163] John F. Beacom and Mark R. Vagins. “Antineutrino Spectroscopy with Large Water Čerenkov Detectors”. In: *Phys. Rev. Lett.* 93 (17 Oct. 2004), p. 171101. DOI: `10.1103/PhysRevLett.93.171101`. URL: `https://link.aps.org/doi/10.1103/PhysRevLett.93.171101`.

[164] Hanyu Wei, Zhe Wang, and Shaomin Chen. “Discovery potential for supernova relic neutrinos with slow liquid scintillator detectors”. In: *Phys. Lett. B* 769 (2017), pp. 255–261. DOI: `10.1016/j.physletb.2017.03.071`. arXiv: `1607.01671 [physics.ins-det]`.

[165] Stefan Schoppmann. “Review of Novel Approaches to Organic Liquid Scintillators in Neutrino Physics”. In: *Symmetry* 15.1 (2023), p. 11. DOI: `10.3390/sym15010011`. arXiv: `2212.11341 [physics.ins-det]`.

[166] J W Choi et al. “Development of water-based liquid scintillator based on hydrophilic-lipophilic balance index”. In: *Physica Scripta* 97.4 (Mar. 2022), p. 045304. DOI: `10.1088/1402-4896/ac5bbd`. URL: `https://dx.doi.org/10.1088/1402-4896/ac5bbd`.

[167] Sun Heang So et al. “Development of a Liquid Scintillator Using Water for a Next Generation Neutrino Experiment”. In: *Adv. High Energy Phys.* 2014 (2014), p. 327184. DOI: `10.1155/2014/327184`.

[168] Lindsey J. Bignell et al. “Characterization and Modeling of a Water-based Liquid Scintillator”. In: *JINST* 10.12 (2015), P12009. DOI: `10.1088/1748-0221/10/12/P12009`. arXiv: `1508.07029 [physics.ins-det]`.

[169] Drew R. Onken et al. “Time response of water-based liquid scintillator from X-ray excitation”. In: *Mater. Adv.* 1 (1 2020), pp. 71–76. DOI: `10.1039/D0MA00055H`. URL: `http://dx.doi.org/10.1039/D0MA00055H`.

[170] E. J. Callaghan et al. “Measurement of proton light yield of water-based liquid scintillator”. In: *Eur. Phys. J. C* 83.2 (2023), p. 134. DOI: `10.1140/epjc/s10052-023-11242-2`. arXiv: `2210.03876 [physics.ins-det]`.

[171] J. Caravaca et al. “Experiment to demonstrate separation of Cherenkov and scintillation signals”. In: *Phys. Rev. C* 95.5 (2017), p. 055801. DOI: `10.1103/PhysRevC.95.055801`. arXiv: `1610.02029 [physics.ins-det]`.

[172] J. Caravaca et al. “Characterization of water-based liquid scintillator for Cherenkov and scintillation separation”. In: *Eur. Phys. J. C* 80.9 (2020), p. 867. DOI: `10.1140/epjc/s10052-020-8418-4`. arXiv: `2006.00173 [physics.ins-det]`.

[173] T. Kaptanoglu et al. “Cherenkov and scintillation separation in water-based liquid scintillator using an LAPPD^{TM}”. In: *Eur. Phys. J. C* 82.2 (2022), p. 169. DOI: `10.1140/epjc/s10052-022-10087-5`. arXiv: `2110.13222 [physics.ins-det]`.

[174] Michael Thomas Nieslony. “Towards a neutron multiplicity measurement with the accelerator neutrino neutron interaction experiment”. eng. PhD thesis. Mainz, 2023. DOI: `http://doi.org/10.25358/openscience-8530`.

[175] Pedro AN Machado, Ornella Palamara, and David W Schmitz. “The Short-Baseline Neutrino Program at Fermilab”. In: *Ann. Rev. Nucl. Part. Sci.* 69 (2019), pp. 363–387. DOI: `10.1146/annurev-nucl-101917-020949`. arXiv: `1903.04608 [hep-ex]`.

[176] Tommy Ohlsson. “Proton decay”. In: *Nucl. Phys. B* 993 (2023), p. 116268. DOI: `10.1016/j.nuclphysb.2023.116268`. arXiv: `2306.02401 [hep-ph]`.

[177] B. Aharmim et al. “Measurement of Neutron Production in Atmospheric Neutrino Interactions at the Sudbury Neutrino Observatory”. In: *Phys. Rev. D* 99.11 (2019), p. 112007. DOI: `10.1103/PhysRevD.99.112007`. arXiv: `1904.01148 [hep-ex]`.

[178] Ulrich Mosel, Olga Lalakulich, and Kai Gallmeister. “Energy reconstruction in the Long-Baseline Neutrino Experiment”. In: *Phys. Rev. Lett.* 112 (2014), p. 151802. DOI: `10.1103/PhysRevLett.112.151802`. arXiv: `1311.7288 [nucl-th]`.

[179] Yoshinari Hayato and Luke Pickering. “The NEUT neutrino interaction simulation program library”. In: *Eur. Phys. J. ST* 230.24 (2021), pp. 4469–4481. DOI: `10.1140/epjs/s11734-021-00287-7`. arXiv: `2106.15809 [hep-ph]`.

[180] Jakub Żmuda et al. “NuWro Monte Carlo generator of neutrino interactions - first electron scattering results”. In: *Acta Phys. Polon. B* 46.11 (2015), p. 2329. DOI: `10.5506/APhysPolB.46.2329`. arXiv: `1510.03268 [hep-ph]`.

[181] Costas Andreopoulos et al. “The GENIE Neutrino Monte Carlo Generator: Physics and User Manual”. In: (Oct. 2015). arXiv: `1510.05494 [hep-ph]`.

[182] Ryosuke Akutsu. “A Study of Neutrons Associated with Neutrino and Antineutrino Interactions on the Water Target at the T2K Far Detector”. PhD thesis. Tokyo U., 2019.

[183] A. A. Aguilar-Arevalo et al. “Bringing the SciBar detector to the booster neutrino beam”. In: (Jan. 2006). arXiv: `hep-ex/0601022`.

[184] Fermilab: Accelerator Division — Operations Department. *Concepts Rookie Book*. URL: `https://operations.fnal.gov/rookie_books/concepts.pdf`. August 2020.

[185] Ubaldo Dore, Pier Loverre, and Lucio Ludovici. “History of accelerator neutrino beams”. In: *Eur. Phys. J. H* 44.4-5 (2019), pp. 271–305. DOI: `10.1140/epjh/e2019-90032-x`. arXiv: `1805.01373 [physics.acc-ph]`.

[186] A. A. Aguilar-Arevalo et al. “The Neutrino Flux Prediction at MiniBooNE”. In: *Phys. Rev. D* 79 (2009), p. 072002. DOI: `10.1103/PhysRevD.79.072002`. arXiv: `0806.1449 [hep-ex]`.

[187] ANNIE collaboration. *ANNIE detector outline*. Accessed 25.01.2022, URL: `https://cdcvs.fnal.gov/redmine/attachments/28735/ANNIEdetectoroutline_reduced.png`.

[188] A. R. Back et al. “Accelerator Neutrino Neutron Interaction Experiment (ANNIE): Preliminary Results and Physics Phase Proposal”. In: (July 2017). arXiv: `1707.08222 [physics.ins-det]`.

[189] A. R. Back et al. “Measurement of Beam-Correlated Background Neutrons from the Fermilab Booster Neutrino Beam in ANNIE Phase-I”. In: *JINST* 15.03 (2020), P03011. DOI: `10.1088/1748-0221/15/03/P03011`. arXiv: `1912.03186 [physics.ins-det]`.

[190] S. Agostinelli et al. “Geant4—a simulation toolkit”. In: *Nuclear Instruments and Methods in Physics Research Section A: Accelerators, Spectrometers, Detectors and Associated Equipment* 506.3 (2003), pp. 250–303. ISSN: 0168-9002. DOI: `https://doi.org/10.1016/S0168-9002(03)01368-8`. URL: `https://www.sciencedirect.com/science/article/pii/S0168900203013688`.

[191] J. Allison et al. “Geant4 developments and applications”. In: *IEEE Transactions on Nuclear Science* 53.1 (2006), pp. 270–278. DOI: `10.1109/TNS.2006.869826`.

[192] J. Allison et al. “Recent developments in Geant4”. In: *Nuclear Instruments and Methods in Physics Research Section A: Accelerators, Spectrometers, Detectors and Associated Equipment* 835 (2016), pp. 186–225. ISSN: 0168-9002. DOI: `https://doi.org/10.1016/j.nima.2016.06.125`. URL: `https://www.sciencedirect.com/science/article/pii/S0168900216306957`.

[193] ANNIE collaboration. *ANNIEsoft/WCSim*. Accessed 31.01.2023, URL: `https://github.com/ANNIEsoft/WCSim`.

[194] Mikhail Polyanskiy. *RefractiveIndex.INFO - Optical constants of SCHOTT - multiple purpose - BOROFLOAT® 33*. Accessed 12.01.2023, URL: `https://refractiveindex.info/?shelf=glass&book=SCHOTT-multipurpose&page=BOROFLOAT33`.

[195] A.V. Lyashenko et al. “Performance of Large Area Picosecond Photo-Detectors (LAPPDTM)”. In: *Nuclear Instruments and Methods in Physics Research Section A: Accelerators, Spectrometers, Detectors and Associated Equipment* 958 (2020). Proceedings of the Vienna Conference on Instrumentation 2019, p. 162834. ISSN: 0168-9002. DOI: `https://doi.org/10.1016/j.nima.2019.162834`. URL: `https://www.sciencedirect.com/science/article/pii/S0168900219312690`.

[196] SCHOTT AG. *webpage of SCHOTT AG*. Accessed 12.01.2023, URL: `https://www.schott.com/`.

[197] Felix Benckwitz. “Application of the Topological Track Reconstruction to ANNIE and study of its potential for water Cherenkov detectors”. MA thesis. University Hamburg, 2019.

[198] Theia collaboration. *Non-published simulation software*. Received 27.01.2020 from Björn Wonsak.

[199] OpenGATE Collaboration. *5. Generating and tracking optical photons*. Accessed 07.02.2023, URL: `https://opengate.readthedocs.io/en/latest/generating_and_tracking_optical_photons.html`.

[200] Hans Steiger. Personal communication. Date: 25. August 2021.

[201] Sergey Burdin, Marko Horbatsch, and Wendy Taylor. “A correction to Birks’ Law in liquid argon ionization chamber simulations for highly ionizing particles”. In: *Nuclear Instruments and Methods in Physics Research Section A: Accelerators, Spectrometers, Detectors and Associated Equipment* 664.1 (2012), pp. 111–116. ISSN: 0168-9002. DOI: `https://doi.org/10.1016/j.nima.2011.10.044`. URL: `https://www.sciencedirect.com/science/article/pii/S0168900211019942`.

[202] B. von Krosigk et al. “Measurement of the proton light response of various LAB based scintillators and its implication for supernova neutrino detection via neutrino-proton scattering”. In: *Eur. Phys. J. C* 73.4 (2013), p. 2390. DOI: `10.1140/epjc/s10052-013-2390-1`. arXiv: `1301.6403 [astro-ph.IM]`.

[203] Geant4 development team. *Reference Physics Lists*. Accessed 09.02.2023, URL: `https://geant4.web.cern.ch/node/155`.

[204] Mihaly Novak. *Short Guide to Choosing Your Physics Lists*. Accessed 09.02.2023, URL: `https://indico.cern.ch/event/776050/contributions/3241826/attachments/1789270/2914266/ChoosingPhysLists.pdf`.

[205] Geant4 development team. *Use Cases - Reference Physics Lists*. Accessed 09.02.2023, URL: `https://geant4.web.cern.ch/node/302`.

[206] H. Rebber et al. “Particle identification at MeV energies in JUNO”. In: *Journal of Instrumentation* 16.01 (Jan. 2021), P01016–P01016. DOI: `10.1088/1748-0221/16/01/p01016`. URL: `https://doi.org/10.1088/1748-0221/16/01/p01016`.

[207] Davide Chicco and Giuseppe Jurman. “The advantages of the Matthews correlation coefficient (MCC) over F1 score and accuracy in binary classification evaluation”. In: *BMC Genomics* 21 (Jan. 2020). DOI: `10.1186/s12864-019-6413-7`.

[208] M. Agostini et al. “Correlated and integrated directionality for sub-MeV solar neutrinos in Borexino”. In: *Phys. Rev. D* 105.5 (2022), p. 052002. DOI: `10.1103/PhysRevD.105.052002`. arXiv: `2109.04770 [hep-ex]`.

[209] Andrea Bizzego et al. “Improving the Efficacy of Deep-Learning Models for Heart Beat Detection on Heterogeneous Datasets”. In: *Bioengineering* 8.12 (2021). ISSN: 2306-5354. DOI: `10.3390/bioengineering8120193`. URL: `https://www.mdpi.com/2306-5354/8/12/193`.

Danksagung (Acknowledgements)

Erst einmal möchte ich mich bei Prof. Caren Hagner bedanken für die Übernahme des Erstgutachtens und all die Unterstützung, insbesondere in der Abschlussphase dieser Arbeit. Besonderer Dank gilt Dr. Björn Wonsak für die Übernahme des Zweitgutachtens und dafür, dass er mir immer mit Rat und Tat zur Seite stand. Einen solchen Quell an hervorragenden Ideen werde ich vermutlich in meinem Leben nicht wieder treffen und es ist schade, dass nicht noch mehr Studenten in den Genuss seiner Anleitung kommen werden. Ich möchte hier betonen, dass auch Björn zu der untenstehenden Liste an ehemaligen Kollegen gehört und ich mich selten mit einem Menschen so gut über Bücher unterhalten konnte.

Weiterhin möchte ich meinen übrigen (ehemaligen) Kollegen danken. Besonders hervorheben möchte ich hier Rosmarie Wirth fürs Korrekturlesen und das offene Ohr. Du hast mir mit deinem Auge für Details und deinem erfrischenden Kommentarstil immens geholfen und fast alles, was in dieser Arbeit steht, gelesen. Ich entschuldige mich hiermit für die Länge dieser Arbeit. Hajo danke ich für all die Gespräche, seine nette Art und seine unerschütterliche Ruhe. Dr. Daniel Bick danke ich dafür, dass er an mich geglaubt und mir die Möglichkeit gegeben hat, diese Arbeit bezahlt zu einem Ende zu bringen. Daniel ist nicht nur ein hervorragender Kollege, sondern auch ein Freund für mich, der eine große Hilfe in Fragen aller Art ist. Dr. Stefan Bieschke, Dr. David Meyhöfer und Dr. Henning Rebber sowie Felix Benckwitz (Team Kriecht-Nicht/Stenckwitz!) und Benedict Kaiser möchte ich danken für die tolle Zeit, die wir zusammen verbringen und für sämtliche Unterstützung, die ich durch euch erfahren durfte. Ihr alle habt diesen Job sich häufig mehr nach Spaß denn als Arbeit anfühlen lassen und ich verspreche, dass ich mich weiter bemühen werde, den Kontakt aufrecht zu erhalten. Ich möchte behaupten, dass mir das bis jetzt einigermaßen gelungen ist.

Besonderer Dank gilt auch Prof. Ralf Möller, der mir ein zweites Zuhause gegeben hat, ohne dass ich diese Arbeit abbrechen oder unterbrechen musste. Ich bin mir sicher, dass diese Arbeit nie das Licht der Welt erblickt hätte, wenn ich die Chance auf einen so passenden Zweitjob nicht bekommen hätte.

I would also like to thank the ANNIE collaboration for the opportunity to be part of such a great experiment and wonderful community. I would like to specially thank Dr. Marcus O'Flaherty, Prof. Michi Wurm, Dr. Michael Nieslony, Dr. Matt Wetstein, Dr. Emrah Tiras and Dr. Teal Pershing.

Michael bekommt noch einen kurzen eigenen Absatz, weil unser Aufenthalt am

Fermilab und die dort ausgesprochenen Buchempfehlungen, sowie der Ausflug nach Chicago bei mir immer noch in sehr guter Erinnerung sind. Auch die aus meiner Sicht hervorragende Zusammenarbeit werde ich vermissen.

Außerdem möchte ich mich bei meinen Freunden Fabian Schmidt und Ole Steg bedanken, die mich diese Zeit überstehen lassen haben und ohne die das Leben allgemein deutlich weniger lebenswert wäre. Nicht unerwähnt lassen möchte an dieser Stelle auch Eveline Steg, die dabei mitgeholfen hat, mich seelisch durch den Abschluss dieser Arbeit zu bringen. Ein riesiges Dankeschön möchte ich meinen Eltern Astrid und Uwe Stender sagen, die immer für mich da waren und mir mit allem geholfen haben. Ich hätte mir keine tolleren Eltern wünschen können.

Unbeschreiblich viel Dank schulde ich meiner Frau, die mich in dieser langen Zeit und insbesondere in den stressigen letzten Wochen, immer unterstützt, aufgebaut und an mich geglaubt hat. Ohne dich und deine unglaubliche Stärke wäre dies nicht möglich gewesen und auf dieser Arbeit sollte mindestens zur Hälfte dein Namen stehen, so oft wie du mir den Rücken freigehalten hast, damit ich weiter daran arbeiten und schreiben konnte. Ich hätte mir niemand Besseren an meiner Seite vorstellen können und ich liebe dich.

Und danke an Linus für seine schnurrige Unterstützung.

Erklärung

Hiermit versichere ich an Eides statt, die vorliegende Dissertationsschrift selbst verfasst und keine anderen als die angegebenen Hilfsmittel und Quellen benutzt zu haben. Die eingereichte schriftliche Fassung entspricht der elektronischen Ausgabe. Die Dissertation wurde in der vorgelegten oder einer ähnlichen Form nicht schon einmal in einem früheren Promotionsverfahren angenommen oder als ungenügend beurteilt.

Malte Stender

Hamburg, den 31.01.2024
Ort, Datum

Unterschrift